UNIVERSITÄT BONN

Physikalisches Institut

Novel magnetic nanoparticles: size and surfactant effects on geometric and electronic structure, probed using X-ray Absorption Spectroscopy

von

Natalie Palina

The investigation of magnetic nanoparticles is of great interest for potential applications. Due to huge surface, the properties of nanoparticles deviate from those of bulk material. In order to understand and control these deviations, X-ray Absorption Spectroscopy has been used in this thesis. Specifically, transition metal nanoparticles, prepared by wet-chemical synthesis which allows control of the size of the particles, were investigated to determine their electronic and geometric structure. For Co nanoparticles, prepared in presence of aluminumtrialkyl compounds, a detailed model of metallic core formation and further stabilization under different synthesis conditions can be established. The size of the particles is sensitive to the initial molar ratio of precursor to aluminium organics and the surfactant used for stabilization. Using a molar ratio of $Co_2(CO)_8$:Al(oct)$_3$ = 10:1 and KorantinSH as a surfactant leads to the production of 10 nm H.C.P. nanoparticles, whereas the addition of a second surfactant results on formation of 10 nm F.C.C. nanoparticles. The thickness of the protection shell, formed around metallic core is dependent on the chain length of aluminumtrialkyl. Application of 'smooth oxidation' to this system leads to the formation of a $CoCO_3$ shell. This metrical can be further modified by different surfactants to obtain air stable ferrofluids. Another sample system discussed in this thesis is CoTi doped $BaFe_{12}O_{19}$. In this system, X-ray Absorption Spectroscopy provides an explanation for the pronounced size-dependent changes in magnetic properties. Magnetic properties are mostly influenced by surface effects, such as chemical re-/decomposition towards the BaO phase, which are found in the nanoparticles below the supermagnetic size limit, i.e. > 10 nm.

UNIVERSITÄT BONN

Physikalisches Institut

Novel magnetic nanoparticles: size and surfactant effects on geometric and electronic structure, probed using X-ray Absorption Spectroscopy

von

Natalie Palina

This thesis is dedicated to my first teacher in Physics, my mother.

Contents

1   Motivation

Nanoparticulate metals are generally defined as isolated particles between l and 50 nm in size. The main interest for potential applications of these materials stems from their huge surface areas, relative to bulk. It has been calculated that *e.g.* an iron cube of 10 nm size exhibits 10% of the atoms at the surface, whereas downsizing these particles to 2.5 nm exposes 60% of the atoms at the surface [Bra94].

Nanoparticulate metal materials can be obtained in the form of *metal nanopowders*, where the grain size ranges between 5 – 50 nm, and *metal nanoparticles* of 1 – 10 nm size having a relatively narrow size distribution. Nanoparticulate *metal colloids* are isolable particles with sizes between l nm and 15 nm where the metal cores are prevented from agglomeration by protecting shells. Metal colloids can be redispersed in organic solvents [Kre01].

Nanostructured metal particles can be obtained either by so called 'top down methods', for example by the mechanical grinding of bulk metals, or via 'bottom-up methods' which rely on the wet chemical reduction of metal salts or, alternatively, the controlled decomposition of metastable organometallic compounds such as metal carbonyls. For the production of nanoparticulate metal particles a large variety of organic compounds, e.g. donor ligands and polymers are used to control the growth of the initially formed nanoparticles and to prevent them from agglomeration. This approach has become one of the most common and powerful synthetic methods in this field [Bön01]. Alternatively, the modified glass crystallization method is another promising technique for producing nanoparticles with a complex structure [Mül03b].

Nanoparticles and *colloids* form the bridge between atoms and molecules on the one hand and bulk material on the other hand. The geometric and electronic structure of nanoparticles with even 1000 atoms still differs significantly from the bulk material [Mar91]. Also the macroscopic chemical [Car02, Mod03], physical: electrical [Muk03], optical [Sal02], thermal and magnetic properties are dependent on the particle size and differ from those of the corresponding bulk material.

Because of their unique properties, nanosized particles are found to be suitable for numerous applications. Ferrofluids, for example, obtained using iron coated nanoparticles are promising candidates for magnetic drug delivery [Loc02]. PtRu nanoparticles are promising electrode materials for Polymerelectrolyte – Membrane fuel cell (PEMFC) heterogeneous catalysts, which can be used in commercially important reactions [Sch94, Pau00, and Cro00]. The high values of magnetic anisotropy and saturation magnetization ensure a wide application of the magnetoplumbite (M-type) ferrites as permanent magnets and for high-density magnetic recording applications [Tur93].

Geometric and electronic information is necessary to characterize nanoparticles in a wider sense and to understand their properties as there is a strong correlation between their composition and structure on the one hand, and physical and chemical properties on the other. For each particular case the following information is important:

- Geometric structure - size of the particles, crystallographic phase, composition;

- Electronic structure – valency, band structure, size dependence of these properties;

- Interaction of the metal core with the protective shell and/or possible support;

- Consequences of the above mentioned properties on the macroscopic chemical properties.

Among the numerous experimental techniques available for obtaining some part of this information, X-ray Absorption Spectroscopy (XAS) turned out to be very powerful, as no long range order is required, in

contrast to X-ray Diffraction (XRD) measurements. X-ray Photoelectron Spectroscopy (XPS) and Ultraviolet Photoelectron Spectroscopy (UPS) provide information about surface composition and oxidation states but fail to determine the geometric structure. Infrared Spectroscopy (IR) provides information of surface composition but no direct access to the interaction between the core and the surfactant. In contrast to that, the mechanism of interaction which takes place during particle formation and further stabilization can be understood from *in-situ* X-ray Absorption Fine Structure (XAFS) measurements. They provide the necessary information, as this technique allows the experiments to be performed in a protective gas atmosphere, to look at the nanoparticle in dispersion or fluids, and to apply heat treatment, as well as offering many other opportunities for monitoring changes which might occur during particle preparation and conditioning. Providing size information is of great importance as numerous types of size-dependent changes in properties of nanoparticles have been observed [Voi00, Jon01, Zha03, and Chr04]. However, the techniques which are generally used for size determination do not always provide complete information on a given system. For example, in the case of size investigation of magnetic nanofluids the hydrodynamic and magnetic diameters observed from Transmission Electron Microscope (TEM), Small Angle Neutron Scattering (SANS) and magnetic measurements (Temperature-dependent magnetorelaxometry – TMRX, zero field cooled magnetization – ZFC and low-temperature coercivity) are different. The hydrodynamic diameter, in case of magnetic fluids, derived from viscous measurements or indirectly from SANS measurements is the sum over core, shell and polymer average chain length diameters. TEM provide a core plus shell diameter and magnetic measurements reveal the magnetic/core diameter. Combinations of these techniques with information which can be obtained from XAFS make it possible to distinguish between core and shell diameters.

To show the importance of size and surfactant effects, two illustrative (non-magnetic) cases are discussed in this thesis. These effects have the most significant influence on extremely small nanoparticles with an average diameter about 1 nm. Studies on the syntheses and properties of *magic size* (chapter 5.1) transition-metal (TM) nanoclusters have attracted significant attention for a long time. Such materials display novel physical properties owing to their large surface areas and/or quantum size effects [Gue76, Boa95], and they can be used to develop new optical [Hag05] and electronic devices [Bar00, Sch98]. Platinum clusters are of particular interest and the subject of intense study, because of their unique electronic and catalytic properties [Sch94]. It has been shown [Wen04] that, following the wet-chemical approach, it is possible to produce single shell Pt nanoparticles. The second interesting research topic is that the size and shape of resulting nanoparticles can be controlled during the synthesis by the addition of 'seeds' (i.e. Pt nanoparticles with an average size of ~ 1 nm.), which accelerate the nucleation and prevent particles from further growth. Thus, another size and shape controlling parameter is introduced into the preparative procedure. The 'seeding' method of synthesis has been developed to control the mode of particle formation from the same precursor and with the same precursor to stabilizer K_2PtCl_4: $[C_6H_9NO]_n \equiv$ PVP ratio regulated only by the amount of seeding. The dramatic influence of seeds on the resulting nanoparticles and their interaction with the surrounding environment were investigated by XANES measurements. Several models of stabilization are suggested based on EXAFS analysis.

Magnetic fluids, where the magnetic particle core is covered by mono- or bilayer of a suitable surfactant, are very sensitive to even slight differences in the preparative conditions and parameters. Here, magnetic nanoparticles and ferrofluids were prepared by a size-selective route, established by Bönnemann AG (chapter 4.1.3), which leads to air stable monodisperse colloidal cobalt nanoparticles via the thermolysis of $Co_2(CO)_8$ in the presence of aluminum alkyl. Previous work has shown that aluminum trialkyl can be used successfully to prepare colloidal mono- and bimetallic nanoparticles by 'reductive stabilization'. Two major advantages of this methodology are: (1) a surfactant is required for the preparation of nearly monodisperse transition metal colloids and (2) these nanoparticles have highly reactive organo-Al groups as colloidal stabilizers, which can be chemically modified to tailor their dispersion characteristics and even to develop 2-D or 3-D nanoparticle networks [Buc02, Köh01]. The importance of surfactants which are used during preparation of nanoparticles became an intensive topic of scientific discussion during the last few years. The study of the stabilization mechanism provoked by different surfactants is an important issue which has to be

taken into account in order to understand the changes in the magnetic properties of nanoparticles. Stabilization of the nanoparticles can be done through two mechanisms, via formation of surface coordinations or a core-shell system. This study shows that the resulting nanoparticles are sensitive to small differences in the synthesis condition, especially when nanoparticles have been produced using a wet-chemical approach. In particular, by applying a 'smooth oxidation' procedure, in the stage of the wet colloids developed by Bönnemann *et.al*, it is possible to modify the protection shell in a way that the metallic core of the particles is no longer affected by exposure to air. Based on X-ray Absorption Spectroscopy measurements presented in this thesis, it is possible to conclude that the oxidation of the metal core by air is inhibited by the presence of a shell consisting of organic compounds such as $CoCO_3$, and not the formation of cobalt-oxides, as would be expected. Thus, the novel 'smooth oxidation' procedure can be treated as an additional type of protection of nanoparticles against oxidation.

Ferrites are magnetic materials with a quite complex structure. Hexagonal ferrites with magnetoplumbite structure have attracted the attention of scientists for a long time [Col90, Cab95]. Barium hexaferrites nanoparticles, which have been investigated in this thesis, have been prepared by Dr. R. Müller IPHT Jena. Recent research within the DFG Priority Program SPP104 'Colloidal Magnetic Fluids: Basics, Preparation and Application of New Ferrofluids' show that the powders prepared by means of a modified glass crystallization method [Mül94] can be a suitable base for magnetic ferrofluids with higher anisotropy and lower magnetic losses than iron oxide–based fluids. Over time, for the iron oxide ferrofluids, the transformation from magnetic magnetite or γ–Fe_2O_3 into diamagnetic α–Fe_2O_3 phase is likely to occur. Thus, they are not very suitable for a long–term application. In contrast to iron oxide–based ferrofluids, the barium hexaferrites ferrofluids have magnetic properties comparable with iron oxide, and show long–term stability. However, it has been observed that magnetic properties change in unexpected ways. There are competitive explanations in the literature: changes in the magnetic properties of hexaferrites nanopowders in comparison with the bulk can be understood as so-called 'dead layer' formation, oxidation of γ–Fe_2O_3 towards α–Fe_2O_3 during synthesis or order-disorder effects. These mechanisms will influence the orientation of magnetic moments, and thus determine magnetic properties. The XAS measurements in combination with theoretical calculation of XANES spectra using FEFF8 code can provide the necessary information to confirm one or the other model. The Ba L_{III}-, Fe K-, Ti K-XANES and EXAFS results, presented in this thesis, support the idea that in this system not only a geometric rearrangement of the atoms as a function of particle size and thus surface energy occurs, but also a chemical de/recomposition. However, this does not lead to the observed deviation of magnetic properties, which are expected for a certain size.

Understanding size and surfactant effects on magnetic nanoparticles using the X-ray Absorption Spectroscopy have been the main aim of this thesis. Finally, it turned out that XAS is a powerful technique which provides enough information for detailed explanations of size dependent changes in the properties of nanostructured materials.

2 Theory of X-Ray Absorption Spectroscopy

Over the last decades X-ray Absorption Spectroscopy (XAS) has emerged as a highly informative probe of the local structure around selected atomic species in solids, liquids, and molecular gases [Che02, Mor98]. Foremost among its strengths are its applicability to amorphous materials, as no medium or long range order is necessary within the sample, and the ability to probe the environments of different elements individually in the sample by selecting the incident x-ray energy.

Although the phenomenon and its basic explanation in terms of a quantum mechanical interference effects have been known since the 1930's (Kronig), the phenomenon did not become a practical experimental tool until two events occurred: the developing of a theory of the essential physical aspects of the processes leading to the standard EXAFS equation, by Stern, Sayers, and Lytle [Say71], and their proposal of a simple method of data analysis. The amount of information available from a single XAS spectrum from a well-chosen experiment is inaccessible in many cases by any other technique.

2.1 Interaction of photons with matter

Throughout the history of modern physical science, X-rays have been used as a powerful tool in analytical, physical, chemical, and structural characterization of matter. The interactions of photons with matter will be described in this chapter.

When a beam of monochromatic photons travels though matter, it loses intensity via interaction with matter. According to the Lambert-Beer's Law, the linear absorption coefficient – μ_l, which consists of coherent (Rayleigh) and incoherent (Compton) scattering coefficient (μ_{sc}), as well as photoelectric (μ_{ph}) and pair production coefficient (μ_{pair}), can be described as:

$$I = I_0 \cdot e^{-\mu_l(E) \cdot t} \tag{2.1}$$

where I_0 is the incident intensity, t is the sample thickness, and I is the intensity transmitted through the sample, as shown in Figure 2.1.
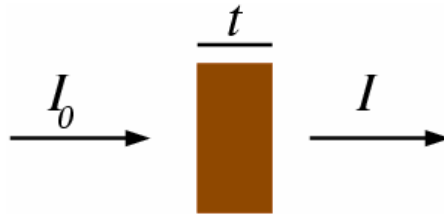

Figure 2.1: Simple scheme of x-ray interaction with matter

At most X-ray energies the dominant attenuation process is photoabsorption. The linear photoabsorption coefficient increases rapidly with the atomic number Z and decreases with increasing photon energy E. The dependence is given by:

$$\mu_{ph} \propto \frac{Z^4}{A \cdot E^3} \tag{2.2}$$

Another effect which takes place when X-rays interact with matter is scattering. The scattering process relates to the fact that X-ray photons can be deflected from their original direction of propagation, either with or without loss of energy, by scattering an electron. The scattering can be categorized into coherent (Rayleigh scattering), when the photon scatters elastically at the atom cores with no loss of energy, and incoherent interference (Compton scattering), where the wavelength is shifted slightly to a higher value as part of the incident energy is transferred to the electron as the photon changes its direction. According to the Klein-Nishina formula, the Compton linear attenuation coefficient – μ_{incoh} is:

$$\mu_{incoh} \quad \propto \quad \frac{\ln(E)}{E} \cdot Z \quad\quad\quad (2.3)$$

Besides these two effects, pair production might take place. Pair production is the process in which a high-energy photon is completely transformed into an electron – positron pair. Therefore, this is a process whereby energy is transformed into matter. The rest mass energy of an electron is 0.511 MeV, so the threshold for electron-positron pair production is 1.02 MeV. Thus, pair production becomes one of the most important interactions with matter for X-ray energies well above 1 MeV, but is of no importance in XAS experiments. The total linear attenuation coefficient can be written as the sum over contributions from the principal photon interactions as:

$$\mu_l = \mu_{ph} + \mu_{sc} + \mu_{pair} \quad\quad\quad (2.4)$$

where μ_{ph} is the atomic photoabsorption effect linear attenuation coefficient , $\mu_{sc} = \mu_{coh} + \mu_{incoh}$, are the coherent (Rayleigh) and the incoherent (Compton) scattering attenuation coefficient, respectively, and μ_{pair} corresponds to electron-positron pair production.

The linear attenuation coefficient is related to the linear cross sections by $\mu_l = \frac{N_A}{A} \cdot \sum_{i=1}^{3} \sigma_i$, where N_A is the Avogadro number, A the atomic weight and σ_i represent photoabsorption, scattering and pair production, described above. Cross section usually expressed in the barns, 1barn$=10^{-24}$ cm^2. Figure 2.2 contributions from different interaction to the total cross section are shown for Cobalt.

During an X-ray absorption experiment, the energy dependence of the photo-absorption cross section is measured. As the wavelength of the X-rays is gradually decreased (or energy of the photons is increased), the linear attenuation coefficient μ_l generally decreases until a certain wavelength is reached where the linear attenuation coefficient increases by several fold. For this rising to occur, the photons must have enough energy to excite the core shell electrons. This effect leads to the appearance of so-called absorption '*edges*'. The minimum photon energy required to eject an electron out of a particular atomic state to the continuum is called ionization energy, $E_0 = h\nu_0 = hc/\lambda_0$, where h is the Planck's constant, c the speed of light, and λ_0 the wavelength for which the photon energy is equal to the absolute value of the binding energy of the electron. Further decrease in λ causes a decrease in μ_l until another edge is reached. In Sommerfelds notation these edges are classified as K, L, M, etc. according to the values of the main quantum number n=1, 2, 3, etc., respectively. Latin numbers characterize the different suborbital of the exited shell; L_I-, L_{II}-, L_{III}-edge for ionization of 2s-, $2p_{1/2}$-, $2p_{3/2}$-electrons, respectively. Each shell has a degeneracy of n^2 and is capable of housing $2n^2$ electrons. Pauli's *exclusion principle* forbids any two electrons in an atom to have the same set of quantum numbers, n, l, m, and s, which are the main, the orbital, the magnetic and the spin quantum number, respectively.
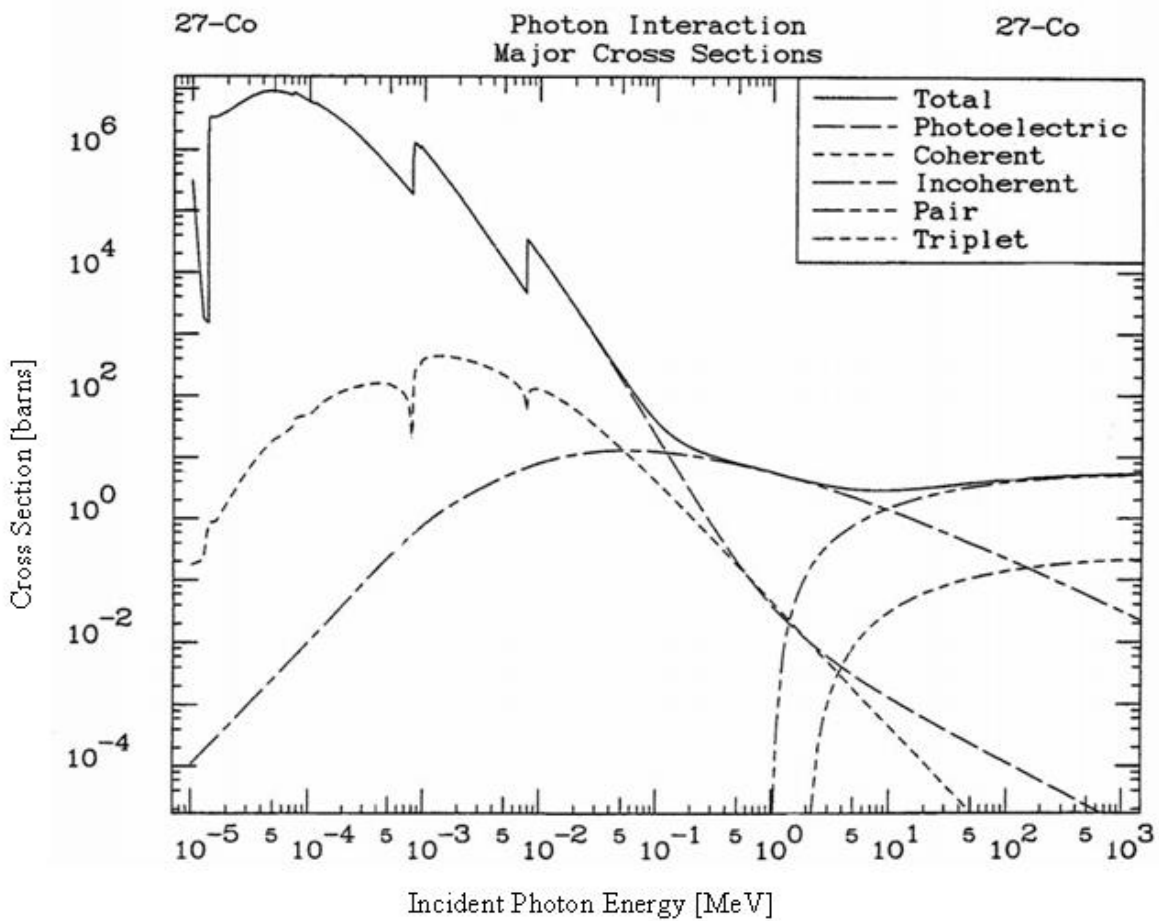
Figure 2.2: Cross section for true X-ray absorption for Cobalt [Der02]

Absorption of a photon leads to the excitation and the following relaxation of the atom via fluorescence or Auger effects. Schemes of these processes are shown in Figure 2.3.
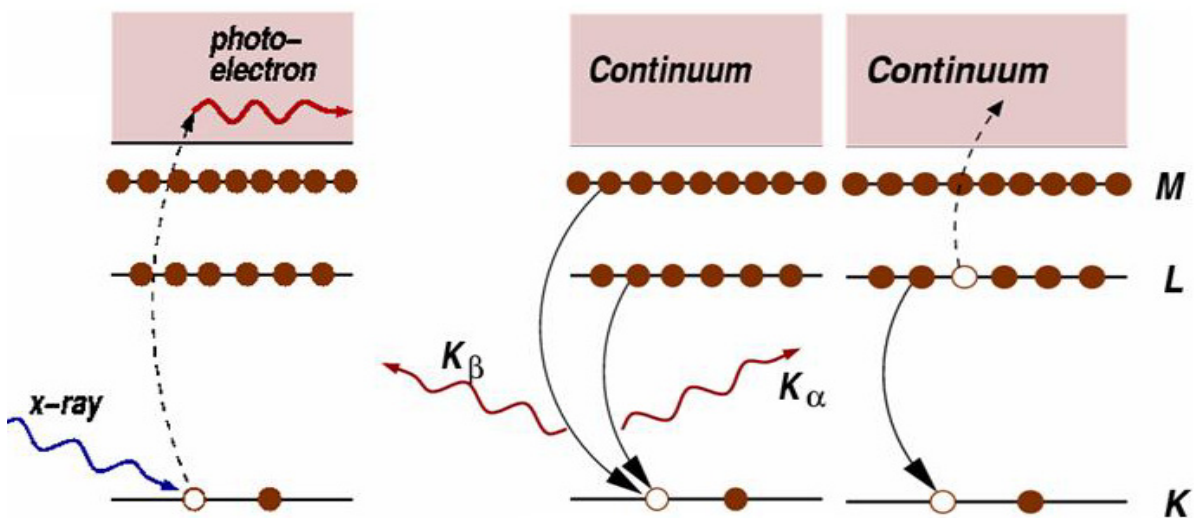

Figure 2.3: The photoelectric effect, in which an X-ray photon is absorbed and a core-level electron is excited into the continuum (left). X-ray fluorescence (middle) and the Auger effect (right), [New03]

The filling of an inner shell vacancy by an outer shell electron produces X-ray fluorescence. For example, an L shell electron dropping into the K level gives the K_α fluorescence line. Fluorescence yield is defined as the ratio of emitted X-ray to the number of primary vacancies created. Alternatively, the Auger effect occurs in which the core vacancy is filled by an electron dropping from a higher shell while the energy gained is transferred to another electron that is excited into the continuum. The dependence of the linear-attenuation coefficient μ_l in fluorescence X-ray or Auger emission can be estimated as:

$$\mu_l \propto \frac{I_f}{I_0} \tag{2.5}$$

where I_f is the intensity of a fluorescence line associated with the absorption process and I_0 is the incident X-ray intensity. The Auger effect plays an important role in surface studies and X-ray fluorescence is used in case of low concentrated samples.

2.2 Extended X-ray Absorption Fine Structure: EXAFS

Normally, X-ray Absorption spectra are divided into two regions, the so-called X-ray Absorption Near Edge Structure (XANES), which usually goes to about 40-50eV above the absorption edge (more detailed description is given in chapter 2.3), and the Extended X-ray Absorption Fine Structure (EXAFS). These two regions are shown in Figure 2.4.

EXAFS refers to the oscillatory variation of the X-ray absorption as a function of the photon energy 40-1000 eV above an absorption edge. In this chapter, a brief description of various aspects of the EXAFS technique will be given. EXAFS is best understood in terms of the wave – like behavior of the photo-electron created in the absorption process when it travels as a wave with a wave number k given by (2.6). Generally, for the further data evaluation, the X – ray energy is converted to k, the wave number of the photo-electron, which has dimensions of 1/distance
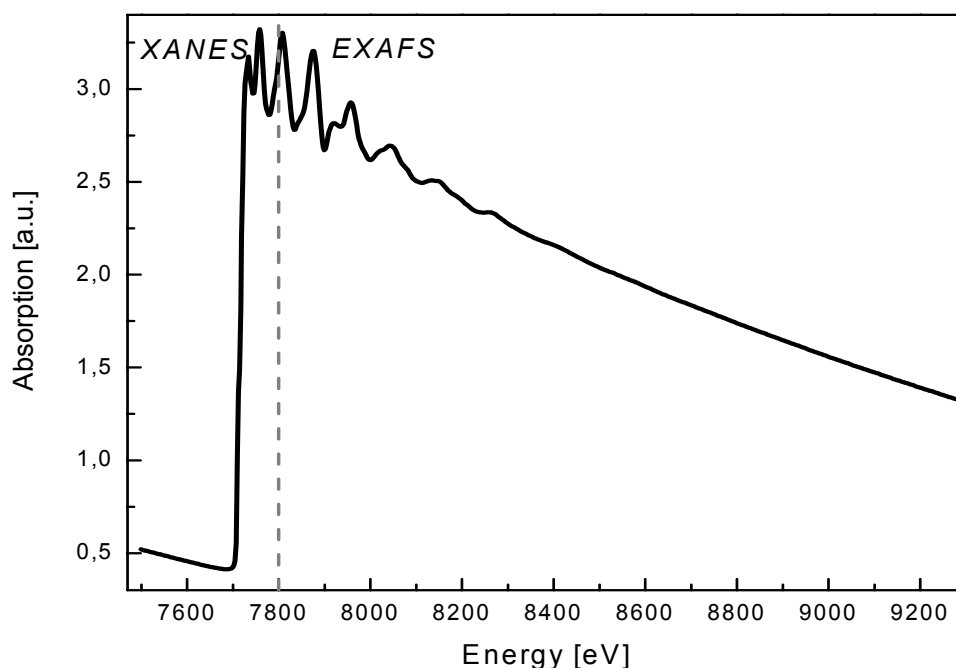

Figure 2.4: X-ray absorption spectrum for Cobalt foil with indication of the XANES and EXAFS regions

$$k = \sqrt{\frac{8\pi^2 m_e}{h^2} \cdot (E - E_0)} \qquad (2.6)$$

where E_0 is the ionization edge energy, m_e is the electron rest mass and h is Planck's constant. The absorption process for an isolated atom is schematically shown in Figure 2.5.
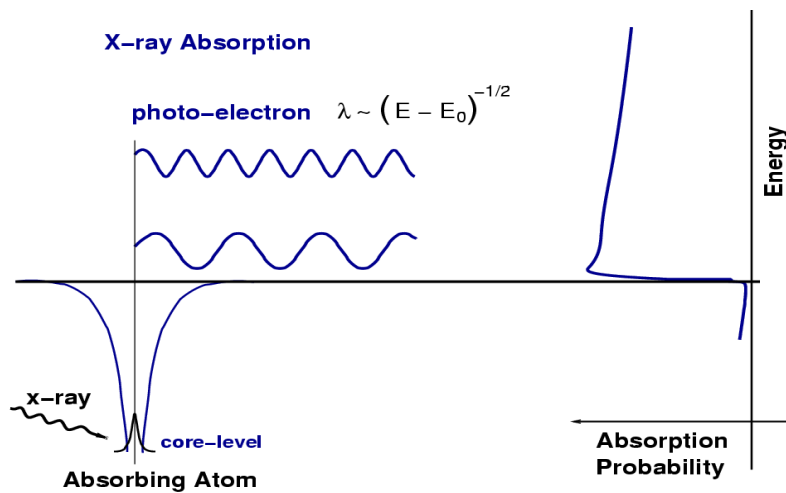

Figure 2.5: Qualitative explanation of an absorption process for an isolated atom [New03a]

When neighboring atoms are included in the absorption process, the outgoing photo-electron wave is scattered from these neighboring atoms, thereby producing an incoming electron wave which interferes either constructively or destructively with the outgoing wave. The final wave is then the sum of the outgoing and all the incoming waves, one from each neighboring atom. This interference between the outgoing and the incoming waves gives rise to a oscillation of the absorption coefficient which is illustrated in Figure 2.6.
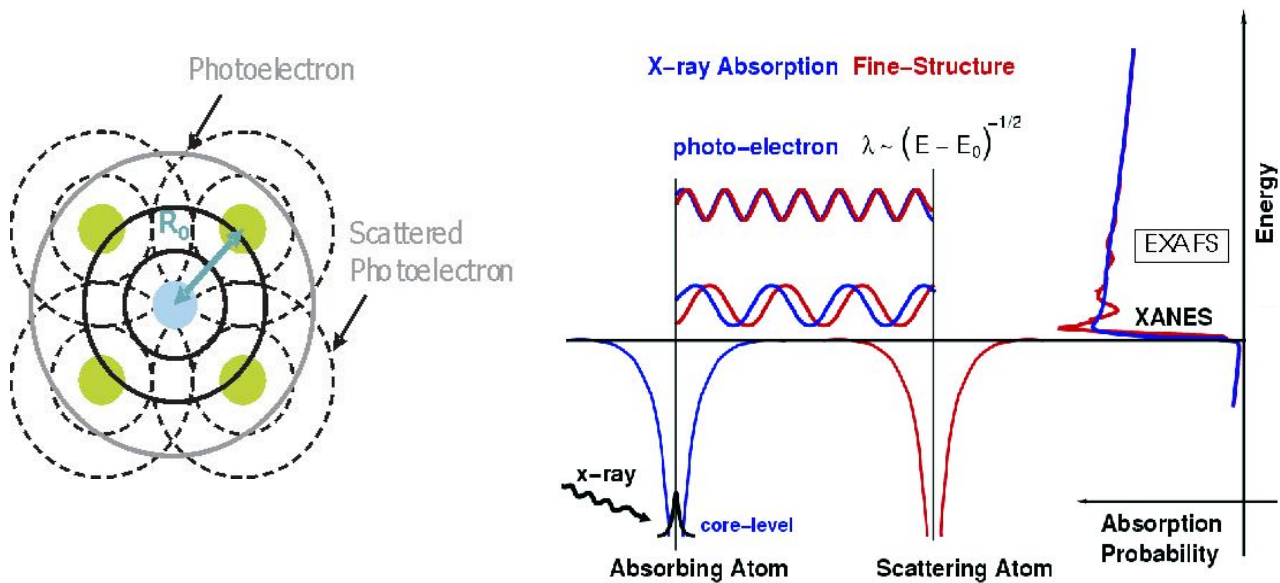

Figure 2.6: EXAFS oscillations as a result of scattering of the photo-electron wave at neighboring atoms [New03a]

A typical EXAFS spectrum is shown in Figure 2.7. The sharp rise in μ(E) at 7709 eV (Co K–edge) is clearly visible in the spectra, as are the oscillations in μ(E) representing the fine structure.
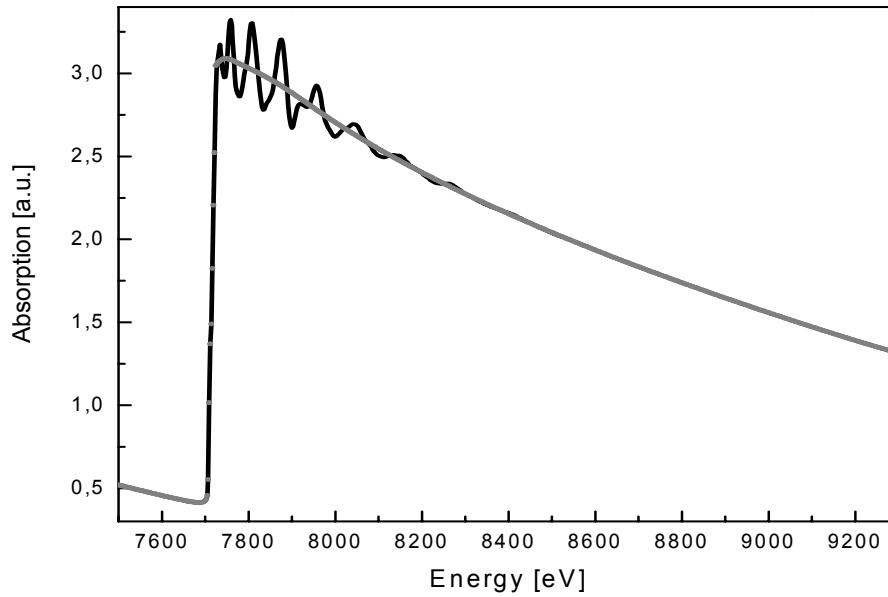

Figure 2.7: μ(E) for Co-foil and smooth background function μ₀(E)

The oscillations well above the absorption edge are described by the EXAFS fine-structure function χ(E), as

$$\chi(E) = \frac{\mu(E) - \mu_0(E)}{\Delta\mu_0(E)} \tag{2.7}$$

where μ(E) is the measured absorption coefficient, $\mu_0(E)$ is a smooth background function representing the absorption of an isolated atom, and $\Delta\mu_0$ is the measured jump in the absorption μ(E) at the threshold ionization energy E_0 which is equal to 7709 eV in the case of a Co-foil [Tho01]. The oscillations in χ(k), which are shown in Figure 2.8, represent the sum over frequencies corresponding to different near-neighbor coordination shells which can be described according to the EXAFS equation (2.8).
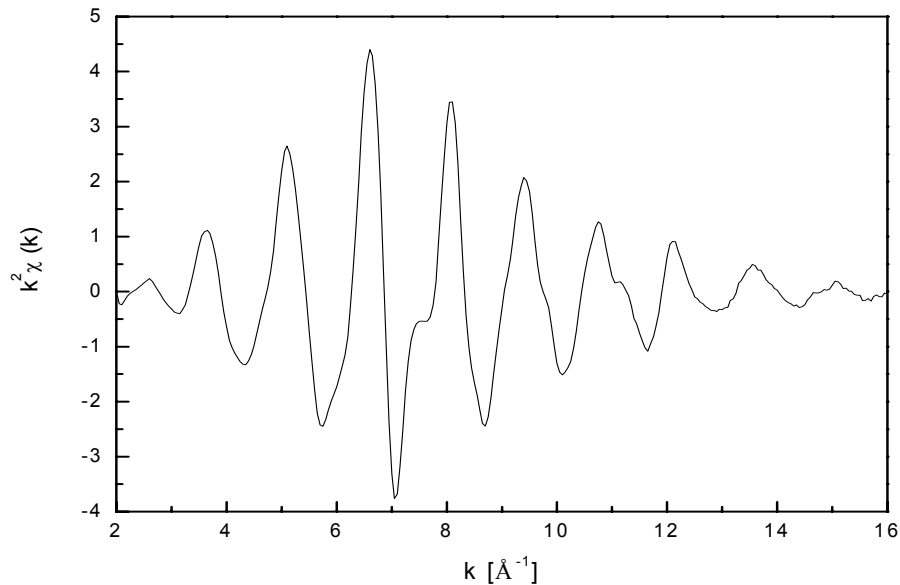

Figure 2.8: Extracted χ(k) function of the Co-foil measurements, where χ(k) is weighted by k^2 to emphasize the quickly decaying features in the high k region

$$\chi(k) = \sum_j A_j(k) \cdot \sin\left[2kR_j + \delta_j(k)\right] \tag{2.8}$$

where $A_j(k)$ is the amplitude, $\delta_j(k)$ the phase shift and R_j the distance to neighboring atoms of type j. The amplitude becomes:

$$A_j(k) = \frac{N_j S_0^2 F_j(k) \cdot e^{-2\sigma_j^2 k^2} \cdot e^{\frac{-2R_j}{\lambda_j(k)}}}{kR_j^2} \tag{2.9}$$

where N_j is the coordination number of the identical atoms of type j at a given distance from the central atom. S_0^2 is the so-called amplitude reduction factor, which takes into account losses caused by multiple excitation of the absorber atom from shake-up (excitation of an electron to a bound state) and shake-off (excitation to continuum) processes. $F_j(k)$ is the backscattering amplitude of atoms of type j. The $e^{-2\sigma_j^2 k^2}$ - term describes thermal and static disorder causing an additional damping of the EXAFS amplitude, especially at large k. σ^2 is a Debye-Waller type factor, defined as the root mean square displacement of the average nearest neighbor distance. The Debye-Waller approximation, assuming that the vibrational/thermal motion is harmonic and the static disorder is Gaussian-like. $\lambda_j(k)$ is the mean-free-path of the photo-electron, which is the average distance traveled by a photo-electron before it scatters inelastically or the core-hole is filled. The $1/(kR_j^2)$ – term describes the decreasing of the amplitude of an outgoing spherical wave with the distance R_j from its origin.

The frequency of each EXAFS wave depends on the distance between the absorbing atom and the nearest neighbors, since the photo-electron wave from the absorber and the scatterer interfere, resulting in EXAFS oscillations. During this process, the phase of the wave is shifted twice at the absorber and once at the scatterer. It has to be mentioned that these phase shifts are k-dependent and thus, the function of the energy E, as a difference in E-E$_0$ will lead to a different k and thus a different phase shift. As the amplitude depends on the number and backscattering amplitude of the neighboring atoms, by analysing the EXAFS spectra, one can access structural information around the absorber. Structural determinations can be accomplished by the Fourier Transform technique, which isolates the contribution of the different shells as a function of the radial distance from the absorber. In such a radial distribution function, the positions of the peaks are related to the distances between the absorber it's and nearest neighbors and the amplitudes are related to the coordination numbers and types of neighboring atoms.

2.2.1 UWXAFS programs package

The analysis of the EXAFS spectra is done using the UWXAFS program package, developed at the University of Washington. The data evaluation is based on simulation results done by the FEFF-code (Version 8.20) and uses the AUTOBK and the FEFFIT program. The experimental data were energy calibrated by the position of the first inflection point for the corresponding metal foil. AUTOBK removes the background and extracts the EXAFS-function $\chi(k)$. For normalization of the absorption-edge, the pre-edge is fitted in the region from -200 to -50 eV, relative to the edge position, using a Victoreen function and is then extrapolated to E$_0$. After the edge, a piecewise polynomial function (spline) is used to approximate $\mu_0(E)$. The spline is adjusted so that the low-R components of the resulting PRDF (Pseudo Radial Distribution Function) signals are minimized and the atomic-like absorption contribution is removed. The number of independent points in the fitting-region is given by

$$N_{bkg} = 1 + \frac{2 \cdot \Delta k \cdot R_{bkg}}{\pi} \qquad (2.10)$$

where R_{bkg} is the maximum distance over which the background function $\mu_0(E)$ is fitted. This value is not phase corrected and chosen in AUTOBK by the user. Δk is the interval of the experimental data in the k-space. Further information is given in the corresponding manual [New93].

As an example, the Fourier transformation and fit result (left) of a χ (k) – function of a Cobalt-foil measurement is presented in Figure 2.9. For the further analysis of the $\chi(k)$-function the program FEFFIT is used. The goal of an EXAFS analysis is to fit the sum of simulated $\chi(k)$-functions to the $\chi(k)$-function given by the experimental results either in R- or in k-space. The reduced $\chi(k)_\upsilon^2$-function which primarily characterizes the quality of the fit

$$\chi(k)_\upsilon^2 = \frac{N_{idp}}{N \cdot \varepsilon^2} \cdot \sum_{i=1}^{N} \{[\mathrm{Re}(f_i)]^2 + [\mathrm{Im}(f_i)]^2\} \qquad (2.11)$$

is minimized in the fit. In this equation ε characterizes uncertainties in the measurement, f_i the difference of the experimental and the theoretical $\chi(k)$ – or $\chi(R)$ – function, $N_{fr} = N_{idp}-N_{var}$ – the number of degrees of freedom in the fit, and N_{var} the number of variables in the fit. N_{idp}, the number of independent data points in a spectrum, is given by:

$$N_{ind} = \frac{2 \cdot \Delta k \cdot \Delta R}{\pi} + 2 \qquad (2.12)$$

where N_{ind} represents the number of knots in the low-R range of $\chi(R)$-between R =[0.0;R_{bkg}].
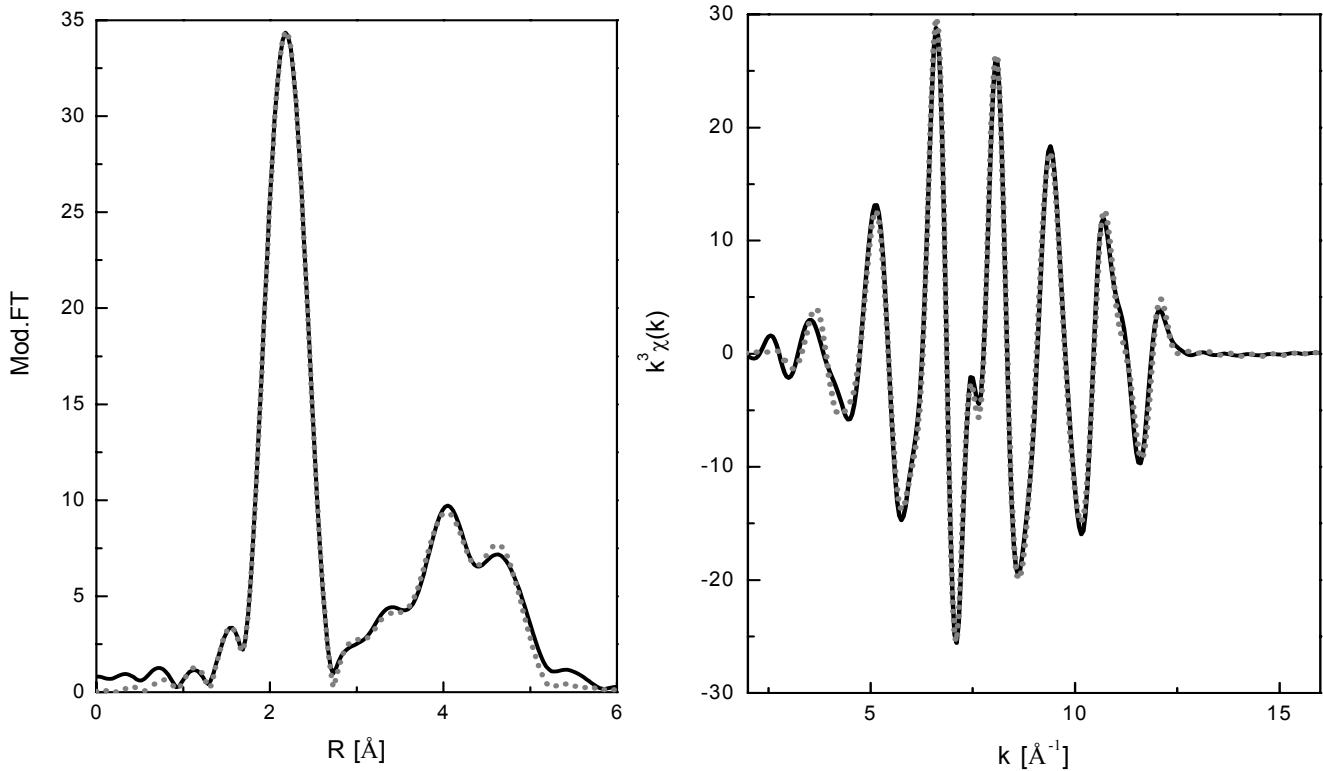

Figure 2.9: Fourier Transformation and back transformed signal fro Cobalt foil experimental data (solid) and fit (dot)

In the fitting procedure variations of the distance to the scattering atom ΔR, the coordination number N, the Debey-Waller-Factor σ^2 and the shift from the energy E_0 are taken into account for each path. The parameters can either be fixed to a defined value or varied during the fit after setting a starting value. If the number of variables provoked by the amount of scattering paths reaches the limit of the degrees of freedom, defined variables have to be combined to reduce the number of parameters. Uncertainties of the variables as well as correlations between variables are calculated by FEFFIT. The results of the fitting procedure in R – and q – space for Co – foil are shown in Figure 2.9. It must be pointed out that the amplitude-reduction factor S_0^2 is slightly energy-dependent, but assumed as a constant value for the calculation within the fit. The coordination-number and distance for the first coordination shell were set as a fixed parameter for the Co-foil data evaluation, then the amplitude reduction factor S_0^2 was calculated and kept constant for every following EXAFS-analysis at the respective edge. The results of the Co-foil evaluation are shown in Figure 2.9 and summarized in table 2.1.

Global variables					
S_0^2		0.825	E_0		4.64±0.75 eV
Paths variables					
Path j	N_{th}	*Degeneracy N_j*	$R_j [Å]$	$R_{eff} [Å]$	$\sigma^2_j [Å^2]$
Feff0001.dat	12	11.2±0.7	2.51±0.01	2.50	0.0063
Feff0003.dat	6	2.7±0.7	3.52±0.02	3.55	0.0063
Feff0010.dat	12	10.8±1.7	4.36±0.01	4.34	0.0063
Feff0028.dat	12	7.8±4.3	4.77±0.05	5.01	0.010
Feff0031.dat	6	5.8±2.6	4.95±0.02	5.01	0.010

Table 2.1: Used paths and fit parameters for analysis of Cobalt foil

Only the five most important paths with relative amplitudes of at least 40% were used for this fit; non-relevant paths were skipped. These five dominant paths represented the first three single-scattering-paths, a double–and triple–scattering-paths. For parameter reduction, the energy-shift E_0 was set to the same value for every scattering path. Only two Debye-Waller-Factors have been used in the fitting routine, one for the single scattering paths (1, 3 and 10) and another for the multiple scattering paths. The $\chi(k)$-function (not presented) was weighted by k^3 and fitted in the region from 2.35 to 12.8 Å^{-1} in k–space and from 0.9 till 5.2 Å in R–space. Figure 2.9 (right) shows the back-transformed $\chi(k)$-function of the first three coordination-shells and demonstrates once more the good agreement in phase and amplitude between the experimental data and the fit.

2.3   X-ray Absorption Near Edge Structure: XANES

The region of the X-ray Absorption Near Edge Structure is approximately 40 – 50 eV above the absorption edge [Aga91]. The limiting energy which separates XANES from EXAFS is by no means exactly defined, since the transition from the one regime to the other is smooth. The XANES region consists of strong absorption features. This is due to the fact that in the XANES region, the electron's kinetic energy is small, compared to the EXAFS region and the multiple scattering resonances on the neighboring atoms tends to be dominant. Thus the energy range of XANES is the region where the single scattering approximation is not valid. This is true for the wave length ($\lambda = 2\pi/k$) grater than the interatomic distance d. Hence in XANES the wave vector is $k < 2\pi/d$, then the energy ($E = \hbar^2 k^2/2m$) range is given by, $E[eV] < 151/d^2 - V$, where V is the

Fermi energy in metals. As the energy depends on *d* and V, the XANES energy range is different for the different substances. As can be understood from the interpretations of XANES spectra close to the beginning of the absorption edge, in most cases a strong rising of the absorption is found. This strong structure is the so-called 'white line'. Features of absorption spectra, which are below the ionization energy, are attributed to transitions to unoccupied orbitals, following the dipole selection rule. Since the density of the final states (states into which excitation can occur) change, and thus the charge density, the profile of the absorption spectrum of the same element is different in different chemical environments. Also, the electron binding energies change dependent on chemical environment around absorbing atom, which results in a shift of the absorption edge towards higher energies and an increase of the 'white line' intensity, in case of 3d metals. Thus, the XANES region provides information of local characteristics of absorber such as formal oxidation state, and the type of bond.

It is possible to extract information on a given sample based only on comparison with suitable reference compounds. This approach is called 'fingerprinting'. As an example, the XANES spectra for different cobalt oxides and bulk Cobalt are shown in Figure 2.10 .

From Figure 2.10 it is clearly seen that the position of the absorption edges are shifted for different cobalt oxides compounds to the higher energy with the increasing of formal oxidation state; this trend is known as a 'chemical shift'.
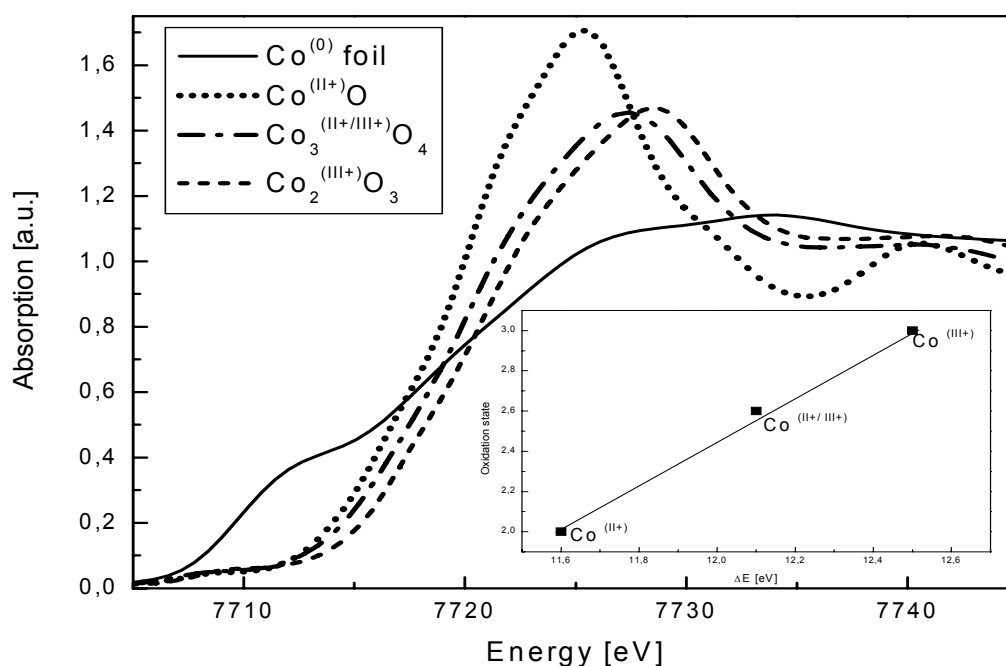

Figure 2.10: K-edge XANES spectra of Co metal and several cobalt oxides

In addition to XANES 'fingerprint' analysis, the qualitative determination of oxidation states of transition metal oxides assuming a linear dependence of the energy position of absorption edge has been widely reported [Aga70, Cap95, Nie01, Bre04]. Capehart et. al. propose a quantitative method to determine the oxidation state of unknown compounds based on comparison with reference compounds. The edge shift, i.e. the difference between the sample and the reference absorption edge energies, has been determined from integrals of the normalized absorption spectra. The area under the XANES spectra is calculated as an integral absorption for the reference and unknown compound till the some energy E_s (sample) and E_r (reference). The area under the XANES spectra is assumed to be the same, so the samples edge shift is defined as:

$\delta E_s = E_s - E_r$ [Cap95]. In particular cases [Bre04] it is possible to use the linear dependence of oxidation state on edge position, and thus determine the oxidation state of more complex compounds (chapter 7).

In particular, for K edge absorption where the initial state is a 1s state, the photo-electron has t o end up in a p state according to the dipole selection rule ($\Delta l = \pm 1$, $\Delta m = 0, \pm 1$). In this notations l=0, 1, 2, 3 correspond to $s-$, $p-$, $d-$, f-subshells, respectively. The presence of characteristic features like pre-edge shoulder in the case K–edge of $3d$ transition metals is understood by transition from $1s$ to hybridized $p - d$ orbitals.

In addition to the electronic information, XANES provides information about the binding geometry around absorbing an atom as the multiple scattering processes, which depends strongly on the angle between scatterers, dominates in this region. As an example, the spectra of Chromium compounds are shown in Figure 2.11, for which formal oxidation states and coordination geometries are summarized in table 2.2.

In the case of the Chromium oxides, appearance of the pre-edge shoulder allows one to distinguish between the coordination geometry, either tetrahedral or octahedral coordination geometry with oxygen, around the absorbing atom. With increasing formal oxidation state, the width of $p -$ and $d -$ band decreases, as does the possible overlap between p and d, leading to a decrease in the intensity of the pre-edge structure. At the same time, the reduction of the bandwidth of the p band leads to a concentration of $p -$ states in the white line region, thus the increasing of intensity of this feature is understood.

Reference	Oxidation state	Coordination geometry
Chromium	0	cubic
Cr_2O_3	III+	octahedral
CrO_2	IV+	distorted octahedral
CrO_3	VI+	tetrahedral

Table 2.2: Summary of oxidation states and coordination geometry for different Cr-oxides

Two main features have to be mentioned in the Cr-oxides XANES spectra: the position of the Cr-K edge (5989 eV) itself and the so-called pre-edge shoulder. An effect of coordination geometry on the fine structure in the K-edge region of transition metal compounds, which has often been observed, is that the pre-edge features appears only in the XANES spectra of tetrahedral coordinated transition metal compounds (spectrum of $Cr^{(VI+)}$ in Figure 2.11).

In CrO_3, chromium is tetrahedrally coordinated with oxygen, lacking an inversion centre, exhibiting a single intense pre-edge shoulder at about 5993 eV in Figure 2.11, which can be assigned to a dipole allowed transition of 1s electron to an unoccupied antibonding orbital.

Comparison with the XANES spectra of compounds with octahedral coordination geometry Cr_2O_3 (doted line in Figure 2.11) immediately reveals to the absence of discussed spectral features.

CrO_2 is a $Cr^{(+IV)}$-containing compound with a slightly distorted octahedral coordination geometry (rutile-structure). Hence, it is not surprising that the structure in the near-edge region of the CrO_2 absorption spectrum is similar to that of Cr_2O_3, which also contains octahedrally coordinated chromium atoms. The Cr_2O_3 XANES spectrum can be regarded as a reference spectrum for compounds where chromium is octahedrally coordinated. On the other hand, the small absorption features in the CrO_2 spectrum before the absorption edge can be explained by the changes in symmetry, a slightly off-centre position of the $Cr^{(+IV)}$ atoms. Since the pre-edge line is interpreted to be dipole-forbidden for coordination geometries that possess an inversion center (octahedral), a weak intensity is indeed expected for CrO_2.

Thus, the XANES can be used as a probe for determining local geometry, formal oxidation state and valence for various different compounds.
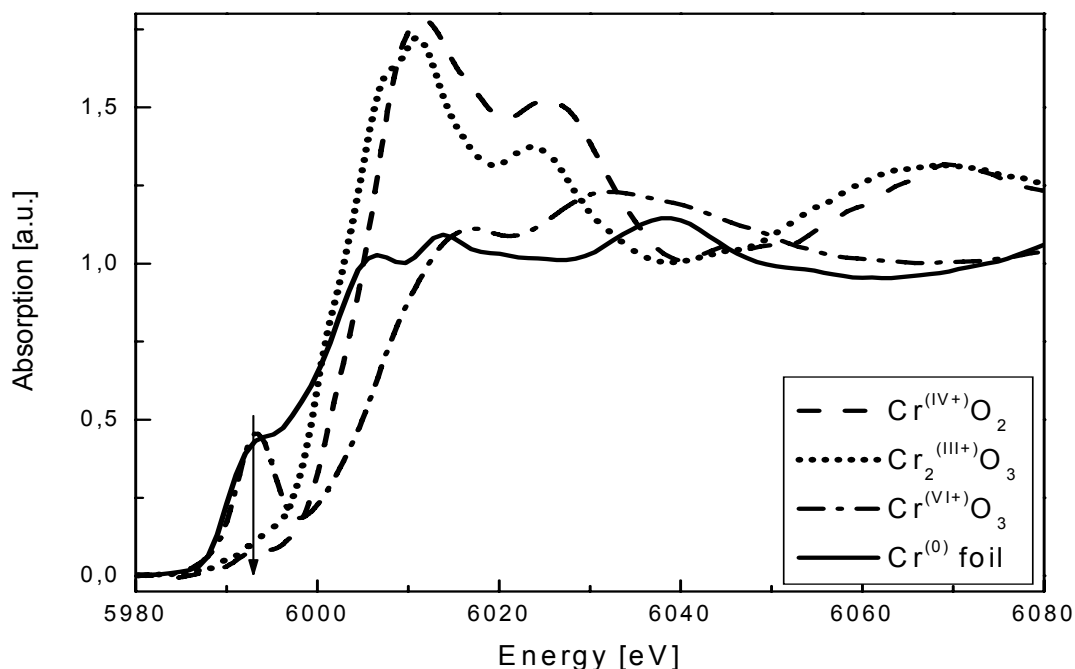

Figure 2.11: Cr K-edge XANES of Cr metal and several Cr oxides

2.3.1   XANES calculation using FEFF8 code

Most of the calculations presented in this thesis have been performed using the FEFF8 code. The code is based on a full multiple scattering (FMS) formalism of Real Space Green's Function (RSGF) theory. Consequently, three ingredients play an important role: the spherical self consistent muffin-tin (MT) potential, relativistic dipole matrix elements between core and continuum states and two center matrix elements of the free propagator. For the construction of the scattering potential, the total electron density is first approximated by overlapped free atom densities. This is done using a relativistic Dirac-Fock code assuming an existing core–hole in the excited level of the absorbing atom. The scattering potential then is a result of solving the Poisson equation, with addition of local exchange and imposing spherical symmetry in MT form. Thus, a new potential is calculated, which leads to the new density of states and this process is iterated until self–consistency is reached. It is also possible to calculate the ground state DOS. The FEFF8 code contains several approximations. For example, many–body effects are incorporated in terms of complex, energy dependent self–energy, the Heldin-Lundqvist electron–gas self–energy [Ank98, Ank02]. This self–energy adds important final states broadening and self–energy shift but does not contribute any new features to the spectra. The self–energy together with core–hole lifetime builds in both loss factor encountered in X–ray absorption spectra of ideally ordered system (0 Kelvin). In the FEFF8 code potential with spherical symmetry is considered. Finally, as a SCF (self–consistent field)   scattering potential is calculated, the parameters of interest (phase shift, matrix elements, etc.) are obtained. Full multiple scattering XANES calculations are done for a specified cluster size.

As an example, the calculation of a hexagonal-closed-packed (hcp, α–phase) Cobalt reference foil is presented in Figure 2.12. The XANES spectrum of bulk α–Co displays a pre-edge feature at approximately 7712 eV, usually assigned to an electron transition from *1s* to a hybridized *p–d* orbital, and a white line consisting of two well resolved peaks at about 7727 and 7733 eV. Good agreement with the experimental spectrum is achieved, with respect to the characteristic pre–edge structure and double-peak white line, where the second peak amplitude is higher than that of the first peak. The profile and position of the shape-resonance in the theoretically calculated spectrum match the experimentally taken spectra. Differences between intensities and the position of the pre–edge features in calculated and experimental spectra can be explained as a consequence of the core hole treatment. In FEFF8 calculations the threshold or Fermi energy of isolated atomic system is calculated in the presence of a screened core hole, in accordance with the final–state rule. In this interpretation, it corresponds to a fully relaxed core hole. However, if the atomic system is not isolated, the relaxation of states is different and thus a systematic energy shift of the pre–edge feature, as a function of exchange potential (real part of self–energy) and a core hole life time is observed.
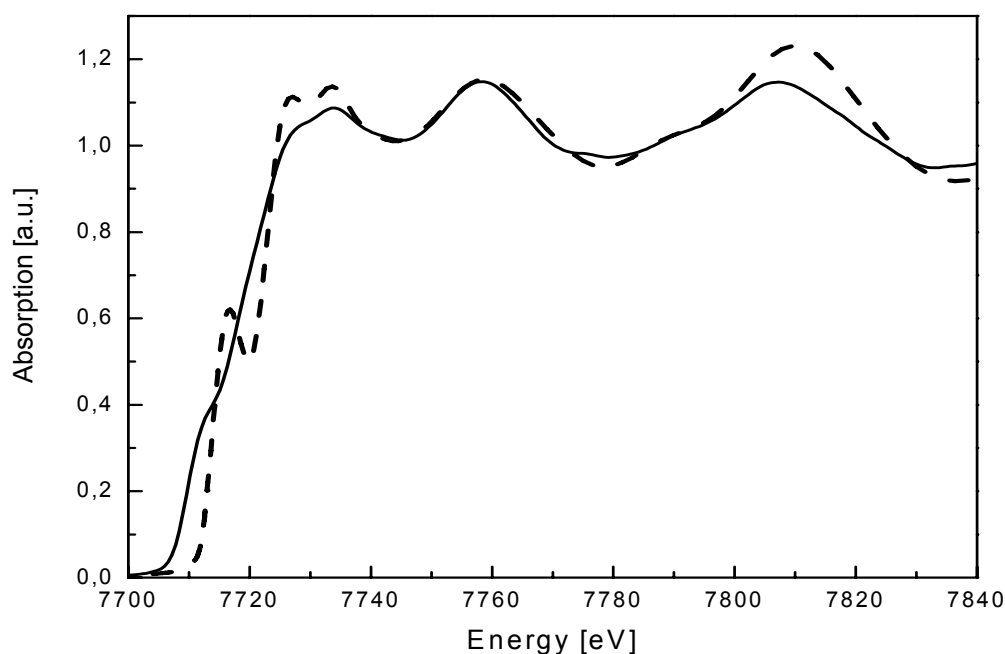

Figure 2.12: Experimental spectrum from Cobalt foil (solid) and calculation using FEFF8 code (dashed)

Finally, one can conclude that the FEFF8 code is a good tool for both XANES and EXAFS calculations, as the characteristic features in the calculated spectra show good agreement with experimental data. It may be helpful in understanding the geometric and electronic structure of an absorbing atom not only if no suitable reference compounds can be found for fingerprint analysis, but also to get an impression about features of absorption spectra for complex compounds.

3 Experiment

In this chapter the two Synchrotron Radiation (**SR**) facilities the **E**lectron **S**tretcher and **A**ccelerator (***ELSA***) at the Institute of Physics Bonn, Germany and the **C**enter of **A**dvanced **M**icrostructures and **D**evices (***CAMD***), Baton Rouge, USA, at which the measurements presented in this work have been performed will be briefly described. The main parameters of the ELSA and CAMD SR facilities are summarized in table 3.1.

3.1 The synchrotron radiation source ELSA and CAMD

Schematic diagrams of ELSA and the CAMD storage ring are shown in Figure 3.1 and Figure 3.2. Basic component of these storage ring are:

- *Particle source and acceleration*

  Typically, storage rings operate with electrons, and the electron source is an electron gun. The power of the emitted synchrotron radiation is proportional to the inverse of the mass of the accelerated particle to the fourth power (3.1).

$$P = \frac{e^2 \cdot c \cdot E^4}{6 \cdot \pi \cdot \varepsilon_0 \cdot r^2 \cdot (m_0 \cdot c^2)^4} \qquad (3.1)$$

  where e, m_0 and E are the charge, mass and energy of the electron, respectively. c is the speed of light ε_0 is the permittivity of free space and r the radius of the bending dipole magnets. The electrons are chosen for synchrotrons as they are the lightest, most readily available particle. To obtain SR, electrons have to be pre–accelerated; for this purpose, a *linear accelerator* (***LINAC)*** is in use in both the ELSA and CAMD ring. In the LINAC, electrons are accelerated in a straight line by an electric field and further acceleration of electrons is provided by a *booster ring.*

- *Vacuum system*

  The lifetime of the electron beam is limited by e.g. scattering from residual gas particles. Therefore, a good ultra-high vacuum (***UHV)*** within the beampipe is required. Typical pressure at ELSA and CAMD ring is in the range of 10^{-7} and 10^{-10} Torr, respectively.

- *Bending and focusing magnets*

  The beampipe of the storage ring does not follow a circular path, but consists of a number of straight sections joined together by bends. At each bend the path of the electron beam is changed by a dipole magnet. Magnetic fields at ELSA and CAMD are typically at around 0.74 and 1.48 Tesla, for 2.3 GeV and 1.3 GeV ring energy respectively. The necessary magnetic field is achieved by conventional electromagnets. For accelerated electrons the bending of the electron beam using the magnet is described by:

$$\frac{1}{r} = \frac{0.2998 \cdot B}{E} \qquad (3.2)$$

where *r* is the radius of the bending dipole magnets in meters, *E* is the energy in GeV and *B* is the field in Tesla. The focusing of the electron beam is done by quadrupole magnets at CAMD which are placed at appropriate points around the ring. At ELSA, a special arrangement of focusing/defocusing quadrupole magnets, known as FODO structures, are used to focus the beam.

- *Operating energy and ring current*

The most important parameters, which characterize a storage ring are the ring current and the operating energy. ELSA usually operates at energies of 1.6 GeV, 2.3 GeV and 2.7 GeV for SR experiments. Maximal currents for the ELSA ring are 65 mA and 35mA for 2.3 GeV and 2.7 GeV, respectively. The operation energy at CAMD is 1.3 GeV and the corresponding maximum current is 250 mA. Spectral distributions for different operation energies at the ELSA and CAMD ring are present in Figure 3.3.

- *Beam position and lifetime stability*

For XAS experiments , especially *in-situ* and *time resolved* measurements, it is vital that the beam does not move significantly on the surface of the sample. For this purpose, beam position monitors and steering magnets are used at the ELSA and CAMD ring. The beam current in a storage ring decays exponentially and the time of this decay is an important parameter, as it determines how rapidly the photon flux (see Figure 3.3) will change during an experiment and how long it will last before the flux is insufficient to be useful, so the beam has to be dumped and the ring refilled. Average lifetime for the Bonn synchrotron in 2.3 GeV and 2.7 GeV operation modes are 120 and 80 minutes respectively. For the 1.3 Gev operating energy at CAMD the average lifetime is 720 min.
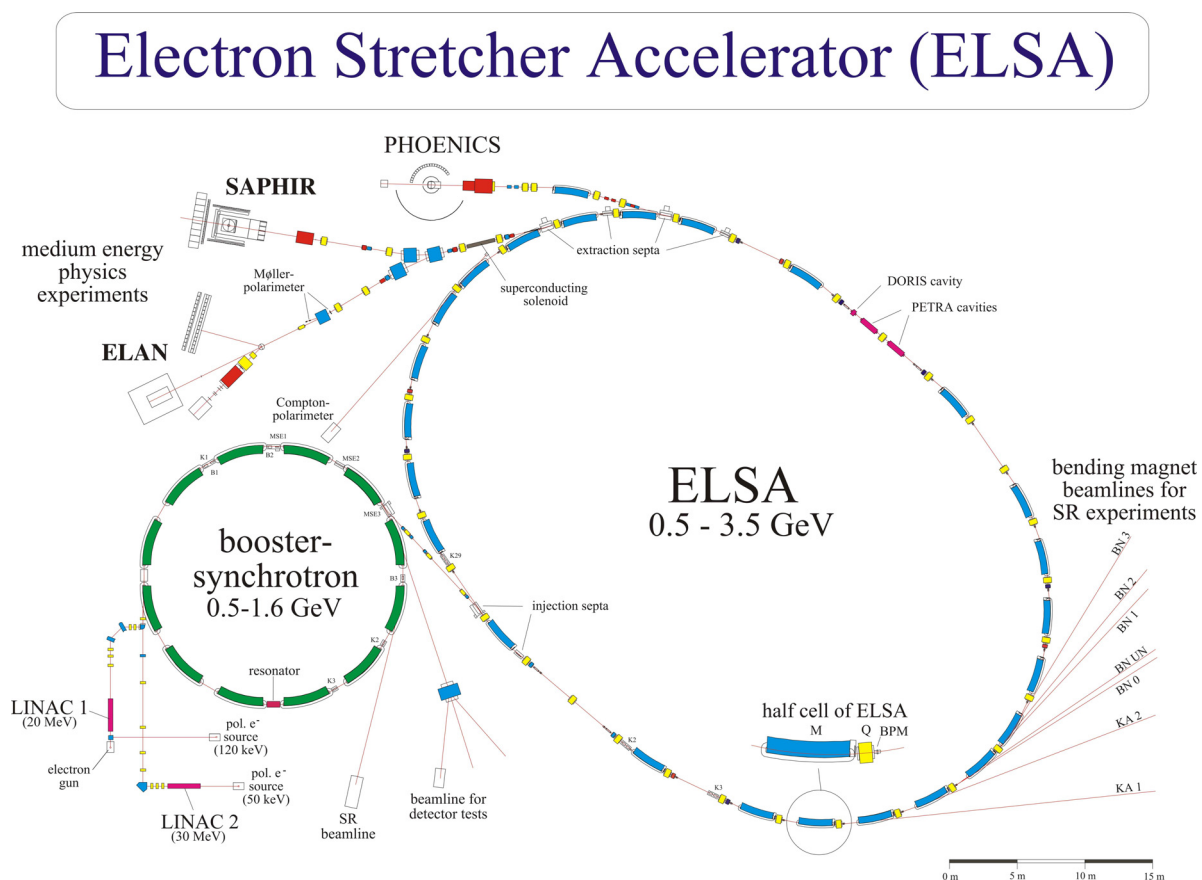
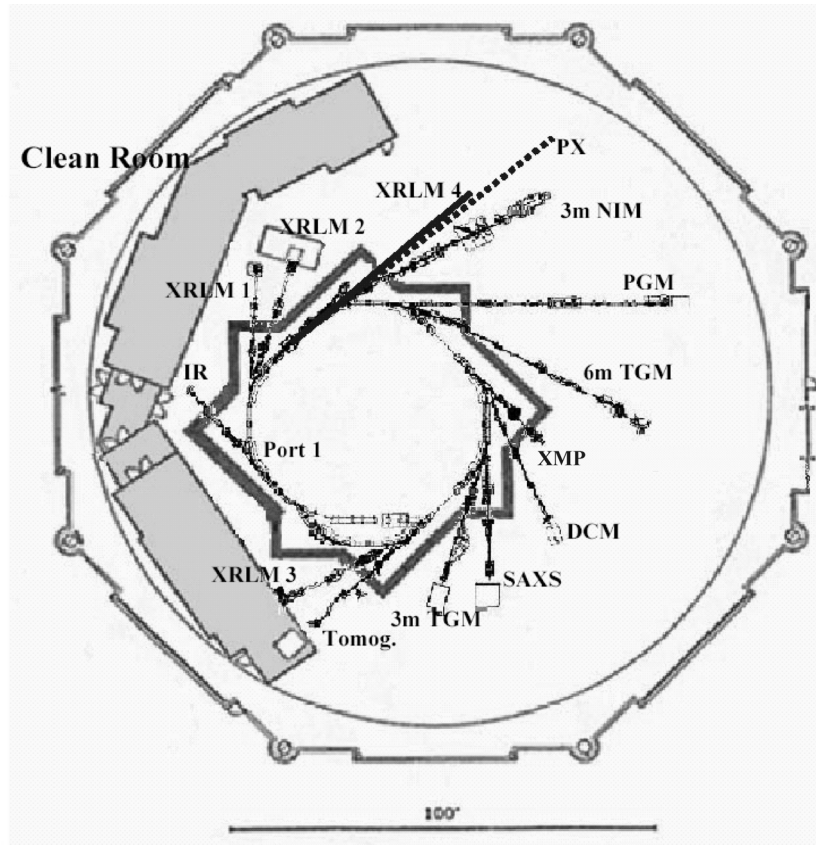
Figure 3.1: Scheme of ELSA at the University of Bonn

Figure 3.2: Floor plan of the CAMD Experiment Hall, Port 1 is noted and the remaining seven ports are at bending magnets and are numbered sequentially from Port 1 in clockwise fashion

Figure 3.3 contains a plot of the radiation characteristics of the CAMD and the ELSA synchrotron radiation emitted from the ring when operated at the typical parameters of 1.3 GeV and 2.3/2.7 GeV, respectively. The (simulated) flux curves (0.1% energy band width) are calculated using LITOP2 program [Dan92].
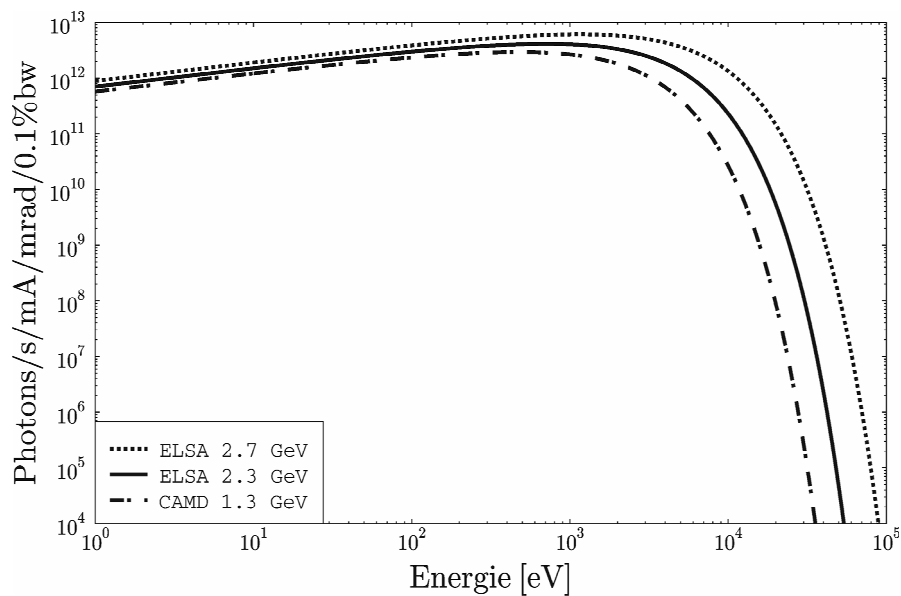

Figure 3.3: Simulated flux for synchrotron radiation at the CAMD (dash-doted) and the ELSA ring operating at 2.3 GeV (solid) and 2.7 GeV (doted) calculated using LITOP2 [Dan92].

Parameter	ELSA	CAMD
Ring energy [GeV]	2.3/2.7	1.3
Maximal current [mA]	65/35	250
Lifetime [min]	120/80	720
Dipole magnets bending radius [m]	10.84	2.928
Dipole magnet field [T]	0.74	1.48
Characteristic wavelength [Å]	5.0/3.1	7.45

Table 3.1: Main characteristics of the ELSA and the CAMD rings

3.2   The BN3 and XMP beam lines

The principal scheme of the beam lines BN3 (ELSA) and XMP (CAMD) is shown in Figure 3.4. At the beam line BN3, as well as in XMP beam line, for which a more detailed scheme is shown in Figure 3.7, a modified Lemmonier-type double-crystal monochromator [Lem78] is used to monochromatize the incident photon beam. Then monochromatic light passes through a window which is separating the pressure within the ionization chambers and the monochromator. In both set-ups this window is made out of 12.5 µm Kapton. The sample is then placed between two ionization chambers and oriented perpendicular to the beam. The signals from the first and second ionization chamber are detected by electrometers (Balzers QM311 and Keithley 617 in Bonn and Baton Rouge, respectively), which detect the current generated by the incident and transmitted radiation. Following the Lambert – Beer's law, the absorption coefficient can be determined from the currents by the two ion chambers.
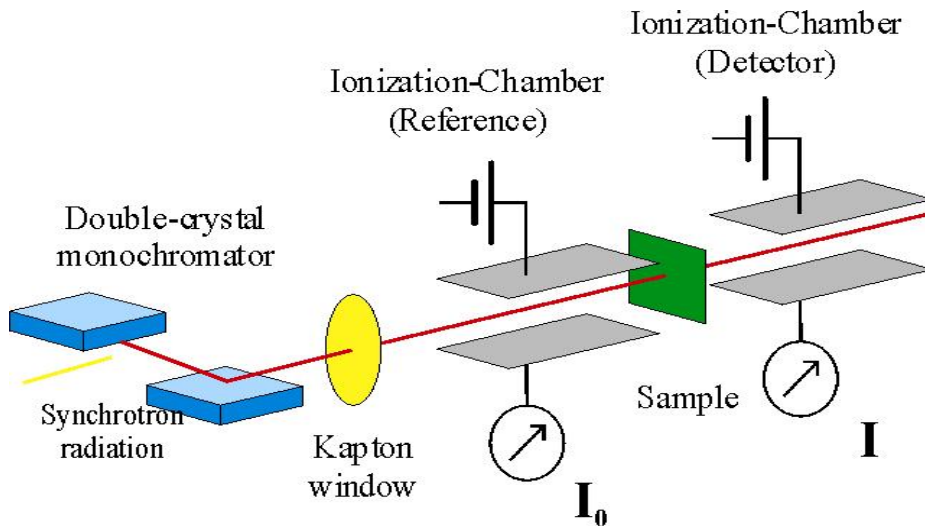
Figure 3.4: Schematic representation of a beam line for XAS experiment in transition mode

The energy of the monochromatic beam is given by

$$E_n = \frac{h \cdot c}{2 \cdot d \cdot \sin \theta} \cdot n \qquad (3.3)$$

This is the Bragg equation (*n* being an integer), where θ is the angle between the X-ray beam and the crystal plane, *c* is the speed of light, *d* is the interplanar spacing between the planes in the atomic lattice, and *h* is a Plank constant. When the incident angle is at the Bragg angle, monochromatic X-rays will remain in phase after reflection and the reflected wave will have a high intensity. Bragg's law allows determining the energy depending on the incident angle of the X-rays which are falling onto the crystals.
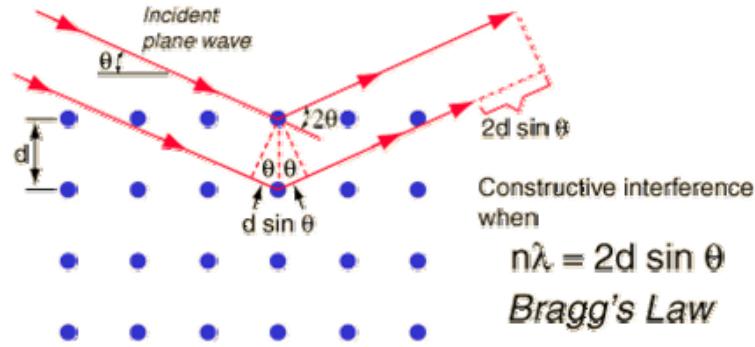
Figure 3.5: Illustration of Bragg's Law

At both beamlines, θ can be varied from 15^0 to 65^0. Bragg's Law holds for an idealized case, as the monochromatic radiation is provided with a double set of crystals and the only factors taken into account are the incident angle and the crystal spacing. In reality, the closeness of the atoms in the crystal lattice contributed to a loss in the intensity of the refracted radiation by scattering processes. Thus, in a real crystal system, the same crystal spacing that provides the monochromatic light influences the intensity of the radiation that is provided. This limits the range of monochromatized radiation that can be provided at high intensity. In practice, for the given crystal set, there is a finite angular width, $\theta - \theta_B$, (θ is the actual angle of incidence and θ_B is the angle calculated from Bragg's Law) where reflection can occur in. This angular range is the so-called Darwin-Prinz curve. The Darwin-Prinz curve for Ge (220) crystal is shown in Figure 3.6. The Darwin-Prinz curve for a given crystal set defines the range of energies and the intensity of the reflected radiation that is provided.
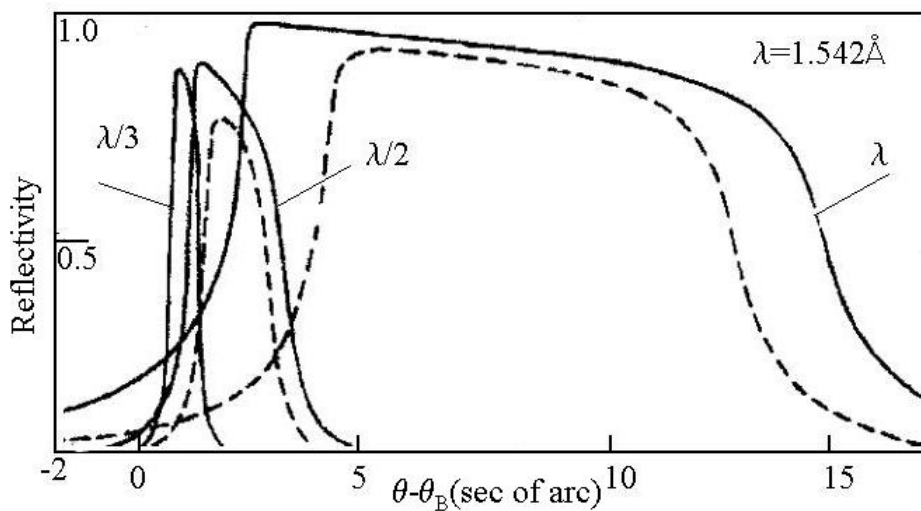

Figure 3.6: Darwin-Prinz curve for Ge (220) crystal, from [Mat80]

$$\theta - \theta_B = \frac{2}{\sin 2\theta_B} \cdot \frac{r_0 \cdot \lambda^2}{\pi \cdot V} \cdot C \cdot |F_H| \cdot e^{-M} \tag{3.4}$$

Equation (3.4) is the Darwin-Prinz curve of a double crystal monochromator [Mat80]. $r_0 = e^2 / m \cdot c^2$, V is the unit cell volume of the crystal, λ is the reflected monochromatic wavelength, C is a polarization factor, e^{-M} is the Debye-Waller factor for the crystal, and F_H is the structure factor of the crystal for the H ≡ (h, k, l) reflection for the unit cell of volume V.

In a double-crystal monochromator, the first crystal serves as a direct monochromator and the second crystal can be used to filter higher harmonics within the Darwin-Prinz width of the reflection curve. As can be seen from Figure 3.6, the reflection curves for the second and third orders is shifted by several seconds of arc and have a decreased reflection width.

At the Co K–edge using Ge (220) crystals energy change is 0.6 eV with every motor step of 0.002°. In comparison to this, at the Pt L_{III}–edge using Ge (422) crystals energy change is 0.77 eV with every motor step.

Another selection criterion for a crystal set is the energy resolution. According to Bragg's Law the energy bandwidth δE of the photon beam is determined by the angular divergence $\delta\theta$. The angular divergence of the photon beam is determined by:

$$\delta\theta = \sqrt{\Psi_v^2 + \frac{1}{2}\delta\alpha^2}$$ (3.5)

where ψ_v^2 is a vertical divergence of synchrotron radiation, $\delta\alpha$ is the spread of the reflection profile from the crystals. The angular spread of SR can be reduced by using optical slits. By considering a point source, the energy resolution due to $\delta\theta$ is given by

$$\delta E = E \cdot \cot\theta \cdot \delta\theta$$ (3.6)

Thus, for the different absorption edges one has to find a suitable pair of crystals as it can be crucial for energy resolution. The characteristics of different crystals, which have been used in this work, are summarized in table 3.2.

Crystal	Interplanar spacing 2d [Å]	Energy region [eV]	Absorption edge
Ge 220 (ELSA)	4.0	3430-12000	3d transition metals,
Ge 422 (ELSA)	2.304	5938-20794	Pt L_{III}
Si 311 (CAMD)	3.276	4000-20000	3d transition metals,

Table 3.2: Different crystals used in this work and their characteristic

The scheme of the XMP beamline is presented in Figure 3.7. The Kapton window is fixed downstream of the monochromator (number 8 on the scheme) for the same reasons as at the BN3 beamline. Beamline vacuum valving and pumping system allows rapid crystal changes. The differential ion pump is set immediately upstream of the monochromator for keeping UHV upstream of DIF with no Be-window. The flux of incident beam is detected by the electrometers of type Keithley 617.
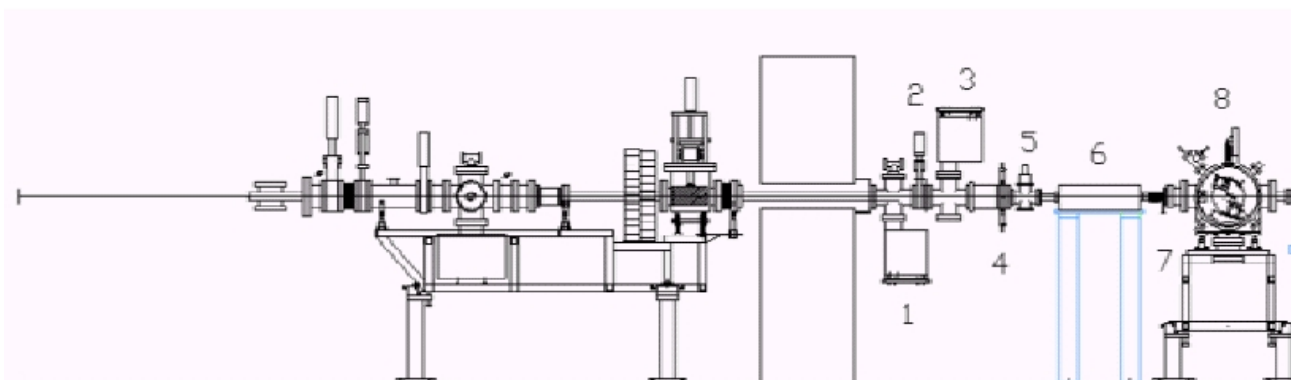
Figure 3.7: XMP beam line at the CAMD – (1) ion pump, (2) gate valve, (3) ion pump, (4) slits, (5) fast shutter, (6) differential ion pump, (7) gate valve 3 (manual), (8) Lemmonier-Bonn double-crystal monochromator, [CAMD]

For the experiments described in this thesis, the XMP beamline at CAMD was operated in fluorescence mode, using a Canberra single element Ge diode as fluorescence detector. The set-up of a fluorescence experiment is different from transmission mode. A scheme of this operation mode is present in Figure 3.8.
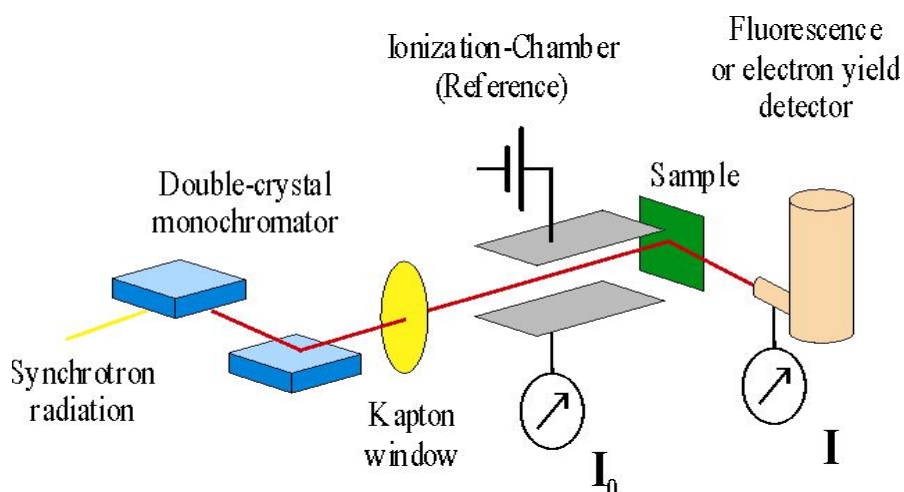
Figure 3.8: Representation of a XAS experiment operated in fluorescence mode

For all samples, which were investigated in this thesis, the XANES spectra were scanned three times from -50 eV to +150 eV, relative to the corresponding edge [Tho01], with 1000 ms integration time per step and then averaged. Afterwards, the EXAFS spectra were recorded twice and then averaged, the energy range of the EXAFS scan was from -200 eV to +1000 eV, with the same, as for XANES, 1000 ms integration time per step. Standard XANES data handling routines were applied, including the subtraction of a linear background fitted to the pre-edge region. For EXAFS evaluation, the UWXAFS program suit was used.

3.3   Sample preparation

The thickness of a sample plays a crucial role in X-ray absorption experiments as it can affect the intensity of the white line and the EXAFS oscillation. Every set of samples require a specific and suitable method of preparation. For example, the sample has to be prepared as homogeneous as possible to exclude the so-called pin-hole which leads to a damping of the spectral features. As a rule, the optimal thickness of the sample is related to the maximum absorption value ($\Delta\mu \cdot d$) which should reach approximate 1.5 a.u. For the experiments at higher energies, for example Pt-L_{III} edge at 11564 eV, one has to prepare relatively thick samples in order to get a sufficient edge jump. For all pellets, with a radius of 13 mm, which are made by pressing the powder, polyethylene (-CH_2CH_2)n can be used as binding material. Air stable powders are prepared as follows: grind the sample to a fine powder, disperse the powder onto adhesive Kapton tape, stick the tape on a frame made of stainless steel, cover the frame with another layer of Kapton tape and place the frame on to the sample holder as shown in Figure 3.9 (middle).

3.3.1   Fluid cell

Very often X-ray experiments deal with a liquid medium such as a colloidal solution and, for this purpose, a fluid cell, was used. The liquid carrier part made out of Teflon with various thicknesses and a hole for the syringe injection was placed between two VA-steel rings with an inner diameter of 12 mm. These three parts are bound by 6 screws. Two Kapton windows are placed between the O-rings of the steel ring and the Teflon part. To prevent air sensitive solutions from getting into contact with air, they were injected in a glove-box and the hole for the syringe injection was covered with Kapton tape, as can be seen in Figure 3.9 (left).

3.3.2   Holder for air sensitive samples

In this work metallic nanoparticles, which are highly air sensitive, were measured. If an oxidation takes place, it can generally be seen in the region of the white line of the absorption spectra (chapter 6.1) In this case, the transportation to the beamline is a very crucial procedure. Depending on the sample concentration, powders were mounted in a glove-box filled with argon to a specially constructed sample holder [Rot97] shown in Figure 3.9 (right). The pellet is pressed with the help of a mini-press and then fixed into the sample holder or by using two screwdrivers, which fit to the gap of sample holder for air sensetive samples, which is 12 mm in diameter. Then the holder could be sealed and safely transported from the glove-box to the beamline. After evacuating the beamline and filling the ionization chambers with protection gas, the sample holder can be opened and the sample position can be adjusted so it will be perpendicular to the center of the beam.
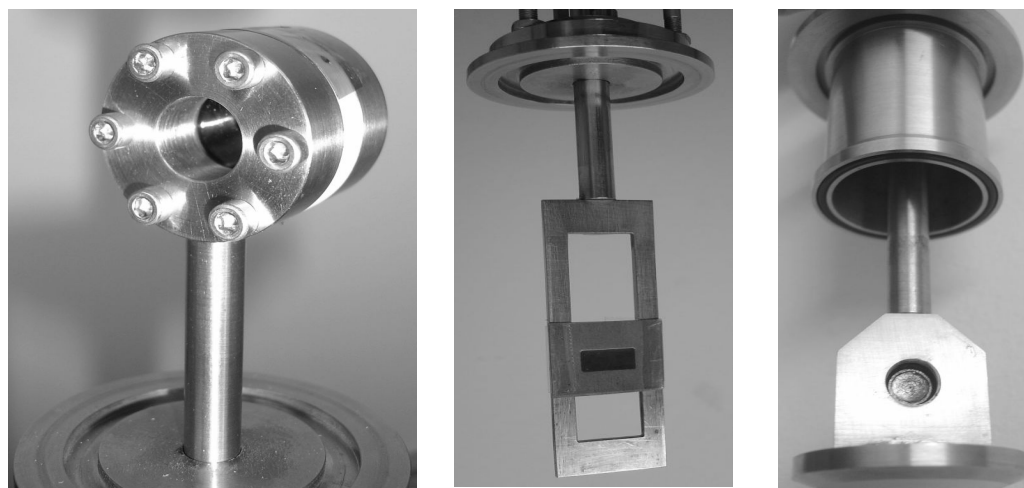

Figure 3.9: Sample holder for liquids (left), powder (middle) and air sensetive (right) samples

4   Synthesis of nanoparticles

Nanoparticles whose particle size deviates less than 10% from the average value are generally addressed as 'monodisperse'. A deviation from the mean particle size of approximately 20% is described as showing a 'narrow size distribution'. During the last few decades considerable knowledge has been gained about these materials [Sch94, Sch03].

The synthesis is expected to be a crucial point in producing nanoparticles with defined properties. It is known that metal colloids can be obtained via so-called 'top-down' methods, e.g., by the mechanical grinding of bulk materials and subsequent stabilization of the resulting nanoparticles by the addition of polymers [Gaf96, Amu98]. The application of metal vapor techniques [Bla79, Kla80] has provided chemists with a very versatile route for the production of a wide range of metal nanoparticles. However, the installation of metal vapor machines is demanding and it is difficult to adjust them to obtain a narrow particle size distribution.

The wet-chemical 'bottom-up method' of nanoparticle preparation basically relies on the chemical reduction of metal salts, electrochemical pathways or the controlled decomposition of metastable organometallic compounds. In the framework of this thesis the 'salt reduction' wet-chemical synthesis has been used by Bönnemann et. al. for Co and Pt nanoparticle preparation. It is well known that properties of nanoparticles are strongly dependent on their size and shape. Thus, the influence of parameters and conditions of the synthesis has become a topic of many scientific discussions. In practice, the tools used by the preparative chemist to control the particle size are size selective separation and size selective synthesis [Ree99, Ter98, and Maa99]. However, size selective separation does not fulfill all demands, as nanoparticles tend to decompose after the protection shell is removed, as in the case of chromatographic separation [Ant97], or it leads to the milligrams of sample after separation, as in the case of ultra-centrifuge separation [Sch00]. Thus efforts have mainly been devoted to the development of size selective synthesis.

In general, two types of mechanisms are considered for the nanoparticle growth, in presence of reducing agent and/or surfactants. The first is a general LaMer [LaM52] mechanism, which suggests nucleation through super–saturation, and then diffusion growth for separating the time parameters of nucleation and growth. The second mechanism, The second mechanism, occurring e.g. when hydrogen is used as a reducing agent, is the Finke mechanism [Wat97]. In this mechanism, a slow continuous low level nucleation, which is far from super – saturation, takes place followed by an autocatalytic growth for obtaining monodispersity of nanoparticles. In the embryonic stage of nucleation [Lei96], the metal salt is reduced to give zero valent metal atoms. These can collide in the solution with further metal ions, metal atoms or clusters to form an irreversible 'seed' of stable metal nuclei. Depending on the strength of metal/metal bonds, the difference in the redox potential between the metal salt and the reducing agent applied the diameter of the seed nuclei can be well below 1nm. For silver, it has been experimentally verified [Lei96] that a stronger reducing agent produces smaller nuclei in the 'seed'. These nuclei grow during the 'ripening' process to give colloidal metal particles in sizes between 1-50 nm which have a narrow size distribution. It was assumed that the mechanism for the particle formation was an agglomeration of zero valent nuclei in the 'seed', or-alternatively–the collision of already formed nuclei with reduced metal atoms. Nowadays it is generally accepted that the size of the resulting metal nanoparticles is determined by the relative rates of nucleation and particle growth. This mechanism of nanoparticle formation was first suggested by Turkevitch [Tur70, Tur85]. The two way scheme of nanoparticle formation is shown in Figure 4.1.

In order to control the growth of the preliminary formed nanoparticles and to prevent them from agglomeration[1], a wide variety of stabilizers, e.g. donor ligands or polymers, are used.

Buffer action of the stabilizer leads to formation of nanoparticles with a different stable shape and a narrow size distribution. The influence can be described as follows:

- A strong absorption of stabilizer would occupy the nanoparticle growth site, thus reducing the growth rate of nanoparticles.

- A full coverage of stabilizer would hinder the diffusion of growth species from the surrounding solution to the surface of the growing particle.

- Moreover, different reducing agents affect the shape and size of nanoparticles as well. A stronger reducing agent causes abrupt concentration of the growth species, resulting in a very high super-saturation, thus resulting in a large number of nuclei [Kin04].
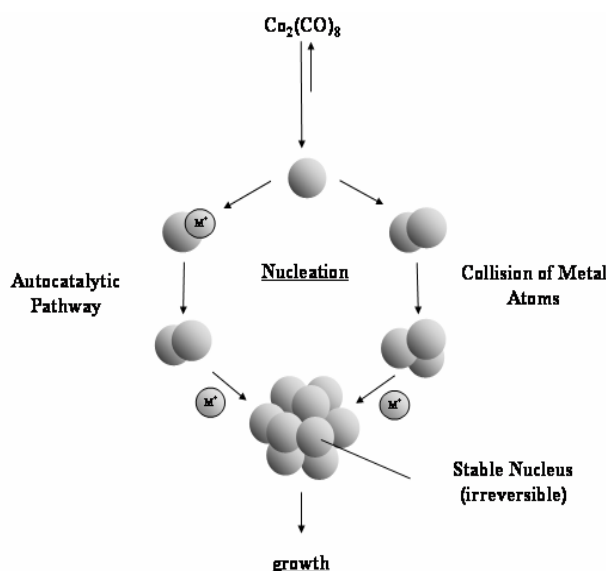
Figure 4.1: Formation of colloidal metal nanoparticles via the 'salt reduction' method, according to Turkevitch [Bön04]

4.1 Wet-chemical synthesis of transition metal nanoparticles: seeding and 'salt reduction' method

The chemical reduction of metal salts in the presence of organo aluminum compounds is a well known method for the preparation of metal nanoparticles of elements of group 6-11 in organic solvents. Here a brief description of the wet-chemical methods, which were applied by Bönnemann et. al. to produce metallic nanoparticles, will be described. In addition to the standard wet chemical method, a modified ('seeding') method of producing the platinum nanoparticles will also be presented.

4.1.1 Formation of small Pt nanoparticles

Small Pt nanoparticles, about 1.2 nm in diameter, have been prepared via so-called 'ship-in-a-bottle' [Wen04] methods, such as incipient wetness impregnation [Ich99] and chemical vapor deposition. Nearly

---

[1] If two particles are allowed to directly touch each other without any interlaying matter, they will spontaneously form one larger particle by exothermic coalescence, in order to reduce the total amount of surface.

monodispersed Pt nanoparticles were obtained by reducing platinum acetylacetonate with trimethyl aluminum [Ang02].

A simple one-pot procedure was recently developed by Bönnemann et.al. to synthesize dimethyl (1,5-cyclooctadiene) platinum (II)–[1.5-(COD)Pt(CH$_3$)$_2$] by introducing 1.5-COD in the beginning of the reduction. The preparation and isolation of Pt clusters by the decomposition of [1.5-(COD)Pt(CH$_3$)$_2$] was done in presence of trialkyl aluminum. The precursor was first dissolved in toluene and then Al(C$_8$H$_{17}$)$_3$ was introduced into the mixture under protection of argon. The reaction mixture was stirred at room temperature for one day, and the resulting black colloidal solution was diluted by a large amount of toluene to obtain a precipitate. After removing the supernatant, further drying under vacuum gave a black powder. **T**ransmission **E**lectron **M**icroscope (TEM) investigations show that very small Pt nanoparticles were generated. After the full decomposition, the size of the Pt clusters was found to be, within the errors of TEM measurements, at about 1 nm. This is related to the one layer Pt cluster – the Pt$_{13}$ cluster. It must be noted that this is the first time that a Pt$_{13}$ cluster has been prepared using a wet-chemical approach. The use of aluminum organics as the compounds preventing the spontaneous agglomeration of the nanoparticles, as well as the novel 'smooth oxidation' procedure (see section 1.1.2), plays an important role in stabilizing small Pt cluster [Wen04].

4.1.2 PVP stabilized Pt nanoparticles

The size and shape controlled synthesis of Pt particles is schematically presented in Figure 4.2. For the shape controlled synthesis, K$_2$PtCl$_4$ (potassium tetracloroplatinate) had been chosen as a precursor. It was dissolved in water with the protecting agent (surfactant) PVP (**p**oly**v**inyl**p**yrrolidone), in 10:1 molar ratio. To reduce the Pt precursors, hydrogen was passed through. After complete reduction, it is supposed that the Pt particles are stabilized by the PVP molecules. From the TEM analysis which is present in Figure 4.3 (left) it can be seen that the nanoparticles have a narrow size distribution –8±1 nm and –tetrahedral shape.
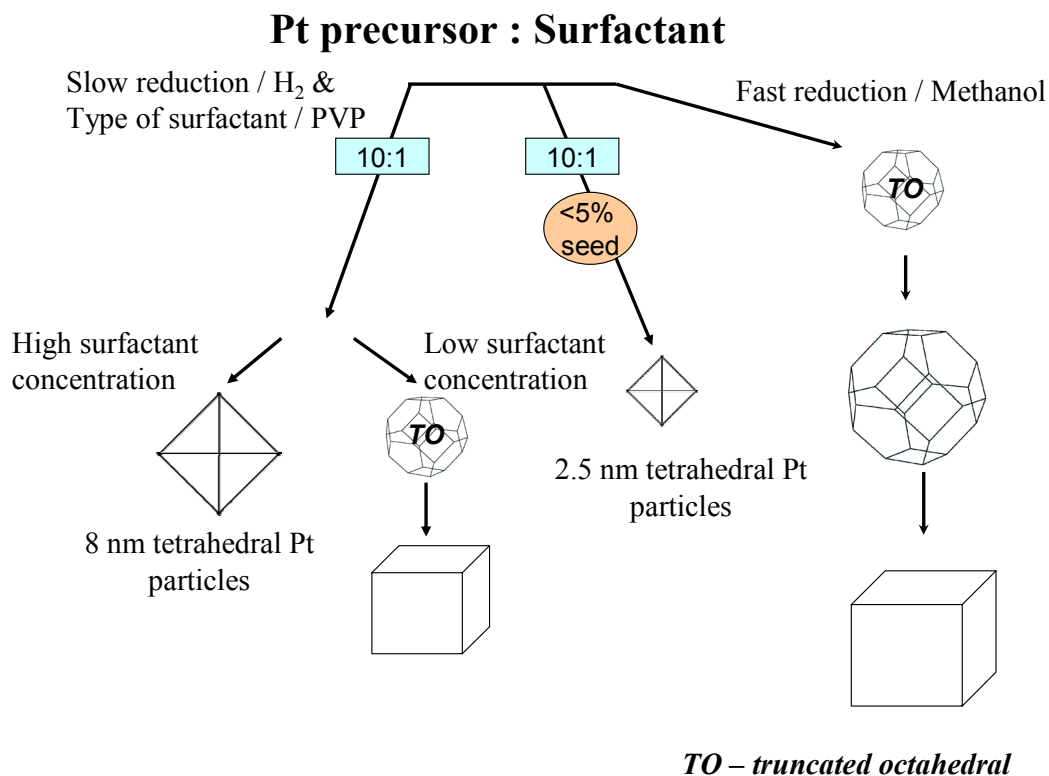
Figure 4.2: Simple scheme of size and shape selective synthesis of Pt-PVP stabilized nanoparticles

To perform the size selective synthesis of nanoparticles, the seeding method was applied for the same set of precursor/surfactant compounds. Before reducing the colloidal solution by hydrogen, Pt particles with an average size of 1 nm were added. These particles act as seeds or nuclei for the particle formation process in this synthesis. After reduction, the TEM picture, Figure 4.3 (right), shows that the size of the particles is reduced dramatically to 2.5 nm. The shape of the nanoparticles stays tetrahedral. Thus, with an addition of nano-seeds, size of the nanoparticles might be varied during particle preparation. The seeds are Pt–REWO nanoparticles, where REWO is Lauryldimethylcarboxamethylammonium, which can be prepared directly by reduction under Hydrogen in aqueous medium [Kin04]. REWO is an amphiphilic surfactant and can be removed by 1:1 mixture of acetonitrite and water. After several washings, the Pt nanoparticles are settled down in water and cannot be further redispersed. Thus, the coating shell is completely removed. The reaction of Pt – REWO NP's production can be presented as follows:

$$PtCl_2 + 5 \cdot LiBet_3 + REWO \rightarrow Pt - REWO + 5 \cdot LiCl \downarrow + 5 \cdot Bet_3H + \frac{5}{2}H_2 \uparrow$$

Consequently, a kinetic of the nanoparticle growth with and without an addition of the seeds is different, and result in nanoparticles with different properties, which can be monitored using XANES and EXAFS techniques (chapter 5.2).
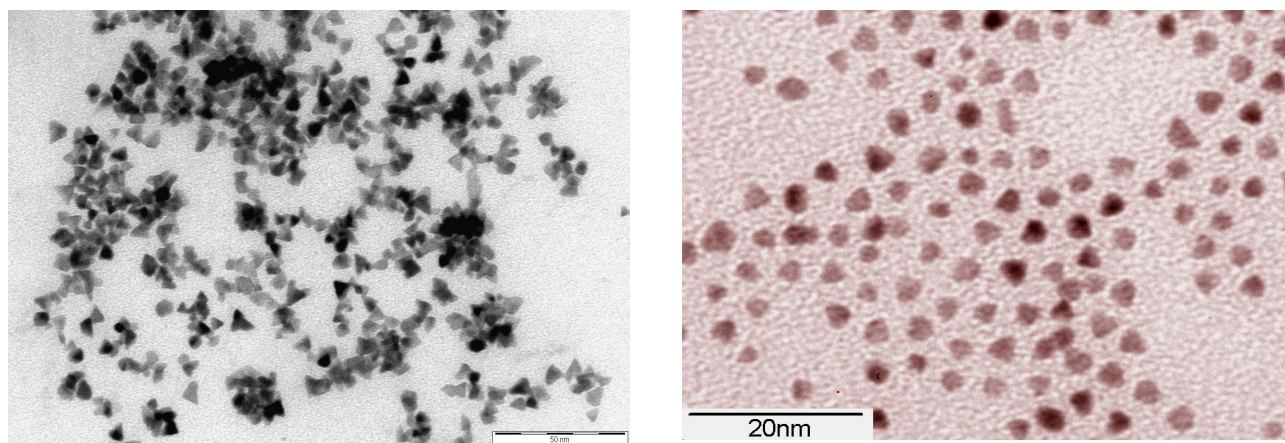
Figure 4.3: TEM picture from tetrahedral Pt particles produced with (2.5 nm left, scale bar 50 nm) and without (8.0 nm right) seeding

4.1.3 'Wet-chemical' approach to producing cobalt magnetic powders and fluids

For the preparation of nanoscopic Co(0) particles, the thermolysis of $Co_2(CO)_8$ is a very convenient and generally applied method [Pap83]. $Co_2(CO)_8$ is a crystalline solid with three isomeric forms in solid, gas and liquid phases [Sum64, Swe77]. It is soluble in organic solvents, sublimes readily, is thermally unstable and undergoes a wide range of reactions, and existence of unstable mononuclear cobalt carbonyls has been studied as well [Han75]. The improved thermolysis of $Co_2(CO)_8$ in presence of aluminumorganic compounds such as $Al(C_2H_5)_3$ and $Al(C_8H_{17})_3$ had been recently developed by Bönnemann et.al. [Bön04], and monodispersed magnetic cobalt nanoparticles and fluids have been obtained.

Magnetic fluids (MF's) with a narrow size distribution exhibit useful properties for a number of technical [Ber96, Zub02, Ode03] and biomedical applications [Rog98, Kim02, Lan03, Par04]. The magnetic properties of ferrofluids depend strongly on the size of the particles and the concentration of the magnetic material in the dispersion. Thus, for every particular application a specific and reproducible synthesis has to be developed. The well known magnetite MF's, for example, have good stability; however, the magnetic

properties of these fluids are not as good as for cobalt based ferrofluids [Kim01, Mor01]. Consequently, stable MF's on the bases of nanosized zero valent colloidal cobalt are a material of interest.

The general procedure of 'wet–chemical' approach to producing Cobalt nanoparticles investigated in this work consists of several steps which are illustrated in Figure 4.5:

Thermolysis: in a necked flask fitted with a mechanical stirrer and a reflux condenser, $Co_2(CO)_8$ was introduced under a flow of argon. Then $Al(C_8H_{17})_3$ dissolved in toluene was added at once (initial ratio Co:Al=10:1) and the mixture was stirred and heated. With CO evolution, the color of the solution changed to dark brown and than a black precipitate was formed from the clear solution.

Smooth air oxidation: the resulting mixture was slowly oxidized as synthetic air (80% O_2 and 20% N_2) bubbled through a capillary into the mixture. The supernatant was decanted and the core-shell particles were isolated in wet form. Afterwards, the particles were dried in a vacuum and the Co powder was obtained.

Peptization[2]: in this particular synthesis, this has to be done to bring nanoparticles into colloidal solution. Co particles (wet or dried powder form) were peptized using suitable surfactants.

Using this general procedure, the thermolysis of $Co_2(CO)_8$ in the presence of $Al(C_8H_{17})_3$, followed by peptization with KorantinSH led to a cobalt organosol of 10.0 ± 1.1 nm size. In Figure 4.4 the result of wet-chemical approach of nanosized particles production in powder and solution is shown.
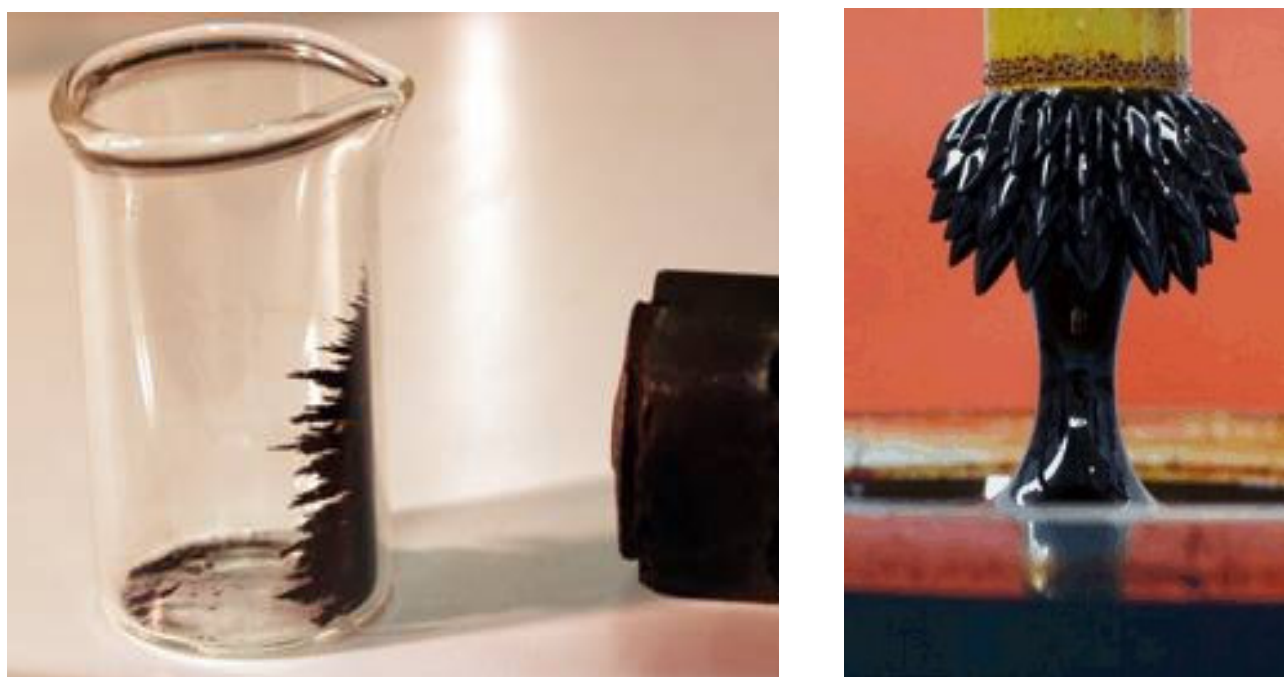
Figure 4.4: Co-based magnetic powder (left) and magnetic fluid (right)

---

[2] the process of converting to a colloidal solution, where dispersing phase is solid and dispersed media is liquid.

Co₂(CO)₈ : Al(R)₃
(thermolysis)

Added at once
Mixture heated and stirred
at 110°C for 18 h
Cooled down to
room temperature

*Co nanoparticles
(suspension)*

'smooth oxidation'
(synthetic air)

Barbatire air through
capillary (slowly)

*Prestabilized
Co nanoparticles*

Washing
(Toluene/Ethanol)

Than particles allow to settle
down for 2 h

Magnetic Fluid

Powder

Peptization
(KorantinSH)

Drying
(vacuum/air)

Figure 4.5: Schematic representation of wet-chemical synthesis of Cobalt nanoparticles and magnetic fluids.

Note that the particles resulting after slow thermolysis in presence of AlR₃ (stage of the wet colloids nanoparticles in suspension) are different from one resulting after application of 'smooth oxidation' procedure (pre–stabilized nanoparticles). Even slight changes in preparative procedure will significantly influence the electronic and geometric structure of nanoparticles, as will be shown later in chapter 6.

4.2 Modified glass crystallization method

The magnetic Barium hexaferrites powders have been prepared by means of a modified crystallization method [Mül94]. Nanocrystalline Ba-ferrites were prepared from BaO and Fe_2O_3, and for CoTi substituted samples the CoO and TiO_2 were used. Numerous investigations have been done to modify the magnetic properties through the substitution of Fe^{+3} ions. This can be accomplished in two ways: direct substitution by trivalent ions (Al^{+3}, Ga^{+3}) or by a combined substitution of divalent and tetravalent ions, here Co^{2+} and Ti^{4+}. Different $BaFe_{12-2x}Co_xTi_xO_{19}$ powders have been prepared with a mean particle size variation: 9 nm, 14 nm, 29 nm and 170 nm. The particles grow during a temperature treatment in a glass matrix and are leached out by dissolving the matrix. The phase composition and the particle size can be influenced by the melt composition as well as the temperature treatment. In order to get very small particles by glass crystallization of the hexaferrites three possibilities should be mentioned: (i) suitable chemical glass compositions, which favor nucleation of barium hexaferrites during annealing of the amorphous flakes, (ii) short enough annealing times, and/or (iii) annealing temperatures as low as possible.

In the glass crystallization synthesis very short annealing times of flakes are not convenient because nucleation and crystal growth by diffusion proceeds at higher temperatures (700 °C) in less then 100 s and at lower temperatures iron oxide compounds are formed. Time intervals in the order of 100 s are too small for the formation of a homogeneous temperature distribution within the flakes. Nanocrystalline particles grow during annealing for longer times at temperatures around 560-580 °C, depending on the chemical composition of the flakes. A reduction of the mean particle size by roughly a factor of four is achieved by Co/Ti substitution.

The substitutions decrease the temperature necessary for the formation of the hexaferrites phase. A step-wise way of the bariumhexaferrite production is shown in Figure 4.6. The size effects in metallic magnetic nanocrystals results in particles with unique properties that are strongly dependent on size, shape, crystallographic structure, and defect distribution [Li00, Les96]. As the particle size decreases, the coercivity decreases until thermal fluctuations overcome pinning of the spins to energetically favorable easy axes. At this point, the original ferromagnetic particle becomes superparamagnetic and the spins can rotate freely between the easy axes [Née49]. The barrier for this transformation is dependent on particle structure.

In the framework of the DFG-Priority Program SPP1104: "Colloidal Magnetic Fluids: Basics, Preparation and Application of New Ferrofluids", Co/Ti doped bariumhexaferrite particles with an average particle size <15 nm were considered as a suitable base material for MF's with supermagnetic fraction and anisotropy/magnetic losses higher than those which are based on iron and iron oxides, as magnetite, and with less toxicity than $Co(CO)_8$ based ferrofluids.

Glass crystallization

Raw materials: α-Fe$_2$O$_3$, Ba$_2$O$_3$, BaO
Substitution: TiO$_2$, CoO

$\Downarrow$ Melting   +   Quenching
(1300 – 1400 ^{0}C)   (ca. 1000 K/s)

Glass

$\Downarrow$ Annealing (T ~ 580 ^{0}C → 800 ^{0}C)

BaFe$_{12}$O$_{19}$ NP's
in borate matrix

$\Downarrow$ Dissolving borate-matrix
with acetic acid & drying
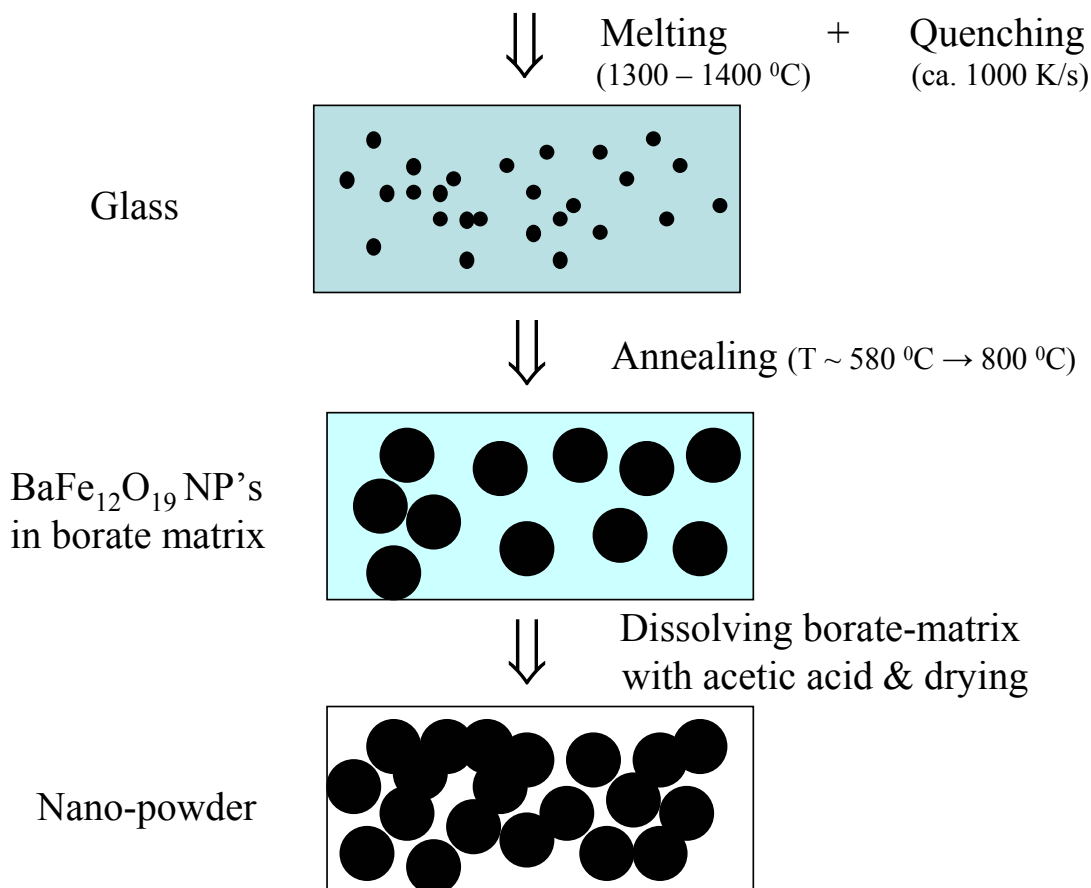
Nano-powder

Figure 4.6: Step-wise scheme for producing magnetic nanosized Bariumhexaferrite powder

5 XAFS on Pt nanoparticles

Two cases of Pt nanoparticles, prepared via wet-chemical synthesis, will be discussed in the present work in an attempt to understand the importance of the surface and surface coordination effects. First of all, the XANES investigation of very small Pt nanoparticles provides an access to the information of surface bond and/or coordination, as the contribution from surface atoms to XANES is strongest. Secondly, under assumption that the binding mechanism between the formed nanoparticles and stabilizer is not size-dependent, XAFS investigation on Pt nanoparticles of different size, prepared using the same stabilizer, allows monitoring of the potential spectral changes as a function of a surface contribution. The results of studies on such 'ideal' systems are discussed in this chapter to create a basis for further analysis, where more complicated systems have been probed by XAS.

5.1 XANES investigation of Pt$_{13}$ cluster

In the present chapter, a special case of organosol preparation via controlled complex decomposition of dimethyl (1,5-cyclooctadiene) platinum (II), $(CH_3)_2PtCOD$, whose molecular structure is depicted in Figure 5.1, in the presence of trialkylaluminum have been investigated by XANES. The nanoparticles prepared in such a way are considered to be one of the most important materials for the heterogeneous catalysis of hydrogenation because of their small hydrogenation energy compared with other metal nanoparticles [Bal87]. In this respect, the determination of electronic and geometric structure of Pt nanoparticles is important because it is a major feature in controlling the catalyst's activity. In particular, it is possible that very small metal nanoparticles have unusual structures and therefore unusual properties. In the case of platinum, Pt$_{13}$ is one of the smallest clusters matching a magic number [Ech81], where a central nucleus is surrounded by an icosahedron of 12 equivalent nuclei. To our knowledge no wet-chemical method has been reported for synthesizing free Pt$_{13}$ clusters with uniform particle size distribution. Often the cluster size distribution is not uniform, but so-called magic numbers of nuclei are strongly preferred since they allow for a maximum coordination of atoms, resulting in various close-packed polyhedron.
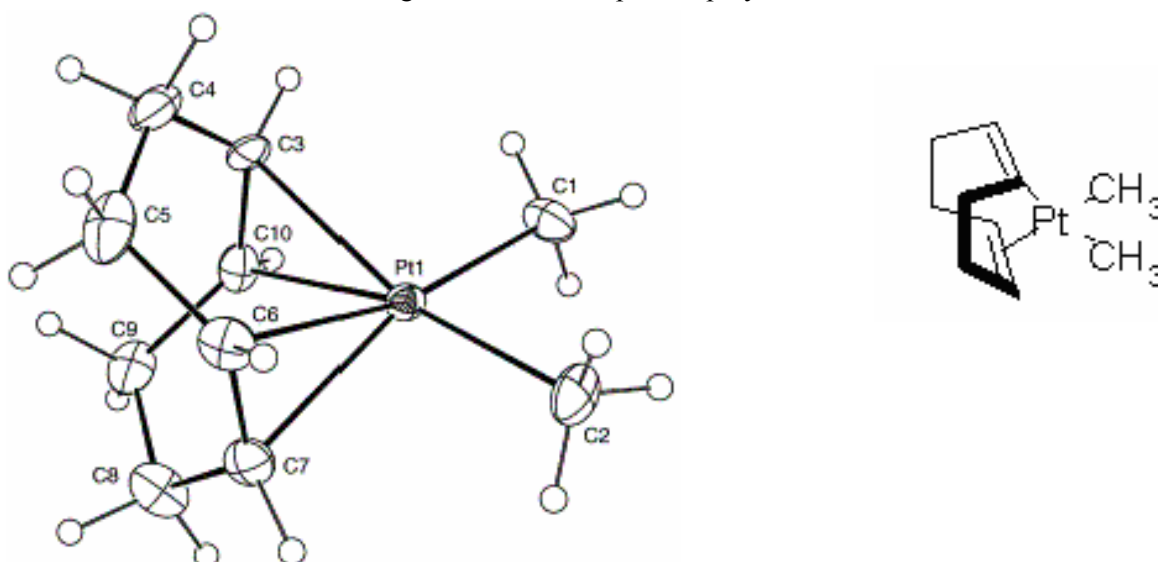
Figure 5.1: ORTEP[3] diagram of (CH$_3$)2Pt(COD), molecular (left) and schematic (right) representation

---

[3] Oak Ridge Thermal Ellipsoid Plot program for crystal structure illustration (ORTEP) had been used for scheme of (CH$_3$)2Pt (cod), molecular.

It has to be emphasized that small (0.75 ± 0.12 nm) Pt clusters are of particular interest since they can be represent by the icosahedral (ICS) and cubo-octahedral (COS) structures depicted on Figure 5.2. Formation of icosahedral or cubo-octahedral structure depends on energetic, thermodynamic and kinetic effects [Bal05]. The energetic effects are referring to the most favored structure of a nanoparticle. Generally, the most favored structure is the global minimum of the potential energy as the function of the coordinates of the electronic cores, the potential energy surface (PES). The sizes of the most stable structure are called *magic sizes*. Magic sizes may correspond either to the completion of a geometrically perfect structure, like icosahedral or cubo-octahedral structure. Both ICS and COS structures consist of 13 atoms [Bal05, Apr03, Yan97], including the center, and 12 are on the surface. Both structures are found for Pt_{13}. The energetic of small Pt clusters has been investigated by several groups employing density–functional study [Gro00, For99]. The simulated calculations gave preference to the icosahedral structure at N=13 [Doy98, Bal02, Mas02]. Therefore, for further analysis the icosahedral structure is assumed for very small Pt nanoparticles. The thermodynamic effects are mostly related to temperature dependent changes on structure, which can induce phase transition. The kinetics effects are strongly correlated with different growth models. In the context of the present work the influence of surface and thus energetic effects on the properties of resulting nanoparticles is the most interesting aspect.
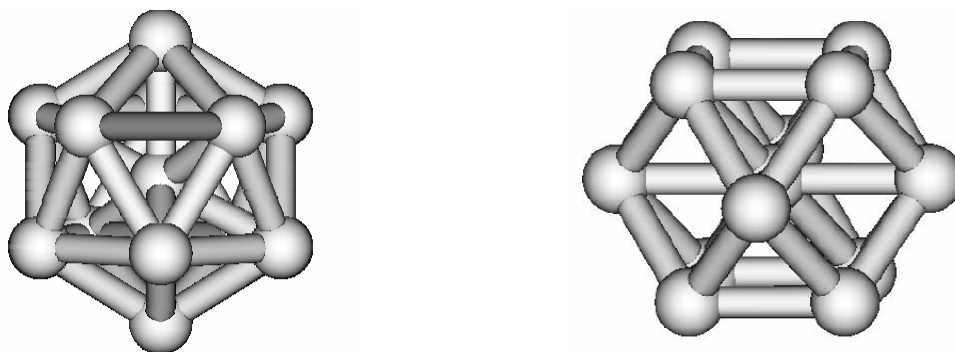
Figure 5.2: Icosahedral (ICS – left) and cubo-octahedral (COS – right) structures of Pt_{13} first closed shell [Apr03]

The Pt L_{III}–XANES spectra of nanoparticles prepared as described above, kept and measured under Argon are presented in Figure 5.3. It is evident from the Figure 5.3 that the Pt L_{III} spectra of small Pt nanoparticles are very different from Pt reference foil as well as bigger Pt nanoparticles [Köh01]. In order to unambiguously identify the presence of a 13-atom Pt cluster, the Pt L_{III} XANES spectrum of Pt nanoparticles dried under vacuum and stored under Argon, was measured and compared to theoretical model obtained using the FEFF8 code. As can be seen from the calculations, the location and the intensity of shape resonances in these spectra turn out to be sensitive criteria for the completeness of shell structures. Bearing in mind that any of the atoms in the nanoparticles can act as the absorber atom, calculations were run for both the coordination geometries present. The resulting site–dependent spectra were then weighted according to their multiplicities and added to produce the theoretical spectrum. At first sight, the agreement between the calculation done for pure Pt nanoparticles and experimental data, where the influence of stabilizer or/and bond formation has to contribute into the spectral features, is astonishing. In the white line region, this observation can be explained if one assumes that physisorption or even van der Waals interaction rather than chemisorption occurs. These ideas are supported by the fact that the alkylaluminum can be completely removed by repeated washing with toluene or/and acetone. In the multiple scattering region the similarity can be understood as follows: first of all, the scattering power of Pt is much higher than the one of the low Z–atoms, contained in the alkylaluminum or it's the so-called by-products, octane, octane, COD or alkyls group which can be presented in the protection shell [Wen04]. Secondly, the coordination via physisorption or van der Waals interaction results with less defined atom position than one in which chemisorption is involved; thus no significant change in XANES spectra of Pt nanoparticles, induced by the protection shell, are found. Small deviations between calculations and experimental data may either reflect that cluster size distribution is not described by a delta-function or reveal some slight influences of the stabilizing molecules.

Sample #	Precursor/Stabilizer	Form	Modification	Storage
WNF-WA-210-08	$[(1.5\text{-COD})Pt(CH_3)_2]/Al(oct)_3$	powder		argon
WNF-WA-210-08*	$[(1.5\text{-COD})Pt(CH_3)_2]/Al(oct)_3$	powder	uncontrolled oxidation	argon
WNF-WA-269-01	$[(1.5\text{-COD})Pt(CH_3)_2]/Al(oct)_3$	solution		argon
WNF-WA-269-02	$[(1.5\text{-COD})Pt(CH_3)_2]/Al(oct)_3$	powder	'smooth' oxidation	argon

Table 5.1: Modifications which were applied on Pt13 clusters and/or their protection shell and theirs storage condition
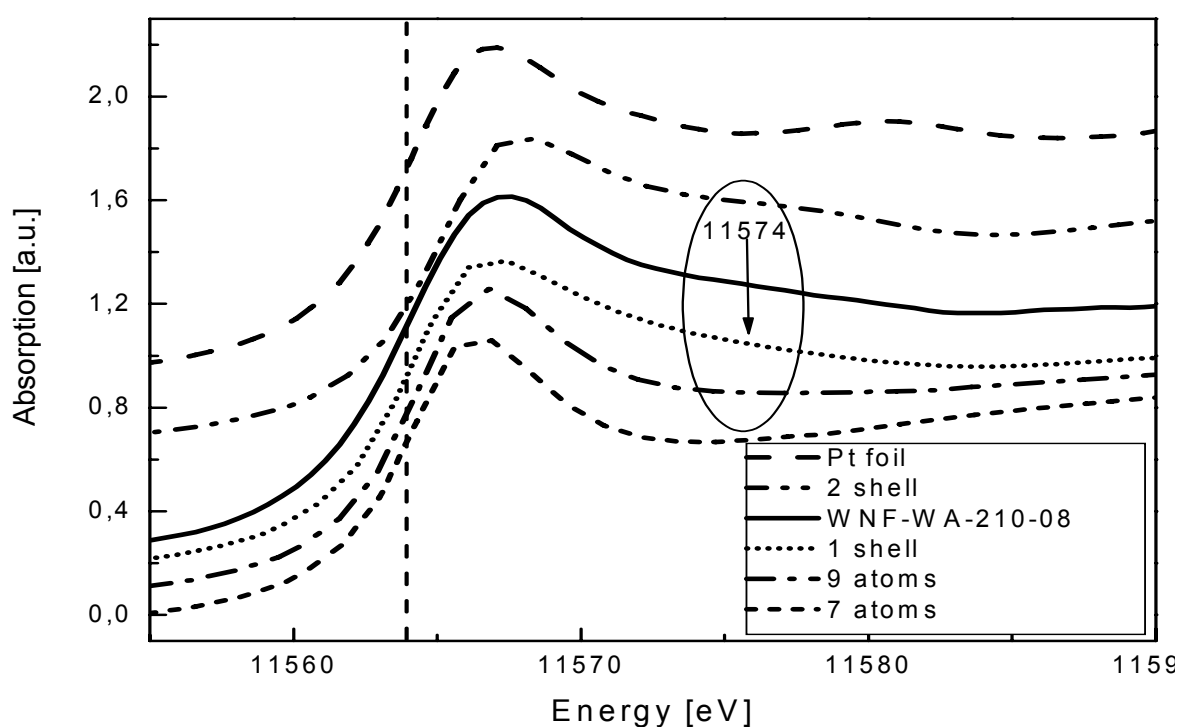
Figure 5.3: Pt L_{III} - XANES spectra of (top to bottom): Pt foil (experiment), 2-shell cluster (theory), 1-shell cluster experiment (solid line) and theory (doted line), 9-atom cluster, 7-atom cluster

The comparison of as prepared Pt nanoparticles in a carrier solution and in powder form measured under Argon is shown in Figure 5.4, and displays extreme similarities of the main spectral features. At the same time, experimental spectra of Pt nanoparticles in solution and powder are in total agreement with the calculated spectra of complete first shell platinum Figure 5.4. This reinforces that the organoaluminum compounds have no significant influence on the metal core of the Pt nanoparticles, as long as the resulting particles were kept under protection gas and no further modification of the protection shell, e.g. 'smooth' oxidation or/and exposure to air , has been applied.
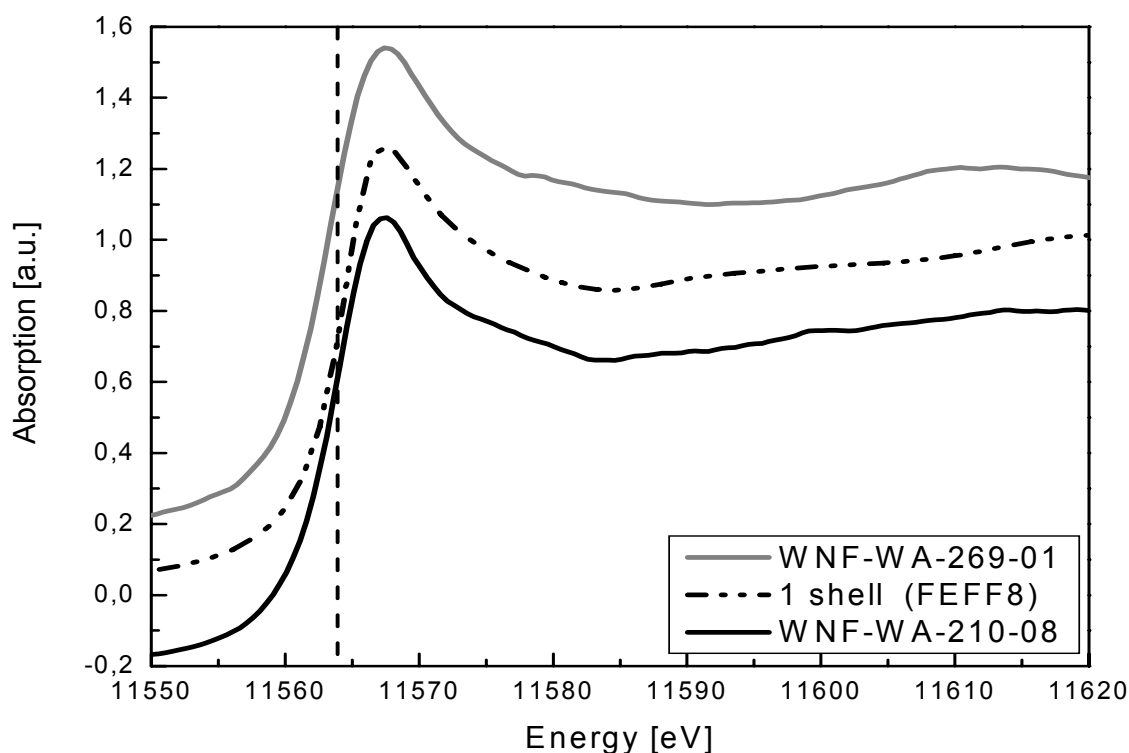
Figure 5.4: Pt L_{III} - XANES spectra of Pt13 cluster in solution (dashed line) and powder (solid line) in comparison with 1 shell Pt cluster spectrum (grey dash-dot-dot line) calculated using FEFF8 code

The only notable change between the spectra of Pt nanoparticles in solution and dried form is the intensity of the shape resonance located at about 11613 eV, which is more pronounced in the case of Pt NP's in solution. This observation may reflect the influence of removal of unreacted organoaluminum groups, e.g. Al – CH_3/Al – C_8H_x from the starting material during drying, which are still present in the stabilizer and have been detected by quantitative protonolysis experiments [Bön04]. It is also known that organoaluminum groups can be modified while bringing the solution into powder form [Wen04], which is why the shape resonance is more pronounced for Pt nanoparticles in solution.

In contrast to this, the changes in the stabilizing shell, which are induced by 'smooth oxidation', i.e. slow and controlled exposure to air, influence the XANES spectra significantly. Figure 5.5 shows the Pt L_{III} spectra before (WNF–WA–269–01) and after modification (with applying the 'smooth oxidation' procedure (WNF–WA–269–02), and after uncontrolled exposure to air (WNF–WA–269–03). All modifications of as-prepared Pt nanoparticles are denoted in table 5.1. The observed increase of the white line intensity is directly correlated to the more electrons drawing enviroment around Pt nanoparticles. Intuitively one would assume formation of a Pt oxide phase, however, the X-ray Photoelectron Spectroscopy (XPS) measurements on the same sample show that the formal valency of the Pt remains zero [Wen04]. As shown in Figure 5.7, deconvolution of the XPS spectrum reveals binding energies of Pt $4f_{7/2}$ and Al $2p_{3/2}$ of 71.3 and 74.1 eV, respectively, which correspond to Pt(0) and Al^{3+}. These results support the idea of Pt nanoparticles dispersed regularly in an aluminum oxide matrix, formed as a result of a protection shell modification (Figure 5.8(c)). Thus, observed changes in the spectral features A and B in Figure 5.5 of sample WNF–WA–269–02 in comparison to the nanoparticles WNF–WA–269–01 must be explained by interaction of aluminum organics and its by-products with oxygen, which leads to the charge transferring from Platinum to Al–O&Al–C_8H_x coordination, during 'smooth oxidation'. A possible mechanism of replacement of octyl group by oxygen during the 'smooth oxidation' procedure is shown in Figure 5.8 (b). One would assume that after particles have been exposed to air, the complete replacement of Al–C_8H_x coordination by Al–O, as shown in Figure 5.8 (c) take place. This replacement would lead to the systematic changes: further increasing in the spectral features A and decrease of the intensity of spectral feature marked B. However, the observed changes in

spectral features A and B of the resulting Pt nanoparticles after the application of the 'smooth oxidation' procedure (WNF–WA–269–02) and further exposure to air (WNF–WA–269–03) cannot be explained within this hypothesis. An additional mechanism has to be considered to understand the changes in spectral features observed for sample WNF–WA–269–03. Bearing in mind high reactivity of the alkyl group and oxygen, one can imagine that with increasing amount of oxygen available for reaction and the rate of oxygen available, e.g. exposure to air (fast and uncontrolled oxidation), the Al–C_8H_x can oxidized to the Al_2O_3. In this case the Al–C_8H_x network is no longer protecting Pt nanoparticles from direct interactions and the coalescence of supported Pt_{13} nanoparticles can occur. This process can also be initiated by the introduction of external energy extracted in the reaction of alkyl group with oxygen. The coalescence of supported nanoparticles has been reported for a variety of metal nanoparticles. E.g., Hendy *et al.* simulated the coalescence of free lead nanoparticles [Hen03]. In this work it has been reported that when two small (magic size) nanoparticles come into contact, many new bonds form, causing a considerable release of surface energy and further increase in temperature. The increase in temperature makes the coalescence process much faster, by enhancing surface diffusion. The reaction of the alkyl group with oxygen leads to the increase of temperature and thus increases the probability of coalescence for Pt nanoparticles. Following this idea, the observed changes in a XANES spectrum of sample WNF–WA–269–03 can be understood by releasing the small Pt nanoparticles from the Al–C_8H_x matrix as it is oxidized towards Al_2O_3. Therefore, surface coordination to electron drawing neighbors is reduced and resulting spectral features are more similar to the Pt foil.
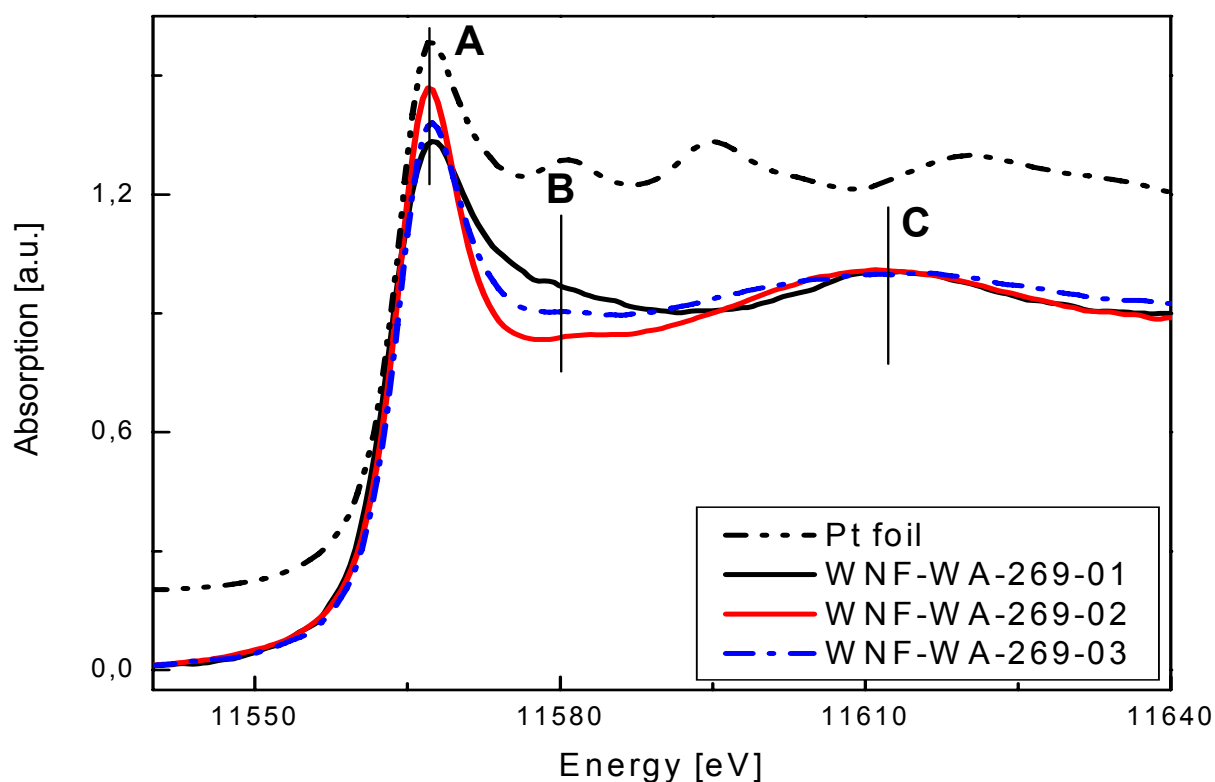
Figure 5.5: Pt L_{III} – XANES spectra of Pt13 cluster in solution (dashed line) after applied 'smooth oxidation' procedure (doted line) and after exposure to air (solid line) in comparison with Pt-foil (dash-dot-dot line)

A similar observation was found from comparison of Pt L_{III}-XANES spectra of nanoparticles exposed to air (WNF–WA–269–03) and those which were accidentally oxidized in the beam line or during the transportation to the beam line caused by the use of non air tight sample holders (WNF–WA–210–08*), i.e. the slow leak of O_2, Figure 5.6. The slightly higher intensity of the white line in the case of particles measured after exposure to air in comparison with WNF–WA–210–08* may be due to a larger amount of oxygen available for reaction and the faster rate of oxidation of Al–C_8H_x surrounding the metallic Pt core as

well as decrease of the reaction time. Here, increasing the time during which the protection shell may be modified, leads to a slight increase of the white line intensity. One can conclude that with increasing time and amount of oxygen which is introduced into the system the ratio of Al–C_8H_x, substitution into Al–O is increased. Differences in the spectral features for particles treated by the 'smooth oxidation' procedure, where the oxidation progressed in a slow rate, and particles exposed to air, may be understood if one bears in mind the possibility of the coalescence/agglomeration of Pt nanoparticle, induced by the increase of temperature due to reaction of alkyl groups with oxygen.
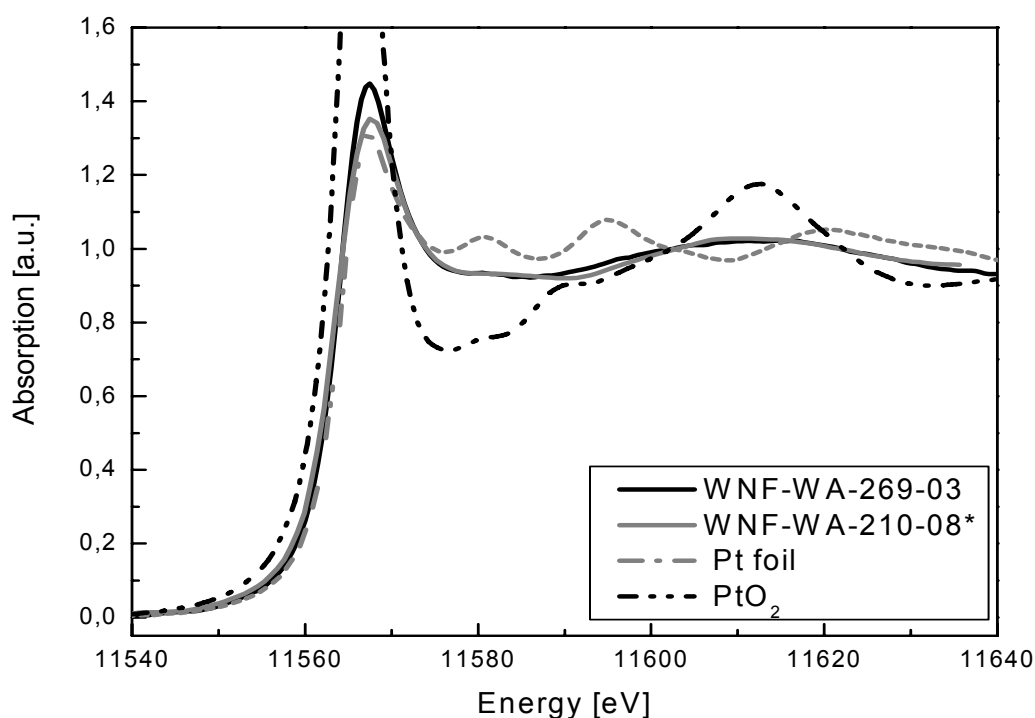
Figure 5.6: Pt L_{III} – XANES spectra of Pt_{13} clusters obtained in the powder after exposure to air (black solid line) and uncontrolled (grey solid line) oxidative process in comparison with reference foil and PtO_2
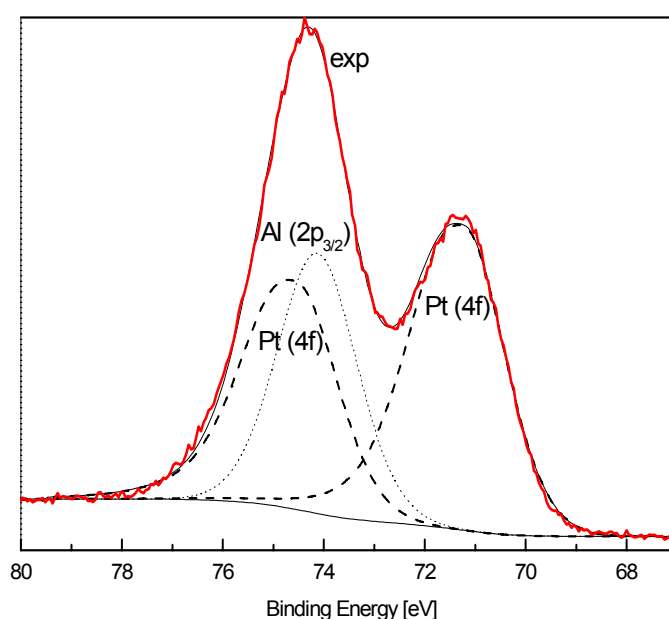
Figure 5.7: X-ray photoelectron spectra of Pt 4f (dashed line) and Al 2p (dotted line) for Pt cluster in powder (Referenced to C 1s: 284.5 eV) [Wen04]

Unfortunately, due to the operation condition of the ELSA ring, it was not possible to carry out EXAFS measurements, which would be very helpful in understanding the complete picture of nanoparticles stabilization and differences caused by further conditioning, e.g. applying the 'smooth oxidation' procedure. However, XANES measurements tend to be very sensetive for investigation of surface effects in case of very small Pt nanoparticles. Several ways of Pt$_{13}$ stabilization and further modification of the protection shell may be done based on findings observed from these analysis. Possible schemes of these processes are presented in Figure 5.8.
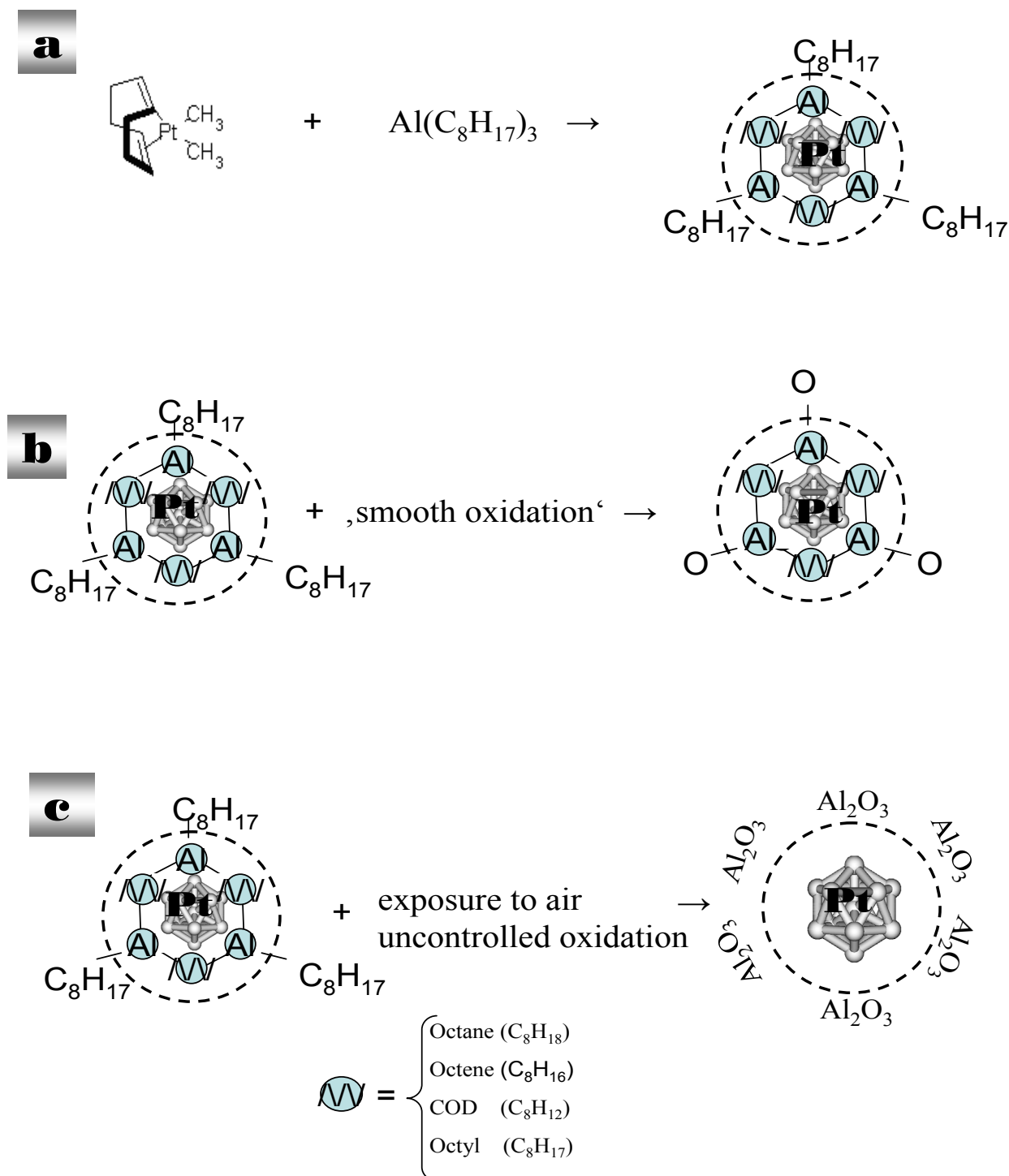
Figure 5.8: Possible schemes of Pt13 formation (a), stabilization after applying of 'smooth oxidation' procedure (b) and modification of protection shell after exposure to air(c).

5.2 Size and shape controlled synthesis of Pt nanoparticles stabilized by polyvinylpyrrolidon (PVP)

Pt–PVP stabilized nanoparticles with different sizes are another system on which the surface effects can be studied in detail. Moreover, the crucial aspects of nanoparticle production such as the kinetics of growth and parameters of synthesis which induce changes in the process of nanoparticle formation can be monitored in this system. As a consequence, more detailed understanding of nanoparticle formation can be extracted from XAS analysis.

5.2.1 XANES analysis

The Pt L_{III}–XANES spectra of Pt–PVP ($[C_6H_9NO]_n$) stabilized nanoparticles produced with (KGE.KA.144.03, 2.5 nm) and without (KGE.KA.144.02, 8.0 nm) addition of seeds during the synthesis are shown in Figure 5.9, along with Pt reference foil. Size information was extracted from the TEM measurements, presented in Figure 4.3. Under the assumption that the interaction between the surface of the nanoparticles and the stabilizer is defined by the stabilizer, one would expect a systematic size dependent change in the spectral features of nanoparticles, which would correlate to the number of surface atoms. As seen in Figure 5.9, the changes in the spectral features of Pt nanoparticles can only partly be described as a function of size. Obviously, for 2.5 nm and 8.0 nm nanoparticles the multiple scattering region is dominated by contribution which can be assigned to the F.C.C. Pt structure, as the position of the shape resonances remains more or less the same. However, the local electronic structure undergoes dramatic changes. Which is follows from the ratio of the white line to edge jump, that is for 8.0 nm nanoparticles is comparable with Pt foil, but significantly smaller for the 2.5 nm Pt nanoparticles. Thus, in contrast to the intuitive explanation, no clear and systematic size dependent trend in the data is found.
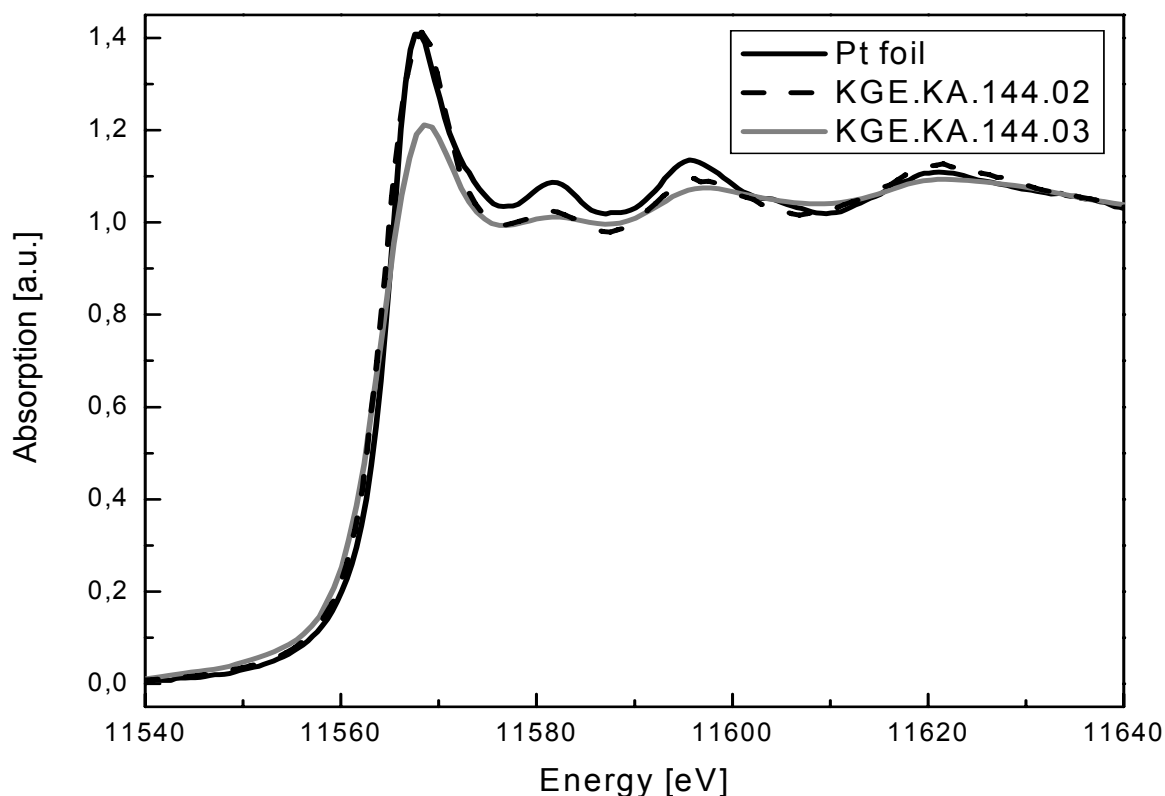
Figure 5.9: Pt L_{III} – XANES spectra of Pt-PVP stabilized nanoparticles prepared with (solid grey line) and without (dashed line) addition of seeds in comparison with Pt-foil (solid line)

In order to understand the unexpected behavior of the spectral features of Pt nanoparticles it is helpful to consider in detail the possible mechanisms of Pt nanoparticles and PVP stabilizer interaction. The PVP has a back bone of polyvinyl as hydrophobic $[N–C_2H_3]n$ and hydrophilic pendant groups Figure 5.10. The studies of the PVP protective mechanism on nanosized silver particles done by Z. Zhang et al. [Zha96], show that the ligand of C–N and C=O in PVP contribute more electronic density to the *sp* orbital of silver ions than H_2O; the silver ions in the Ag—PVP complex may obtain electrons from oxidizing or C–N agent more easily than those in Ag—H_2O. This model can be transferred directly to the case of the Pt nanoparticles. The mechanism of PVP interaction with Pt nanoparticles may be divided into three stages. Firstly, PVP donates lone pair electrons of oxygen or nitrogen atoms to *sp* orbitals of platinum atoms, thus forming the coordinative complex of Pt atoms and PVP in aqueous solution. It has to be stressed that the influence of nitrogen and oxygen on nanoparticles is hard to separate and monitor in the XANES spectra, as they have very similar electronegativity following the Pauling scale. Secondly, PVP promotes the nucleation of the metallic platinum because the Pt atoms–PVP complex is more easily reduced by hydrogen than the pure Pt atoms. Thirdly, PVP prohibits Pt nanoparticle aggregation and grain growth as a result of its steric effect.

The schematic representation of different ways of interaction between the PVP functional polymer and Pt nanoparticles is shown in Figure 5.10. Even if stabilization of Pt nanoparticles by PVP is assumed to be dependent on the particle size, a change of these configurations cannot resolve the question why the dramatic changes in electronic structure are encountered for the 2.5 nm particles at the L_{III} edge which probes mostly *d* states, whereas charge donation occurs in *s* and *p* states.
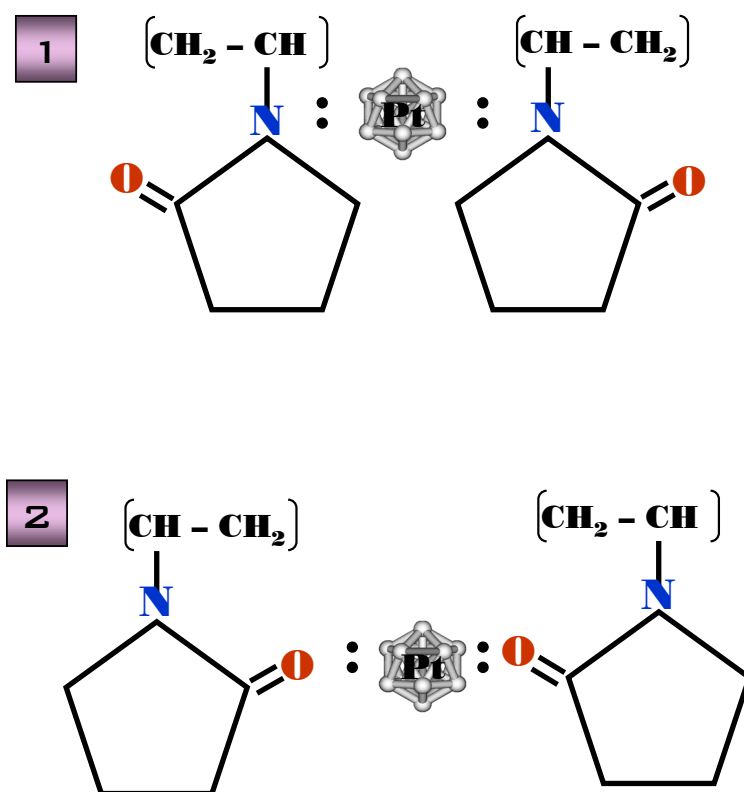
Figure 5.10: The schematic representation of interaction between the PVP functional polymer $[C_6H_9NO]_n$ and precursor for the Pt NP's – K_2PtCl_4

Here, the mechanism of nanoparticle formation can help understand observed changes in spectral features of 2.5 nm Pt nanoparticles. Generally, the formation of monodispersed nanoparticles poses two major challenges. Firstly, the morphology and shape selection of particle formed by interplay of nucleation and aggregation processes. Secondly, the size-selection mechanism, i.e., the kinetics of generation of narrow

particle size distribution. In the initial induction stage, solutes are formed to yield a supersaturated solution, leading to nucleation. The nuclei then grow by diffusive mechanism to form the primary particles (singlets), which in turn aggregate to form secondary particles. The secondary particles are sufficiently sparsely positioned in solution to conclude that their evolution is largely independent. It is also possible that singlets forming secondary particles may undergo restructuring and rearrangements resulting in more compact structures and leading to the shape selection. It was found that, in many systems, nuclei produced rapidly in a supersaturated solution, grew to nanosized singlets, which then coagulated to form much larger final nanoparticles in a process dominated by irreversible capture of these singlets [LaM52, Bal05]. In the case of Pt–PVP nanoparticles, addition of the seeds may lead to the faster rate of nucleation, and thus the growth by aggregation of singlets must be considered coupled to the process of formation of these singlets, which is time dependent. Due to the fact that Pt:PVP molar ratio has been kept the same, addition of the seeds may also cause that the precursor is in abundance and will not fully react/decompose to the Pt(0), during the particle formation. In this scenario, seeds can be treated as stable centers of growth thus the time of the growth which is needed for Pt–PVP nanoparticle is reduced. Bearing in mind the slow rate of reduction caused by H_2, some amount of the precursor can still be unreacted. Thus, pure Pt nanoparticles can be trapped in an unreacted K_2PtCl_4 droplet, to result in the double phase nanoparticle. This can explain the reduction of the white line intensity in the case of 2.5 nm Pt nanoparticles (KGE.KA.144.03), as the combination of XANES spectrum of K_2PtCl_4 compounds, calculated using FEFF8, and the Pt foil will result in the decrease of the white line intensity and first shape resonance located at about 11574 eV. Comparison of 2.5 nm Pt nanoparticles L_{III}–XANES spectra with Pt foil and calculated K_2PtCl_4 is shown in Figure 5.11
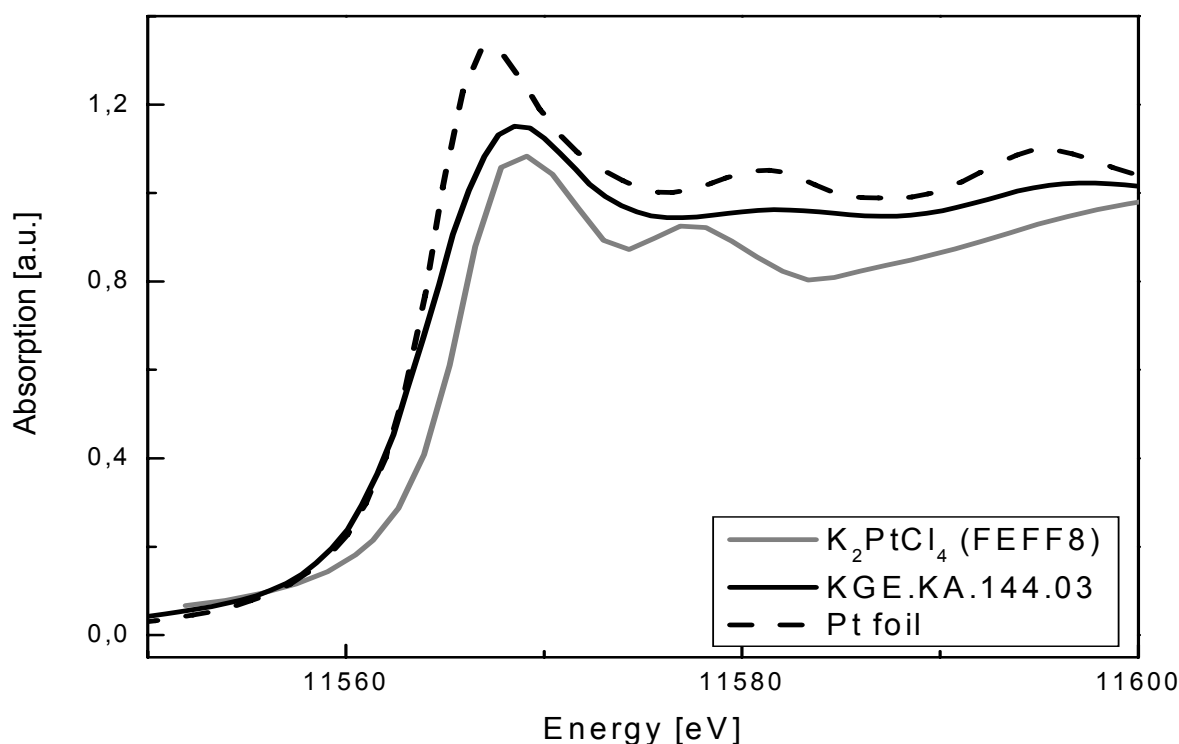
Figure 5.11: Pt L_{III} XANES spectra of 2.5 nm Pt nanoparticles in comparison with Pt foil (dashed) and precursor K_2PtCl_4 (solid grey)

Additional information, which can either prove or reject this hypothesis, can be extracted from the EXAFS analysis.

5.2.2 EXAFS data analysis

The raw EXAFS spectra and calculated background functions are shown in Figure 5.12 for the samples prepared with and without the addition of seeds. The data were Fourier transformed from 3.05 Å^{-1} to 10.8 Å^{-1} in k–space. To perform a two shell fit, a region from 1.2 Å to 4.9 Å has been used in R–space. The filtered and weighted (k^3) EXAFS data are shown in Figure 5.13, and show that the EXAFS signals from 8.0 nm and 2.5 nm Pt nanoparticles are different already in a third maximum, where a well resolved double peak shape is observed for small nanoparticles. The discrepancy is becoming more pronounced with the increase of k and, at k above 9 Å^{-1}, the oscillation is even shifted in phase. These findings suggest that another backscatterer contributes to the EXAFS signal, in case of 2.5 nm Pt nanoparticles, which is also reproduced in the Fourier transformed EXAFS data, as a clear shift of the center of the first pronounced peak is observed. The MFT of samples KGE.KA.144.02 and KGE.KA.144.03, along with MFT of Pt foil data present in Figure 5.14. The larger EXAFS amplitude of the particles prepared without addition of seeds points to a larger Pt-Pt contribution and bigger particle size, which is confirmed by TEM analysis Figure 4.3.
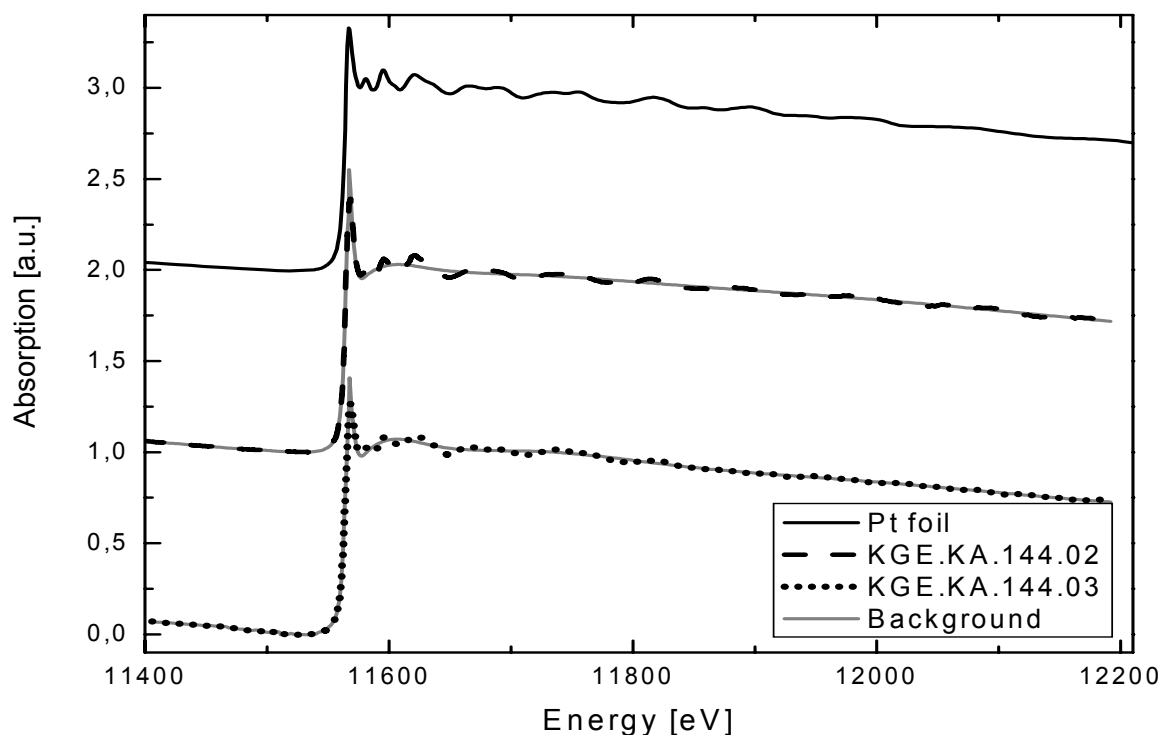
Figure 5.12: Pt L$_{III}$ – EXAFS spectra of 2.5 nm tetrahedral Pt nanoparticles (short dot) and 8 nm Pt nanoparticles (dashed line) in comparison with Pt-foil. Background is shown in grey

To obtain the amplitude reduction factor S_0^2 and Debye-Waller factor correspondent to metallic Pt, Fourier transformation with the same weighting (k^3) and over the same k range was done for the EXAFS data of Pt foil (Figure 5.14 solid grey line). For better illustration, the magnitude of the Pt foil MFT was adjusted until the first well pronounced peak in the Fourier transformation scaled with the corresponding peak derived from the samples KGE.KA.144.02. As mentioned above, the first Pt–Pt peak in Fourier transformation of 2.5 nm nanoparticles appears at lower (2.2 Å) R–distance, in comparison with Pt–Pt distance characteristic for bulk platinum (2.4 Å). This shift of the maximum to lower value can be explained by the presence of the lighter backscatterer in a first coordination shell.

As expected, it turns out that the single Pt–Pt contribution is not enough to obtain a reasonable fit of the first coordination shell (Figure 5.14), especially in the case of smaller nanoparticles (Figure 5.16). At the distances around 2 Å contributions of several light backscatterers, such as nitrogen, carbon, oxygen or chlorine, can be presented. To clarify the nature of the soft backscatterers at low R, the fit parameters

characterizing the Pt and N/O/Cl contribution were optimized in both k^1 and k^3 weighting to avoid overestimating or underestimating either the high-Z (Pt–Pt) or low-Z (Pt-N/Pt-O/Pt-Cl) contribution. Once a good fit has been obtained to estimate the EXAFS parameters with k^1 and k^3 weightings, the fit was optimized by allowing a few of the parameters to be varied (R, N, E_0 in table 5.2, KGE.KA.144.02), while the others were kept fixed.

Whereas the MFT of 2.5 nm Pt particles shows almost no structures at distances higher than 4.8 Å, MFT of 8.0 nm particles data shows the presence of higher coordination shells which are quite identical to the ones presented in the MFT of Pt foil data. The double structure of the peak at about 4 Å represents second shell coordinated Pt–Pt. Shape and magnitude of the peak in FT for 2.5 nm are very different from those of bigger particles. The well pronounced peak at 4 Å in case of MFT of sample KGE.KA.144.03 does not correspond to the characteristic peak of pure Pt–Pt coordination. However, the position of the calculated EXAFS signal of the Pt salt used as a precursor, corresponded reasonably well with the particles where additional contribution are needed for the adequate description of the data. The MFT of K_2PtCl_4, using the same range in R–space is presented in Figure 5.16. In fact, using an additional Pt–Cl and Pt–FK path, a good EXAFS fit can be obtained. Therefore, one can conclude that the two phases are supercomposed to give the resulting profile of NP's prepared with addition of the seeds. Further improvement may be obtained by the addition of another soft backscatterer, but the number of the free parameters available for the fit is insufficient for this inclusion. After all, for both samples, the distances and coordinations number resulting from the fit are in agreement with one of the references compounds.
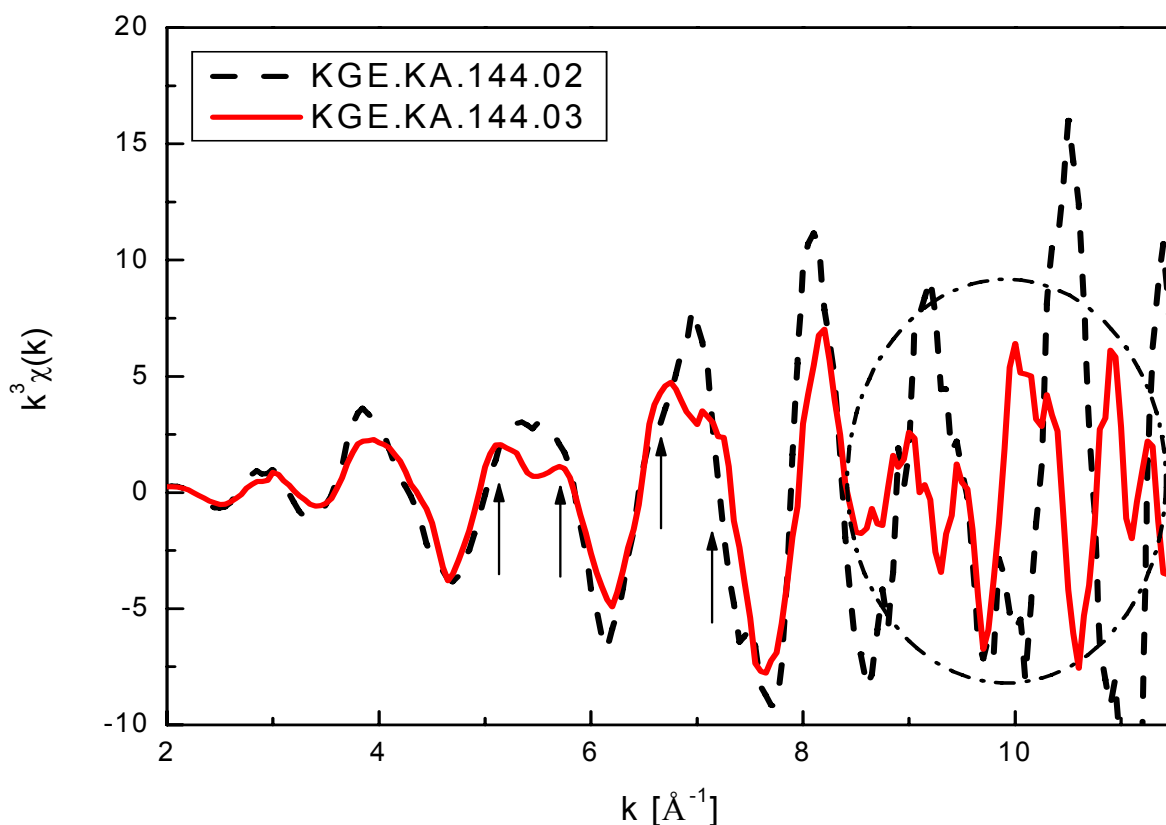
Figure 5.13: χ(k)-function derived for 2.5 nm tetrahedral Pt nanoparticles (short dot) and 8 nm Pt nanoparticles (dashed line)
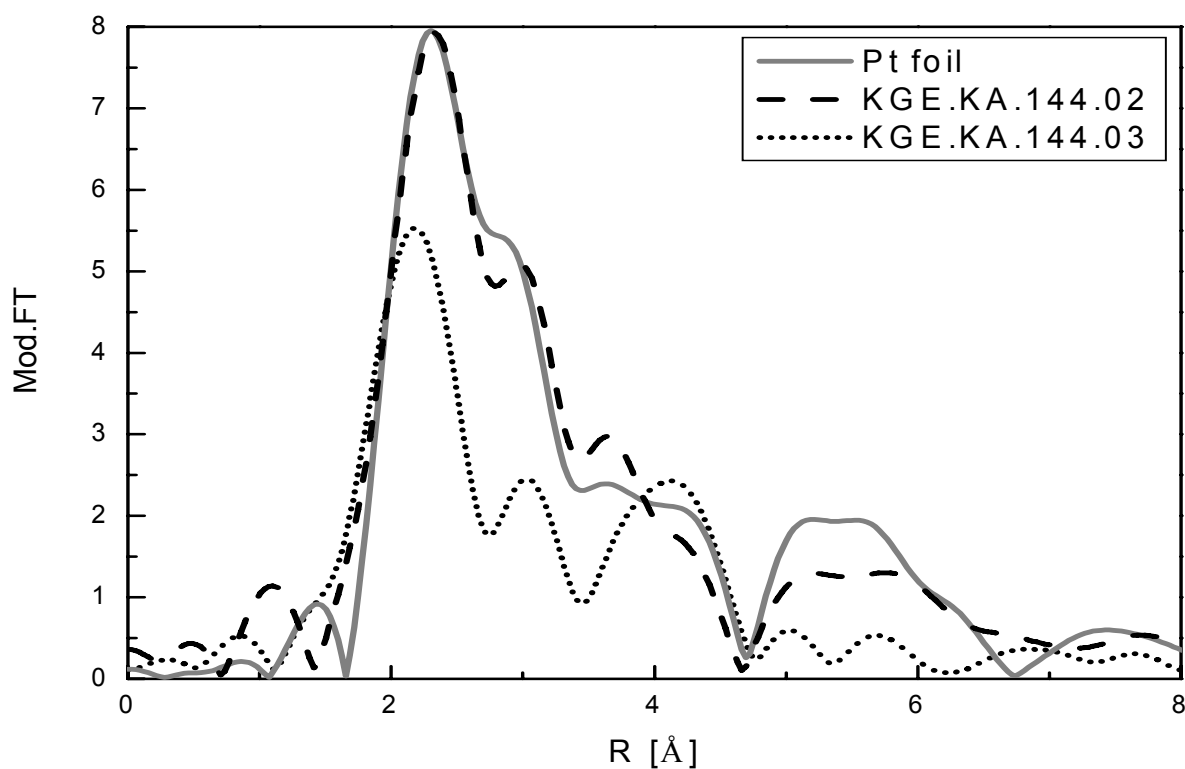
Figure 5.14: Modified Fourier transforms of Pt-PVP stabilizes nanoparticles prepared with (short dot line) and without (dashed line) addition of seeds, along with FT of Pt-foil (grey). The same k- and R-range have been used
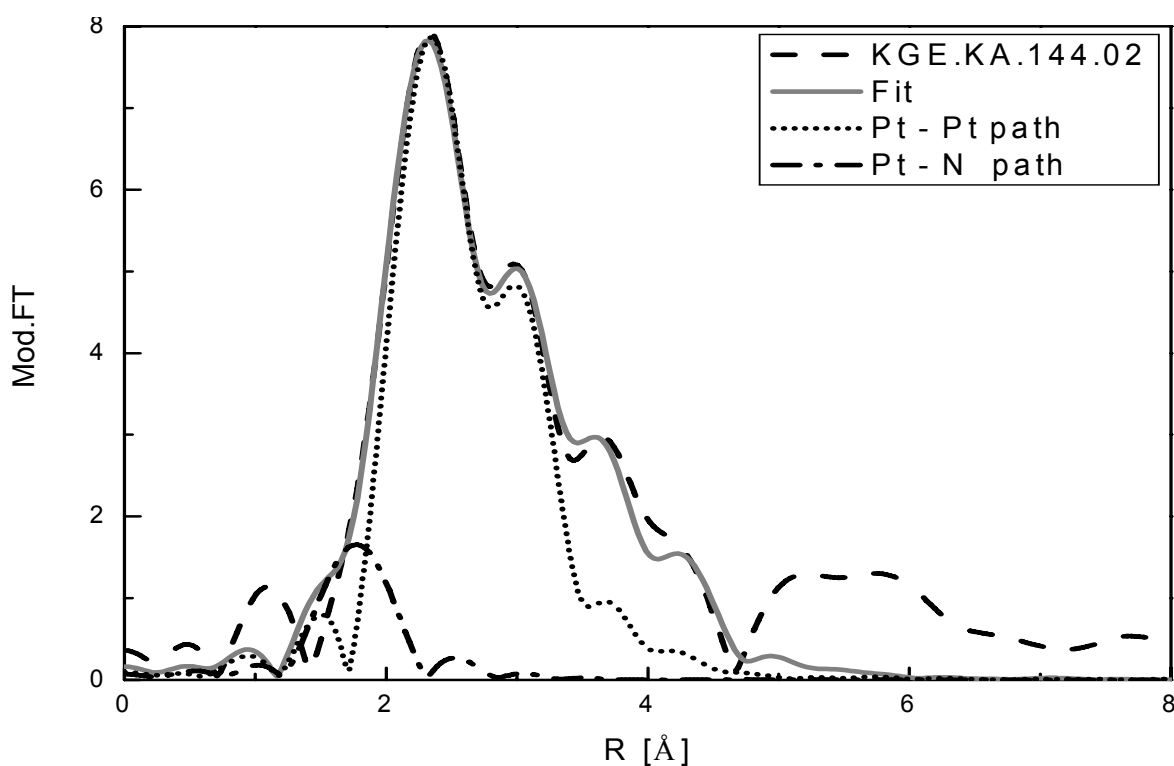
Figure 5.15: Modified Fourier transform of Pt-PVP stabilized 8 nm nanoparticles (dashed line) with two shell fit results (grey line) and used paths contributions
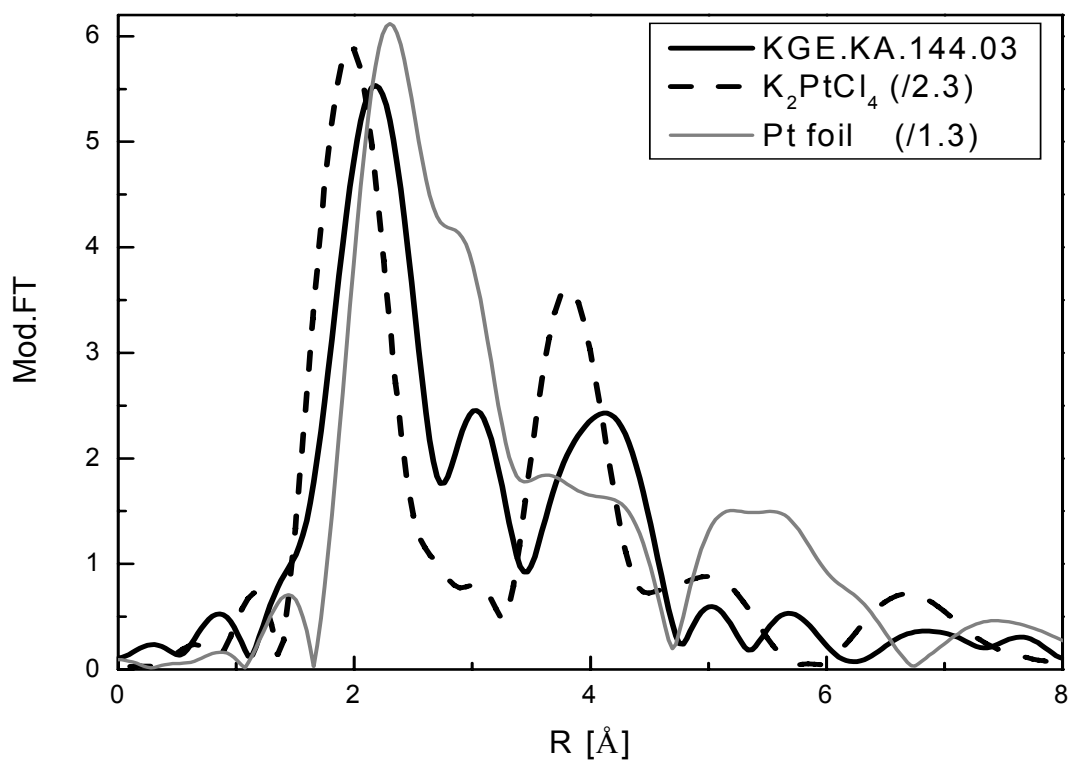
Figure 5.16: Modified Fourier transformation of 2.5 nm Pt-PVP nanoparticles (solid line)in comparison with Pt foil (grey solid line) and K₂PtCl₄ (dashed line) transforms
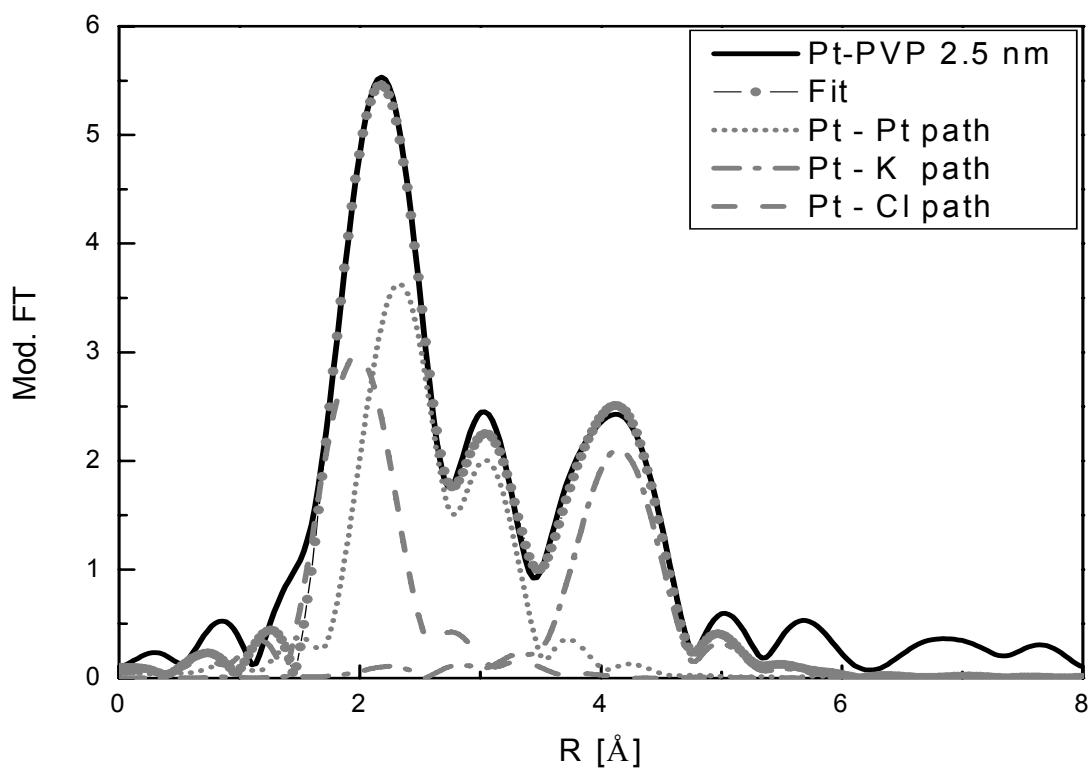
.Figure 5.17: Modified Fourier transforms of 2.5 nm nanoparticles (solid line) with two shell fit results (grey dash-dot line) along with paths contribution, used in the fit

These results confirm the hypothesis of the bi-phase character of 2.5 nm. The Pt-Cl (2.39 Å) and Pt-K (4.43 Å) distances are in agreement with one of the K_2PtCl_4 complex, which are 2.35 Å and 4.1 Å, respectively. In the case of Pt nanoparticles KGE.KA.144.02, EXAFS analysis confirms the presence of nitrogen or oxygen as a light backscatterer in a first coordination shell. The typical Pt–O and Pt–N distances are about 2.02 Å (PtO)/2.05 Å $Pt(NS)_4$ respectively, and thus can hardly be distinguished in EXAFS analysis. The electronegativity of nitrogen and oxygen is comparable, which is why under assumption that the interaction between Pt and N or O is weak (physisorption or van der Waals), no significant influence of this interaction is observed in XANES. From the distance results after the fit (2.17 Å), one can conclude that nitrogen or oxygen is found on the surface of the Pt nanoparticles as it is larger than the typical Pt–N/Pt–O distances. The Pt–Pt coordination number decreases from 11 to 7.2 and from 6.9 to 1.9 for the first and second coordination shell, respectively. On the one hand, these results are consistent with the size obtained from TEM. On the other, the significant decrease of second shell Pt-Pt coordination number in case of 2.5 nm nanoparticles, a consequence of the fact that smaller nanoparticles exhibit less order. Moreover, the decreasing of Debye-Waller factor is consistent with increasing particle size. However, the first and second shell Pt–Pt distances of 2.79 Å and 4.0 Å, respectively, are consistent with the presence of metallic Pt particles even in the case of 2.5 nm Pt nanoparticles.

Sample (k=3)	Backscatterer	R [Å]	N	$\sigma^2 [Å^2]$	$E_0 [eV]$
KGE.KA.144.02	N/O	2.17±0.02	1.2±0.3	0.0032	8.7±2.1
(8 nm without seeds)	Pt	2.79±0.01	11.0±0.6	0.0054	12.5±3.9
	Pt	4.0±0.04	6.9±1.8	0.0046	8.7±2.1
KGE.KA.144.03	Cl	2.39±0.02	1.2±0.2	0.0030	9.3±2.9
(2.5 nm with seeds)	Pt	2.79±0.02	7.2±0.4	0.0094	9.3±2.9
	Pt	4.0±0.05	1.9±0.1	0.0016	13.6±3.5

Table 5.2: Structural parameters of two shell fit for Pt-PVP stabilized particles prepared with (KGE.KA.144.03) and without (KGE.KA.144.02) additions of seeds

Therefore, based on the EXAFS analysis, contamination of the system with unreacted precursor material seems to be probable.

5.3   Conclusions

To summarize, the decomposing complex $(CH_3)_2Pt(COD)$ in the presence of trioctylaluminum, leads to the formation Pt nanoparticles stabilized by alkylaluminum groups via van der Waals or physisorption interaction. The size of the particle is not changing drastically after modification of storage condition such as 'smooth oxidation' process. TEM micrographs of Pt colloids in powder show monodisperse Pt particles of 0.75±0.10 nm and 0.82 ± 0.16 nm, respectively, before and after oxidative processes have been applied, which are identical within the error limits of TEM measurements. In particular, the particle size can be frozen at 0.75 nm when trioctylaluminum is used. These results confirm the weak interaction between Pt nanoparticles and stabilizer, as either formation of the core-shell nanoparticles or chemisorption that would lead to an increase of particle size.

Comparison of the XANES spectra with theoretical calculations confirmed the presence of Pt_{13} structure in case of Pt nanoparticles in solution and powder, if they were kept strictly under argon. XPS reveals that the as-prepared Pt nanoparticles are truly zerovalent and the signature out of Al-oxide can be detected once they were exposed to air. Exposure to air leads to dramatic changes in the electronic structure of Pt_{13} nanoparticles, as the rest of the alkyl aluminum group will react with large amount of air, resulting in the formation of Al_2O_3 matrix on the one hand and agglomeration of the Pt nanoparticles on the other, initiated by loosing coordination with $Al-C_8H_x$ active groups. The XANES analysis on this system establishes the step-wise model of the surface modification in dependence to time and amount of oxygen available for reaction. This is the first example of a Pt_{13} nanoparticles prepared by a wet-chemical method.

The XAFS investigation on Pt–PVP nanoparticles with different size has been carried out in order to obtain more understanding of the surface effects on resulting electronic and geometric structure. The surplus of precursor, which occurs due to addition of the seeds, leads to the presence of some unreacted amount of precursor. As a sequence, resulting nanoparticles are not contamination free, thus the monitoring of the pure surface effects is no longer possible. Instead of this, more detailed understanding in the kinetic of nanoparticles growth can be indirectly obtained from the XAFS analysis. For example, the difference in coordination geometry of resulting nanoparticles was proved by EXAFS analysis. Stabilization of Pt nanoparticles via Pt–N or Pt–O weak interaction found to be more preferable in case of 8.0 nm particles. In contrast to that, supercomposition of two phases, bulk Pt and one of precursor, was found in case of 2.5 nm particles. High similarity of the main spectral features between Pt reference foil and Pt nanoparticles observed by XANES fingerprint comparison, suggest that we are still dealing with F.C.C. platinum. These results confirm the presence of zerovalent platinum, this is in consistence with statement that once the Pt oxidation state is formed, the addition of PVP cannot change it drastically, as no regular chemical bond between Pt nanoparticles and N or C=O lone pair is formed.

6 Co-nanoparticles and their properties

One important scientific topic is to understand size *effects* on the physical and chemical properties of materials which become crucial, especially in the nanoscopic size region [Cal04, Nie03, and Gam03].

Nanometer size particles (NP's from 1 nm to 50 nm) display many properties which are both quantitatively and qualitatively different from the respective bulk materials. As will be shown below, it is possible to tune specific properties of NP's, such as geometric and electronic structure, by varying the particle size. Recently, the study of size effects of metal NP's has intensified with the promise of utilizing novel properties in new materials and devices [Sun99]. The magnetic properties of NP's, for example, depend strongly on the size of the particles. Typically, nanosized particles show superparamagnetic properties and magnetic materials, such as cobalt, become very important for their applications in magnetic storage technology. Moreover, cobalt nanoparticles are found to be a suitable base for producing magnetic fluids (MF's). These magnetic fluids with a narrow size distribution of the corresponding NP's exhibit properties useful for a number of applications, e.g. magnetic fluids are used for the cooling of loudspeakers in high performance HiFi systems, which allow increasing maximum power of the system [Ode03]. Besides this thermal application, ferrofluids are used in mechanical systems like bearings as frictionless sealing [Ber96] or in biomedical applications for drug targeting [Ale01] and for magnetic hyperthermia [Her98] in cancer treatment.

The thermolysis of $Co_2(CO)_8$ is one of the convenient and frequently applied methods for the preparation of nanoscopic Co(0) particles (chapter 4.1.3). Unfortunately, the Co particles obtained by this procedure show a broad size distribution. However, it has been found by Bönnemann et. al. [Bön04] that in the presence of organo aluminum compounds it is possible to control size and 'monodispersity' of the zerovalent magnetic nanoparticles resulting from the thermolysis of $Co_2(CO)_8$ [Pap83]. Another important aim of nanosized particles synthesis is to achieve stability against air and moisture. A novel 'smooth oxidation' procedure has been developed and applied to the synthesis of transition metal nanoparticles in order to modify the protection shell. The influence of the 'smooth oxidation' procedure on the resulting nanoparticles will be described in more detail in chapter 6.1.3 of the present thesis. Peptization of nanoparticles using a suitable surfactants leads to the modification of the protection shell formed around the metallic core during the 'smooth oxidation' procedure. The formation of different crystallographic phases can also occur during this synthesis (chapter 6.1.2). For the cobalt nanoparticles investigated in this thesis, main parameters of the synthesis are summarized in Appendix A.

6.1 Stabilization of nanoparticle against agglomeration

In the previous chapter it was shown that in the case of small particles the changes in the electronic and geometric structure can be understood as a function of surface–induced effects. In contrast to the bulk materials, where metallic surfaces have a large supply of electrons, the electron supply in the case of nanosized particles is finite. As a consequence, the influence of surfactant becomes more important and even dominates on the nanoscale. For practical implementation of cobalt NP's, for example in biomedical applications, nanoparticles with a narrow size distribution have to be prepared. For this purpose, monodisperse nanoparticles are desired. It should be mentioned that stabilization of nanoparticles against agglomeration by a protection shell of surfactant molecules is one of the most common approaches. Understanding the changes in electronic and geometric structure of nanoparticles caused by chemical interactions at the surface is critical in the detailed characterization of nanoparticles.

One of the possible starting points in the wet-chemical approach used for the production of nanoparticles is thermolysis,–dissociation by heat. It must be mentioned that decomposition of $Co_2(CO)_8$, the precursor for Co nanoparticles, can take place even at room temperature. Co particles resulting after thermolysis show a wide size distribution and have a tendency towards agglomeration and oxidation [Kre01].

Figure 6.1 shows the TEM image of Co particles obtained after slow thermolysis in toluene (left, the scale bar is 200 nm) and in the presence of Al(R)$_3$ (right, an average size is 10.0 ±1.1 nm). As can be seen in Figure 6.1 (left), thermolysis in the absence of Al(R)$_3$ leads to the formation of dense agglomerates, whereas in the presence of Al(R)$_3$ and KorantinSH well defined particle size can be reached–Figure 6.1 (right). In addition to this, recent investigations of the synthesis parameters and conditions, by Bönnemann et.al., reveal that the presence of surfactant not only prevents particles from agglomerations, but also has a significant influence on the electronic structure of the resulting particles [Chi02, Yu03 and Bön03].
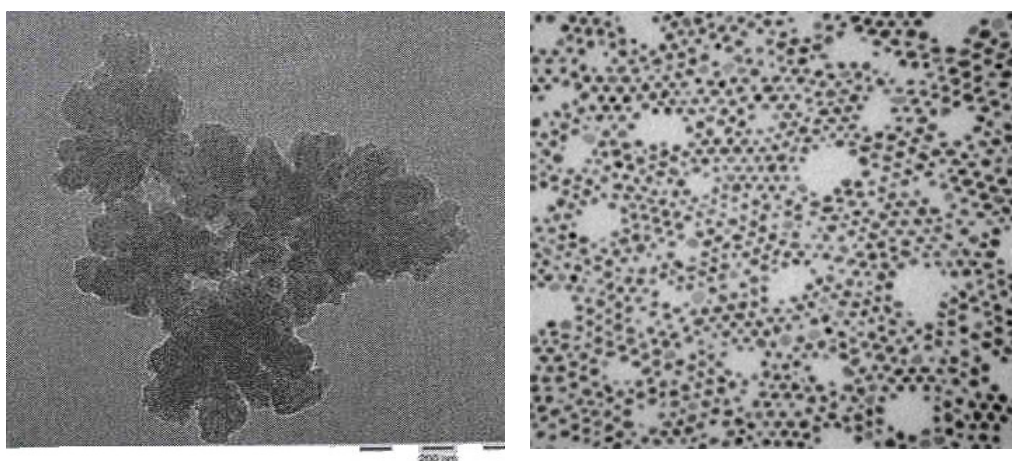
Figure 6.1: TEM image of NP's resulting after thermolysis in toluene (left)
and in the presence of Al(C$_8$H$_{17}$)$_3$ (right) [Boen]

Before one starts to derive some information from the XANES and EXAFS data, it is always good to test the reliability of the results which can be extracted. For this purpose a set consistent of two samples prepared following the same synthesis procedure, but in at different times, will be discussed below. The main information on synthesis condition, as well as the size of the nanoparticles, can be found in Appendix A. It should be mentioned that spectra of these two samples have been taken during different beam–times at beam line BN3, providing an opportunity to verify the reproducibility of the synthesis and, in addition to that, the independence of data generation with respect to operating conditions of the ring.

Figure 6.2 shows the Co K–edge XANES spectra of samples labeled MTV–MA–053 and MTV–MA–084–01 along with their difference. As can be seen, the spectra are identical to each other and the highest discrepancy in absorption is less than 0.03 a.u. in the energy region of the absorption edge and the white line. This value can be used as an error in the XANES 'fingerprint' analysis. This 'fingerprint' comparison also proves a high sensitivity of the XANES spectra to even small changes in the electronic and geometric structure of investigated materials, which is independent of operating conditions.
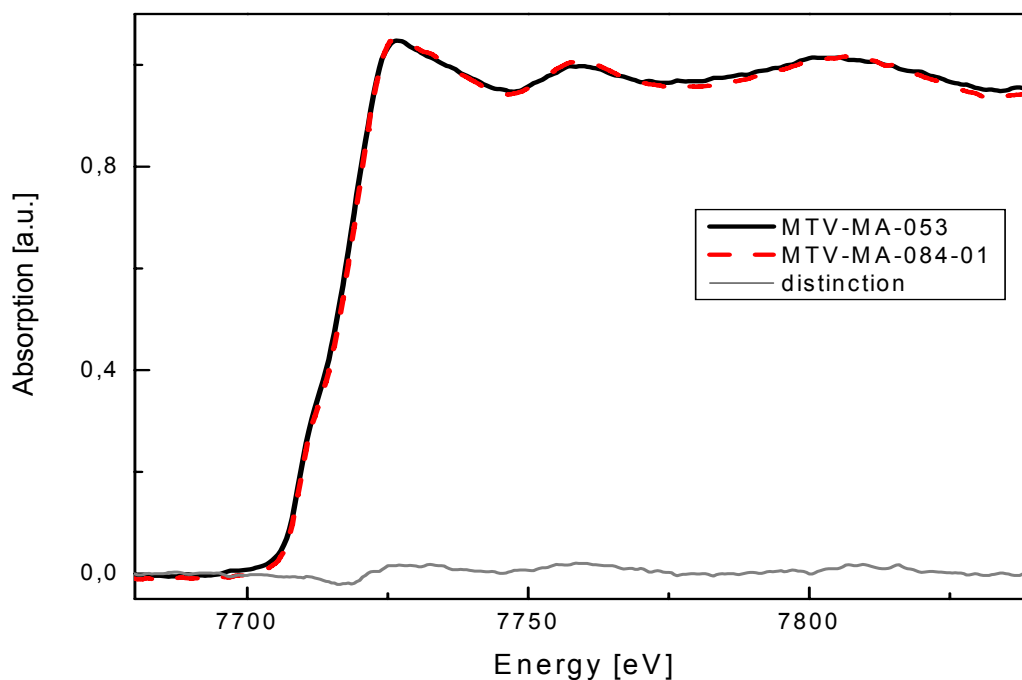
Figure 6.2: Co K–XANES spectra of samples MTV-MA-053 and MTV-MA-084-01 with their distinction

For the EXAFS analysis a fitting procedure was done following the standard data evaluation routine. Data range varies from 2.8 Å^{-1} to 12 Å^{-1} and from 0.9 Å to 2.8 Å, in k– and R– space, respectively. The amplitude reduction factor was fixed at the value of $S_0^2 = 0.825$, extracted from fit of a Co foil. For simplification, only the MFT are presented in the Figure 6.3 with a fit of the first coordination shell. However, the profile of the MFT's is somewhat different the resulting values of nearest Co–Co distance (2.5 Å) match the typical values known from the crystallographic data. The value of coordination number obtained from the fit (CN=5) is lower than the calculated if one assumes that for 3.5 nm nanoparticles about 60% of atoms are on the surface (CN=8.4).

Sample	Backscatterer	R[Å]	N	σ^2[Å^2]	E$_0$[eV]
MTV-MA-053	Co	2.51±0.03	4.9±0.1	0.0076±0.0002	3.9±0.2
MTV-MA-084-01	Co	2.49±0.01	4.9±0.3	0.0076±0.0001	2.6±1.5

Table 6.1: Fit results of nanoparticles MTV-MA-053 and MTV-MA-084-01 obtained from the EXAFS analysis

The deviation in the values resulting after fit which have the same level of error with the one presented in table 6.1, will be considered as identical for further EXAFS evaluations.
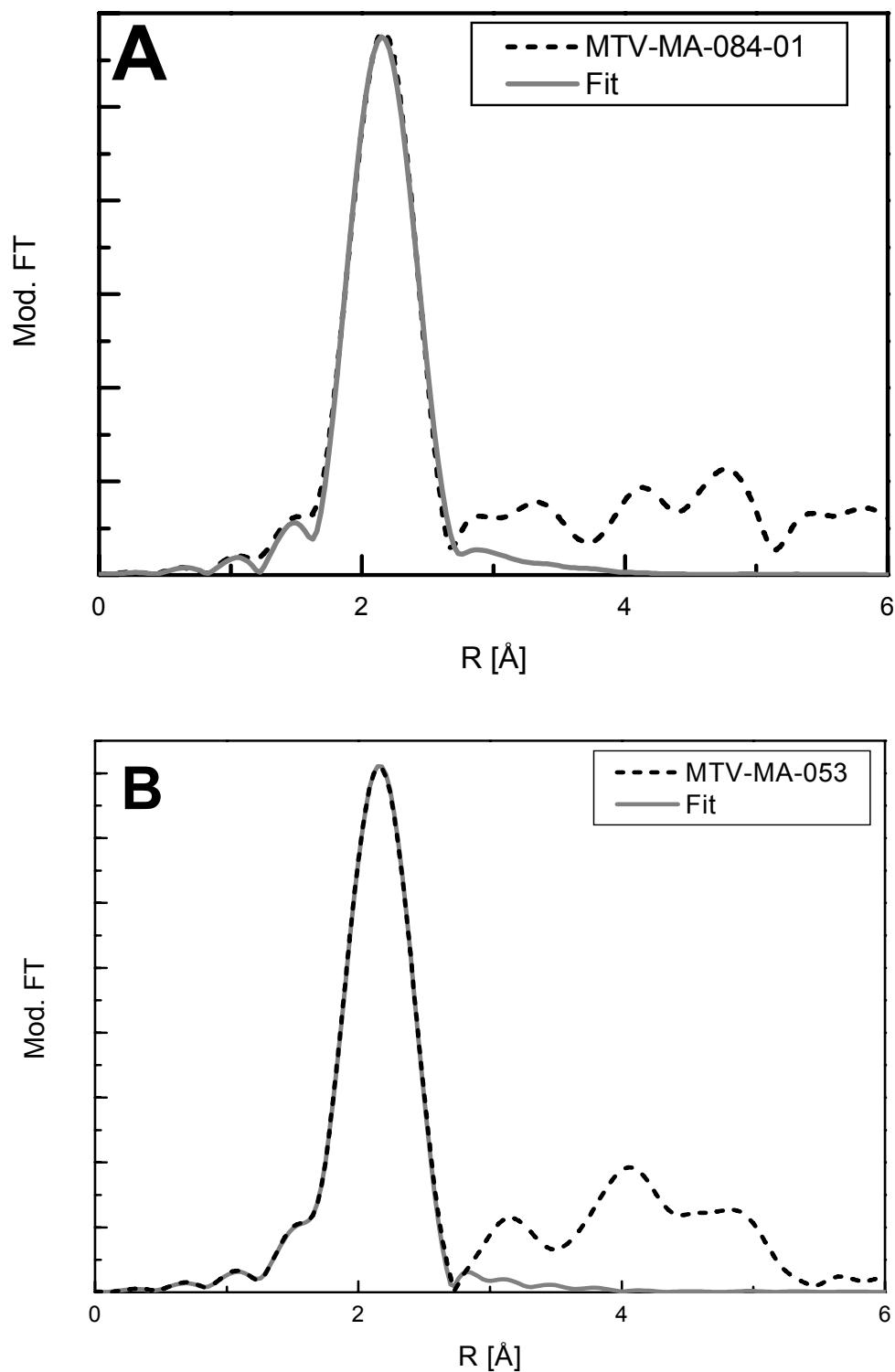
Figure 6.3: Modified Fourier transforms of nanoparticles MTV-MA-084-01 (A) and MTV-MA-053 (B)

6.1.1   Surfactant influence on Cobalt nanoparticles

In Figure 6.4 and Figure 6.5 the Co K-XANES spectra of particles dispersed in vacuum oil L9 with addition of KorantinSH (MTV–MA–033) and dispersed with a combination of KorantinSH and LP4 (MTV–MA–49) are shown in comparison with reference Co foil. It has to be stressed that these nanoparticles have been prepared following the same synthesis procedure and were strictly kept and measured under Argon. In this

case the only parameter which can influence the electronic and geometric structure of the resulting nanoparticles is the additional LP4. Main parameters of the synthesis are summarized in table 6.2.

Sample #	Form	Size	Initial ratio Co:Al	Al(R)$_3$ chain length	Surfactant
MTV–MA–049	magnetic fluid	10.0 ± 1.1 nm	10:1	Al(C$_8$H$_{17}$)$_3$	KorantinSH, LP4
MTV–MA–033	magnetic fluid	10.0 ± 1.1 nm	10:1	Al(C$_8$H$_{17}$)$_3$	KorantinSH

Table 6.2: Main parameters of the synthesis for nanoparticles MTV-MA-049 and MTV-MA-033

For the XANES 'fingerprint' comparison the spectra were normalized at 7825 eV and the energy scale calibrated to the first inflection point of bulk Cobalt 7709 eV [Tho01]. As can be seen from Figure 6.4, spectral features of the nanoparticles MTV–MA–49 are identical with the Co foil spectra. As a consequence, it is possible to conclude that the produced particles have an H.C.P. structure and the surrounding environment of the absorbing atom is not different from the one in the bulk material. The shape resonances are less pronounced in comparison with Co foil due to the small particle size.
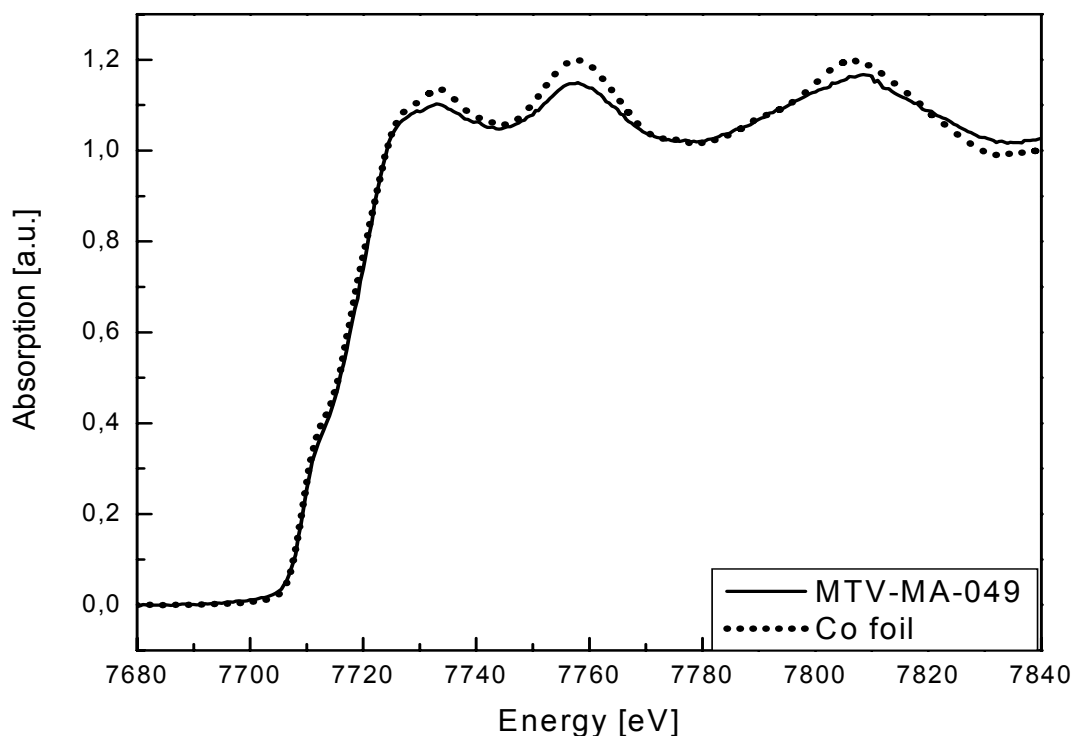
Figure 6.4: XANES spectrum of Co foil (doted) and nanoparticles MTV-MA-049 (solid), produced following the general procedure

In contrast to results observed for nanoparticles MTV–MA–049, the XANES spectrum of MF MTV–MA–033 is significantly different from a Co foil spectrum, as can be seen in Figure 6.5.
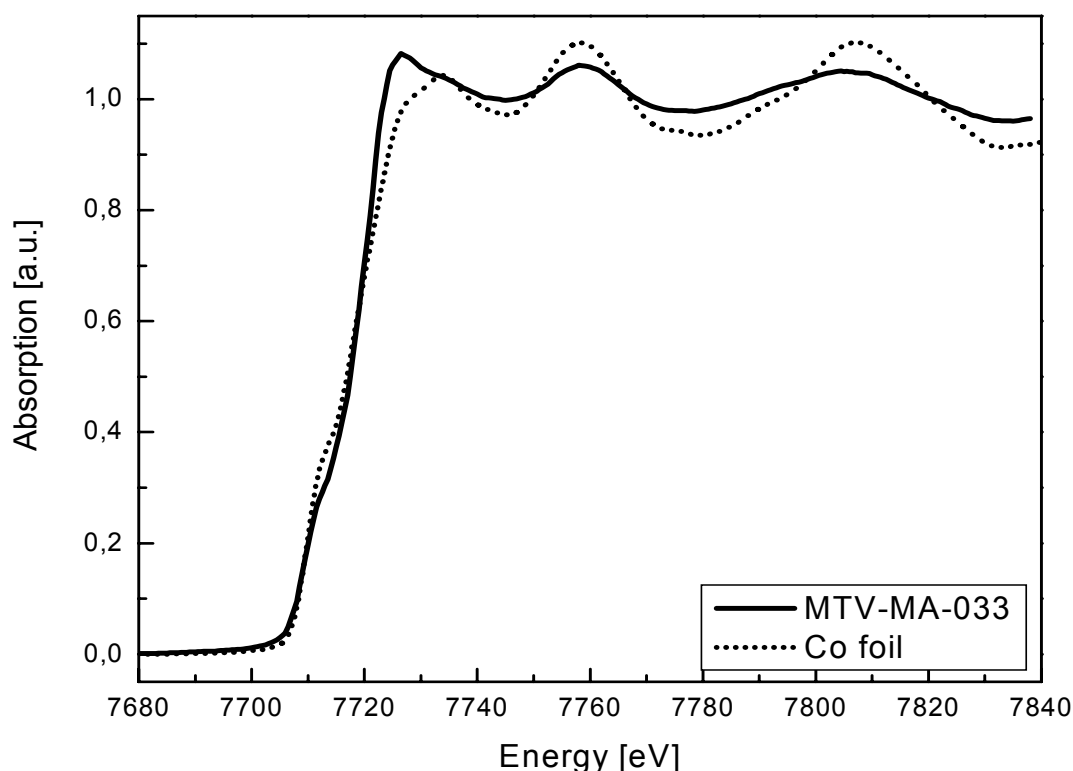
Figure 6.5: XANES spectrum of Co foil (doted) and nanoparticles MTV-MA-033 (solid), produced following the general procedure

The Co K–XANES spectrum of the MF MTV–MA–033 shows that the intensity of the pre–edge peak is comparable with Co foil while the height of the white line increases and its maximum is shifted towards lower energies. One possible way to understand these changes is to assume that a partial oxidation of nanoparticles occurs. However, the storage and measurements have been performed in Argon atmosphere and, therefore, even a partial oxidation is unlikely to occur. Moreover, the position of the shape resonances is extremely similar to the metallic Cobalt. Further on it can also be seen that the EXAFS analysis does not support the possibility of partial oxidation. On the other hand, the spectral features for sample MTV–MA–033 can be interpreted as an influence of the surfactant which leads to a charge transfer between the surface of the nanoparticles and COOH– groups of the surfactant. Virtually all vapor–liquid–solid interfaces acquire charge by dissociation or adsorption of ionic constituents. In addition to electrostatic interactions, short-range chemical interactions between ions and the surface can lead to pronounced effects, resulting in a decrease of the intensity of the pre–edge shoulder. However, the contribution from metal–metal interaction is dominated upon metal–surfactant interaction as the positions of the shape resonances are identical with Co foil. Besides this, in nanosized scale, contribution of the surface energy term includes a complete or partial phase transition. Therefore, the change in intensity of the white line peaks might be correlated with the formation of a phase different from elemental Co phase (H.C.P.) structure [Qad01].

6.1.2   Phase formation during preparation

To gain an understanding of the observed changes in spectral features of sample MTV–MA–033, the K–edge XANES spectra of different crystallographic phases known for elemental Cobalt has been calculated using FEFF8 code. In the literature, four phases are reported for cobalt. The stable forms for elemental bulk cobalt are hexagonal-close-packed (H.C.P./α-phase) below 425 °C and face-centered-cubic (F.C.C./β-phase) at higher temperatures. Apart from these forms, two other structure types of cobalt are described: a 'forced'

body-centered-cubic (B.C.C.) phase was postulated by Prinz [Pri85]. Dinega and Bawendi [Din99] reported formation of addition crystal structure, the epsilon-phase (ε-phase). The ε-phase has the complex cubic symmetry of the β-phase of manganese. Sun and Murray confirmed the existence of ε-phase [Sun99]. To illustrate the coordination geometry for the above phases their crystal structures are presented in Figure 6.6.
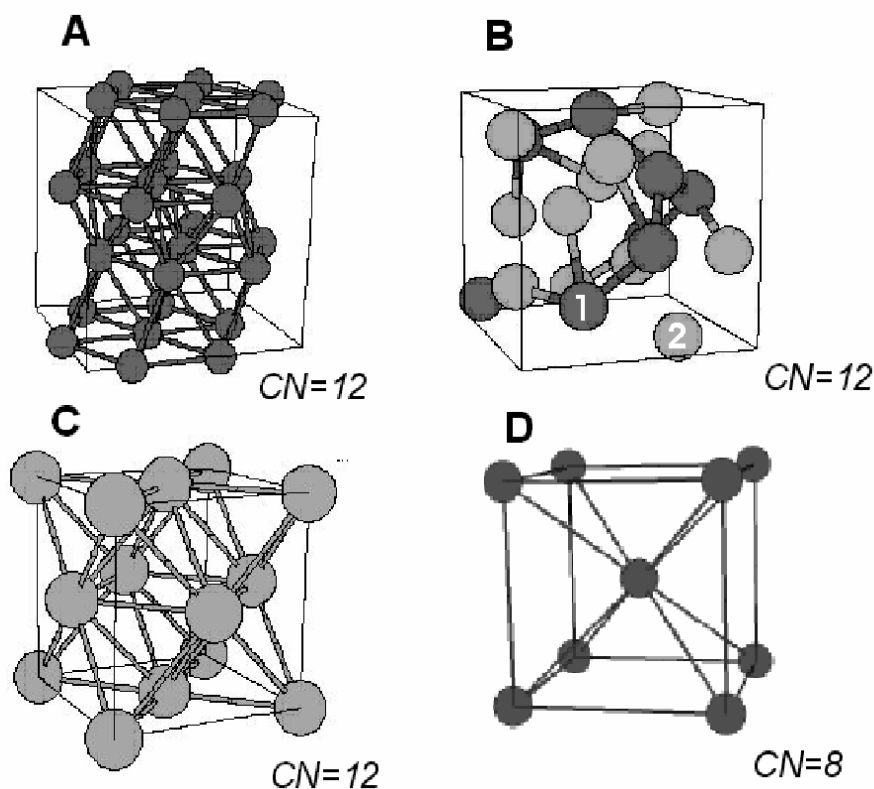
Figure 6.6: H.C.P. (A), ε-phase (B), F.C.C (C) and B.C.C. (D) crystal structures which are known for elemental cobalt and corresponding coordination numbers (CN)

Different bonding geometry leads to the appearance of different features in the XANES spectra. Theoretical XANES spectra for F.C.C., B.C.C and ε-phase structures are shown in Figure 6.7 and plotted along with the experimental spectrum of a cobalt foil for the 'fingerprint' comparison of the positions and intensities of the main spectral features. As mentioned previously (chapter 2.3.1), the XANES 'fingerprint' comparison can be used to determine the crystal structure of the Co nanoparticles. The main XANES spectral features of bulk H.C.P. cobalt are: the pre-edge feature at approximately 7712 eV with an inflection point at 7709 eV, usually assigned to an electron transition from *1s* to a hybridized *p-d* orbital, the white line consisting of two well resolved peaks at about 7727 eV and 7733 eV. The intensity of the second peak is higher than for the first peak.

Two well resolved peaks in the white line region are characteristic for the F.C.C. structure as well. In contrast to the H.C.P. phase, intensity of the second peak is lower than the intensity of the first peak and position of the peaks is shifted to higher energies, relative to corresponding peaks of H.C.P. phase. The calculated spectrum of the epsilon cobalt not only shows a reduced pre-edge intensity, but also a larger energy splitting between the pre-edge structure and the main absorption edge. The slight reduction of the intensity of the pre-edge structure might thus be interpreted as a result of a complex cubic geometry (P4₃32) where Co atoms populate two different sites, which are marked as **1** and **2** in Figure 6.6(B). As can be seen from Figure 6.7, the deviations in calculated spectra of different phases are significant. The suitability of the FEFF8 code to obtain detailed information on the electronic and geometric structure has been shown in a number of previous studies [Mod03b, Gil03 and Hal02].
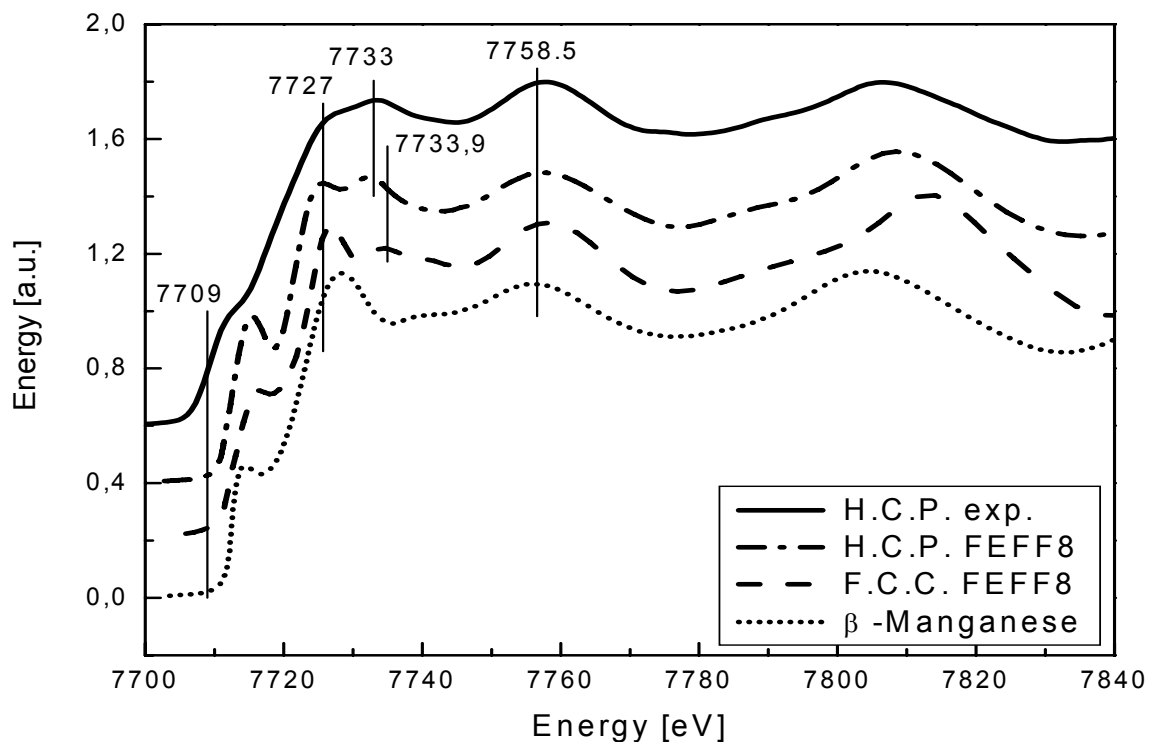
Figure 6.7: Experimental spectrum for metallic Cobalt foil (solid) compared to spectra calculated using FEFF8 code: F.C.C. (dashed), H.C.P. (dash-dot line) and ε-phase (doted)
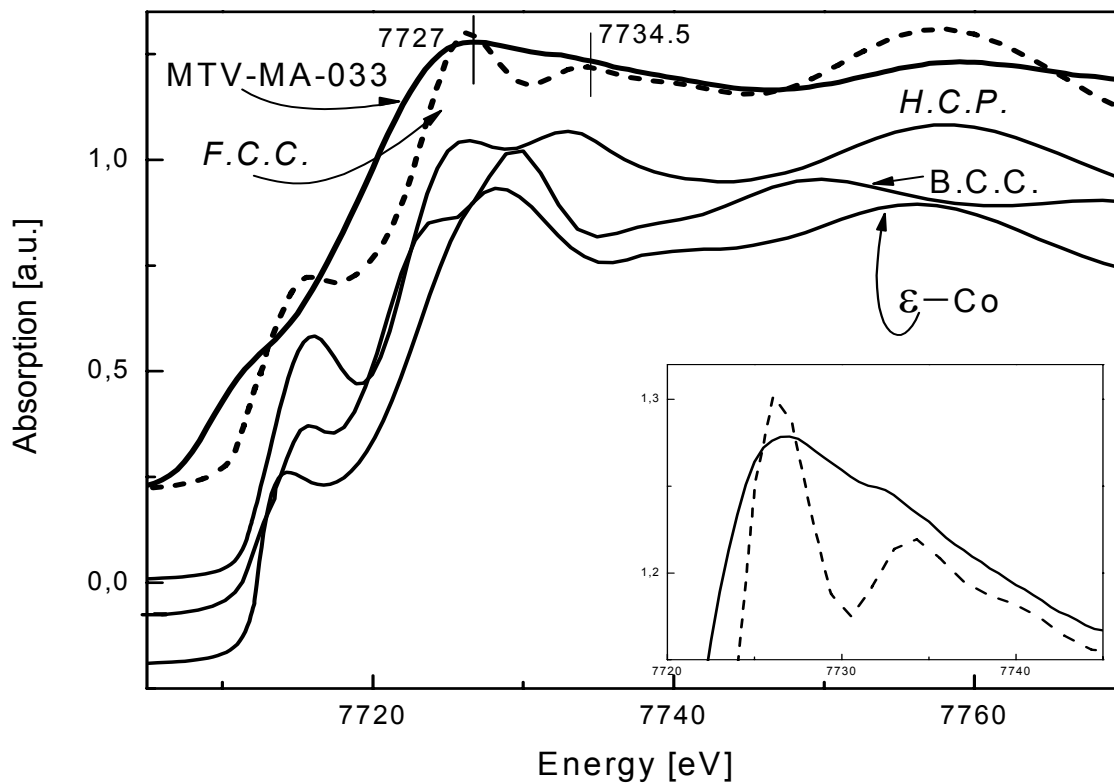
Figure 6.8: XANES spectra of nanoparticles MTV–MA – 033 (solid) and calculated (from top to bottom) F.C.C. (dashed line), H.C.P., B.C.C. and ε – phases

The position of the maximum of the white line in the calculated XANES spectrum for F.C.C. cobalt is consistent with the one of the sample MTV–MA–033 and located at about 7727 eV; the second peak is found at about 7734.5 eV. The position of the first and second peaks (see enlarged inset of the white line region in Figure 6.8) is consistent with values obtained from FEFF8 calculations for F.C.C. phase of Cobalt. As a consequence, one can conclude that using the combination of KorantinSH and LP4 surfactants during the synthesis leads to the formation of 10.0 nm F.C.C. nanoparticles. The formation of a different phase induced by surfactants and/or size effects has been widely reported for Cobalt nanoparticles by different groups [Qad01, Gui02, and Gui04].

To verify the idea of a cubic structure formation during nanoparticle production, an EXAFS analysis was performed for the samples MTV–MA–049 and MTV–MA–033. The Co K–edge absorption spectra of nanoparticles, Co reference foil and background are presented in Figure 6.9. MFT of nanoparticles MTV–MA–049 and MTV–MA–033 with fit results are presented in Figure 6.10 and Figure 6.11, respectively. Fit parameters and result are summarized in table 6.3.

As can be seen from Figure 6.10 and Figure 6.11, the maximum of the MFT appears at around 2.3 Å that is lower than the true bond length, which is usually 2.49 Å for nearest Co-Co. Distances in the FT EXAFS spectra are not phase-shift corrected and thus shifted to lower values compared to the true bond length. Theory predicts that for the H.C.P. phase the first shell consists of two subshells of 6 atoms at 2.50 Å and 2.51 Å, respectively. In contrast to that, the F.C.C. phase has a single coordination shell at 2.51 Å and in the epsilon phase the 12 nearest neighbors are distributed over a range of 2.28 Å to 2.58 Å. In addition to distances, the profile of the higher coordination shell is different for different Co phases and can thus be used as a criterion for the phase determination.
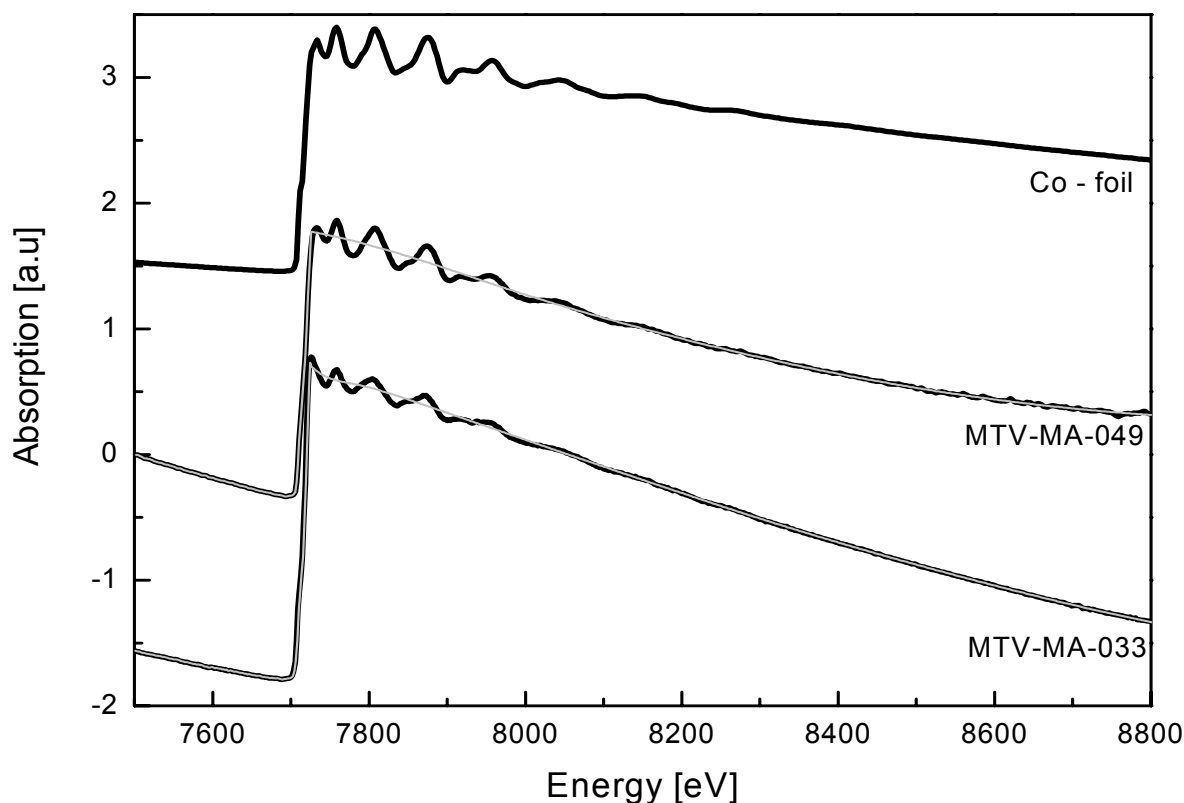
Figure 6.9: The raw EXAFS spectra, from top to bottom, of Co-foil, sample MTV-MA-049 and MTV-MA-033 with background-function (grey)
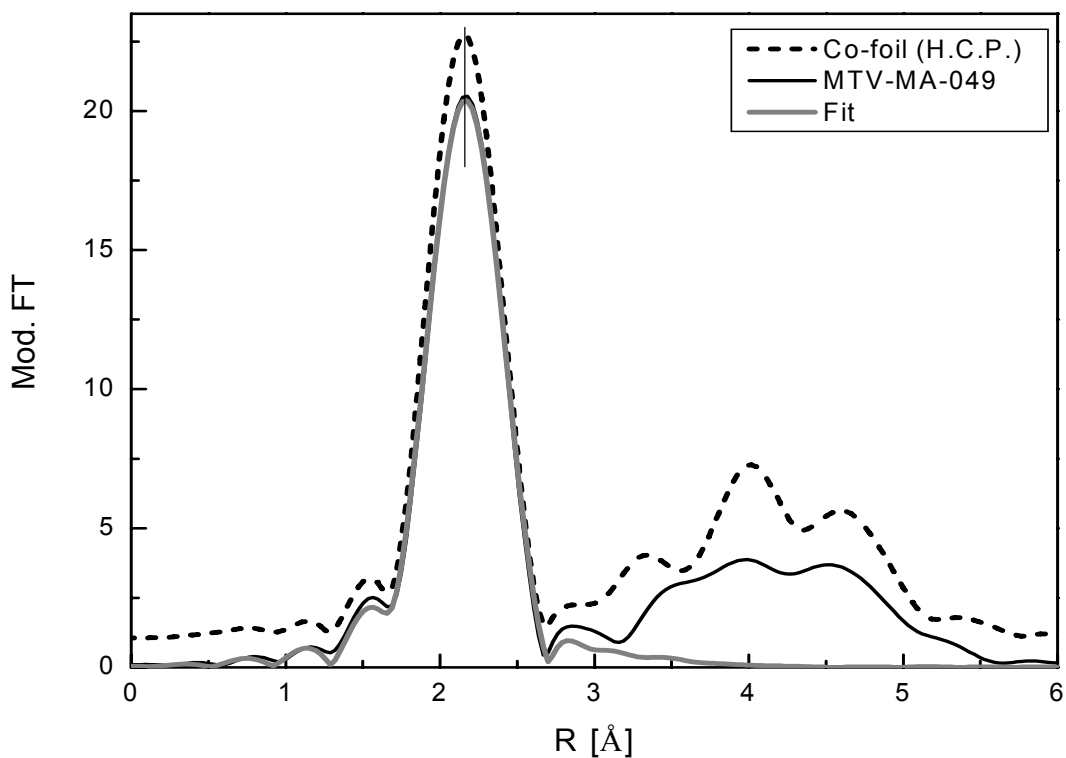
Figure 6.10: Modified Fourier transforms of sample MTV-MA-049 (solid line) in comparison with MTF of H.C.P. phase of Cobalt (dashed line) and first shell fits result (grey)
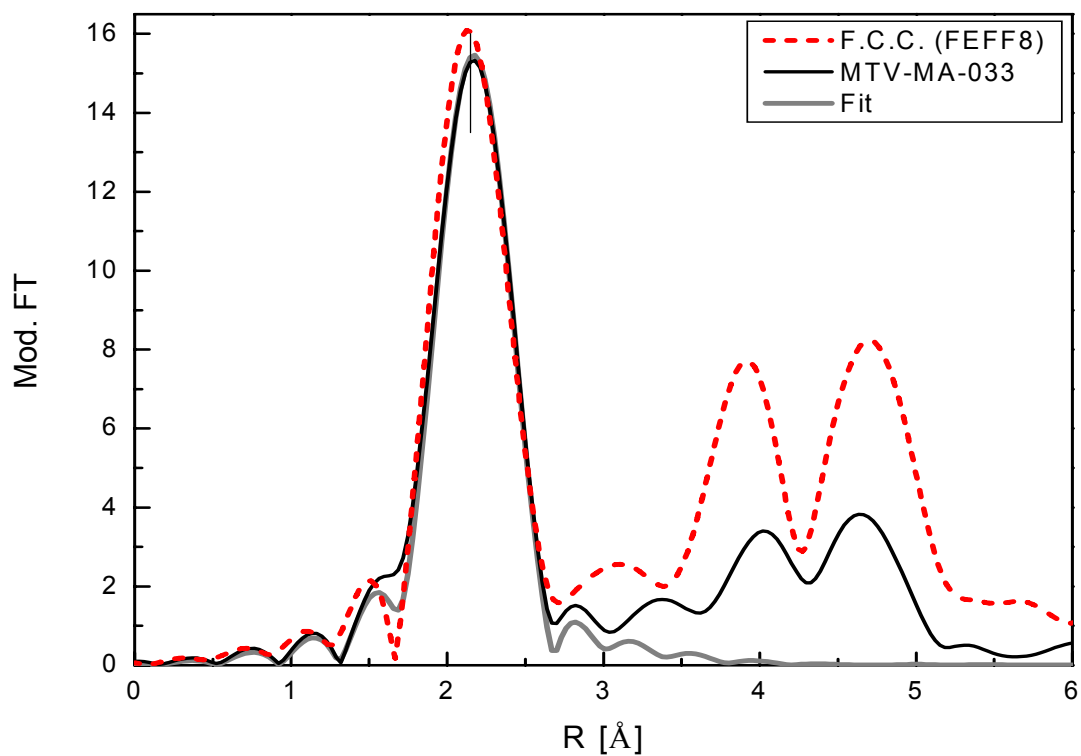
Figure 6.11: Modified Fourier transform of sample MTV-MA-084-02 (solid line) and Co-foil F.C.C. (dashed line) and first shell fit results (grey)

Even from a quick visual analysis of the MFT profile of samples MT-MA-033, it can be concluded that the profile of higher coordination shells has only two well resolved maxima which refer to the F.C.C. crystallographic phase. Whereas, the MFT of sample MTV–MA–049 shows three quite pronounced peaks in higher coordination shell which is similar to MFT of H.C.P. Co-foil. It has to be mentioned that without the information obtained from XANES 'fingerprint' analysis Figure 6.8 it would be hard to distinguish different crystallographic phases, as the differences in the MTF are within the error level discussed in case of samples MTV–MA–053 and MTV–MA–084–01.

It must be stressed that in contrast to the intuitively expected partial oxidation or presence of chemical interaction, no contribution from a soft backscatterer is observed by EXAFS analysis. The best fit results confirm the presence of only metal–metal bond in the first coordination shell of cobalt nanoparticles. From the fitting results which are shown in table 6.3 it can be seen that the distance for NP's MTV–MA–049 and MTV–MA–033 fit to the typical distance for H.C.P. or/and F.C.C. phase. The coordination numbers for nanoparticles are reduced in comparison with bulk Co, which, on the one hand, can be explained by the small particle size. For nanoparticles with an average size of 10.0 ± 1.1 nm, 10% of atoms are on the surface, and thus the expected coordination number should be about 11.4. The reduced values of coordination numbers achieved from the fit in comparison with the expected values may be due to partial disorder in nanoparticle, which is also supported by the increased Debye–Waller factor (MTV–MA–033).

Sample, k=3	Backscatterer	R [Å]	N	σ^2 [Å^2]	E_0 [eV]
MTV–MA–049 KorantinSH&LP4	Co	2.50±0.01	6.7±0.2	0.0060±0.0002	4.5±0.9
MTV–MA–033 KorantinSH	Co	2.50±0.01	5.1±0.3	0.0076±0.0005	3.8±1.9
Co foil	Co	2.51±0.01	11.2±0.7	0.0063±0.0002	4.6±0.8

Table 6.3: Fit results for MTV-MA-049 and MTV-MA-033 Co nanoparticles in comparison with first shell fit of Co foil

The partial disorder in the structure of resulting nanoparticles can be understood if one bears in mind that as synthesized particles may display a multiple twinned crystal structure and chemical contamination from stabilizing agent (surfactant), that may influence their electronic and geometric properties. From solid-state physics, it is known that Cobalt H.C.P. to F.C.C. transformation can occur by a/6 [$11\bar{2}$] displacement on alternative planes [Wal03]. In order to explain the H.C.P. and F.C.C. formation of nanosized cobalt the thermodynamic properties and the stability of grain boundaries in nanometric metals and the concept of the lattice stability, described in [Ros84, Fec90], was used. Following this approach, from the thermodynamic point of view, a nanopowder is in a metastable state if its Gibbs free energy is greater than that of the bulk state.

The Gibbs free energy, for the isothermal process, is given by $\Delta G(V,T) = \Delta H(V,T) - T\Delta S(V,T)$, $\Delta V = 0$ corresponding to the bulk state, where ΔH, ΔS and ΔV are the Enthalpy, Entropy and volume gradient, respectively. The existence of activation energy is suggested during thermolysis as additional heat is introduced into the system. Using the concept of lattice stability, it is possible to estimate the Gibbs energy of F.C.C. and H.C.P. phases. The lattice stability parameter of an element is taken as the difference between the free energy of the phase that is being described (F.C.C.) and the free energy of the other phase, used as a reference (H.C.P.) [Kau70]. The lattice stability parameter for cobalt (H.C.P.) with respect to cobalt (F.C.C.) is $Co^{fcc \rightarrow hcp} = [-460 + 0.628T](Jmol^{-1})$ [Lim00]. At 300K (room temperature), the value of the lattice stability parameter is about -271.6 Jmol^{-1} or $-28 \cdot 10^{-4}$ eV/atom,– i.e., a very small value. As the temperature increases during the synthesis, the lattice stability parameter becomes even smaller. The Gibbs

free energies of the H.C.P. and F.C.C. phases thus become almost equal, so both phases can be formed during the production of NP's. In order to transform to the F.C.C. phase, the Co atoms belonging to the interfacial component of the H.C.P. phase have to overcome activation energy. J.C. de Lima et al., have calculated the activation energy for nanosized cobalt at 300 K to be equal to the 0.059 eV/atom. The authors believe that the value of activation energy depends on the average temperature and the time when nanoparticles were formed.

In addition to phase transition which can be explained in terms of Gibbs free energy, the influence of surfactants on the phase formation has to be considered. The surfactant can occupy the growth sites and thus will block the formation of complete H.C.P. phase. It is known that the H.C.P. packing geometry has the primitive cell, which can be occupied by surfactant. The free Co atoms, which are still available after thermolysis, can be absorbed in a primitive cell to form the F.C.C. structure [Sun99]. These facts together with results obtained from XANES and EXAFS analysis in the case of Co nanoparticles labeled MTV-MA-033, support the idea of the F.C.C. phase formation.

Another issue which can be indirectly derived from the XAS analysis performed on magnetic ferrofluids MTV–MA–049/033 is related to the role of aluminumorganic in the synthesis. As will be shown later, the molar ratio of $Co_2(CO)_8$ to $Al(R)_3$ as well as the chain length R_3 influences the size of nanoparticles. At this point, main attention is paid to the strength of interaction between formed nanoparticles and $Al(R)_3$. Any strong (chemical) interaction should be observed in the XANES spectra as it leads to changes in the electronic structure, as well as a weak interaction via physisorption on the surface or van der Waals interaction can be monitored in XANES measurements. Therefore, it is possible to conclude that the $Al(R)_3$ plays a more catalytic role in the slow thermolysis of $Co_2(CO)_8$ and does not react directly with formed Co nanoparticles, but rather detaches the CO from the $Co_2(CO)_8$. Thus the rate of nucleation and formation of the free Co atoms is increased. Stabilization of the so-prepared nanoparticles is done by the surfactants which can be adsorbed on the surface of the nanoparticles. Here it must be stressed that formed nanoparticles are not necessarily 'naked', as some CO can be still adsorbed on the surface of nanoparticles. The schematic sketch of Co nanoparticle including their surfactant is presented in Figure 6.12. It has to be mentioned that in this 'brush like' model, some amount of $Al(R)_3$ could also be present. The stability of the particles against agglomeration holds for so-prepared nanoparticles unless there is introduction of oxygen into the system. The $Al(R)_3$ is highly reactive with oxygen and once it is introduced into the system one should expect a reaction, and thus changes in the electronic enviroment around nanoparticles and/or theirs partial agglomeration, as had been shown in the case of small Pt nanoparticles in chapter 5.1. It is then possible that these changes can be traced in XANES measurements.
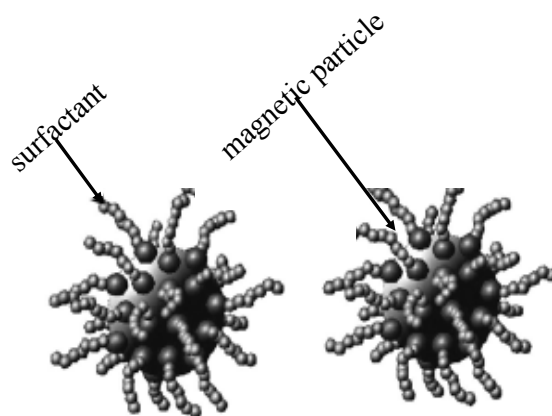
Figure 6.12: Schematic sketch of Co nanoparticle including their surfactant

6.1.3 Stabilization of nanoparticles against oxidation: novel 'smooth oxidation' procedure *v.s.* exposure to air.

It is known that nanosized (3-10 nm) colloidal $Co^{(0)}$ particles cannot be redispersed after exposure to air because they are immediately oxidized both in solution (toluene) and in powder form. The exposure to air which leads to the immediate oxidation of Co nanoparticle hereafter is called *uncontrolled oxidation*. If the addition of oxygen is precisely controlled, for example by using synthetic air, then the process will be called *controlled oxidation*. An example of uncontrolled oxidation is $N(oct)_4^+Br^-$ stabilized $Co^{(0)}$ particles, which are oxidized in air to give colloidal CoO nanoparticles [Ree96]. The process was followed by HRTEM, UV-visible spectra and magnetic susceptibility measurements. The resulting CoO particles were supported on alumina. Small CoO and Co_3O_4 particles have been obtained in polymer matrix dispersion by solid state oxidation of 1.6 nm $Co^{(0)}$ particles. The structural changes which occur during the oxidation process were monitored using physical analytic methods, such as Infrared spectroscopy (IR). It was shown that oxidation at room temperature leads to surface passivation, and resulting particles have a metallic core which is surrounded by an oxide surface layer. [Ver99].

A new process of *controlled oxidation* was recently reported for stabilizing magnetic cobalt nanoparticles by Bönnemann AG. This is the so-called 'smooth oxidation'; here the synthetic air (80% of O_2 and 20% of N_2) was added to the carrying medium after thermolysis (Figure 4.5), through a capillary. Synthetic air was slowly bobbling into the medium and the medium was continuously stirred. The practical representation of this novel procedure is pictured in Figure 6.13. The main difference is that synthetic air is added in the stage of Cobalt nanoparticles in suspension which has not been decanted. The as pre-stabilized particles then have been left to settle down in the carrying solution over night and after that the process of decantation and vacuum drying is applied for these particles. No direct signal from CoO or Co_3O_4 was detected by IR measurements before and after introducing oxygen to the system. In contrast to that, a $CoCO_3$ signal is found in the IR spectrum of cobalt nanoparticles after the 'smooth oxidation' procedure had been applied.
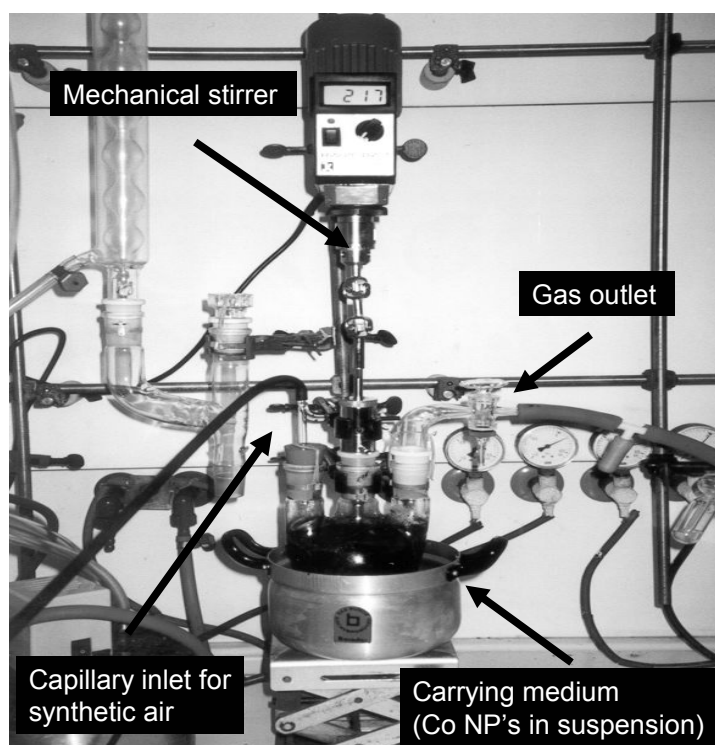
Figure 6.13: Practical representation of 'smooth oxidation' process invented by Bönnemann AG

Thus, one assumes that the process of smooth oxidation plays a crucial role in the formation of a shell surrounding the metallic core of nanoparticles. The selections of the synthesis stages, which allow monitoring of the influence of 'smooth oxidation' procedure *v.s.* exposure to air with a list of correspondent samples, are presented in Figure 6.14.
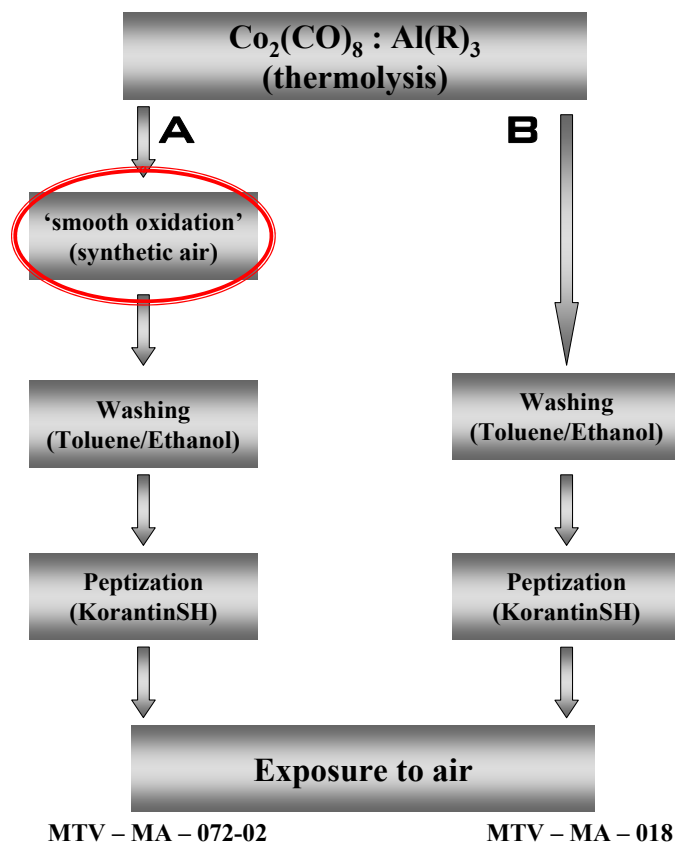
Figure 6.14: Selection of synthesis stages for illustration an influence of 'smooth oxidation' procedure on resulting nanoparticles

The knowledge which has been collected in a previous investigation of nanoparticles resulting after thermolysis of $Co_2(CO)_8$ in presence of $Al(R)_3$ show that even slight modifications of the synthesis condition or the order, through which nanoparticles are obtained, lead to different products. Thus, the nanoparticles obtained via routes A and B presented in Figure 6.14, should exhibit different properties. The only difference in the synthesis is the addition of the 'smooth oxidation' procedure to samples MTV–MA–77–02. It has to be mentioned that a different molar ratio of $Co_2(CO)_8$ to $Al(oct)_3$, which was 10:1 and 8:1 for samples MTV–MA–18 and MTV–MA–77–02, respectively had been used. However, the size of nanoparticles determined by TEM reveals the same values of 10.0 nm; thus, the size effects, induced by use of different molar ratio can be neglected.

XANES measurements

Figure 6.15 shows the Co K–XANES spectra of nanoparticles resulting after thermolysis in the presence of $Al(C_8H_{17})_3$ with (black) and without (grey) application of 'smooth oxidation procedure' after they were exposed to air. As can be seen, the nanoparticles resulting after thermolysis and peptized using KorantinSH, exhibit spectral features which are identical to reference CoO spectrum, after exposure to air. Previous XAS investigations done on the Co NP's prepared in presence of $Al(R)_3$ [Buc02] show the presence of interaction between of metallic Co and $Al-(R)_3$ compounds. Moreover, following these findings exposure to air would cause fast reaction of $Al(R)_3$ and the instantaneous oxidation of Co nanoparticles. The precise procedure of

interaction cannot be explained in a trivial way, as different energetically preferable reaction channels occur simultaneously. Presence of the surfactant (KorantinSH, LP4, etc.) on the surface of NP's can potentially slow down the oxidation reaction after peptized particles are exposed to the air. However, the presence of the surfactant only is not sufficient to prevent particle from oxidation. The oxidation of the nanoparticles stabilized only by KorantinSH, exposed to air, is clearly seen in XANES measurements of sample MTV–MA–018. The significant increase of the white line intensity (B) in combination with decrease of pre–edge feature A as well as presence of only one broad shape resonance (C) which is located at higher energy in comparison to Co foil, indicates that nanoparticles became more CoO like.
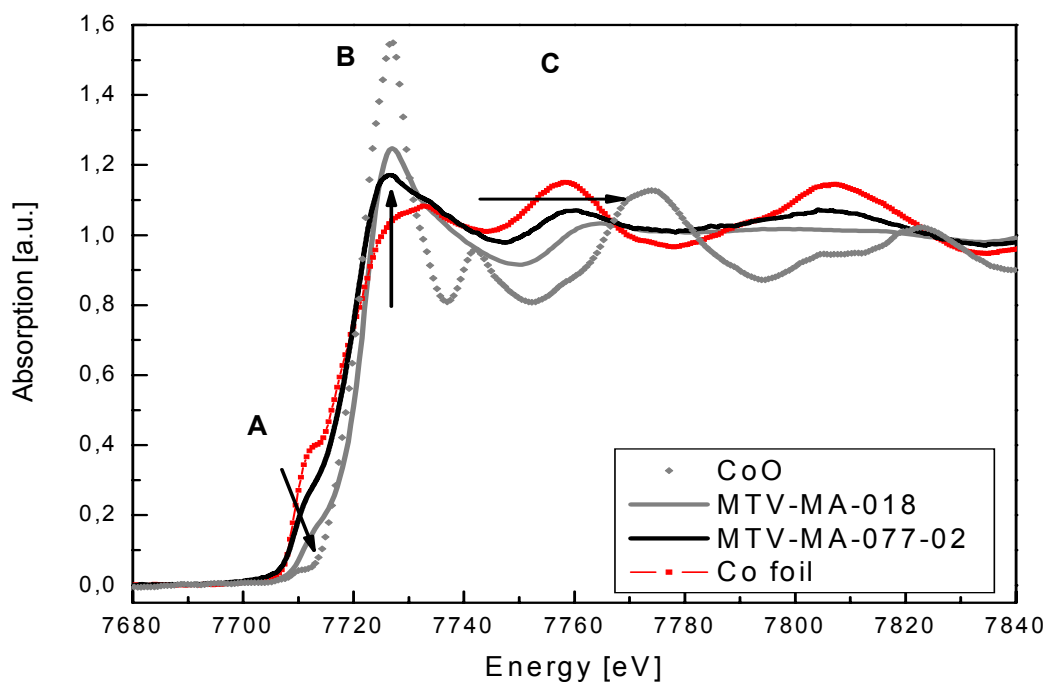
Figure 6.15: Co K – XANES spectra of nanoparticles MTV–MA–018 (grey) and MTV–MA–077– 02 (black) measured after exposure to air in comparison with Co foil (doted) and CoO (doted)

Based on these observations, the reaction between $Co_2(CO)_8$ and $Al(R)_3$ can be imagined in the following way: (i) once $Co_2(CO)_8$ and $Al(R)_3$ are added into the toluene and stirred the decomposition of $Co_2(CO)_8$ occurs. This decomposition undergoes different stages and some intermediate compound such as $Co_4(CO)_{12}$ can be formed. The $Al(R)_3$ is used as a catalyst and detaches the C–O groups from dicobaltoctacarbonyl, thus becoming more metallic. The complexity of the reaction allows formed Co nanoparticles to have some C–O coordination which adsorbed on the surface; at the same time some amount of CO can be vaporized. The coordination between Co nanoparticle and CO is weak and that is why it is hardly observed in the XANES spectra (Figure 6.4); (ii) one of the $Al(R)_3$ radical group can either replace one of C-O bond or react with the present one, thus preventing further particle growth. This gives a hint as to why the type and amount of $Al(R)_3$ determines the size of the resulting nanoparticles. These two stages will be considered as basic and Co nanoparticles resulting after thermolysis are stabilized via physisorption of $Al(R)_3$, which are still highly reactive. Further peptization of nanoparticles using suitable surfactants not only stabilized them against agglomeration but also leads to the replacement of some $Al(R)_3$ coordination by surfactant radical group or molecular itself.

In contrast to sample MTV–MA–018, the XANES spectrum of sample MTV–MA–077–02 reveals that slow and controlled access of the oxygen, e.g. 'smooth oxidation' procedure, caused different reactions with AlR_3. The reduced intensity of the pre–edge feature B, as well as shift of the shape resonance C to a slightly higher energy position relative to the one of the Co reference foil, indicates the presence of partial oxidation.

However, the position of the inflection point, which is identical to the Co foil, reveals that we are still dealing with nanoparticles for which the contribution from the Co$^{(0)}$ dominates in the spectral features. Observed changes in the spectral features of the sample labeled MTV–MA–077–02 can be understood if one bears in mind the possibility of a shell formation around the metallic core and the influence of the surfactant which had been added in order to obtain magnetic ferrofluids. As will be shown later, a CoCO$_3$ shell can be modified during the peptization process and thus spectral features become comparable to one which could be attributed to the nanoparticles which partially oxidized. The main difference is that in case of the sample MTV–MA–077–02, the same trend in the spectral features as for oxidation process is due to modification of the protection shell and not oxidation of the metallic core of the nanoparticle.

EXAFS analysis performed on this sample confirms the presence of a light backscatterer in the first coordination shell and thus the possibility of shell formation. Fitting was done in the data range from 2.8 Å^{-1} to 12 Å^{-1} and from 0.9 Å to 2.8 Å, in k- and R- space, respectively. The amplitude reduction factor was fixed at the value extracted from fit a of a Co foil $S_0^2 = 0.825$. The MTF of sample MTV–MA–077–02 is presented in Figure 6.16. As can be seen in Figure 6.16 an additional contribution from light backscatterer is found at about 1.6 Å. In this case one intuitively assumes formation of CoO layer on the surface of nanoparticles and nearest coordination with oxygen. Moreover, bearing in mind the possibility of CO adsorption on the surface of the nanoparticles, one would assume the presence of a carbon phase as well. The distance between cobalt atoms and the soft backscatterer varies from 1.92 Å to 2.13 Å depending on what compounds are taken as a reference. From the crystallographic data it is known that the nearest distances for CoO (only oxygen), Co$_2$C (only carbon) and CoCO$_3$ (carbon and oxygen) are 2.13 Å, 1.92 Å and 1.96 Å, respectively. The best fit values, which are presented in table 6.4 show a distance of 2.1 Å, which is within the level of error in EXAFS analysis, and can be correlated with both Co–O/Co–C coordination from the compounds listed above. It has to be stressed that scattering phase and amplitude are too similar to allow one to distinguish these types of atoms.
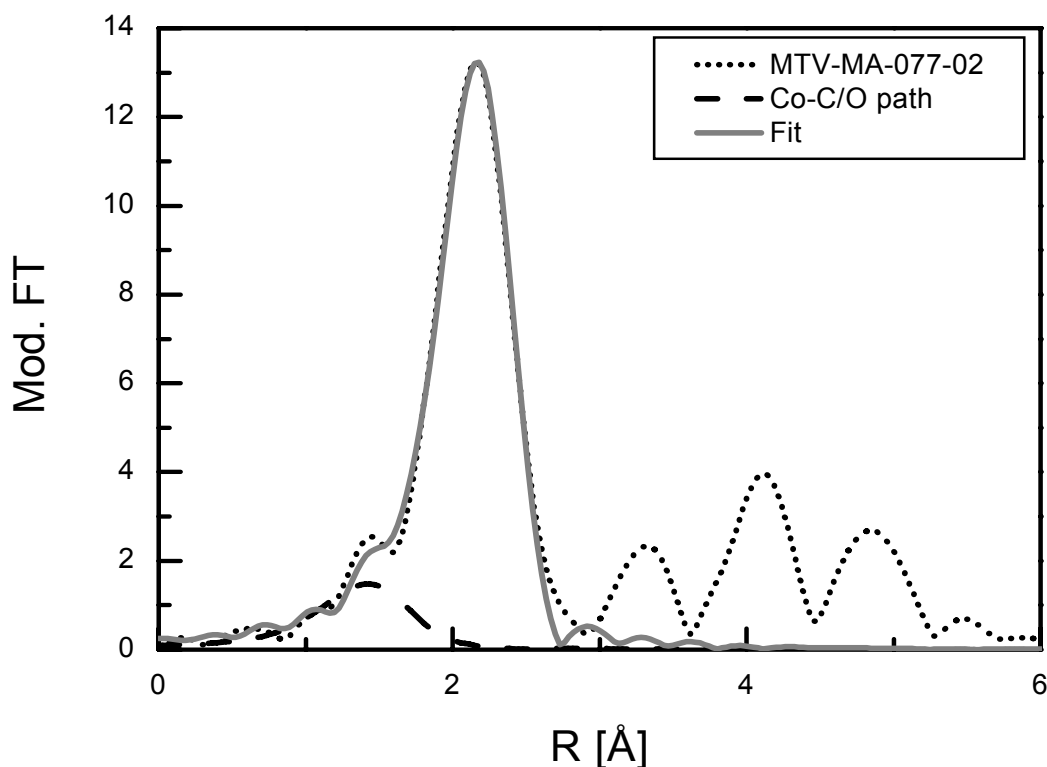
Figure 6.16: Modified Fourier transform of sample MTV–MA–077–02 with fit result and Co-C/O paths contribution

Sample	Backscatterer	R[Å]	N	$\sigma^2[\text{Å}^2]$	$E_0[eV]$
MTV-MA-077-02	Co	2.49±0.1	4.5±0.4	0.006±0.0001	3.2±0.8
	C/O	2.10±0.1	2.9±1.4	0.020±0.0001	2.1±0.7

Table 6.4: EXAFS fit results of sample MTV–MA–077–02

Assuming a CoO shell formation around the metallic core, it should be possible to reproduce the XANES spectra of nanoparticles by linear combination of foil spectrum and CoO. However, it has turned out to be impossible to achieve a reasonable linear fit of sample MTV–MA–077–02 based on Co foil and CoO as can be seen in Figure 6.17.(upper panel). Surprisingly, the linear fit is improved significantly if one uses in addition the $CoCO_3$ as a reference compounds, and shows 27% of $CoCO_3$ contribution, whereas only 7% of CoO is determined from the fit. Thus, for this sample instead of the assumed CoO shell, a $CoCO_3$ shell is formed during the 'smooth oxidation' procedure. A small contribution from CoO can be understood if one bears in mind the influence of the surfactant, after 'smooth oxidation' nanoparticles had been peptized. In this case, the surfactant radical group (COOH-R) can interact with the protection shell ($CoCO_3$) of nanoparticles, which would lead to the additional contribution of CoO in the spectral features.
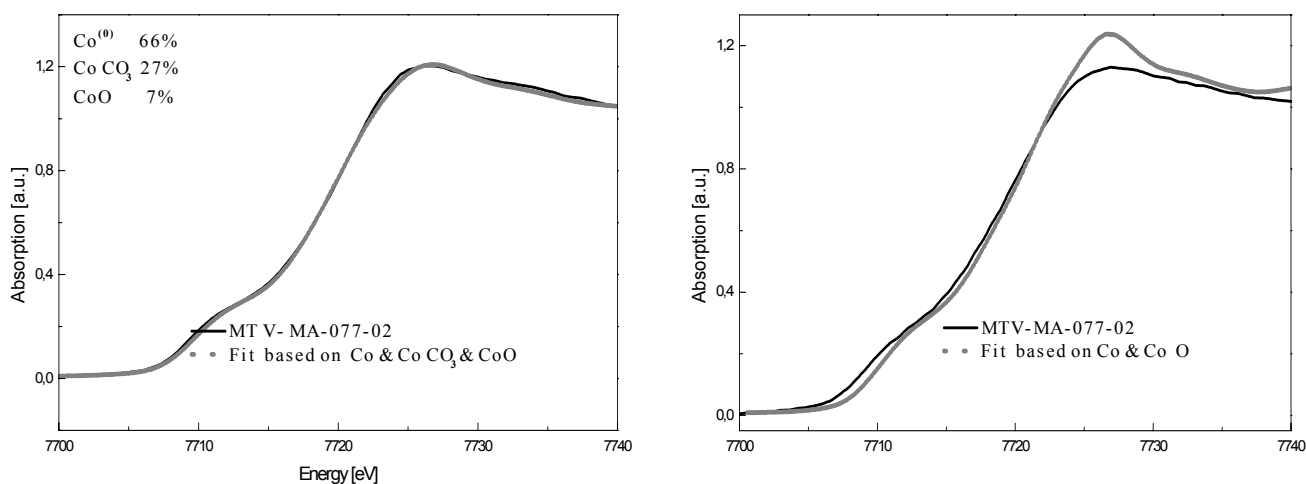
Figure 6.17: Linear fit results (doted) of samples MTV–MA–077–02 based on Co&CoO (right) and Co&CoO&CoCO$_3$ (left)

The process of peptization leads to the change of surface coordination. Schematically, peptization of core-shell nanoparticles can be illustrated as shown in Figure 6.18 (lower panel). In the upper panel of Figure 6.18 (from left to right), prestabilized magnetic nanoparticles and ferrofluids are shown. To verify the idea of $CoCO_3$ shell formation linear fit based on Co and $CoCO_3$ has been done for the sample MTV–MA–077–01, which is identical to the MTV–MA–077–02, the only difference is that the resulting nanoparticles have been achieved in a powder form. Fit results are present in upper panel of Figure 6.19 and completely support the idea of the carbonate shell formation. The contribution of $CoCO_3$ is identical to the one obtained for the same nanoparticles in the magnetic fluid. That reveals that we are dealing with core–shell particles.
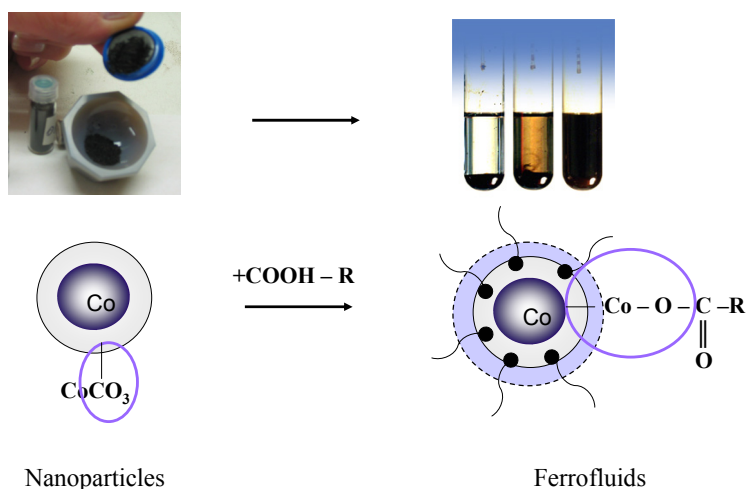
Figure 6.18: Simple representation of modification of the protection shell during the peptization process

The EXAFS analysis performed for the sample MTV-MA-077-01 using the fit range identical to the one used for MTV-MA—077-02, supports the idea of the $CoCO_3$ formation. The MFT of the powder sample is presented in Figure 6.19 and the fit results are summarized in table 6.5. Whereas the coordination number of Co-C/O and Co-Co bonds are very similar to one obtained from the fit of magnetic fluid, the distance to the nearest neighbor is somewhat different and contradicts the 2.10 Å distance obtained from sample MTV-MA-077-02. A typical Co-C/O distance characteristic for $CoCO_3$ is 1.96 Å. The fit results obtained for sample MTV-MA-077-01 are further evidence which supports the idea of Carbonate formation during 'smooth oxidation' procedure.
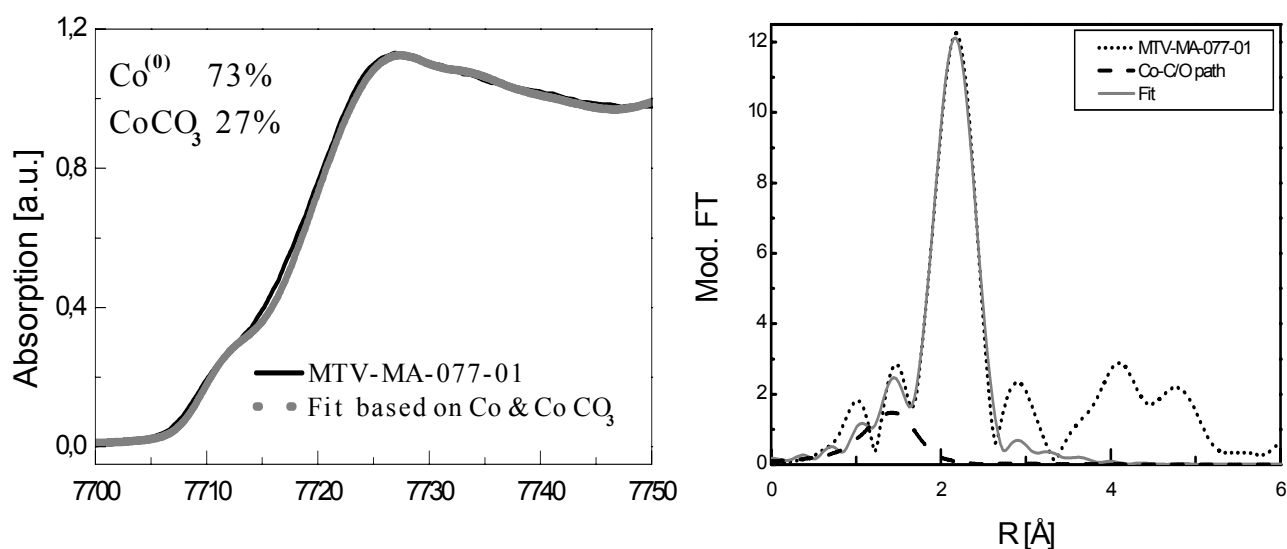
Figure 6.19: Linear fit results (left grey) and MFT (right grey) of sample MTV-MA-077-01 based on Co&CoCO$_3$

Sample	Backscatterer	R[Å]	N	$\sigma^2[Å^2]$	E_0[eV]
MTV-MA-077-01	Co	2.49±0.1	4.5±0.7	0.006±0.0001	3.1±0.8
	C/O	1.96±0.1	2.6±0.8	0.020±0.0002	1.4±0.3

Table 6.5: EXAFS fit results of sample MTV-MA-077-01

As has been shown in the XANES and EXAFS analysis, the $CoCO_3$ is the most likely candidate for the protection shell around the metallic core of Co nanoparticles. Coordination on the surface of nanoparticles with C–O in a stage of wet suspension is also confirmed by IR measurements as well as carbonate coordination after 'smooth oxidation' has been applied. IR spectra and possible surface coordination for Co nanoparticles before and after 'smooth oxidation' process are shown in Figure 6.20.
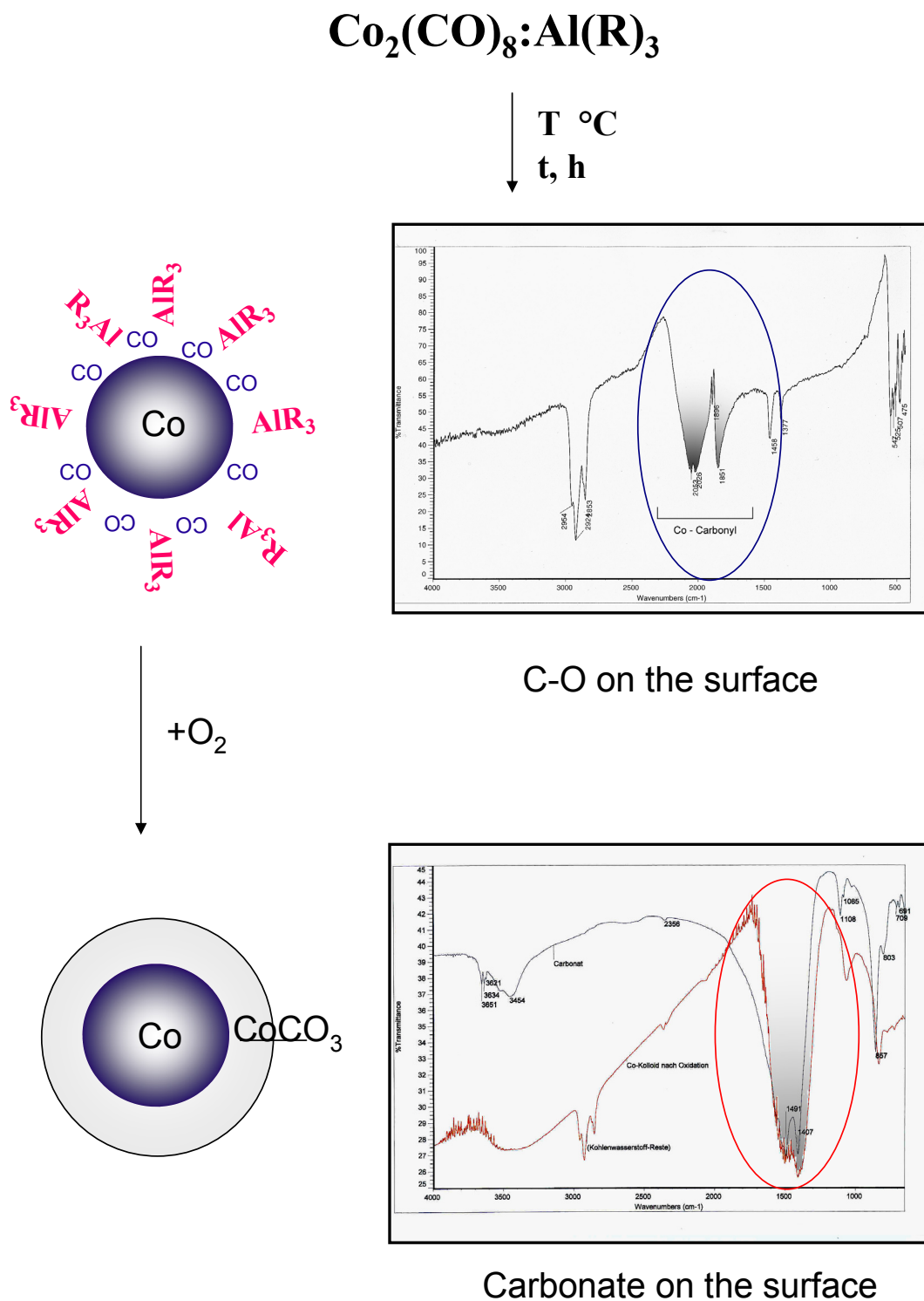
Figure 6.20: Schematic representation of core-shell formation (right) and IR spectra taken before (top right) and after (bottom right) applying 'smooth oxidation' procedure

67

Based on the observed results, the $CoCO_3$ shell formation can be understood as follows: (i) after thermolysis the Co NP's with some CO adsorbed on the surface and $Al(R)_3$ can weakly interact; (ii) addition of the synthetic air in a very slow and controlled rate leads to reactions between $Al(R)_3$ and CO, which mechanism depends on the type and concentration of AlR_3. In the presence of oxygen, AlR_3 will oxidize to result in, for example, Al_2O_3. At the same time, CO will also react with O_2, bearing in mind the presence of active Co centers on the surface of the nanoparticle and some amount of free Co atoms the formation of $CoCO_3$ occurs. It is difficult to establish the precise mechanism of this reaction, but formation of $CoCO_3$ seems to be more preferable with a slow inlet of oxygen.

In the following example, for all samples prepared using 'smooth oxidation', a core-shell system is considered where the shell consists of $CoCO_3$. Next, it is useful to study the influence of the 'smooth oxidation' procedure on nanoparticles with a different size. Figure 6.21 shows a set of two samples prepared with variation of aluminum organics and with applying the 'smooth oxidation' procedure, after they have been exposed to air. The 'smooth oxidation' process was applied at the stage of Co nanoparticle in suspension, e.g. having some C-O as well as $Al(R)_3$ interaction. The main difference in producing nanopowder is the stage on which the 'smooth oxidation' procedure has been used. For samples MTV-MA-052/055, it has been done before decantation and further washing, and for samples MTV-MA-050/51, after it. It has to be stressed that in this scheme, drying with air is a process similar to 'smooth oxidation'. In both cases the slow inlet of air is added in the suspension.
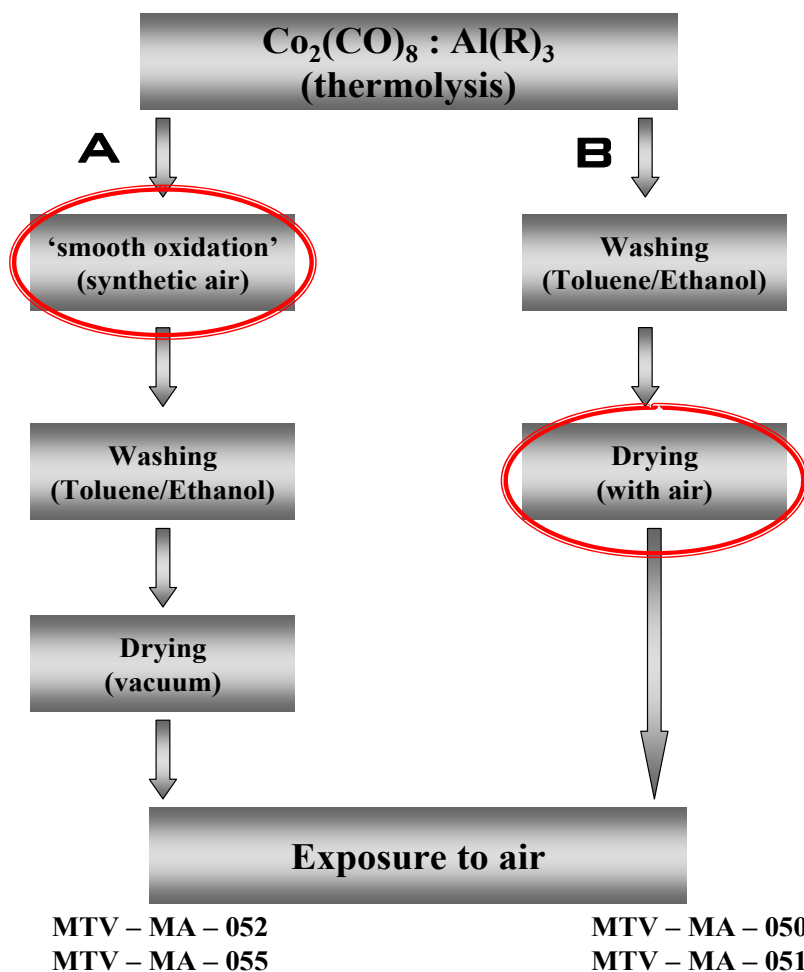
Figure 6.21: Selection of the synthesis stages in which the 'smooth oxidation' procedure can be applied with corresponding samples

As can be seen in Figure 6.22 Co K-XANES spectra show almost identical features independent on stage at which 'smooth oxidation' has been applied. Slight increase of the white line intensity in the case of nanoparticles prepared in the presence of Al(eth)$_3$ MTV-MA-050/55 is mainly due to the size (5.0 ±1.6 nm) effect, as smaller particles have larger contribution of the surface into the spectral features in comparison with bigger particles. For the size of the nanoparticles see Appendix A. However, more attention has to be addressed to the spectral features itself. For samples MTV-MA-051/052 (10.0 ± 1.1nm) the intensity of pre–edge shoulder is identical to the one observed for Co foil. This observation refers to the fact that the cobalt core is not directly affected after exposure to air but protected by a shell. Thus, the increased intensity of the white line for the 5.0 nm particles in comparison to the 10.0 nm NP's is understood as a contribution from the shell dominates in smaller particles. Another important feature that has to be mentioned is the position of shape-resonances which stay at a quite similar energy position with Co foil, especially in the case of nanoparticles prepared in the presence of Al(oct)$_3$ and a shift of the shape resonances towards slightly higher energy is correlated to the size effects, which will be discussed in more detail in the next chapter.
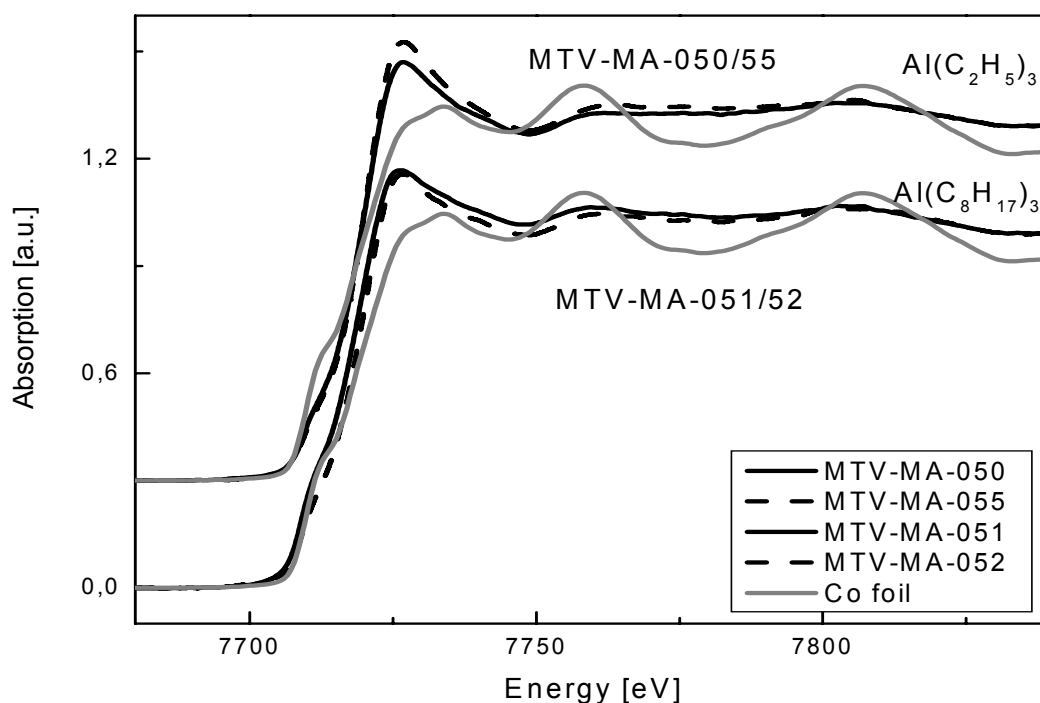
Figure 6.22: Co K-XANES spectra of NP's prepared with (grey solid) and without 'smooth oxidation' procedure in samples 050 (dashed line, upper panel) and 051 (dotted line, lower panel) in comparison with Co-foil

Before one starts to discuss changes in the electronic and geometric structure caused by size effects, it is useful to summarize the results, which have been presented here. Two aspects of stabilization have been probed by XAS measurements. On the one hand, the surfactants importance is clear for the quest of stabilization against agglomeration. The weak interaction of Co core with either surfactant or/and Al(R)$_3$ used in the synthesis is confirmed by XANES and EXAFS analysis. In this case the so-called 'brush like' particles are formed. One the other hand, stabilization of nanoparticles against immediate oxidation, once they are exposed to the air, can be done by application of the 'smooth' oxidation procedure. In this case, the core-shell particles are formed and the shell consists of CoCO$_3$ which follows from the XANES and IR spectra.

Only one sample from the system MTV–MA–050/055 and MTV–MA–051/52 will be used below for EXAFS analysis (chapter 6.2.2), as from the XANES it follows that the application of either 'smooth oxidation' or drying with air results with an identical core–shell nanoparticles, once Co:Al ratio and type of AlR$_3$, have been kept the same.

6.2 Size effects on nanoparticles

6.2.1 Molar ratio $Co_2(CO)_8$:Al(R)$_3$

The size and monodispersity of the Co particles can be controlled by the initial molar ratio of aluminumorganic to Co precursor, between 1.4 nm and 10.0 nm. The aluminumorganic is noted as Al(R)$_3$, where R-is a radical or the functional group. The sizes of nanoparticles, according to TEM analysis, as a function of the $Co_2(CO)_8$ to $Al(C_8H_{17})_3$ ratio, are given in table 6.6. The question of stabilization of nanoparticles has been described in detail in chapter 6.1. The 'smooth oxidation' procedure has been applied for all samples which will be presented in this chapter.

$Co_2(CO)_8$:Al(C$_8$H$_{17}$)$_3$	d [nm]
10:1 (MTV-MA-051)	10.0 ± 1.1
5:1 (MTV-MA-053)	3.5 ± 1.6
1:1 (MTV-MA-073-02)	1.4 ± 0.2

Table 6.6: Dependence of the size of nanoparticles from molar ratio $Co_2(CO)_8$:Al(R)$_3$

Figure 6.23 shows the Co K–XANES spectra of samples produced with three different ratios of $Co_2(CO)_8$:Al(C$_8$H$_{17}$)$_3$/Al(oct)$_3$, presented in table 6.6. Notable and systematic changes can be observed comparing the spectra of samples MTV–MA–073–02 and MTV–MA–051: with increasing the molar ratio and thus particle size, the pre–edge structure gains intensity and the white line intensity is reduced significantly. The case of nanoparticles prepared with Co:Al(oct)$_3$ molar ratio 5:1 (MTV–MA–053) seems to be quite different from nanoparticles labeled MTV–MA–051 and MTV–MA–073-02. Moreover, as has been shown before, the EXAFS analysis on sample MTV-MA-053 did not support the presence of a soft backscatterer in the first coordination shell as one would expect for the core-shell nanoparticles. As was discussed above, even the spectrum of the largest particles (MTV-MA-051) is significantly different from the one of bulk H.C.P. cobalt. The deviations in the spectral features are understood via the formation of core-shell particles, independent of size. If one assumes the formation of the same crystallographic phase during the synthesis of nanoparticles, then it should be possible to obtain a reasonable linear fit for sample MTV-MA-051 (10.0 nm nanoparticles) based on bulk H.C.P. crystallographic phase and the smallest nanoparticles (MTV-MA-073-02). The experimental spectrum of samples MTV–MA–051 can be fitted to a good agreement using the spectra of the smallest nanoparticles and sample MTV–MA–053, as can be seen in Figure 6.24 (C).

The formation of a shell around the metallic core of nanoparticles is a nontrivial process which goes through different stages depending on the synthesis parameters and conditions. The fact that, in the case of sample MTV-MA-053, no significant contribution of the shell is present is not understood. At the moment, the formation of some protective layer on the surface of the particles is assumed. Following this assumption, further investigations should aim an answer the question: can this layer be considered as a shell which protects the nanoparticle from oxidation?

To answer this question, let's first gather the information which can be obtained by an other technique,– the SEM (Scanning Electron Microscope) measurements that are shown in Figure 6.28 for nanoparticles MTV-MA-051 (top right), MTV-MA-053 (bottom right) and MTV-MA-055 (will be discussed in chapter 6.2.2, left panel). The presence of an additional layer on the surface of nanoparticles MTV-MA-051 and MTV-MA-055 can be seen in SEM pictures, whereas SEM of nanoparticles MTV-MA-053 doesn't show this presence so clearly.
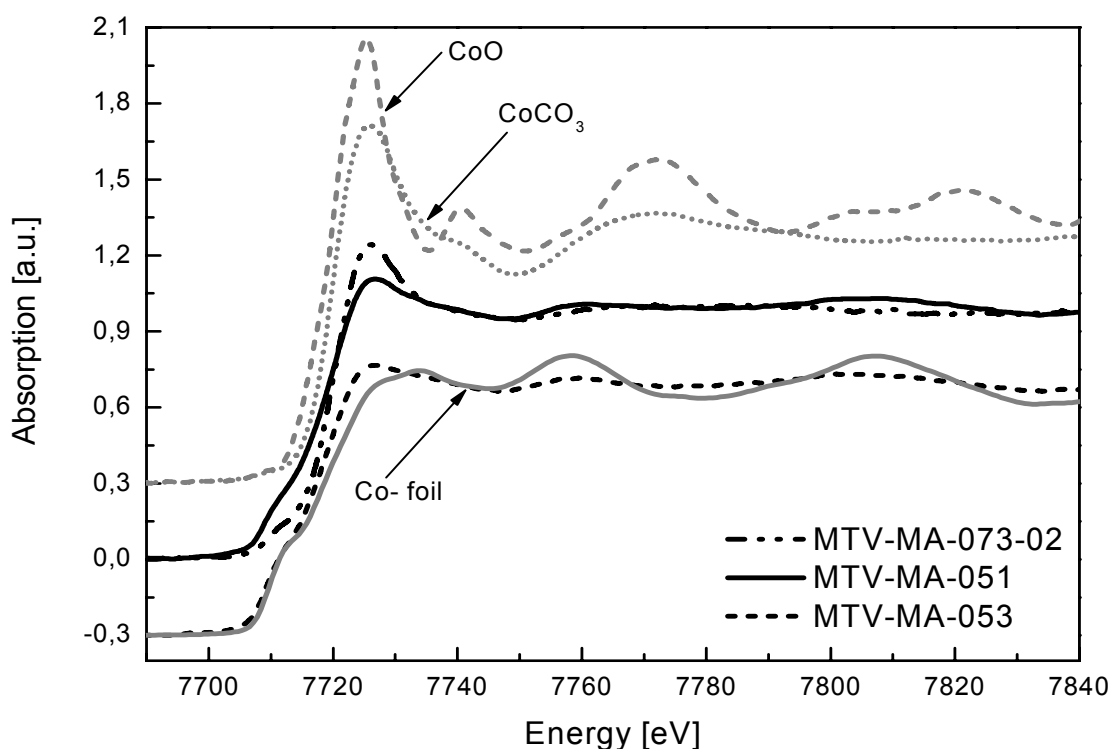
Figure 6.23: Co K-edge XANES spectra of magnetic nanoparticles prepared with varies molar ration of Co₂(CO)₈ to Al(oct)₃ in comparison to Co-foil (grey solid line),CoO (grey dashed line) and CoCO₃ (grey doted line)

A CoCO$_3$ shell would react with oxygen, as the oxidation of CoCO$_3$ towards CoO is known for bulk CoCO$_3$ reference even at room temperature. In this case, changes related to the presence of an oxidation process should be notable when comparing as-prepared nanoparticle and nanoparticle after long term exposure to air. Figure 6.27 shows the Co K-XANES spectra of samples (MTV-MA-051/053) exposed to air for 18 months in comparison with Cobalt oxide and Cobalt Carbonate. For the nanoparticles MTV-MA-053, one can see that after long-term exposure to air the spectra of the particles become more and more similar to the spectrum of CoO, whereas the spectra of NP's MTV-MA-051 are almost identical. Decrease of the intensity of the pre-edge shoulder in the case of the particles MTV-MA-051 can be understood as a slow oxidation of the protection shell. Thus, one can assume that the protection shell is oxidized slower than some CO layer on the surface, which was suggested in case of nanoparticles MTV-MA-053. According to this observation, the answer to the question, if the layer on the surface on nanoparticles can be considered as a protection shell, is negative but only in case of nanoparticles prepared with molar ration of Co$_2$(CO)$_8$ to Al(oct)$_3$ = 5:1. Obviously, formation of the shell around the metallic core is not just a function of application of the 'smooth oxidation' procedure but also of the molar ratio which had been used in the synthesis.

Now one has to answer the question of whether the shell consists of CoCO$_3$ or CoO in the case of the smallest particles. From the 'fingerprint' comparison, shown in Figure 6.23, it is hard to conclude if the shell consists of CoO or CoCO$_3$ as the spectral feature of 1.4 nm NP's are similar to both (CoO and CoCO$_3$) compounds. If CoO is what formed the shell, it should be possible to reproduce the XANES spectrum of the smallest particles by a linear superposition of bulk Co and the Co oxide, which fails for CoO as the white line intensity of the oxides is too high relative to its spectral contribution, Figure 6.24 (F). If one bears in mind that for smaller particles the surface contribution in the spectral features is dominant, the intensity of the pre-edge shoulder should be reduced in the case of smaller particles in comparison with bigger ones, which is clearly seen in Figure 6.23.

On the other hand, one has to remember that the $Co_2(CO)_8$ precursor, for which the molecular structure is schematically present in Figure 6.25 (left), decomposes in a non trivial way via the formation of several intermediate compounds. One possible candidate to be formed in this reaction channel is $Co_xC_yO_z$, in which Co is coordinated with carbon or/and oxygen. The linear superposition of bulk Co and the Cobalt Carbonate ($CoCO_3$) is intuitively expected, as both Co-C/Co-O bond are presented in the $CoCO_3$ compound. In the case of MTV-MA-073 nanoparticles the linear fit works pretty well with respect to fitting the white line region and the characteristic pre-edge shoulder. From the linear fit presented in Figure 6.24 (B), the $CoCO_3$ is about 71%. The linear fit of 10.0 nm nanoparticles (MTV-MA-051) based on bulk Co and CoO shows about 27% of CoO contribution, Figure 6.24 (A). These fits and TEM results indicate the presence of the shell around the metallic core, which consists of $CoCO_x$. The error range for these numbers can be estimated to be $\pm$ 5%. From this, one can assume that the nanoparticles described in this chapter can be schematically imagined as shown in Figure 6.25 (right). In this scenario, 1.4 nm particles would have a larger effect of shells in comparison to the 10.0 nm nanoparticles. The most interesting result in this respect is a behavior which shows 3.5 nm nanoparticles produced with molar ratio 5:1, as the spectral features cannot be reproduced by any linear superposition, applied to the other particles Figure 6.24 (D). Here the so-called 'naked', without protection shell, but weakly coordinated with carbon or/and oxygen on surface, were produced. If one assumes the same nature of the forming shell, it has to be possible to reproduce the spectrum of the nanoparticles with a thinner shell (MTV-MA-051), based on a spectra of 'naked' (MTV-MA-053) nanoparticles, and one with a thicker shell (MTV-MA-073-02). The results of the fit are shown in Figure 6.24 (C).
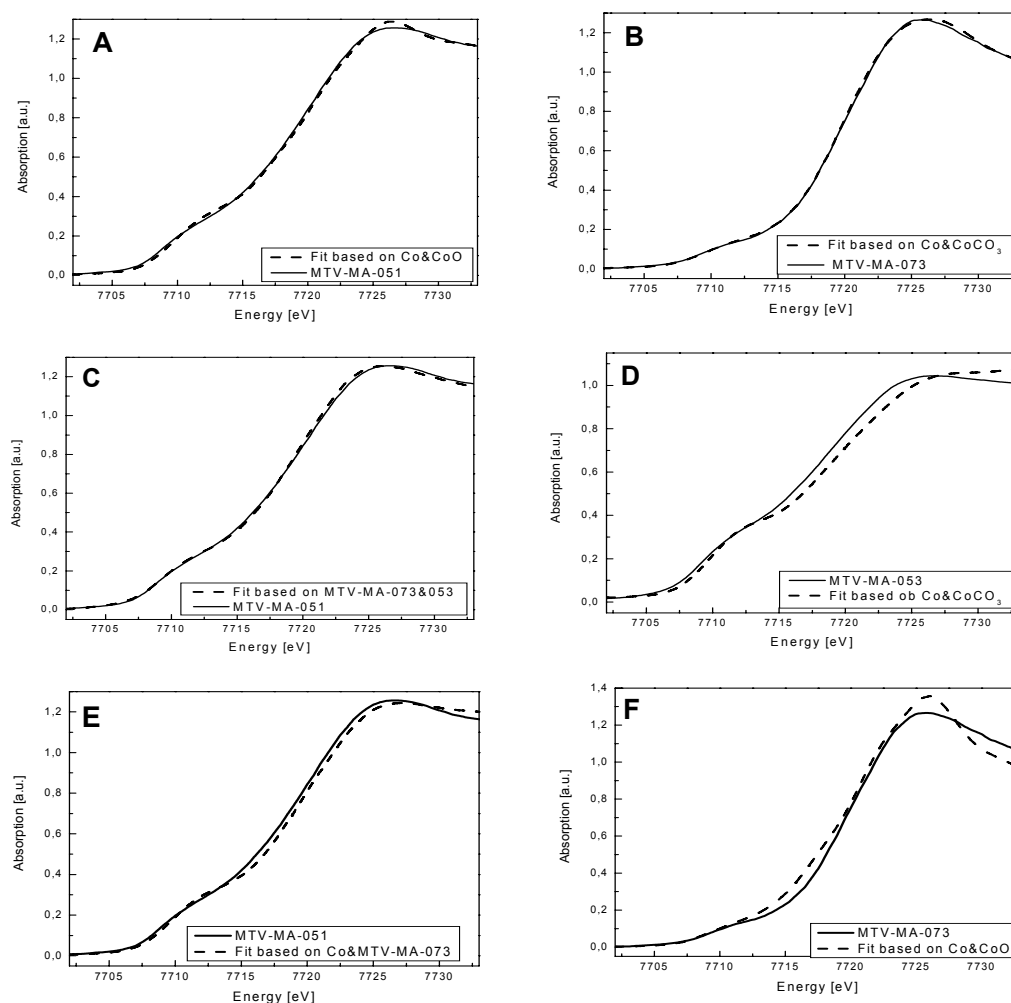
Figure 6.24: Linear fit results (dashed) of sample MTV-MA-051 (solid, left panel) and NP's MTV-MA-073-02 which have thick shell (solid, right panel) and assumed to be 'naked' MTV-MA-053 (dashed, right panel)
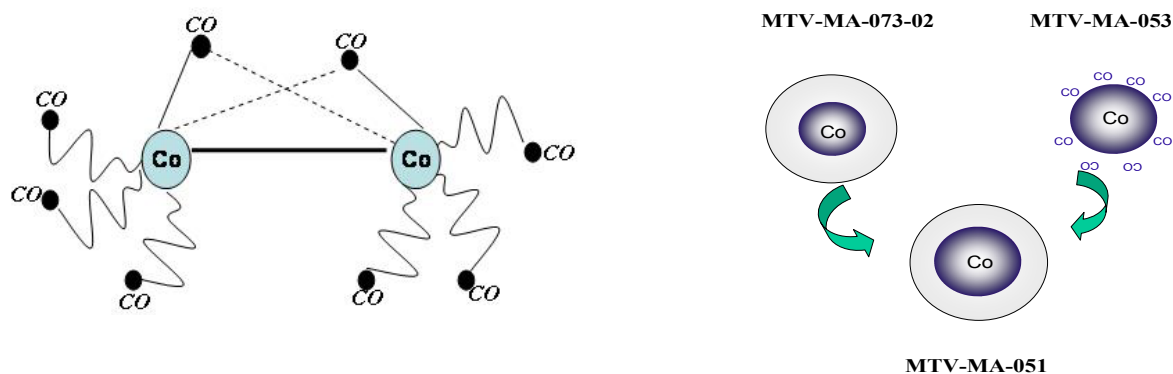
Figure 6.25: Schematic representation of dicobaltoctacarbonyl molecular (left) and possible core-shell formation during synthesis with different $Co_2(CO)_8$:$Al(oct)_3$ ratio (right)

Additional structural information, which can be derived from EXAFS analysis, can be very useful in understanding the core-shell formation during NP's preparation. For the EXAFS analysis, extracted $\chi(k)$ was weighed by k^3 for these samples. For the analysis of the first coordination shell of nanoparticles with molar ratio 5:1 and 10:1, the data from k = 2.7 to 12 Å^{-1} and R = 1.2 to 2.7 Å, respectively, were used. Intervals from 4.1 to 12.7 Å^{-1} and 1.2 to 3.5 Å were used in k–and R –space, respectively, to perform a higher coordination shell fit, in case of NP's prepared with Co:Al(oct)$_3$ =1:1 ratio. The amplitude reduction factor was fixed at $S_0^2 = 0.825$.

Fourier transformed EXAFS spectra of NP's, prepared with a different molar ratio, are presented in Figure 6.26 (left). As can be seen, the maximum at about 2.3 Å in case of NP's MTV-MA-053 (Figure 6.26 (B)) and MTV-MA-051 (Figure 6.26 (C)) corresponds to the nearest Co-Co bound (shifted to the lower R values compared to the true bond value 2.5 Å, due to the fact that no phase correction was applied). In contrast to that, the first maximum in FT of NP's MTV-MA-073-02 (Figure 6.26 (A)) is located at a lower value of 2.1 Å, and in addition to this it has a quite pronounced second maximum at about 3 Å, which is not present in FT neither of NP's MTV-MA-053 produced with 5:1 ratio nor H.C.P. Co.

As a first approach, determination of the NP's structure was attempted by fitting each experimental spectrum with an H.C.P. structural model. This approach only worked pretty well for NP's MTV-MA-053; there the single Co-Co contribution is located almost at the exact distance which is characteristic for H.C.P. structure. It has to be mentioned that the information which can be derived from EXAFS evaluation is quite similar for H.C.P and F.C.C. structure. In the other cases, only Co is not sufficient to achieve a reasonable fit, but a soft backscatterer is needed. Its presence can be explained by assuming the presence of a shell which consists of CoCO$_3$ compounds. The low-R shoulder expected to be caused by Co-C or Co-O interaction in the spectra of the biggest particles. One would assume that during the synthesis, some amount of precursor or intermediate compounds, such as CoCO$_3$ are still presented. Therefore, the next step is modeling the sample structure with two different types of nearest neighbors: C atoms at ~ 2 Å and the Co atoms in the first coordination shell of the F.C.C. phase. The use of this second model resulted in a dramatically improved fit for 10.0 nm NP's and more convincing results are obtained also for 1.4 nm NP's. The maximum in MFT of samples MTV-MA-073-02 found to be at a lower position than in the MTV-MA-051/053 samples. Moreover, the additional peak at about 3 Å can not be interpreted as a standard Co-C bound. That becomes clearer if one plots together the MFT of CoCO$_3$ which has a second maximum at exactly the same position Figure 6.26 (A). Cobalt Carbonate has a trigonal symmetry (R-3 C) and, thus, has 6 carbon and oxygen atoms located at 2.97 Å and 3.23 Å, respectively. Using shell-by-shell approach a quite reasonable fit is achieved for the 1.4 nm particles. As can be seen from table 6.5, results show that both C/O and Co coordination numbers depend on the nanoparticles sizes.
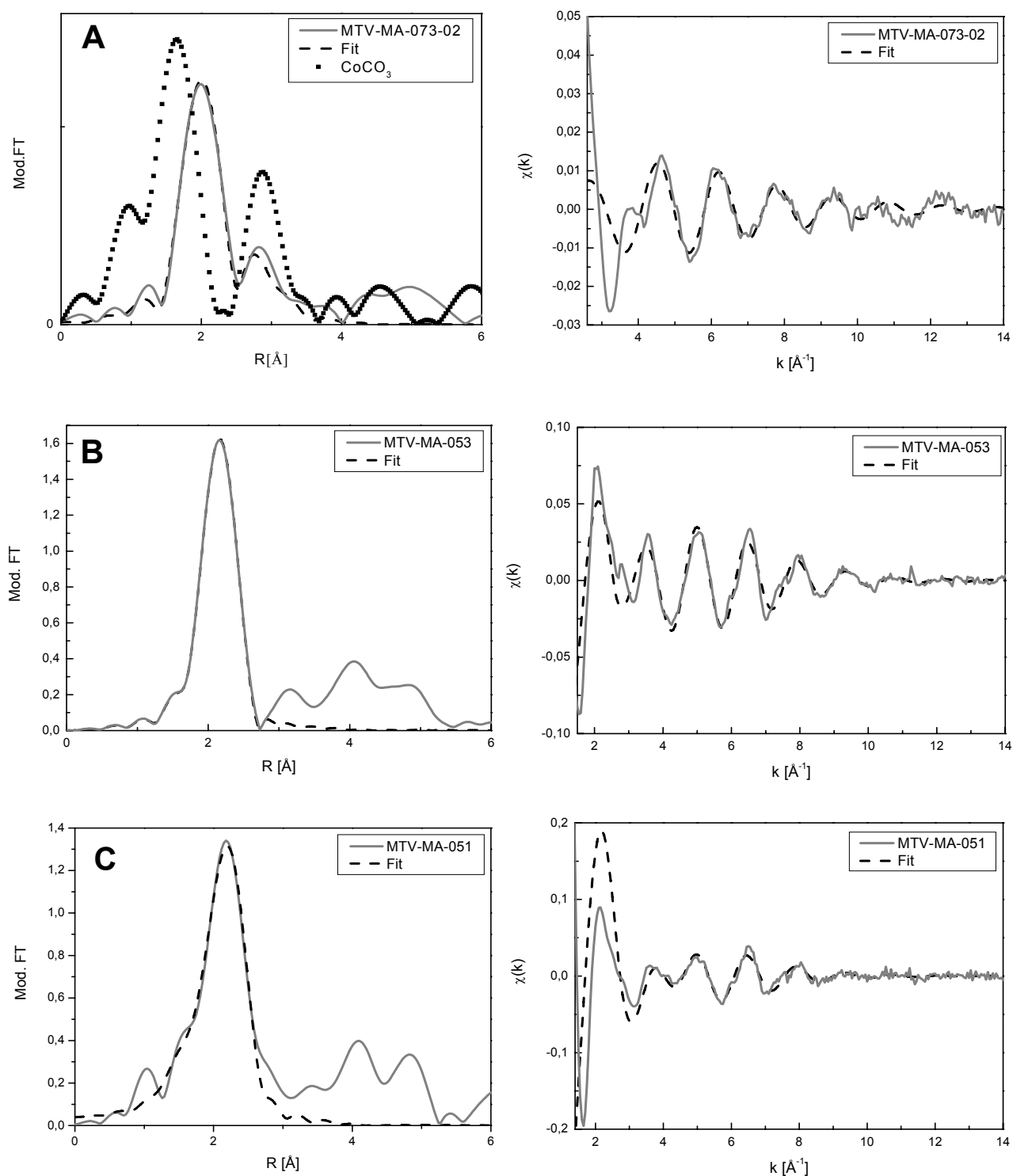
Figure 6.26: Modified Fourier t transforms (right panel) and extracted χ(k)-functions (left panel) with fits (black dashed line) of NP's prepared with varied molar ratio of $Co_2(CO)_8$ to $Al(C_8H_{17})_3$, 1:1 (top), 10:1 (middle) and 5:1 (bottom) sections

Sample, k=3	Backscatterer	R [Å]	N	σ^2 [Å^2]	E$_0$ [eV]
MTV-MA-051	Co	2.52±0.02	5.8±1.2	0.0070±0.0020	3.8±0.4
	O/C	2.10±0.03	3.4±0.8	0.0110±0.0012	3.8±0.4
MTV-MA-053	Co	2.51±0.01	4.9±0.1	0.0076±0.0002	3.9±0.2
MTV-MA-073-02	O	2.12±0.01	0.5±0.2	0.0036±0.0002	6.5±5.9
	Co	2.47±0.02	1.3±0.1	0.0034±0.0002	9.9±3.6
	O/C	3.12 ±0.03	3.3±0.8	0.0030±0.0001	9.9±3.6

Table 6.7: Fit result for Co nanoparticles prepared with three different Co:Al(oct)$_3$ molar ratios

From these results, it becomes clear that the molar ratio is an important parameter which influences not only the size of resulting nanoparticles, but also acts on the shell formation around the metallic particles core. The presence of aluminum organic thus determines chemical interactions of the particle shell with the surrounding environment.
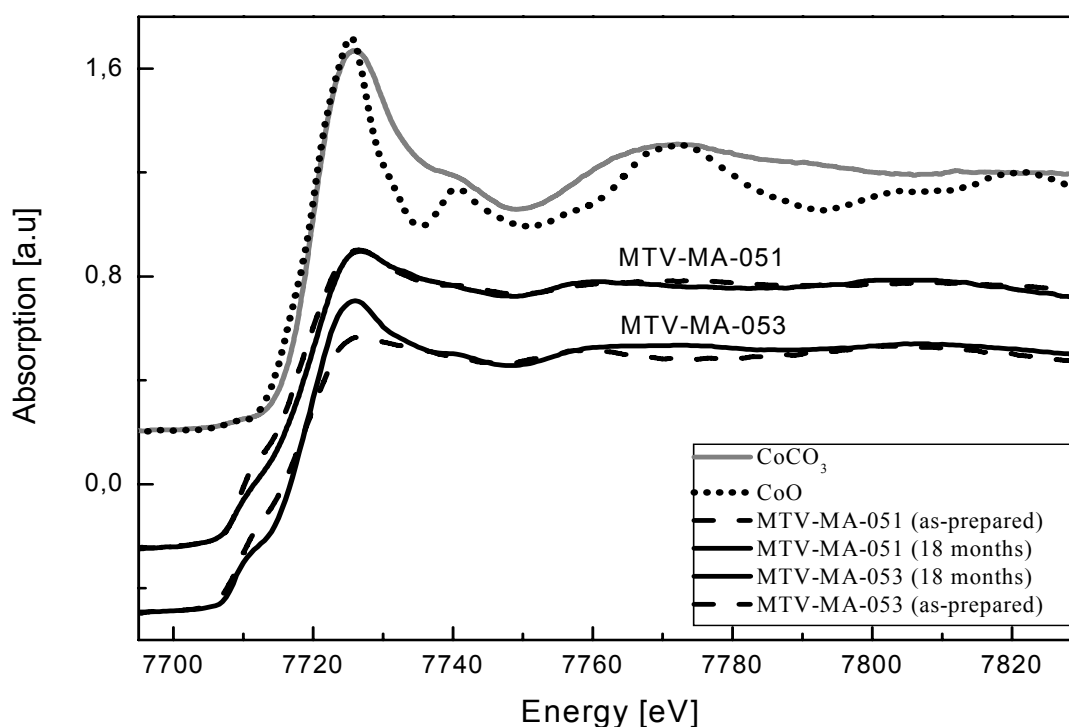
Figure 6.27: Co K-XANES spectra of NP's prepared with different Co:Al(R)$_3$ molar ratio (lower spectra set) as prepared and after 18 month stored under air (black solid) in comparison with CoO (doted upper panel) and CoCO$_3$ (grey solid upper panel)
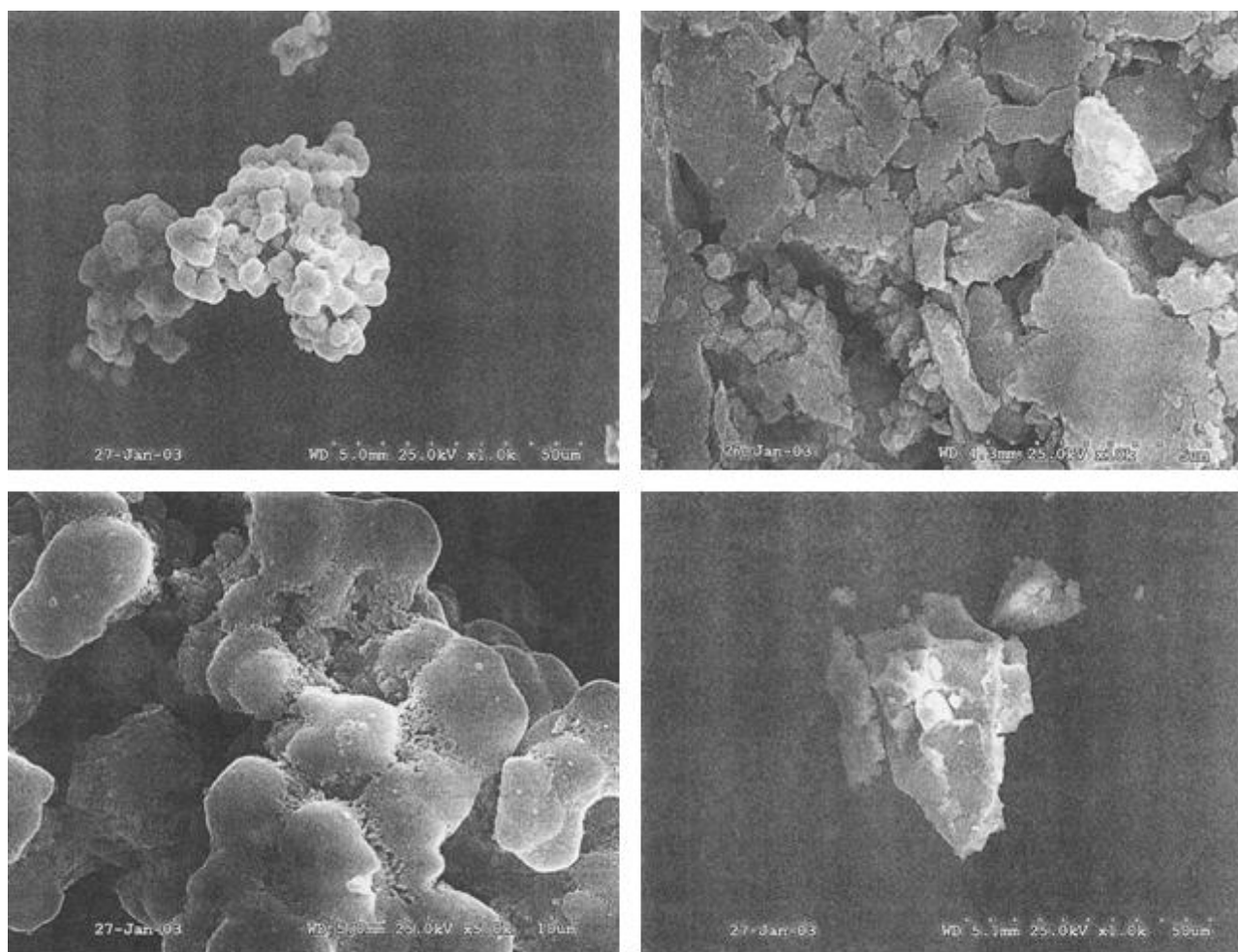
Figure 6.28: SEM picture of Co nanoparticles MTV-MA-051 (right top) and MTV-MA-053 (right bottom) and MTV-MA-055 (left top & bottom)

6.2.2   Chain length of *–R* in Al(R)$_3$

In order to find an optimum condition of synthesis in order to obtain magnetic nanoparticles and ferrofluids, different types of Al(R)$_3$ were used during thermolysis of Co$_2$(CO)$_8$ in toluene. The size results presented in table 6.5 show that there is a clear influence of the alkyl chain length on the size of the resulting Co nanoparticles. Here, influence of two different alkyl groups on the electronic and geometric structure of nanoparticles will be studied by X-ray Absorption Spectroscopy. The molar ratio of Co$_2$(CO)$_8$ to Al(R)$_3$ has been fixed to 10:1 for all samples, which will be discussed in this section.

Type of Al(R)$_3$	d [nm]
Al(C$_2$H$_5$)$_3$ (MTV-MA-055)	5.0±1.6
Al(C$_8$H$_{17}$)$_3$ (MTV-MA-051)	10.0±1.1

Table 6.8: Dependence of Co nanoparticles on the type of Al(R)$_3$
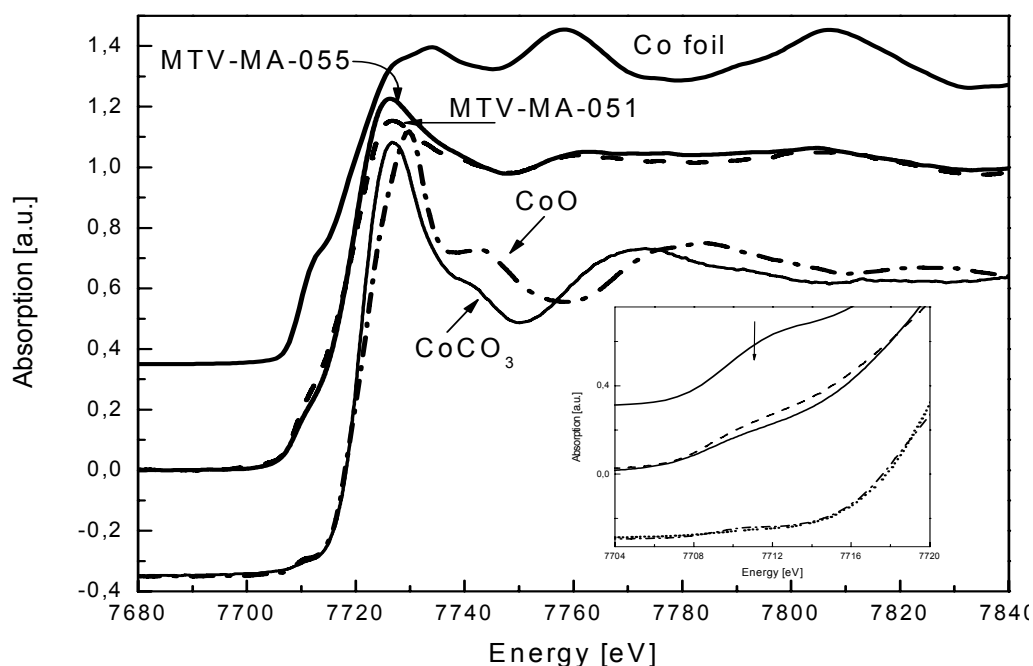
Figure 6.29: Co K-XANES spectra of NP's prepared with Al(oct)$_3$ and Al(eth)$_3$ in comparison to Co foil (grey solid); CoO (grey dash-dot line) and CoCO3 (dashed)

In Figure 6.29, Co K-XANES spectra of particles produced in the presence of different kinds of aluminum organics are displayed. The spectrum from particles with aluminumtriethyl addition during the thermolysis exhibits a slightly increased intensity of the white line and reduced pre-edge shoulder in comparison to the spectra of aluminumtrioctyl. For better illustration, the difference in the intensity of the pre-edge shoulder is shown in inset of Figure 6.29. There are several ways to interpret this observation: with decreasing particle size, the surface contribution to the spectral features increases significantly. Bearing in mind the core-shell nanoparticles, which have been produced with molar ratio of Co$_2$(CO)$_8$:Al(oct)$_3$ =10:1/1:1, displayed in Figure 6.23, the changes in the spectral features is understood as follows: (i) using the Al(eth)$_3$ s smaller, in comparison with Al(oct)$_3$, particles are produced, (ii) the shell which is formed around 5.0 nm particles is thicker, than in the case of 10.0 nm NP's, due to the chain length of aluminium organic compounds, (iii)a shell consists of CoCO$_3$ as it was proved above for NP's prepared with molar ratio of Co$_2$(CO)$_8$:Al(oct)$_3$ =10:1 (chapter 6.2.1). Another important observation is the position of the inflection point. 7709 eV: is the same as for Co-foil, which indicates a dominant contribution of Co$^{(0)}$ in samples MTV-MA-051 and MTV-MA-055.

Further evidence that the particles have a significant contribution of zerovalent Co are the shape resonances located at about 7758 eV and 7807 eV, respectively, which are almost at the same positions as for bulk Cobalt. Fingerprint comparison of nanoparticles spectra with Co-oxide displays a significant difference in the white line intensity, which is much higher in case of CoO, and the position of the maximum absorption is shifted to higher energy (7728.5 eV) in CoO spectrum, in comparison with spectra to nanoparticles (7726 eV), whereas the CoCO$_3$ spectrum has a maximum of absorption at about 7725eV. Moreover, the positions of shape resonances are strikingly different in the case of CoO from the ones of the nanoparticles. Thus, from the XANES analysis, one can see that substitution of long octyl chains by short ethyl chains lead to notable changes in the spectra. Additional information of shell formation and further modification can be extracted from the XANES 'fingerprint' comparison of spectra as prepared NP's with those which have been kept under air, −Figure 6.30 (dashed). To complete the picture of core-shell formation and modification the sample labeled MTV-MA-053 will be discussed along with samples MTV-MA-051&055. The schematic representation of core-shell formation/modification is displayed in Figure 6.31.
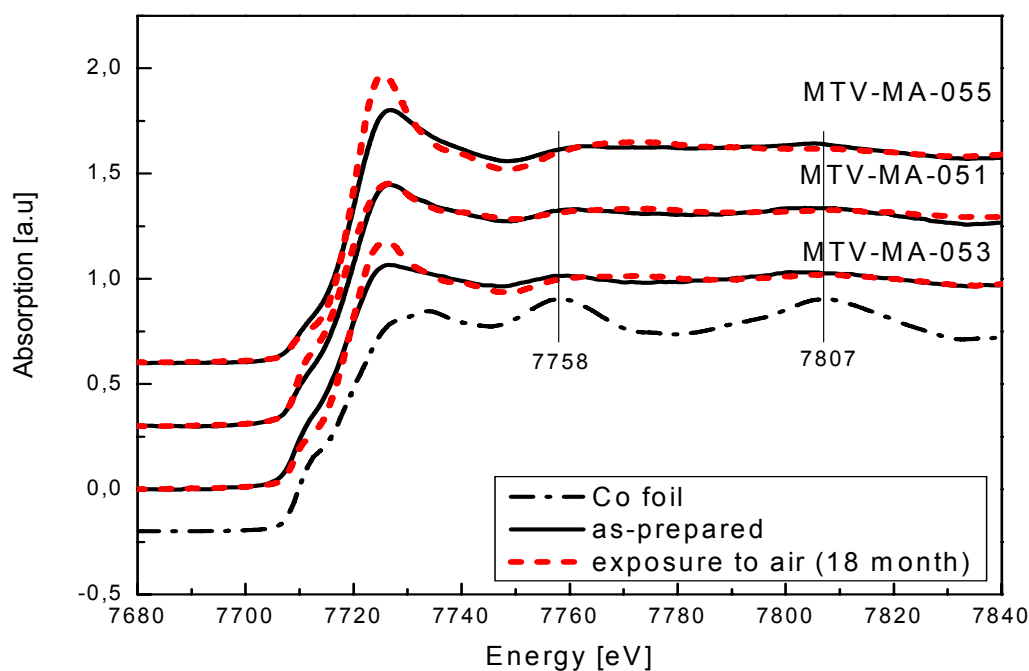
Figure 6.30: XANES spectra of as prepared nanoparticles (solid) and after the exposure to air for 18 months (dashed)
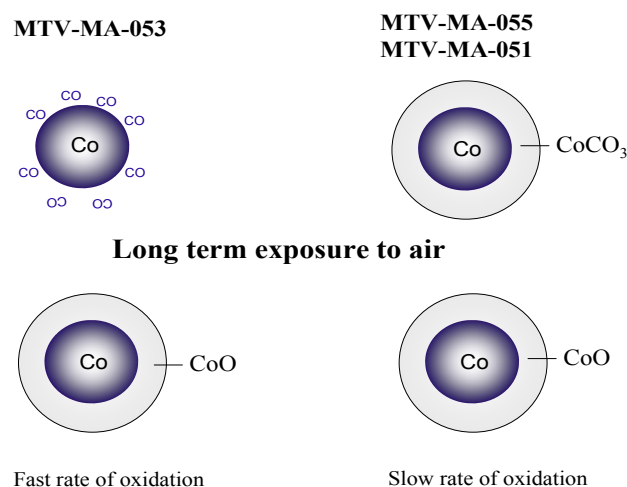
Figure 6.31: Schematic representation of shell modification after NP's has been kept under the air

Fourier transformed EXAFS spectra of NP's prepared with different chain lengths are presented in Figure 6.31. As can be seen, the maximum at about 2.3 Å in the case of NP's MTV-MA-055-(eth)$_3$ and MTV-MA-051-(oct)$_3$ corresponds to the nearest Co-Co bound. Best fit values for distances in case of Co-051 and Co-055 nanoparticles are the same, 2.52 Å and 2.53 Å, respectively. The coordination number is reduced in the case of nanoparticles prepared in presence of aluminumtriethyl groups. This can be understood if one keeps in mind that particles prepared with this type of aluminum organics have smaller sizes than those prepared with Al(oct)$_3$ compounds. In both cases, EXAFS analysis indicates the presence of 'soft' backscatterers in the first coordination shell near to the Co atoms. Two candidates, oxygen and carbon, can both be assumed as backscatterers. In the fitting procedure, the scattering phase and amplitude are too similar to distinguish these types of atoms. As well as the case of nanoparticles prepared in presence of Al(oct)$_3$, molar ratio 1:1 (MTV-MA-073), the FT of MTV-MA-055 has a maximum which is located at about 3 Å. This maximum is more pronounced for Al(eth)$_3$ particles. From the distance comparison, this does not

correspond to any known Co-oxides distance, as it is far too close to be the second Co-O shell, which is located at 3.4 Å and 3.7 Å for Co_3O_4 and CoO, respectively. It may correspond to Co-C distances, which are characteristic for $CoCO_3$ and found at around 2.97 Å. This also explains why this maximum is more pronounced for smaller particles, as they should have thicker shells in comparison to the bigger particles and thus the contribution of this shell is more obvious in MFT for smaller particles. These results may refer to the fact that around smaller particles $CoCO_x,- CoCO_3$ is formed as a preferable protection shell. Bigger particles, however, have no direct indication of $CoCO_3$ but some other $CoCO_x$ compounds. The presence of Co-oxide has a low probability, as no trace of oxidation of the nanoparticles after exposure to air is observed.
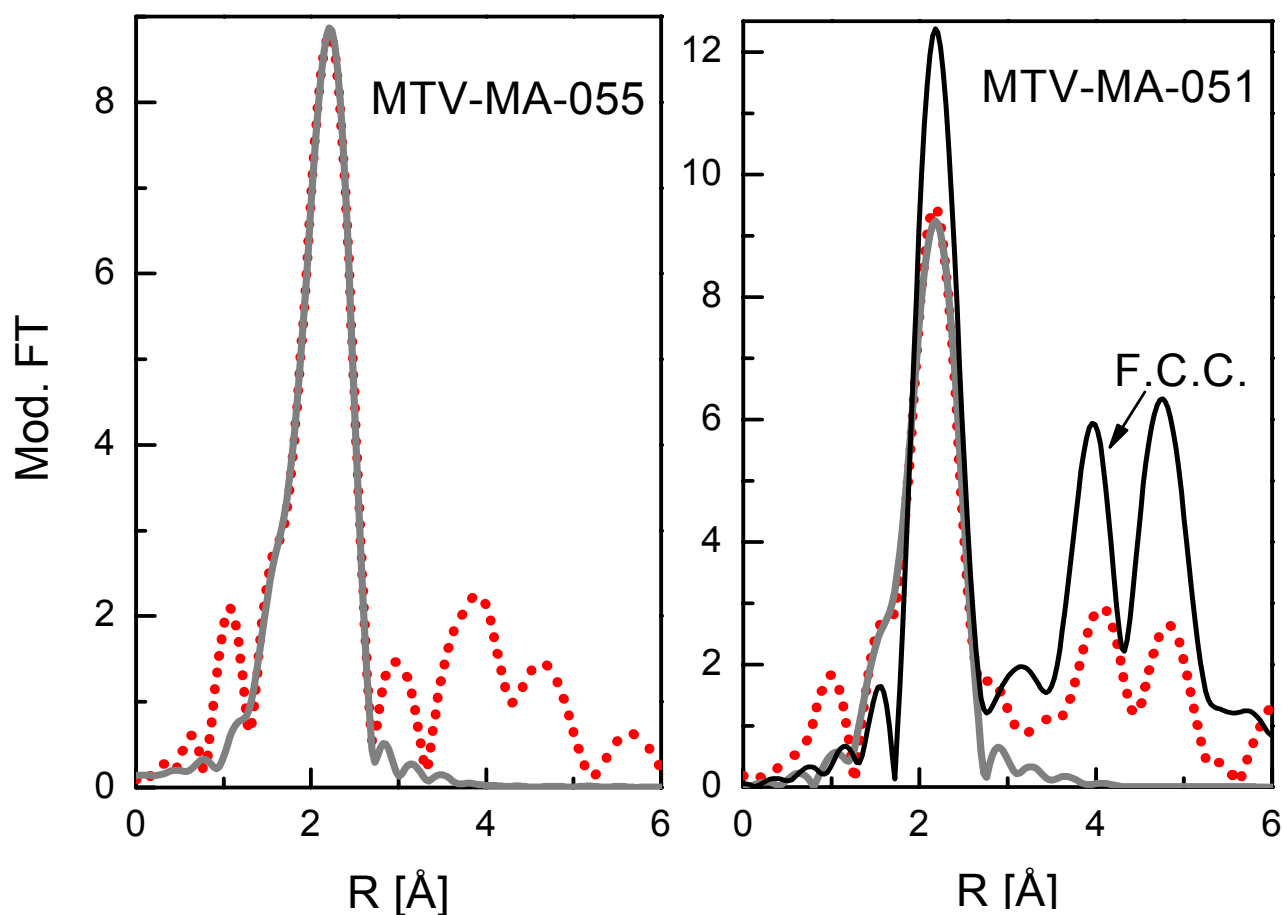
Figure 6.32: Modified Fourier transform of Co nanoparticles prepared in presence of Al(eth)₃ (left) and Al(oct)₃ (right) (dashed lines) and Fit (grey solid line)

Sample, k=3	Backscatterer	R [Å]	N	σ^2 [Å^2]	E_0 [eV]
MTV-MA-051	Co	2.52±0.02	5.8±1.2	0.007±0.002	3.8±0.4
	C/O	2.10±0.03	3.4±0.8	0.011±0.001	3.8±0.4
MTV-MA-055	Co	2.53±0.01	4.3±0.4	0.009±0.001	6.5±0.8
	C/O	2.11±0.02	1.5±0.7	0.008±0.003	7.4±2.5

Table 6.9: Fit result for Co nanoparticles prepared with a three different chain lengths in aluminium organic compounds

6.3   Conclusions

With decrease of the size of the nanoparticle the reactive contribution of the surface increases and also the magnetic properties become more influenced by surface effects. It is known that nanoparticle can be protected from agglomeration by, for example, a layer of surfactant surrounding the metallic core. The presence of a protection layer on the one hand potentially reduces the magnetic properties of the particle due to the nonmagnetic surface composition. On the other hand, it prevents the particles from agglomeration. As a result, monodisperse particles, favourable for several applications, are formed. To elucidate the effect of the surfactant on the structural properties of Cobalt nanoparticles and ferrofluids prepared as described in Appendix A were examined by XAS. The nanoparticles prepared resulting after thermolysis in presence of aluminumorganic can be stabilized against agglomeration via CO adsorption on the surface and $Al(R)_3$ physisorption. These nanoparticles are very air sensitive and oxidize immediately once exposed to air (MTV–MA–018). It has been shown that surfactant effects influence nanoparticle properties notably or even drastically, as in small particles the electron supply is finite; consequently the entire particle can be affected by surfactants as shown for particles stabilized with KorantinSH (MTV–MA–033) and KorantinSH&LP4 (MTV–MA–049) dispersed in vacuum oil L9. In this sample set a surfactant induced phase transformation occurs, as H.C.P. and F.C.C. crystallographic phases are determined by XAFS analysis for 10.0 nm nanoparticles, labels MTV–MA–049 and MTV–MA–033, respectively. It must be stressed that the protection of the particles by the surfactant alone is not enough to stabilize particles against oxidation.

In order to obtain air stable nanoparticles, the 'smooth oxidation' procedure has been introduced to the preparative routine. After thermolysis of $Co_2(CO)_8$ in the presence of $Al(R)_3$ the Co–C/O bonds are formed, which can still be modified to a complete shell by applying the 'smooth oxidation' procedure. After the 'smooth oxidation' procedure, a shell consisting of $CoCO_3$, is formed. The novel procedure can be seen as a stabilization routine against oxidation and moisture. The slow supply of oxygen, which is introduced into the system, leads to a complex reaction, which follows a significantly different way compared to exposure to air. The presence of the $CoCO_3$ shell inhibits oxidation and allows the particles to be air stable for a sufficiently long time. The presence of CO and carbonate on the surface of nanoparticles has been detected by IR spectra before and after application of the 'smooth oxidation' procedure, respectively.

A model of the core-shell particle formation and further modification is presented in Figure 6.33. Only four main steps are displayed as follows: (1) thermolysis–formation of the metallic core with CO adsorbed on the surface and weak interaction with $Al(R)_3$, 2) 'smooth oxidation'–formation of a $CoCO_3$ protection shell around the magnetic core, (3) peptization–modification of the surface coordination and (4) long term exposure to air–modification of the $CoCO_3$ towards the CoO shell.

10.0 nm   1.4nm

$Co_2(CO)_8 + Al(R)_3$

T °C, t h

R_3Al AlR_3 AlR_3
CO CO AlR_3
CO   CO
CO   **Co** AlR_3
CO   CO
R_3Al CO CO AlR_3
AlR_3

+ O$_2$ → **Co** — $CoCO_3$

+ COOH-R

Co — $Co - O - C - R$
                    $\parallel$
                    O

← **Long term exposure to air**

Co — CoO

$Co:Al(R)_3 = 10:1$ $Co:Al(R)_3 = 1:1$

$Al(oct)_3$ $Al(eth)_3$
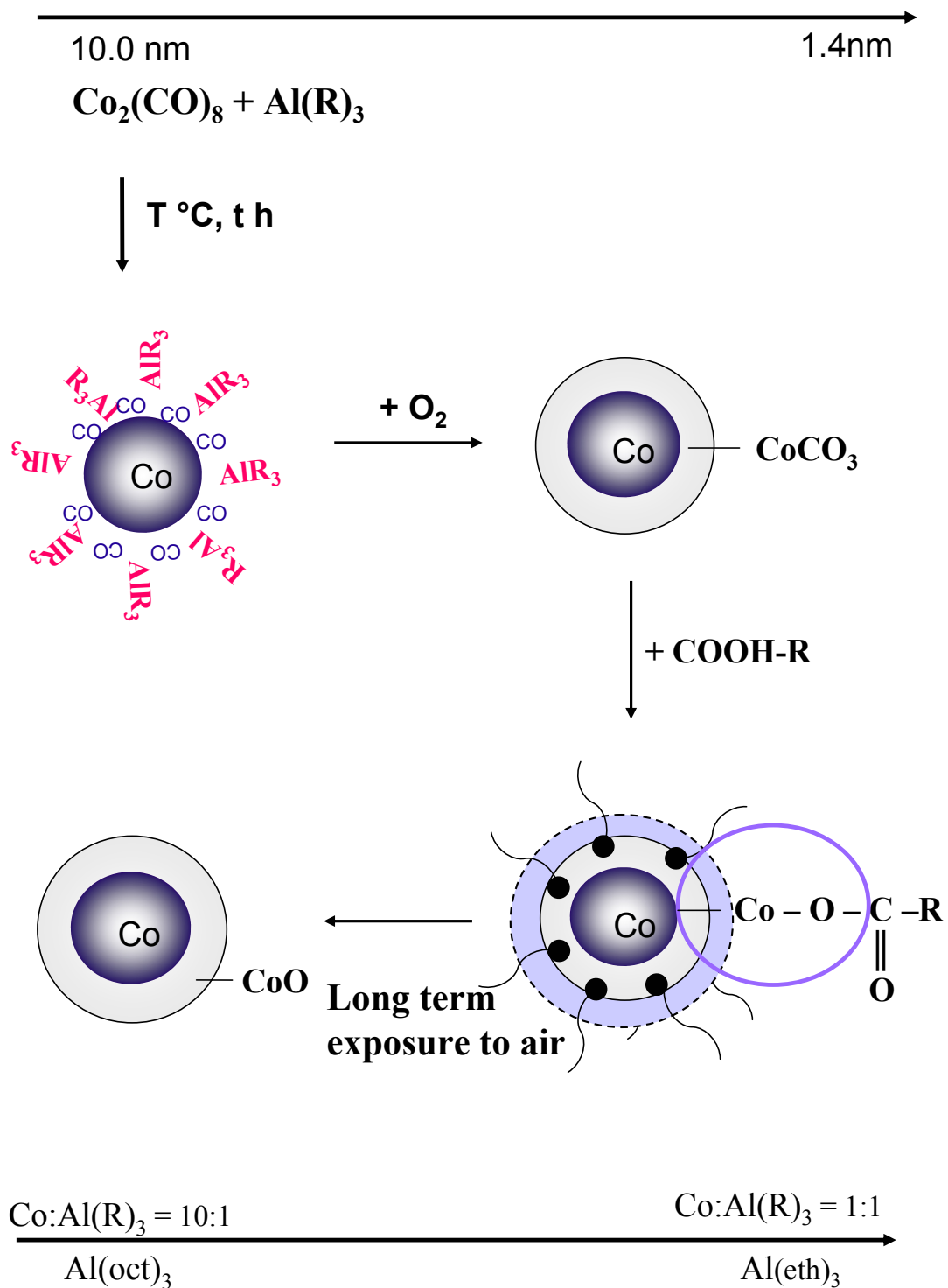
Figure 6.33: Schematic representation of the core – shell particle formation theirs and further modification in different preparative steps of synthesis

7 Co/Ti doped Bariumhexaferrite

7.1 The nature of size dependent magnetic properties

The ferrites with hexagonal magnetoplumbite structure, so-called M-type ferrites whose unit cell is shown in Figure 7.1, have attracted the attention of researches for a long time [Ami25, Smi60, Koj82, Col90, and Cab95]. One reason for this is the great potential of this material for applications which are based on the high values of magnetocrystalline anisotropy, in combination with high saturation magnetization. The ordering of the magnetic moments of ferric ions and the strong superexchange interactions explain the excellent magnetic behaviour of this material [Gor57]. In the past few years, a renewal of the interest in hexagonal ferrites has been induced by the arrival of new application, e.g. magneto-optical storage [Tur93], millimetre wave devices [Ric70], and magnetic recording [Yok84]. At the same time, these new applications have increased the requirements to ferrite with respect to homogeneity, morphology (hexagonal plates) and to a better control of particle size (from 10 nm to1 μm and larger) and shape of the materials. Many efforts have been devoted to the development of new synthesis procedures, since the conventional ceramic method no longer fulfils these demands. Recently, $BaFe_{12}O_{19}$ has been produced by hydrothermal synthesis [Kiy76], salt melting method [Var91], aerosol pyrolysis [Cab94], or sol-gel method [Zho97]. The bariumhexaferrite nanoparticles which will be described in this chapter have been produced by the modified glass crystallization method [Mül94].

The new methods of preparation provide smaller and smaller nanoparticles for which size dependence of the magnetic properties can be observed. As an example of size dependent effects, the main characteristics of $BaFe_{12}O_{19}$ nanoparticles which were derived from magnetic measurements (Institute für Physikalische Hochtechnologie Jena) are summarized in table 7.1. As can be seen from the table, for some of the physical entities it does not seem surprising that the size dependence is observed, as in case of coercivity Hc. The size dependent character of coercivity is known for magnetic materials [Sor01]. In fact, the expected reduction of coercivity, which is favourable for fast read-write processes in recording devices, is one of the reasons for the desire to create smaller particles.

In addition to that, size dependent changes are observed for the parameter such as saturation magnetization (M_s) which is normally assumed as a material constant. The size dependent character of saturation magnetization cannot be explained in a trivial way. From the literature it is known that doping can reduce the anisotropy, i.e. H_c and saturation magnetization, in comparison with the one of bulk material [Gu94]. Besides which, the influence of the annealing temperature on the morphology and thus the magnetic properties of nanoparticles has to be considered. To produce the series of Ba-ferrites NP's with a different size investigated in this chapter, the annealing temperature was varied from 500 °C to 800 °C. Particles with an average size of 29nm, 14nm and 9nm were obtained. From the magnetic measurements it follows that a particle with a size bigger than 20 nm exhibits magnetic properties closer to the doped bulk than undoped nanoparticles to undoped bulk [Mül04]. This is explained by the fact that the critical diameter for ferromagnetic to superparamagnetic transition for Ba-ferrites NP's at about 10 nm. Thus, one can conclude that particles above 10 nm are ferromagnetic with crystal structure characteristic for Ba-ferrites. Although several researchers have investigated the causes for the observed reduction in saturation magnetization with decreasing size of nanoparticles using a variety of techniques, the common knowledge which has been collected is not enough to explain the size dependent changes in a specific saturation magnetization. Commonly, the change in geometric structure for M-type Ba ferrite is known, as the shape of the crystallites is no a longer hexagonal platelet once the particle size is smaller than a critical value (< 10 nm). Macroscopically, the deviation from bulk $BaFe_{12}O_{19}$ properties manifests itself by a significant reduction of the magnetization of the material, the cause of which is not completely understood. Although different hypotheses conflict and remain debatable, three of the most common approaches can be found in the literature.

From one point of view, the so-called 'dead layer' caused by an asymmetric environment effect of the surface atoms, leading to a reduction of magnetic properties, has been reported [Sat87, Gro81, Mül94, Gaj02 and Pan04]. From the other point of view, the transition from magnetic γ–Fe_2O_3 structural subunits within the $BaFe_{12}O_{19}$ matrix, to antimagnetic α–Fe_2O_3 phase might occur [Cho99, Kuz01, and An02]. This should go along with a decomposition of the type BaO:6·Fe_2O_3. In this case, a linear dependence of saturation magnetization (Ms) on a particle size is expected and has been reported by several research groups [Mol77, Mor99]. The deviation from the linear trend is assumed to be due to the amorphous nature of NP's. Another way to explain the decrease of magnetic properties with the decreasing of particle size is an order-disorder characteristic of the particle structure. The order-disorder characteristic can be investigated by XRD. Morales et. al. investigated the structural effect of magnetic properties of iron oxide NP's, synthesized in different ways [Mor99]. The XRD and IR results suggest that particle surface defects and order-disorder structural characteristics both influence the magnetic properties. There also exists some proposals to correlate such effects and changes in magnetic properties, e.g. by broken exchange bonds at the particle surface which can induce surface spin disorder [Kod99]. The intrinsic nature of the mentioned effects makes it difficult to incorporate the size dependence magnetic properties into a generalized theory [Pop95].

Additional information, which can explain the nature of size dependent changes in magnetic properties and possible geometrical rearrangement of Bariumhexaferrite structure, can be extracted from XAS analysis. For the sample set presented in table 7.1 the XANES and EXAFS measurements were performed for Ba L_{III}–, Fe K–; and Ti K–edges at the XMP beam line at CAMD (chapter 3.2). Herein sample 2717 has been used as a reference of nanosized $BaFe_{12}O_{19}$.
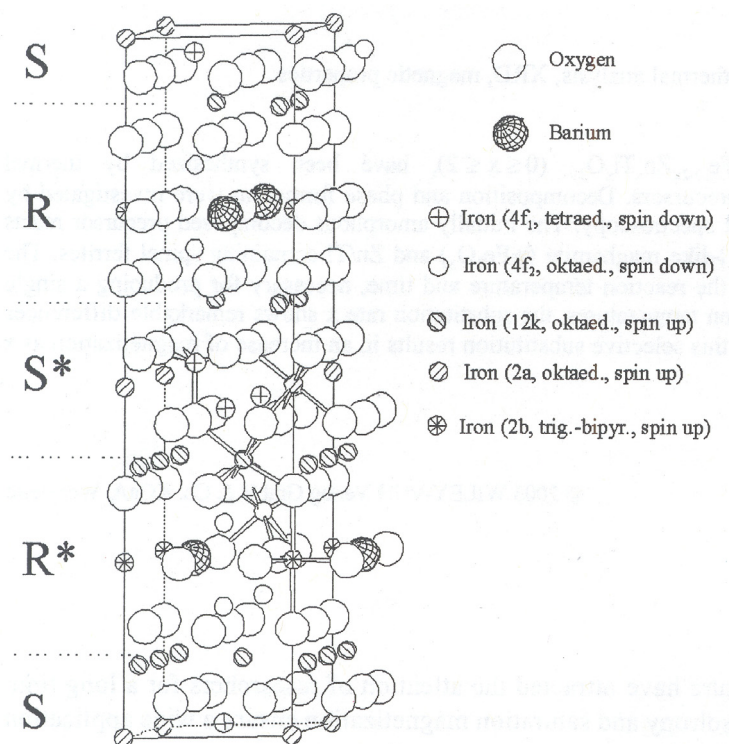
Figure 7.1: Unit cell of Bariumhexaferrite based on two formula units of BaFe₁₂O₁₉

Before one starts to discuss the results obtained from XAS measurements it is worth summarizing further results of different methods of nanoparticle characterization performed on a series of Co/Ti doped Bariumhexaferrite samples. The particle size was determined by TEM and the **B**runauer, **E**mmett and **T**eller– BET method, assuming a spherical shape, which is true only for the 9 nm nanoparticles [Mül04]. According to the BET method, the surface of a (ceramic) powder can be calculated from the N_2-isotherm, which is observed at the boiling point of liquid nitrogen. By the analysis of the adsorption curves within the

relative pressure ranges p/p$_0$ ~ 0,05 and p/p$_0$ ~ 0,2 the volume V is determined which, according to the theory of Brunauer, Emmett and Teller corresponds to the quantity of nitrogen which is necessary for a monomolecular layer. The surface needed for one nitrogen molecule is 16.2 Å^2. From this value the specific surface of the sample can be determined in m^2/g [Bru38]. The results achieved from TEM agree with the mean values calculated from the specific surface, the BET method for 9 nm and 14 nm NP's, respectively (see table 7.1).

Besides TEM, the particle size distribution was reconstructed from magnetization data at room temperature by solving the Langevin integral equation (7.1) under the assumption of a lognormal particle size distribution [Cha78, Gör91].

$$M = M_s \cdot \int_0^\infty \rho(V) \cdot L \cdot \left(\mu_0 \cdot \frac{M_{sbulk} \cdot V}{k_B \cdot T} \right) \cdot dV \qquad (7.1)$$

where M$_s$ is the measured saturation magnetization and M$_{s\ bulk}$ is the theoretical bulk saturation magnetization. K$_B$ is Boltzmann's constant, T is the temperature at measurement, V is the particle volume and ρ(V) is the lognormal distribution function, μ$_0$ is the magnetic permeability and L is the Langevin function. Typical size distribution curves, derived from Langevin integral equation (a, b) and from Small Angular Neutron Scattering (SANS) measurements are presented in Figure 7.2.
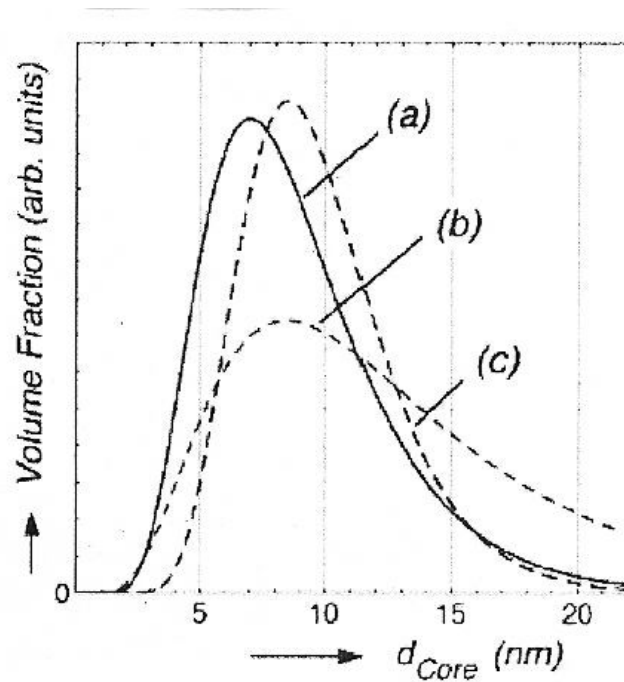
Figure 7.2: Lognormal core size distribution calculated from magnetization data for 9nm (a) and the 14 nm (b) nanoparticles using the saturation magnetization. For comparison the SANS curve (single particle) of 9nm particles is added (c), (taken from [Mül02])

It has to be mentioned that SANS experiments on NP's lead to a bimodal size distribution consisting of single magnetic particles (mean diameter, 9 nm) and aggregated magnetic particles (mean diameter, 22 nm). That is why the size distribution for 9 nm particles observed from SANS technique (marked (c) in Figure 7.2) is shifted to a somewhat higher diameter value in comparison with the lognormal size distribution curve for 9 nm nanoparticles (marked (a) in Figure 7.2). The mean particle size, which can be derived from the lognormal distribution, is not the maximum value of the size distribution curve. The mean diameter is the

arithmetic average particle diameter of the distribution, which is usually located on the right side of the distribution.

A linear dependence of the specific saturation magnetization with the size of Ba-ferrites NP's prepared by the modified crystallization method and size is shown in Figure 7.3: Linear dependence of the specific saturation magnetization (Ms) of Ba-ferrites NP's on size. The constant value of specific saturation magnetization above 100 nm corresponds to transition from a single domain (ferromagnetic) to multidomain (ferrimagnetic) nanoparticles [Lax62].

Number	Specific active surface (BET)	Size	sp. Saturation Magnetization	Coercivity	
	(m^2/g)	(nm)	Ms/m (Am^2/kg)	H_c (kA/m)	M_{exp}/M_{th} (%)
2717*	6.7	170	69.1	322.0	97
2230	40	29	57	80.8	99
2730	81	14	42.6	44.5	74
4064	120	9	22.8	1.1	40

Table 7.1: Size dependent changes in magnetic properties of $BaFe_{12-2x}Co_xTi_xO_{19}$ nanoparticles. The substitution rate for all samples was x=0.8. * x=0, used as a reference for pure Bariumhexaferrite structure
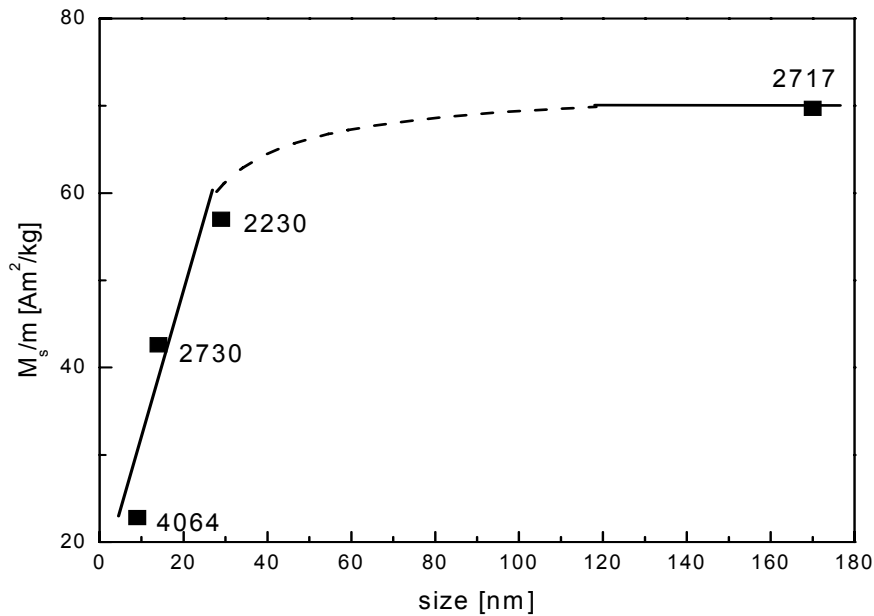
Figure 7.3: Linear dependence of the specific saturation magnetization (Ms) of Ba-ferrites NP's on size

Before one starts to discuss the spectral features it is useful to mention that, from stoichiometric point of view, the $BaFe_{12}O_{19}$ unit cell can be represented as $BaO \cdot 6(Fe_2O_3)$ or divided to spinel–like $BaFe_2O_4$ structure and $Fe_{10}O_{15}$, without disturbing the stoichiometry. The order and completeness of the unit cell of Ba-ferrites will influence the orientation of the magnetic moment within the cell and thus magnetic properties. In the hexagonal Ba-ferrites structure, each Fe^{3+} contributes $5\mu_B$, where μ_B is a Bohr magnetons; according to the spin orientation (see table 7.4) the total saturation magnetization of the formula unit is $5\mu_B \times \left(1[Fe1] + 1[Fe2] - 2[Fe3] - 2[Fe4] + 6[Fe5] \right) = 20\mu_B$. This value is in excellent agreement with

corresponding experimental measurements of magnetization at low temperatures [Lax62]. Distortion from the stoichiometry, caused by either substitution or structural re-/decomposition, will lead to the reorientation of the single magnetic moments and thus to the reduction of the total magnetization.

7.1.1   Ba L_{III} – XANES and EXAFS analysis

Figure 7.4 shows the Ba L_{III} XANES spectra of a series of Co/Ti doped Barium M-type ferrite nanoparticles with varying particle size and BaO and BaO_2 reference spectra. As can be seen from table 7.1, the specific surface is increased by a factor of three, when one compares the values of 29 nm and 9 nm Co nanoparticles, respectively. Thus the surface contribution is growing in the spectral features of smaller particles in comparison with bigger Ba-ferrites nanoparticles. Overall, with the decrease of particle size, a clear shift of the white line towards the energy position of the Ba(II) oxide reference spectrum is found. These observations can be interpreted as an indicator for a partial decomposition of the $BaFe_{12-2x}Co_xTi_xO_{19}$ into a Barium oxide phase on the surface and/or surface–induced segregation process.
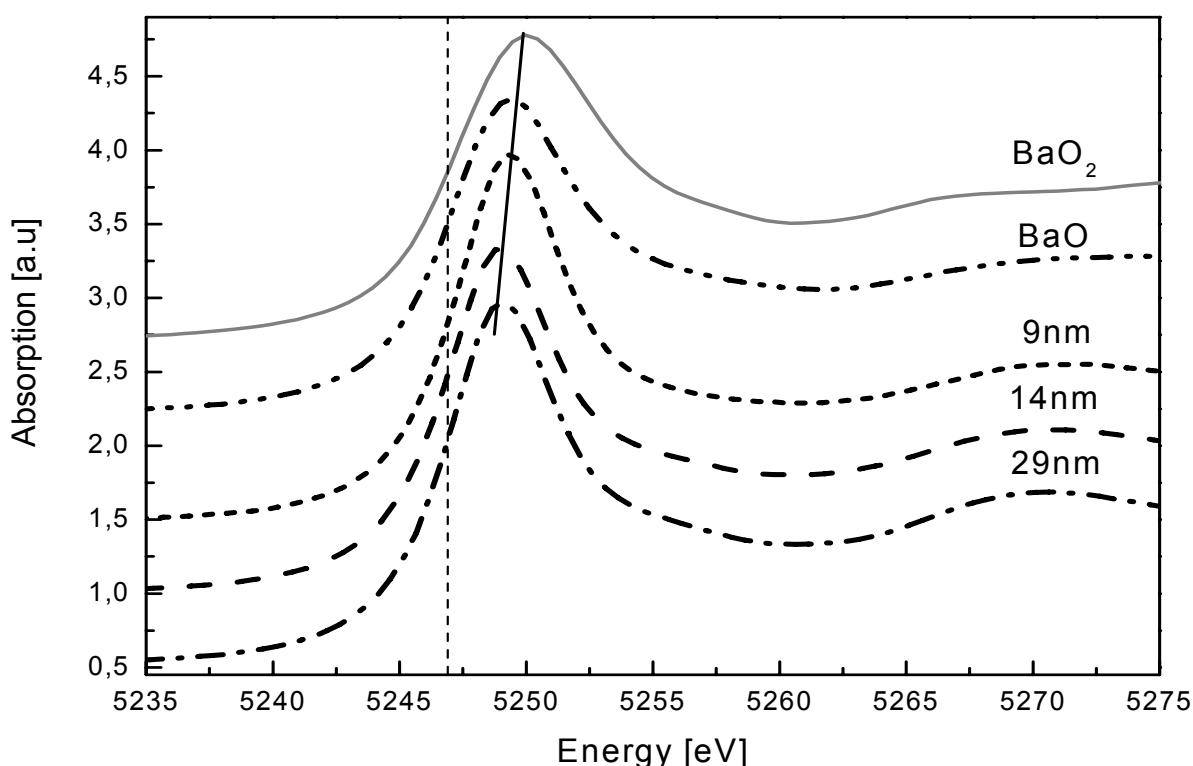
Figure 7.4: Ba L_{III}-edge XANES spectra of 9 nm, 14 nm, 29 nm, 170 nm bariumhexaferrite particles, and the reference compounds BaO (dash-dot-dot line) and BaO_2 (grey solid line).

The trend towards the BaO phase with decreasing of size can also explain the decrease of magnetic parameters, as a paramagnetic BaO phase (or so-called 'dead' layer) formed on the surface will lead to a decrease of the magnetic properties.

To obtain additional structural information on this system, EXAFS data were analyzed. The raw Ba L_{III} EXAFS spectra along with background subtracted $\mu_0(E)$ functions from the nanosized $BaFe_{12}O_{19}$ reference (2717) and Co/Ti doped Ba-ferrites samples are shown in Figure 7.5.
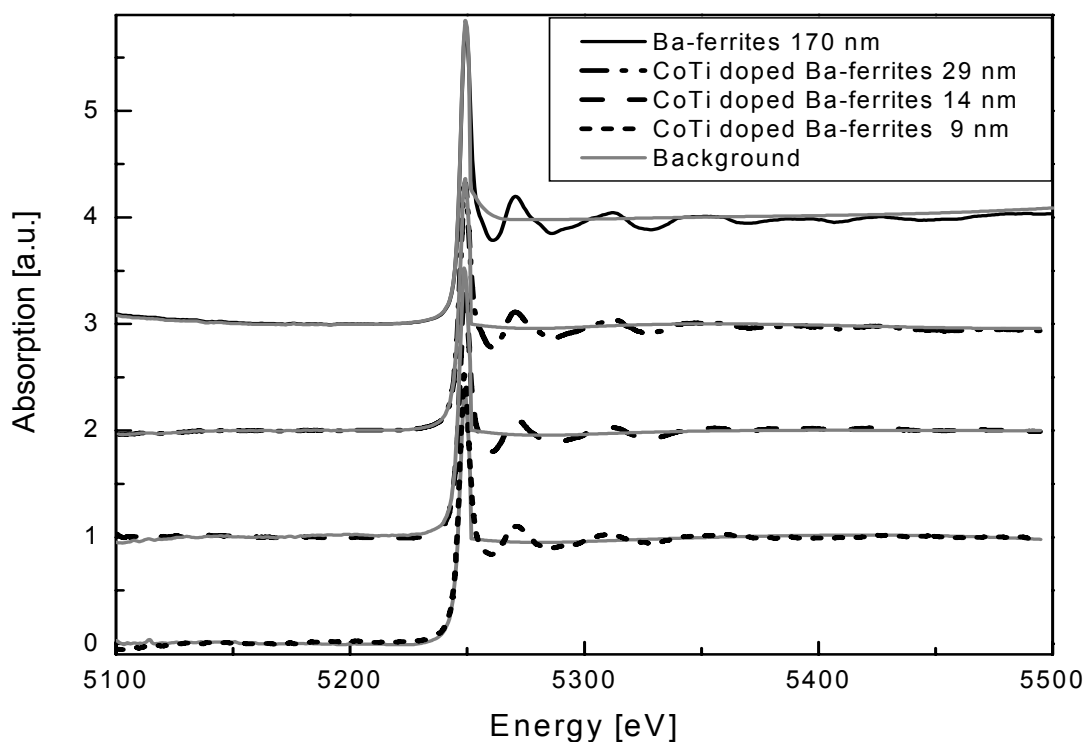
Figure 7.5: Normalized EXAFS spectra of pure and CoTi doped Ba-ferrites nanoparticles with background function
$\mu_0(E)$ *(grey)*

In spite of the fact that the k–space which can be used for evaluation is limited to 7.0 Å^{-1} by the onset of the barium L_{II}–edge (5624 eV), the inspection of EXAFS data presented in Figure 7.6 support the hypothesis of size dependent surface–induced segregation processes. The amplitude of $\chi(k)$-function oscillations is decreasing with decrease of particle size, which is attributed to a less ordered structure around the barium absorber atom (see the amplitude of peak located at about 4 Å^{-1}). The trend towards the BaO phase is more pronounced for 9 nm Co/Ti doped Ba-ferrites nanoparticles, as can bee seen from Figure 7.6 (marked with an arrow for better illustration), and it points out the existence of re-/decomposition towards the BaO phase in dependence of particle size. This trend is further seen in the MFT of EXAFS data presented in Figure 7.7. As the Fourier transformation is sensitive to the k range used for calculation of radial distribution function, the same k range has been used for comparison of theoretically calculated spectra of $BaFe_{12}O_{19}$ and BaO with experimental data.

Already a glance visual inspection of the non–phase corrected MFT of the samples clearly shows that the Ba–Fe coordination is reduced significantly with decreasing particle size. Following the crystallographic information of $BaFe_{12}O_{19}$, it is known that in its complex structure, consisting of five iron sites, octahedral and tetrahedral coordinated, the average Ba–O bond distance is located at about 2.9 Å. The Ba–Fe$_O$ and Ba–Fe$_T$ is located at about 3.3 Å and 3.6 Å, respectively. Here Ba–Fe$_O$ corresponds to octahedral and Ba–Fe$_T$ to tetrahedral coordinated iron. Beyond 4 Å, the peak in FT represents higher Ba–O bond. These distances and correspondent backscatterers are added to the Figure 7.7. The reduction of the Be–Fe coordination in dependence of the particle size is further fully supported by the analysis; the best fitting results are presented in table 7.2.

In contrast to the position of the Ba–Fe peak, which remains to be the same for different particles size, the position of the Ba–O peak has a tendency to be shifted towards the barium oxides phase as was expected. These observations are clearly seen in Figure 7.8, where the dotted lines, corresponding to the Ba–O and Ba–Fe distances are shown. The Ba–O and Ba–Fe peaks have amplitudes 2 to 3 times smaller than one of the

references, indicating a smaller Fe–O coordination number and greater atomic disorder around the Ba ions in the ferrites nanoparticles.
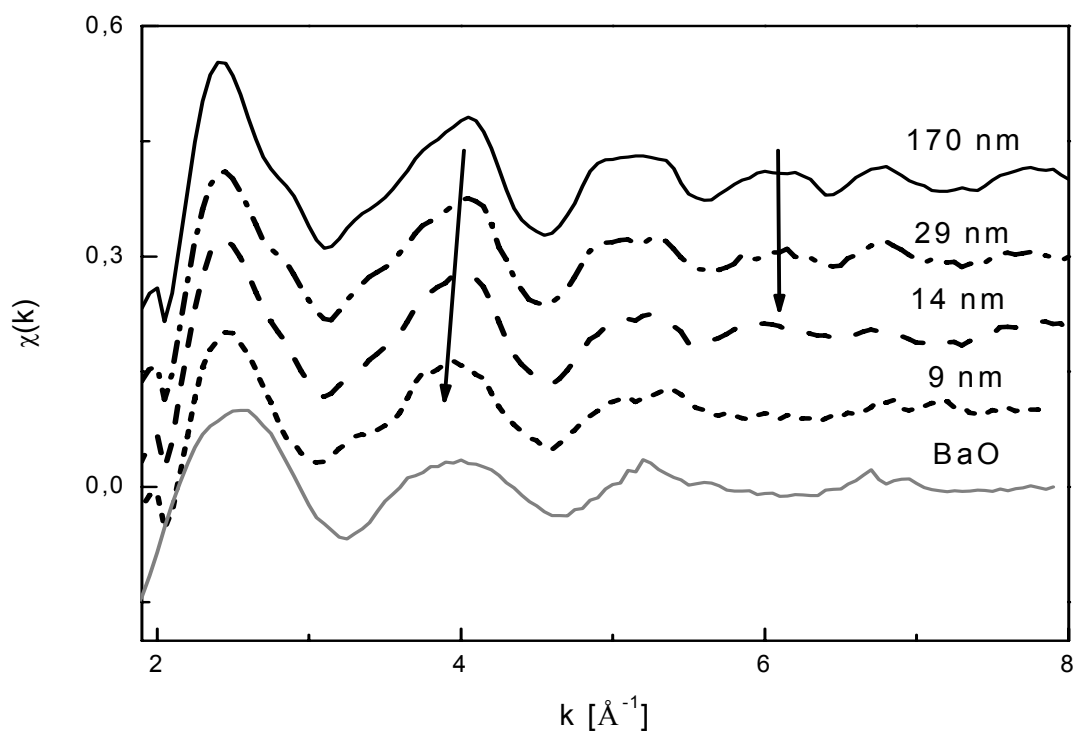
Figure 7.6: EXAFS $\chi(k)$-function of pure (170 nm) and CoTi doped Ba-ferrites nanoparticles along with BaO standard $\chi(k)$-function (grey
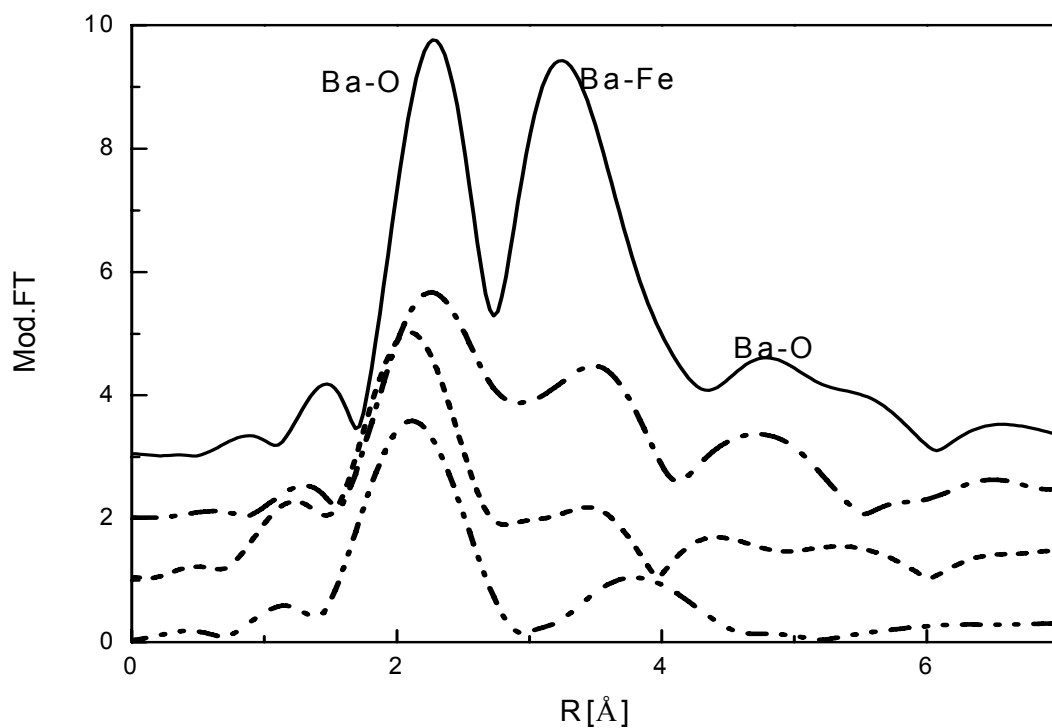
Figure 7.7: Fourier transforms of the Ba L_{III} – edge EXAFS oscillations of the theoretically calculated barium hexaferrites – BaFe12O19 (black solid line), barium oxide – BaO (dash-dot-dot line) in comparison with BaFe$_{12-2x}$Co$_x$Ti$_x$ nanoparticles of 29 nm (dash-dot line) and 9 nm (short dash line) size

In order to achieve quantitative information about the local structural environment around the Ba ions, the EXAFS analysis have been performed in R range from 3.3 Å to 3.95 Å. A single scattering fit for Ba–Fe path with an average distance was used in k range from 2.1 to 7.0 Å^{-1}. The σ^2 was fixed at the value of 0.0042 Å^2 for each sample. The experimental EXAFS signal $\chi(k)$ was weighted by k^3 for each sample. As can be seen from Figure 7.8, the fit of Ba-Fe contribution is broadened due to an attempt to fit the double peak feature with a single backscatterer Ba–Fe path. From the structural point of view, in the BaFe$_8$Co$_2$Ti$_2$O$_{19}$ compounds, the only Ba–Ti/Ba–Co bond is found at the distance about 3.7 Å, similar to the Ba–Fe contribution. A good agreement of theoretically predicted distance and coordination number, R = 3.6 Å and CN = 15, for Ba–Fe bond in crystalline BaFe$_{12}$O$_{19}$ undoped sample 2717 is gained from the fit and the observed reduction of coordination is even in a smallest particle too big to be explained just by under coordination of the outmost shell of Ba atoms. At the same time, the Ba–Fe bond contribution is still present in MFT for 9 nm particles, which means that the decomposition of Bariumhexaferrite is not complete.

Sample	Backscatterer	CN's	R [Å]	σ^2 [Å^2]	E$_0$
2717 (170 nm)	Ba-Fe	15.1±4.8	3.71±0.11	0.0042	10.3±7.9
2230 (29 nm)	Ba-Fe	11.4±3.9	3.71±0.02	0.0042	9.9±8.8
2730 (14 nm)	Ba-Fe	10.1±1.9	3.72±0.02	0.0042	10.6±0.1
4069 (9 nm)	Ba-Fe	3.9±1.3	3.70±0.03	0.0042	9.5±0.1

Table 7.2: Fit results for Ba-Fe coordination, performed at Ba L$_{III}$ – edge of undoped (sample 2717 only) and CoTi doped Ba-ferrites nanoparticles
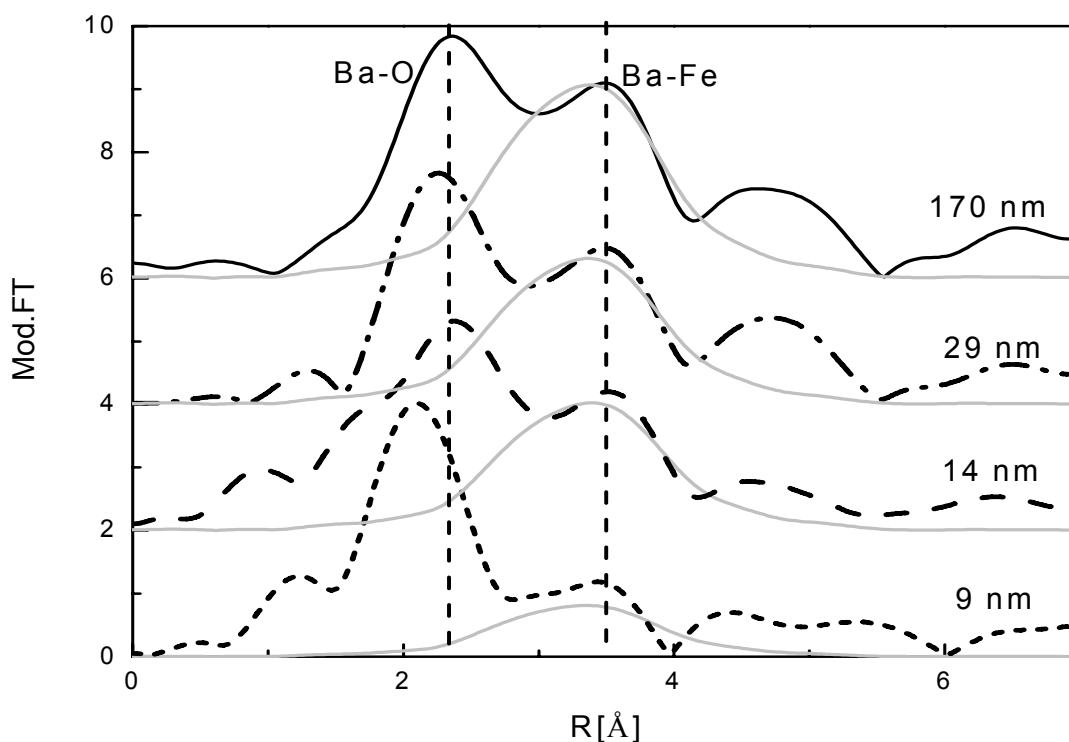
Figure 7.8: Fourier transforms of the Ba L$_{III}$ – EXAFS of BaFe$_{12-2x}$Co$_x$Ti$_x$ nanoparticles of 29 nm (dash-dot line), 14 nm (dashed line) and 9 nm (short dash line) size as well as undoped BaFe$_{12}$O$_{19}$ nanoparticles (solid) with fits obtained for Fe-Ba contribution (grey)

7.1.2   Fe K– XANES and EXAFS analysis

A trend towards a notable reduction in Ba–Fe coordination, which is clearly seen in Ba L_{III}–EXAFS data, is also confirmed when analyzing the Fe K–edge EXAFS. The modified Fourier transforms of undoped and Co/Ti doped nanoparticles, along with the fits, are presented in Figure 7.9.

The problem in the precise qualitative analysis of Fe–O bonding is that the local coordination of a given Fe atom varies notably; there are three different Fe–O distances present in the crystal structure of the bulk material (found at about 1.8 Å, 2.2 Å and 3.5 Å). Due to the multiplicity of the iron sites in the Ba-ferrites structure (table 7.3), the EXAFS evaluation of Fe–O coordination is nearly impossible. The multiplicity of the Fe–O bounding also influences the Fe–Fe and Fe–Ba coordination, which is contributed in the second pronounced peak in MFT.
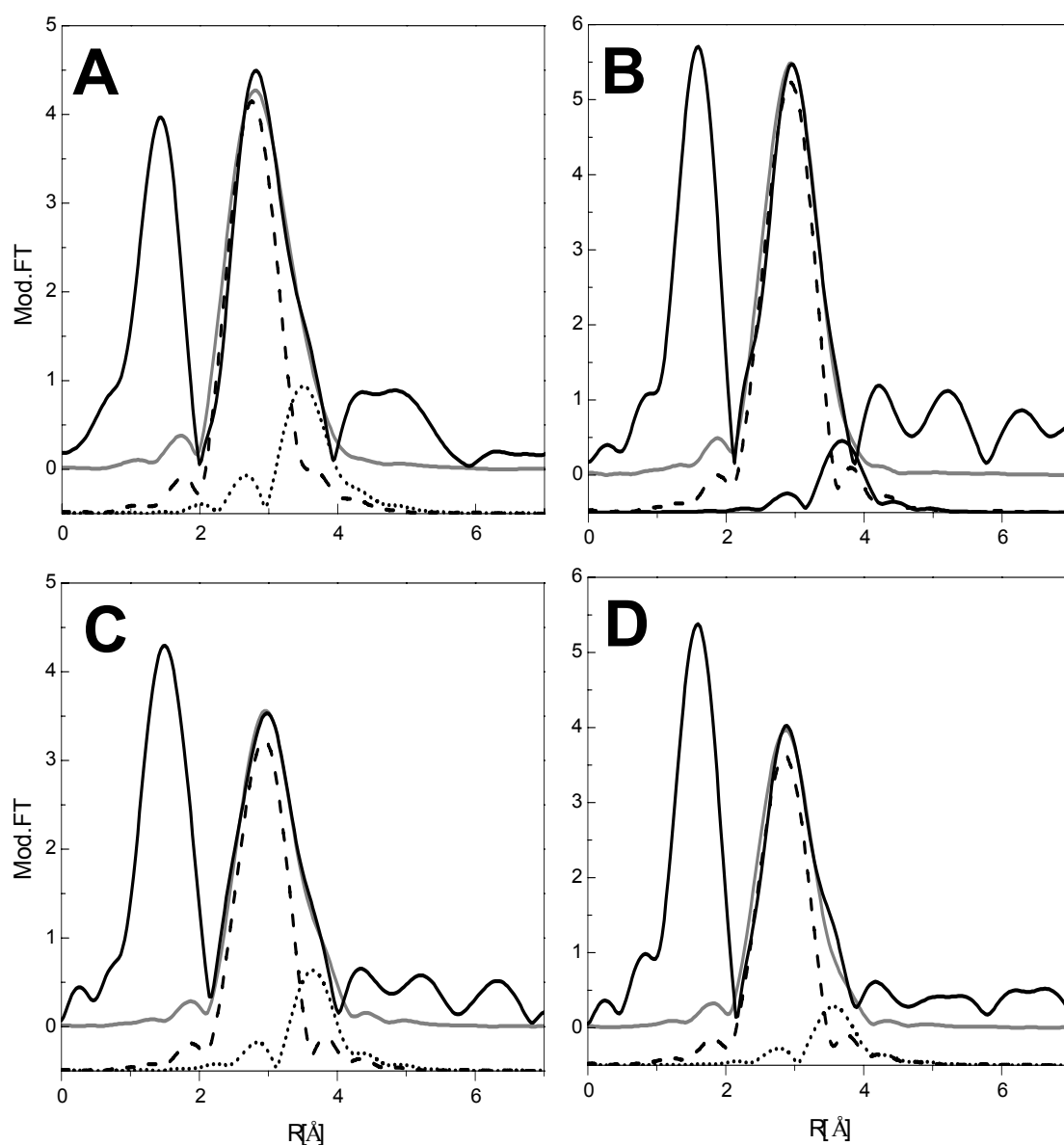
Figure 7.9: Modified Fourier transformation with k3 weighted χ (k) – function of undoped BaFe$_{12}$O$_{19}$ nanoparticles (black solid line) 170 nm (A), 29 nm (B), 14 nm (C) and 9 nm (D) with the fit of second coordination shell (grey solid line) with Fe-Fe (dashed line) and Fe-Ba (doted line) paths

According to the crystallographic data, the first averaged Fe–O peak is expected to be located at about 1.8 Å. The first Fe–Fe distance can vary between 3.0 Å and 3.4 Å depending of which Fe ion site was used as central atom. Although only Fe2 and Fe4 central sites are coordinated to Barium at distances of 3.35 Å and 3.62 Å, respectively, the Fe1 site was used as central for the fitting procedure. It has to be noted that amplitude and position of peaks are different for different Fe central sites which can be used in the analysis. As can be seen from Figure 7.9, the Fe–O peak has nearly the same amplitude and R value for all samples in the investigated system. Thus, the nearest Fe-O environment must be nearly the same independent on the size of nanoparticles. Still, looking at the changes in the MFT presented in Figure 7.9, one recognizes a systematic reduction of the relative intensity of the second coordination shell, which consists of a mixture of Fe and Ba atoms. A fit of this structure using one single Fe–Fe and one single Fe–Ba path can not be expected to produce correct coordination numbers due to the notable oversimplification of the model. Yet even using this crude approach, the trend towards a reduced Fe–Ba coordination is found. The Fitting results are summarized in table 7.3.

Sample	Backscatterer	CN	R [Å]	σ^2 [Å^2]	E_0
2717 (170 nm)	Fe-Fe	0.8±0.1	3.13 ±0.02	0.008	-2.7±1.5
	Fe-Ba	0.9±0.2	3.73±0.01	0.0046	-3.65±1.5
2230 (29 nm)	Fe-Fe	0.8±0.05	3.14±0.01	0.0075	12.4±3.3
	Fe-Ba	0.6±0.2	3.74±0.03	0.0070	10.9±0.6
2730 (14 nm)	Fe-Fe	0.6±0.05	3.15±0.01	0.008	10.5±0.8
	Fe-Ba	0.5±0.2	3.7±0.01	0.0036	10.8±0.8
4069 (9 nm)	Fe-Fe	0.6±0.06	3.1±0.01	0.008	6.9±1.2
	Fe-Ba	0.36±0.05	3.66±0.04	0.0046	8.1±0.9

Table 7.3: Fit results for Fe-Fe and Fe-Ba coordination, performed at Fe K – edge of undoped (sample 2717 only) and CoTi doped Ba-ferrites nanoparticle

Iron site in $BaFe_{12}O_{19}$	CN of nearest oxygen	Bond distance Å	Relative direction of magnetic moment	multiplicity/geometry
Fe1	6	2.05	↑	2a/octahedral
Fe2	5	1.87	↑	2b/ trigonal bipyramidal
Fe3	4	1.78	↓	4f$_1$/tetragonal
Fe4	6	2.02	↓	4f$_2$/octahedral
Fe5	6	2.07	↑	12k/octahedral
α-Fe_2O_3	6	1.95		4c/trigonal
γ-Fe_2O_3	4	2.15		8b/tetragonal

Table 7.4: Metal sites exist in M-type Ba-ferrite, hematite and maghemite phase of iron(III) oxide

At first sight, the results presented so far seem well suited to support the idea that a magnetically dead layer is formed, as one may assume that a decomposition into $BaO:6 \cdot Fe_2O_3$ occurs, which could then render two phases with interior magnetic properties, BaO and Hematite (α–Fe_2O_3).

Following this assumption, in the Fe K-XANES spectra of these particles, indications for a Fe_2O_3 contribution should rise. However, there are two possibilities which could be found: Hematite or Maghemite phase, the α–Fe_2O_3 and γ–Fe_2O_3, respectively. The presence of one or other of these phases would have a crucial influence on magnetic properties of nanoparticles. Hematite is a stable form of iron (III) oxide, but not magnetic, and the presence of this phase on the surface of the particles would lead to reduction of magnetization or, in other words, a 'dead layer'. In literature, contradicting statements with respect to the transition into α-Fe_2O_3 phase are found. The X-ray diffraction investigation for magnetic properties of Barium M-type ferrites prepared by sol-gel method, annealed at 950°C, revealed no α–Fe_2O_3 phase [Sun02]. However, X-ray diffraction measurements on Co/Ti-doped M–type ferrites, prepared by **S**elf-propagating **H**igh-temperature **S**ynthesis (SHS), identify Hematite as impurities [Kuz01]. In contrast to that, Maghemite will not quench the magnetic properties as drastically as Hematite.

The Fe K-XANES presented in Figure 7.10 were background subtracted and calibrated to the first inflection point of bulk iron, 7112 eV [Tho01]. Surprisingly, the comparison of Fe K–edge XANES spectra with reference Fe oxides does not support the hypothesis that Hematite is formed. In general, the variation between the spectra of particles with different size is small. This is true even for the comparison between the 9 nm and 170 nm nanoparticles. The seemingly paradoxical situation is resolved, when recalling that the γ-Fe_2O_3 phase can be found as a building block in the $BaFe_{12}O_{19}$. This fact also explains the extreme structural similarity between the Fe K–edge XANES spectra of this material and bulk Bariumhexaferrite.
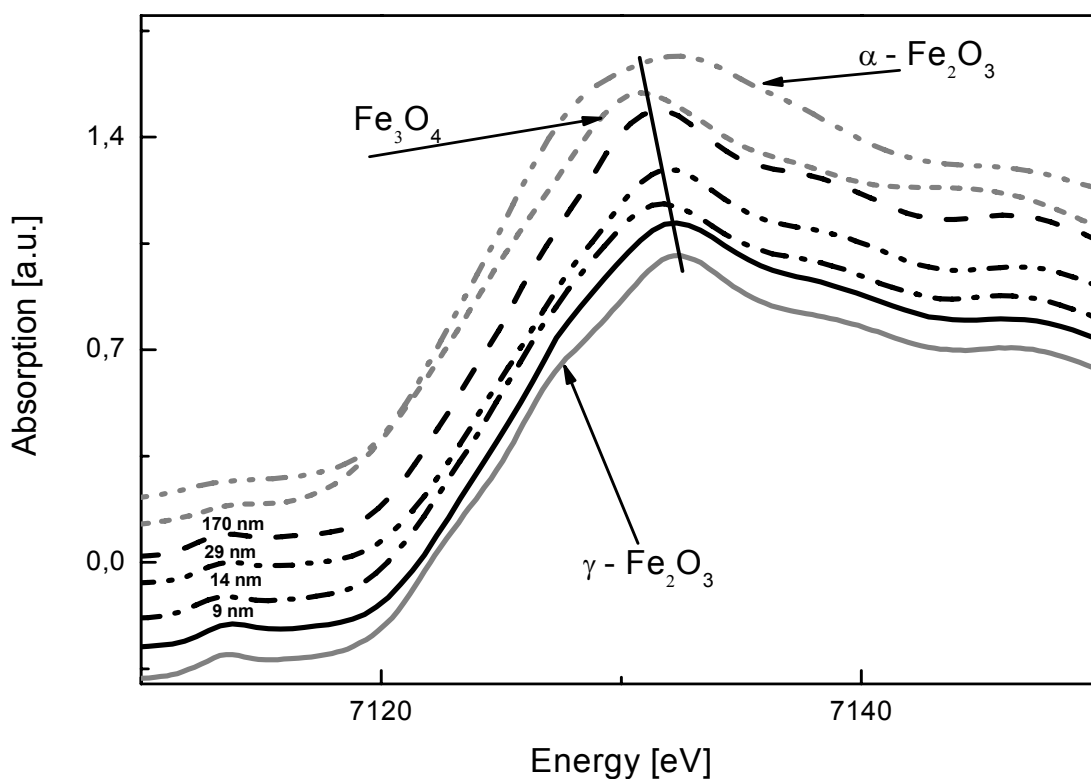
Figure 7.10: Fe K-XANES of $BaFe_{12-2x}Co_xTi_xO_{19}$ particles with different size and the reference compounds Magnetite-Fe_3O_4 (grey short-dash line), Hematite-α-Fe_2O_3 (grey dash-dot-dot line) and Maghemite-γ-Fe_2O_3 (grey solid line)

In this thesis the different iron and later titanium oxides spectra along with respective bulk spectra have been used as a reference spectra to determine the oxidation states of Fe and Ti in Co/Ti doped Be-ferrites NP's. Following the calculation which has been previously described in chapter 2.3, the edge shift, relative to the iron foil edge position, for different iron-oxides is presented in Figure 7.11 (right panel). The edge shift for different Ba-ferrites NP's are not systematic and within the level of error, that is why an average result is displayed as lines in Figure 7.11 (right panel). As can be seen, the oxidation state of iron in Ba-ferrite is (3+) and is closer to the γ-Fe_2O_3 phase.
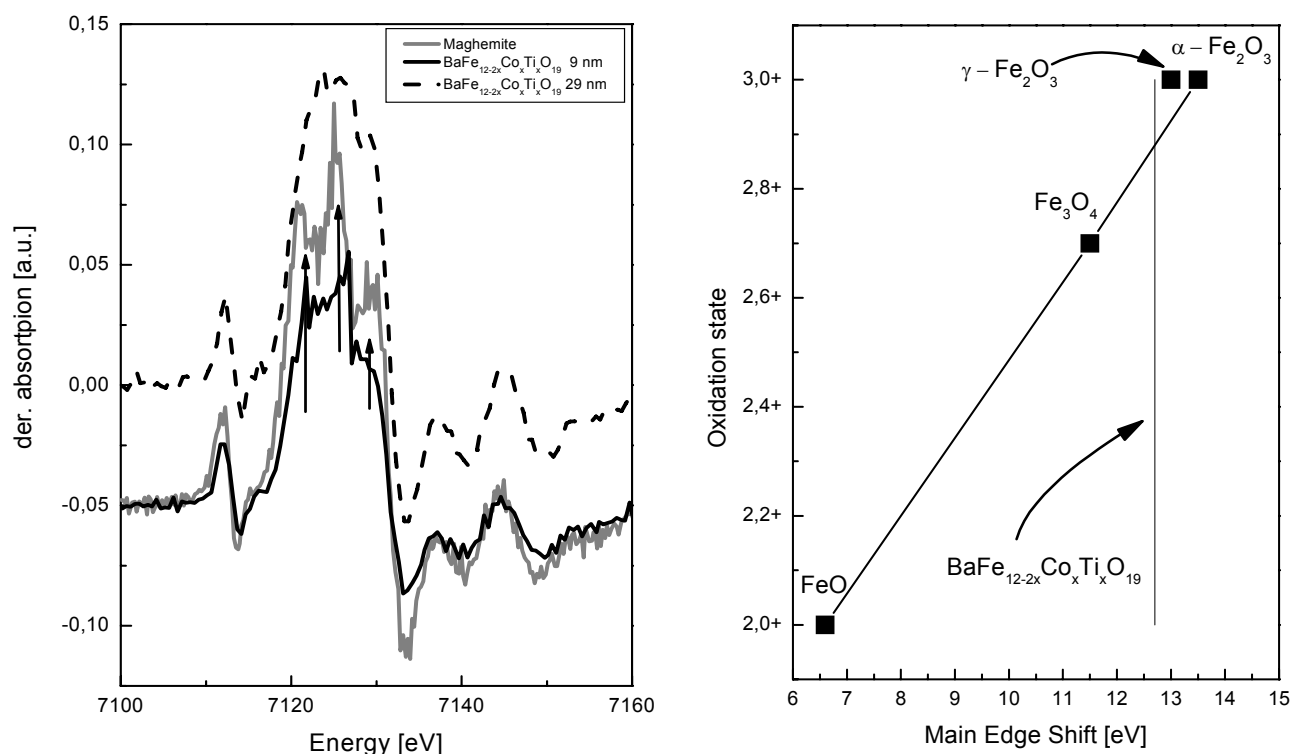
Figure 7.11: Determination of the oxidation states of iron for Ba-ferrites NP's based on the main edge shift calculations (right) .Derivatives of Be-ferrites in comparison with $\gamma - Fe_2O_3$ (left)

In addition to the edge shift calculation, the derivative of Fe K-XANES, displayed Figure 7.11 (left panel), shows the size dependent tendency towards γ-Fe_2O_3 phase of iron oxide. As a consequence, the magnetic properties of the material which are mainly determined by these building blocks should be preserved; even a complete BaO shell is not sufficient to lead to the observed reduction of magnetic properties.

Bearing in mind the exclusion of Hematite and Magnetite phase formation for Ba-ferrites, which follows from XANES analysis, the maghemite phase is preserved in Co/Ti doped Ba-ferrites nanoparticles. The formation this phase also explains the relatively good magnetic properties even for the smallest Ba-ferrites NP's. The crucial point now is the understanding of the factors which would stabilize the metastable phase. In this respect the role of the dopant atoms in the system has to be discussed. In the literature, a recent investigation on tin- and titanium-doped maghemite by XRD and EXAFS prove that the doping of the Bariumhexaferrite materials by Co and by tetravalent Ti improves the magnetic performance [Hel01]. These results are of great interest as they show that by the substitution of tetravalent ions γ–Fe_2O_3 can be stabilized against transformation to α–Fe_2O_3, even at high temperatures [Ber99, Ste92]. In addition to that, barium ions are able to stabilize the maghemite structure at temperatures above 400 °C [Sar93]. The most important question now associated with the structural and physical properties of Co/Ti doped Ba-ferrites concerns the occupation by the dopant. In the earlier works the homogeneous distribution of Co and Ti was assumed [Mül03].

To have a complete picture of the influence of dopant atoms cobalt and titanium K–edge XANES analysis is needed. Experimentally, the occupation of Fe sites by Co atoms could not be analyzed using X–ray absorption because on the one hand the dopant concentration is too low to allow for measurements in the transition mode, whereas in fluorescence mode the Co Kα line is strongly superimposed by the Fe Kβ emission. However, because of the co–doping of Co and Ti, indirect information about Co is also accessible from the Ti K–edge spectra which could be measured.

7.1.3   Ti K– XANES analysis and FEFF8 calculations

Figure 7.12 displays the Ti K-edge XANES spectra for 9nm, 14nm and 29nm $BaFe_{12-2x}Co_xTi_xO_{19}$ particles along with different titanium oxides.
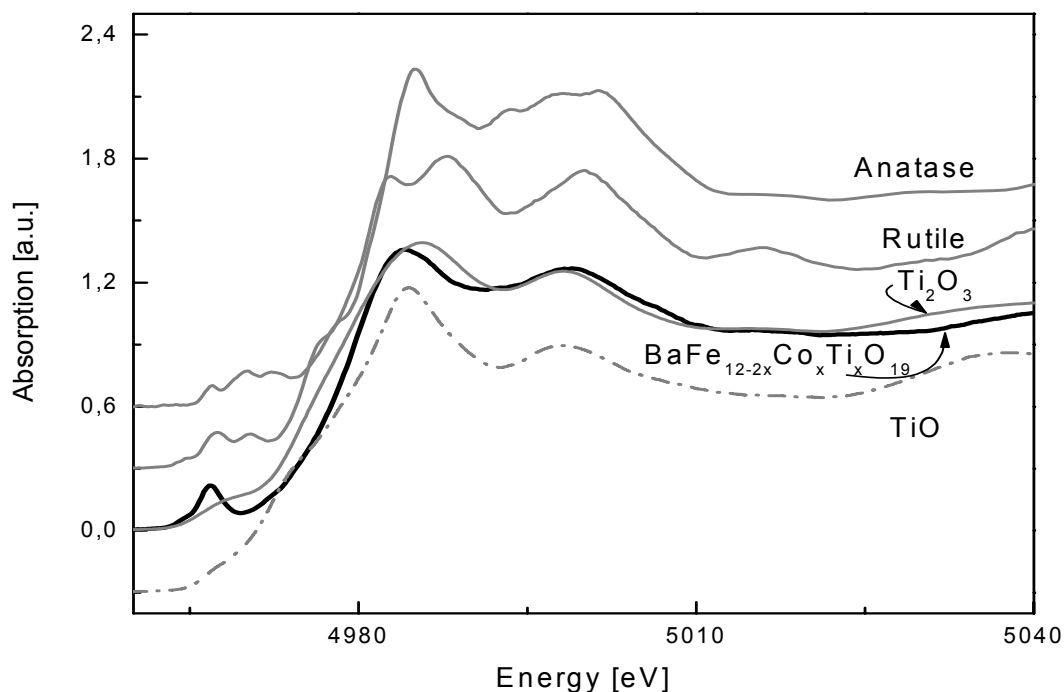
Figure 7.12: Ti K-XANES spectra of $BaFe_{12-2x}Co_xTi_xO_{19}$ nanoparticles with varied size along with different titanium oxides spectra

The first step of the analysis consists in the determination of the formal valency of Ti in the system by comparison with a systematic series of reference spectra. The notable difference in the spectral features of Ba–ferrites particles and titanium oxides are clearly seen, especially with respect to the edge position. The XANES 'fingerprint' analysis provides no evidence of possible recomposition to the TiO or Ti_2O_3 phase, as the spectrum of Co/Ti doped Ba–ferrites nanoparticles is very different from TiO and Ti_2O_3 reference spectra. This suggests, that the Ti atoms should have formal valency 4+.

In addition to observations from fingerprint analysis results, the absorption edge shift calculations have been done to confirm that the formal valency of the Ti absorbing atom is the same as for the initial compounds TiO_2 and independent of the size of the particles. The enlarged Ti K-XANES spectra of 9 nm, 14 nm and 29 nm Co/Ti doped Ba-ferrites are shown in Figure 7.13 (left). The notable difference in the spectral features which are seen for 14 nm nanoparticles are due to the fact that, only this data has been taken at the BN3 beam line. The absorption edge shift analysis for determination of oxidation states confirm that, for the investigated nanoparticles, the oxidation state is close to 4+, Figure 7.13 (right). These results suggest charge

compensation via the presence of Co (2+). Variation in Ti valency between the individual samples is not systematic and within the level of error, that is why the averaged result is presented in Figure 7.13 (right).
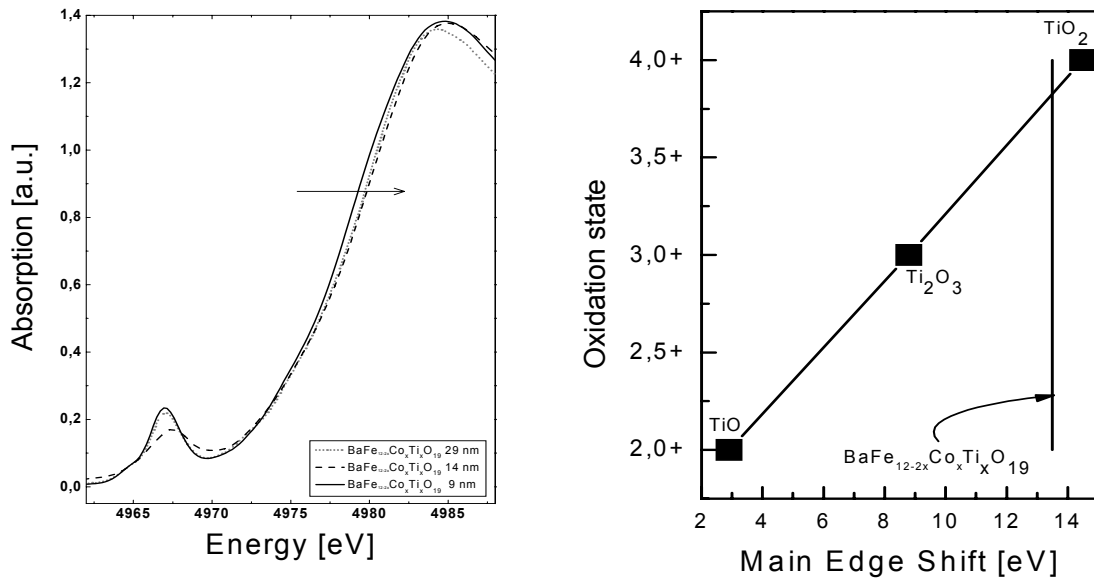
Figure 7.13: Determination of the oxidation states of iron for Ba-ferrites NP's based on the main edge shift calculations (right) .Enlarged Ti K – XANES spectra of Co/Ti doped Ba-ferrites NP's (left)

Next, one can try to identify the position at which the Ti atoms are located using FEFF8 calculations. The calculated Ti K–XANES spectra for different site occupation are shown in Figure 7.14. The splitting of the two dominant structures labelled 1 and 2 is 14.1 eV in the experimental data, but it is 16.7 eV for the Fe2, 18.7 eV for the Fe3 and 16.3 eV for the Fe4 site, respectively. Also, sites Fe2 and Fe4 feature a very intense pre–edge peak, which is not encountered in the experimental data. The only site which remain as candidates for the substitution site are those of octahedral symmetry. Potentially, the Fe1 site seems to be a more promising candidate because of the position of the shape resonance at about 5040 eV, but this spectral feature does not appear in sufficient clarity in the experimental data to make this assignment binding.
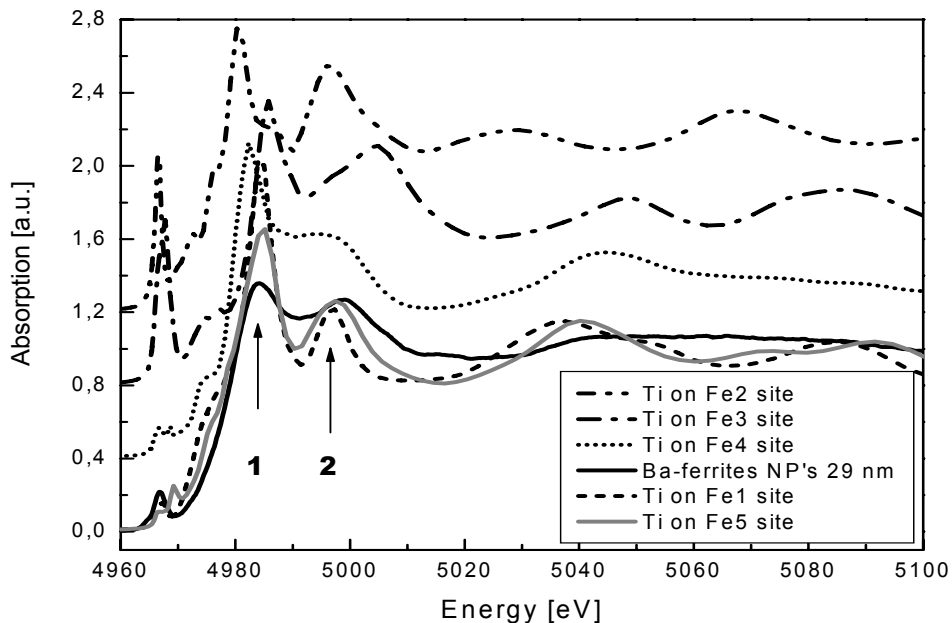
Figure 7.14: Experimental Ti K-XANES of 29 nm Ba-ferrites nanoparticles (black solid line) in comparison with calculated using FEFF8 code Ti K-XANES for different Ti ions occupations in hexagonal structure of $BaFe_{12}O_{19}$

Further evidence for the site selective occupations for Ti and Co can be better understood from the magnetic investigation performed on Co/Ti doped $BaFe_{12}O_{19}$ nanoparticles. The structure of γ–Fe_2O_3 which, preserved by Co/Ti doping, contains one tetrahedral iron site and tree octahedral iron sites. Two of the octahedral iron sites are fully occupied and the third is only 1/3 occupied [Fle96]. Following these facts, one can conclude that the substitution is taking place in γ–Fe_2O_3 substructure, where iron exhibits octahedral coordination with oxygen to complete the structure.

In addition to that, recent determination of magnetic moment of Co/Ti doped Ba-ferrites NP's using Mössbauer spectroscopy shows that magnetic properties of nanoparticles can be stabilized if the substitution of Fe ions by Co and/or Ti is taking place in the octahedrally coordinated sublattice [Bat91 and Wil00]. The substitution into the tetrahedral structure will lead to the reorientation of magnetic moment in a particular plane (2a, $4f_2$, or 12k) and thus, the decrease of the resulting magnetic properties of nanoparticles. There are three iron sites which have octahedral coordination with oxygen: Fe1, Fe4 and Fe5. Better magnetic properties would result if the substitution is taking place in the sites with a same relative orientation of magnetic moment. The only possibility is then site selective substitution of Fe atoms in Fe1 and Fe5 sites. Thus, a site selective substitution of Fe ions by Co and/or Ti is taking place in the Fe1 and Fe5 sites.

7.2   Conclusion

The result for the site selective occupation in the matrix provides an explanation for the increased stability of magnetic properties of the doped particles, as it is known from previous studies that the maghemite phase is stabilized by inclusion of other 3d metal atoms [Gen04, Har 02 and Tou98]. To summarize, it is possible to unite the seemingly divergent reports encountered in literature. In fact, the formation of a surface layer, due to surface decomposition towards BaO and Fe_2O_3, is observed. However, the decomposition leaves the γ–F_2O_3 building block contained in bariumhexaferrite unit cell quite intact. The stability of such a building block is increased by partial substitution of Fe atoms by 3d metals. As the magnetic properties of $BaFe_{12}O_{19}$ are mainly determined by these building blocks, the decomposition itself is not suitable to explain the massive effects on magnetic properties, thus identifying surface effects like defects. Surface reconstruction and spin disorder as the relevant cause of the observed changes in magnetic properties of Co/Ti doped Bariumhexaferrite materials.

8   Summary and Conclusions

The results of the X–ray Absorption Spectroscopy investigations presented in this thesis contribute to the DFG–Priority Program SPP1104:'Colloidal Magnetic Fluids: Basics, Preparation and Application of New Ferrofluids'. Here, the influences of size effects on the electronic and geometric structure of transition metal nanoparticles, resulting after size and shape selective synthesis, have been studied. In addition to that, the influence of the stabilizing procedure and surfactants on the structural properties of nanoparticles and ferrofluids has been probed in order to complete the set of parameters which determine the properties of nanoparticles.

The importance of the surface and surface coordination effects has been clearly shown in the case of small Pt_{13} nanoparticles. In the Pt–PVP system crucial aspects of nanoparticle formation such as the kinetics of growth have been traced. In addition, the changes in the electronic and geometric structure of nanoparticles as a function of a surface contribution have been studied in detail. The knowledge extracted from the XAS investigation of the Pt nanoparticle created a basis for further analysis, where more complicated systems have been probed. In the case of the magnetic Cobalt nanoparticles and ferrofluids, the size and surfactant effects had to be considered simultaneously in order to develop a detailed model of the nanoparticles formation, resulting in particle stable against agglomeration and oxidation. For the series of Co/Ti doped Bariumhexaferrite nanoparticles, the size dependent changes in the magnetic parameters, which are normally assumed to be a material constant, have been understood. The main results, which have been obtained on these three systems, can be summarized as follows:

1. The importance of the $Al(C_8H_{17})_3$ compound, which stops the growth of metal cluster, has been confirmed for the synthesis of small Pt clusters. TEM micrographs of Pt nanoparticles in powder depict monodisperse Pt particles of 0.75 ± 0.10 nm. To our knowledge, this is the first time a monodisperse Pt cluster with a mean diameter less than 0.8 nm was obtained by wet–chemical methods.

2. Pt nanoparticles of this size are supposed to form a single shell structure. The presence of Pt_{13} cluster structure has been confirmed by XANES 'fingerprint' comparison of experimental spectra and calculated ones using the FEFF8 code. The structure remains the same for Pt nanoparticles in solution as well as in powder form, when kept strictly under argon (chapter 5.1).

3. Exposure to air in case of Pt13 nanoparticles leads to dramatic changes in the electronic structure of the Pt_{13} cluster. XANES measurements allow tracing time dependent changes in the electronic and geometric structure of small Pt clusters as well as the influence of the amount of accessible oxygen. On the one hand, large rates of oxygen available for the reaction with $Al-(C_7H_{18})_3$ lead to the formation of an Al_2O_3 matrix in which Pt nanoparticles are homogeneously distributed and the agglomeration of the Pt nanoparticles on the other hand. The XPS measurements reveal that as–prepared Pt nanoparticles are truly zerovalent and the Al oxide signal can be detected once they were exposed to air.

4. In contrast to that, application of the 'smooth oxidation' procedure results in a somewhat different reaction of oxygen with aluminumorganic. Slow rate of oxygen access leads to the reaction in which only some $Al-C_8H_x$ coordination is replaced by Al–O. A step–wise model of the surface modification in dependence on time and the amount of oxygen available for reaction (Figure 5.8) has been developed based on the results achieved from XANES analysis.

5. The stabilizing character of one surfactant (PVP) has been investigated in case of the Pt–PVP stabilized nanoparticles with different sizes (chapter 5.2). XANES measurements of 2.5 nm and 8

nm tetrahedral Pt nanoparticles confirm the presence of zerovalent platinum nanoparticles. Thus, the non aggressive character of the PVP stabilizing, in contrast to $Al(C_7H_{18})$, has been confirmed in the way that once the Pt oxidation state is formed, addition of PVP cannot change it any more.

6. The Pt particle size varies inversely in relation to the amount of the seeds. This has significant impact in catalysis as shape and size control of nanoparticles determine their electronic, as well as catalytic, properties due to imposed boundary conditions.

7. Stabilization of Pt nanoparticles via Pt–N or Pt–O weak interactions is found to be preferable in the case of 8 nm particles. In contrast to that, a mixture of metallic Pt and K_2PtCl_4 phases is found for 2.5 nm nanoparticles. The faster rate of nucleation, caused by addition of the seeds, and the fact that the amount of the precursor is in surplus, leads to the presence of impurities, which can be determined as unreacted precursor. As a consequence, the presence of a contamination in case of 2.5 nm Pt nanoparticles makes it impossible to study the pure surface effects. Alternatively, a more detailed understanding in the kinetics of nanoparticle growth was indirectly extracted from XAFS analysis.

8. The use of the $Al(C_7H_{18})_3$ and $Al(C_2H_5)_3$ compounds in 'bottom-up' wet-chemical approach for the preparation of magnetic Cobalt nanoparticles prevents them from agglomeration and leads to a quasi monodisperse size distribution. Moreover, it has been found that the particles resulting after thermolysis in presence of aluminumorganic compounds have a weak surface coordination with Co–C and Co–O. The presence of the CO bonds on a surface is also supported by IR measurements.

9. The stabilizing of magnetic nanoparticles, after thermolysis in the presence of $Al(R)_3$ compounds, can be done by using suitable surfactants or by applying the novel 'smooth oxidation' procedure. In the first case, the stabilization against agglomeration is achieved. A surfactant induced phase transition has been observed for Co nanoparticles. Application of the 'smooth oxidation' leads to the formation of a core–shell system and the shell consists of $CoCO_3$. In this case, stabilization of nanoparticles against oxidation is reached.

10. Further peptization of the particles, pre–stabilized by 'smooth oxidation', by surfactants, *e.g.* KorantinSH, LP4, oleic acid, surrounds the particle with an additional dense organic shell. In the process of peptization, the $CoCO_3$ shell is modified. It has been shown (chapter 6.1.1) that surfactant effects influence nanoparticle properties notably. Additional contribution from CoO bonds, which are the result of interactions between the $CoCO_3$ protection shell and active (COOH–R) groups, is detected by XANES measurements and proved in EXAFS analysis.

11. The thickness of the protection shell depends on the chain length of the aluminumorganic compounds used during the synthesis, and the molar ratio of $Co_2(CO)_8$ to $Al(R)_3$. Long term exposure to air leads to transformation of the shell into CoO. However, the presence of the shell inhibits further oxidation and allows the particles to be air stable for a long time.

12. The phase transformations are easily induced in nanostructured systems due to the influence of the surface energy term. Formation of the F.C.C. phase of metallic cobalt seems to be preferable during the synthesis of magnetic cobalt nanoparticles in presence of $Al(C_7H_{18})_3$ compounds. This observation is also supported by FEFF8 theoretical calculation of different phases, which are known for metallic cobalt (chapter 6.1.2).

13. As a third system, the size dependent changes in the local geometric and electronic structure of $BaFe_{12}O_{19}$ nanoparticles, prepared by the modified crystallization (chapter 4.2) method have been investigated by XANES and EXAFS techniques (chapter 7). A size dependent re-/decomposition towards the BaO phase is observed for Co/Ti doped Bariumhexaferrite particles in XANES measurements and confirmed by EXAFS analysis. These observations suggest the formation of a

magnetically 'dead layer' (BaO and α–Fe_2O_3) causing a decrease of the magnetic properties with decrease of the particle size. Surprisingly, even for the smallest nanoparticles, the magnetic properties are better, than one would expect, assuming formation of α–Fe_2O_3.

14. Even for the particles beyond the supermagnetic size limit (10 nm), no α–Fe_2O_3 phase was detected using the 'fingerprint' comparison of XANES spectra with different Iron oxides. The results obtained from XANES analysis conclude that in this system, Fe^{3+} in a Magnetite phase is stabilized. The stabilization of γ–Fe_2O_3 is a function of doping.

15. In contrast to the homogeneous distribution of Cobalt and Titanium ions in the hexagonal structure of ferrite, which was previously suggested, the site selective occupation of Fe sites for Ti and Co were obtained from XANES analysis. FEFF8 calculations done for Fe and Ti K-XANES confirm that Fe1 and Fe5 – octahedral sites in the crystalline structure of ferrites, are preferable candidates for Co/Ti substitution.

16. The results for the site selective occupation in the $BaFe_{12}O_{19}$ matrix provides an explanation for the increased stability of magnetic properties of the doped particles Thus, it is possible to unite the seemingly divergent reports encountered in literature. Surface reconstruction towards BaO and spin disorder remains a relevant cause of the observed changes in magnetic properties of Co/Ti doped Bariumhexaferrite materials.

Summarizing all that has been mentioned above, one can conclude that XAS is a suitable technique which allows tracing of the size and surfactant effects on magnetic nanoparticles and ferrofluids, prepared by different synthesis methods. The search for new magnetic materials with unusual chemical and physical properties pushes the need for particles with a smaller and smaller size. However, as the particle size decreases the reactivity of the particle increases and the magnetic properties become affected more by surface effects. The nature of size – and surface – effects and the influence of these effects on the resulting properties of transition metal nanoparticles has been clarified in the case of two magnetic nanoparticle systems by means of X-ray Absorption Spectroscopy.

A   Appendix

Sample #	Form	AlR$_3$ chain length	Co : AlR$_3$ ratio	Surfactant	Carrier medium	Protection shell modification	Size [nm]	Storage condition
MTV-MA-018	magnetic fluid	Al(C$_8$H$_{17}$)$_3$	10 : 1	KorantinSH	Toluene		10.0*	Air
MTV-MA-028	magnetic fluid	Al(C$_8$H$_{17}$)$_3$	10 : 1	KorantinSH	Toluene		10.0*	Argon
MTV-MA-033	magnetic fluid	Al(C$_8$H$_{17}$)$_3$	10 : 1	KorantinSH	L9		10.0*	Argon
MTV-MA-049	magnetic fluid	Al(C$_8$H$_{17}$)$_3$	10 : 1	KorantinSH, LP4	L9		10.0*	Argon
MTV-MA-050	powder	Al(C$_2$H$_5$)$_3$	10 : 1			air during drying	5.0**	Air
MTV-MA-051	powder	Al(C$_8$H$_{17}$)$_3$	10 : 1			air during drying	10.0*	Air
MTV-MA-052	powder	Al(C$_8$H$_{17}$)$_3$	10 : 1			'smooth oxidation'	10.0*	Air
MTV-MA-053	powder	Al(C$_8$H$_{17}$)$_3$	5 : 1			'smooth oxidation'	3.5**	Air
MTV-MA-055	powder	Al(C$_2$H$_5$)$_3$	10 : 1			'smooth oxidation'	5.0**	Air
MTV-MA-073-02	powder	Al(C$_8$H$_{17}$)$_3$	1 : 1	KorantinSH		'smooth oxidation'	1.4***	Air
MTV-MA-077-01	powder	Al(C$_8$H$_{17}$)$_3$	8 : 1			'smooth oxidation'	10.0*	Air
MTV-MA-077-02	magnetic fluid	Al(C$_8$H$_{17}$)$_3$	8 : 1	KorantinSH	Toluene	'smooth oxidation'	10.0*	Air
MTV-MA-084-01	powder	Al(C$_8$H$_{17}$)$_3$	5 : 1	KorantinSH		'smooth oxidation'	3.5**	Air
MTV-MA-084-02	Magnetic fluid	Al(C$_8$H$_{17}$)$_3$	5 : 1	KorantinSH, LP4	L9	'smooth oxidation'	3.5**	Air

Table 1: Main parameters and conditions of the magnetic nanoparticles and ferrofluids synthesis

All samples have been prepared according to the general procedure, described in chapter 4.1.3. * ± 1.1 nm, ** ± 1.6 nm, *** ± 0.2 nm

References

[Aga91]   Agarwal, B.K., *X-ray Spectroscopy*, Springer-Verlag (1991)

[Ami25]   Aminoff, G.: Geol. Foren. Stockholm Forhandl. **47**, 283 (1925)

[Amu98]   Amulyavichus, A., Daugvila, A., Davidonis, R., Sipavichis, C.: Fiz. Met. Metallovedenie **85**, 111 (1998)

[An02]   An, S. Y.; Lee, S. W.; Lee, S. W.; Kim, C. S.: *Magnetic properties of $Ba_{1-x}Sr_xFe12O19$ grown by a sol-gel method,* Journal of Magnetism and Magnetic Materials **242,** 413-415 (2002)

[Ang02]   Angermund, K; et. al.: Angew. Chem. Int. Edit. **41**, 4041 (2002)

[Ank02]   Ankudinov, A. L.; Bouldin, C. E.; Rehr, J. J.; Sims, J.; Hung, H.: *Parallel calculation of electron multiple scattering Lanczos algorithms*, Physical Review B **65**, 104107 (2002)

[Ank98]   Ankudinov, A. L.; Ravel, B.; Rehr, J. J.; Conradson, S. D.: *Real-space multiple-scattering calculation and interpretation of x-ray-absorption near-edge structure*, Physical review B **58** (12), 7565 (1998)

[Ant97]   Antonietti, M., Göltner, C.: Angew. Chem. Int. Ed. Engl. **36**, 910 (1997)

[Apr03]   Aprà, E., Fortunelli, A: *DF calculations on platinum nanoclusters: Pt_{13}, Pt_{38}, Pt_{55}*, DOI: 10.1388/SSC2003-CM-218 (2003)

[Bal05]   Baletto, F.; Ferrando, R.: Structural properties of nanoclusters: Energetic, thermodynamic, and kinetic effects, Reviews of Modern Physics, **77**, 371 (2005)

[Bal87]   Balasubramanian, K.: *Electronic states of Pt_2*, The Journal of Chemical Physics **87**, 6573 (1987)

[Bar00]   Bard, A. J.; Faulkner, L. R.: Electrochemical Methods: Fundamentals and Applications, John Wiley & Sons, New York (2000)

[Bat91]   Batlle, X.; Obradors, X.; Rodríguez-Carvajal, J.; Pernet, M.; Cabanas, M. V.; Vallet, M.: *Cation distribution and intrinsic magnetic properties of Co-Ti-doped M-type barium ferrite*, J. appl. Phys. **70** (3), 1614 (1991)

[Ber96]   Berkovsky, B. M.; Bashtovoy, V.: *Magnetic Fluids and Applications Handbook*, New York: Begell House Inc. (1996)

[Ber99]   Berry, F.J., Greaves, C., Helgason, Ö., McManus, J.: J.Mater. Chem. **9**, 223 (1999)

[Bla79]   Blackborrow, J. R., Young, D.: Metal Vapor Synthesis, Springer-Verlag, New York (1979)

[Boa95]   Boag, N. M.; Ravetz, M. S.: Journal of the Chemical Society-Dalton Transactions, 3473 (1995)

[Boen]   http://www.mpi-muelheim.mpg.de/kofo/institut/arbeitsbereiche/boennemann/boennemann.html

[Bön01]   Bönnemann, H.; Richards, R. M.: *Nanoscopic Metal Particles – Synthetic Methods and Potential Applications*, European Journal of Inorganic Chemistry, 2455 (2001)

[Bön03]   Bönnemann, H.; Brijoux, W.; Brinkmann, R.; Matoussevitch, N.; Waldöfner, N.; Palina, N.; Modrow, H.: *A size-selective synthesis of air stable colloidal magnetic cobalt nanoparticles*, Inorganica Chimica Acta **00**, 1-8 (2003)

[Bön04]   Bönnemann, H.; Brijoux, W.; Brinkmann, R.; Feyer, M.; Hofstadt, W.; Khelashvili, G.; Matoussevitch, N.; Nagabhushana, K.: *Nanochemistry Colloids Powders*, The Stream Chemiker **XXI** (1), (2004)

[Bra94]   Bradley, J. S.: Clusters and Colloids, ed. Schmid, G.: VCH, Weinheim, 477 (1994)

[Bre04]   Brendebach, B.: *Röntgenabsorptionsspektroskopie an Phosphorsalzperlen: Bestimmung der geometrischen und elektronischen Struktur von metalloxid-dotierten Natriumphosphatgläsern*, Dissertation Universität Bonn, BONN-IR-2004-03 (2004)

[Bru38]   Brunnauer, S.; Emmet, P. H., Teller, E.: Journal of the American Chemical Society **60**, 3091 (1938)

[Buc02]   Bucher, S.: *Charakterisierung der Kern-Hülle-Wechselwirkung von unterschiedlich stabilisierten Übergangsmetall-Nanopartikeln mittels Röntgenabsorptionsspektroskopie*, Dissertation Universität Bonn, BONN-IR-07-2002 (2002)

[Cab94]   Cabañas, M. V.; Conzález-Calbet, J. M.; Vallet-Regi, M.: *Synthesis of barium hexaferrite by pyrolysis of an aerosol*, Journal of Materials Research **9**, 712 (1994)

[Cab95]   Cabañas, M. V.; Conzález-Calbet, J. M.; Vallet-Regi, M.: *Co-Ti Substituted Hexagonal Ferrites for Magnetic Recording*, Journal of Solid State Chemistry **115**, 347 (1995)

[Cal04]   Calvo, E., Doye, J. P. K.:Physical Review B. Condensed Matter and Materials Physics **69**, 125414 (2004)

[CAMD]   Annual Report CAMD 2005; www.camd.lsu.edu

[Cap95]   Capehart, T. W.; Herbst, J. F.; Mishra, R. K.; Pinkerton, F. E.: *X-ray absorption edge shifts in rae-earth – transition-metal compounds*, Physical Review B **52** (11), 7907 (1995)

[Car02]   Carnes, C. L.; Klabunde, K. J.: *Unique chemical reactivity of nanocrystalline metal oxides towards hydrogen sulfide*, Chem. Mater. **14**, 1806-1811 (2002)

[Cha05]   Chakrabarti, S.; Mandal, S. K.; Chaudhuri, S.: *Cobalt doped γ-Fe₂O₃ nanoparticles: synthesis and magnetic properties*, Nanotechnology **16**, 506-511 (2005)

[Cha78]   Chantrell, R.: *Measurements of particle size distribution parameters in ferrofluids*, IEEE Trans. Magn. **14**, 975 (1978)

[Che02]   Chen, L.X.; Liu, T.; Thurnauer, C.; Csencits, R.; Raih, T.: *Fe₂O₃ Nanoparticle Structures Investigated by X-ray Absorption Near-Edge Structure, Surface Modifications, and Model Calculations*, J. Phys. Chem. B **106**, 8539-8546 (2002)

[Chi02]   Chikan, V.; Kelley, D. F.: *Size-dependent spectroscopy of MoS₂ nanoclusters*, J. Phys. Chem. B **106**, 3794-3804 (2002)

[Chr04]   Christy R. Vestal and Z. John Zhang: *Magnetic spinel ferrite nanoparticles from microemulsions*, Int. J. of Nanotechnology **1**, Nos. ½ (2004)

[Col90]   Collongues, R.; Gourier, D.; Kahn-Harari, A.; Lejus, A. M.; Thery, J.; Vivien, D.: *title*, Annual Review of Materials Science **20**, 51 (1990)

[Cro00]   Crown, A.; Kim, H.; Lu, G. Q.; Moraes, I. R.; Rice, C.; Wieckowski, A.: *Research toward designing high activity catalysts for fuel cells: structure and reactivity*, Journal of New Materials for Electrochemical Systems **3**, 275-284 (2000)

[Dan92]   Dany, R.: *Untersuchungen zur Optimierung des Spektrums der Synchrotronstahlung für die Röntgentiefenlithographie, Diplomarbeit, Physikalisches Institut der Universität Bonn, BONN-IR-92-32 (1992)*

[Der02]   Dermott E.; Cullen J.; Hubbell, H.; Kissel, L.: *PROGRAM EPICSHOW - A Computer Code to Allow Interactive Viewing of the EPIC Data Libraries (Version 2002-1)*, University of California Lawrence Livermore National Laboratory (2002)

[Din99]   Dinega, D. P.; Bawendi, M. G.: Angewandte Chemie, Int. Ed. **38**, 1788 (1999)

[Dur90]   Durmeyer, O.; Kappler, J. P.; Beaurepaire, E.; Heintz, J. M.; Drillon, M.: J. Phys. Condensed Matter **2**, 6127 (1990)

[Ech81]   Echt, O.; Sattler, K.; and Recknagel, E.: *Magic Numbers for Sphere Paching: Experimental Verification in Free Xenon Clusters*, Phys. Rev. Let. **47**, 1121-1124 (1981)

[Fec90]   Fecht, J. H.: Acta Metall. Mater. **38**, 1927 (1990)

[Fle96]   Flether, D. A.; McMeeking, R. F.; Parkin, D.: J. Chem. Inf. Comput. Sci **36**, 746 (1996)

[Gaf96]   Gaffet, E.; Tachikart, M.; Kedim, O. El.; Rahouadj, R.: Mater. Charact. **36**, 185 (1996)

[Gaj02]   Gajbhiye, N. S.; Balaji, G.; Ghafari, M.: *Magnetic Properties of Nanostructured MnFe2O4 Synthesized by Precursor Technique*, physica status solidi (a) **189** (2), 357-361 (2002)

[Gam03]   Gambardella, P; Rusponi, S.; Veronese, M.; Dhesi, S. S.; Grazioli, C.; Dallmeyer, A.; Cabria, I.; Zeller, R.; Dederichs, P. H.; Kern, K.; Carbone, C.; Brune, H.: *Giant Magnetic Anisotropy of Single Cobalt Atoms and nanoparticles*, Science **300**, 1130 (2003)

[Gen04]   Gendler, T. S.; Shcherbakov, V. P.; Dekkers, M. J.; Gapeev, A. K.; Gribov, S. K.; McCelland, E.: *The lepidocrocite-maghemite-haematite reaction chain – I. Acquisition of chemical remanent magnetization by maghemite, its magnetic properties and thermal stability*, Geophys. J. Int. **160**, 815-832 (2005)

[Gil03]   Gilbert, B.; Frazer, B. H.; Belz, A.; Conrad, P. G.; Nealson, K. H.; Haskel, J. C.; Lang, J. C.; de Stasi, G.: J. Phys. Chem. A **107**, 2839 (2003)

[Gor57]   Gorter, E. W.: Proc. IEEE **104B**, 225 (1957)

[Gör91]   Görnert, P.; Sinn E.; Rösler M.: *Preparation and characterisation of hexaferrites powders*, Key Eng. Mater. **58**, 129 (1991)

[Gro81]   Groenland, J. P. J.; Fluitman, J. H. J.: *Measurement system for two-dimensional magnetic field distributions, applied to the investigation of recording head fields*, J. Phys. E: Sci. Instrum. **14**, 503-508 (1981)

[Gu94]   Gu, B. X.; Zhang H.Y.; Zhai, H. R.; Lu, M.; Miao Y. Z.: *Magnetic properties of sputtered BaCoTiFe$_{10}$O$_{19}$ films*, J. Phys.: Condens. Matter **6**, 1047 (1994)

[Gue76]   Guerrieri, F.; Salerno, G.: Journal of Organometallic Chemistry **114**, 339 (1976)

[Gui02]   Guirado- López, R.; Aguilera-Granja, F.; Montejano-Carrizales, J.M.: Electronic structure and stability of polycrystalline cobalt clusters, Phys. Rev. B **65** (4), ID045420-1 (2002)

[Gui04]   Guilin, Z.; Wu, Z. Y.; Li, A.; Wang, Y.; Zhang, J.; Abbas, M. I.; Hu, R.; Ni, X.; Tong, Y.; Hwu, Y.: *XANES investigation of the local structure of Co nanoclusters*, Ag. Phys. Rev. B. **69**, ID115405-1 (2004)

[Hag05]   Haglmuller, J.; Matyushin, V.; Rauter, H.; Mayer, C.; Winkler, H.; Bauer, G.; Schalkhammer, T.: *Nanocluster Optical Resonance Devices for Molecular Structure Transduction,* Current Nanoscience **1**, 3 (2005)

[Hal02]   Hallmeier, K. H.; Uhlig, L.; Szargan, R. J.: J. Electron Spectrosc. Relat. Phenom. **122**, 91 (2002)

[Han75]   Hanlan, L. A.; Huber, H.; Kündig, E. P.; McGarvey, B. R.; Ozin, G. A. J.: Am. Chem. Soc. **97**, 7054 (1975)

[Hel01]   Helgason, Ö.; Greneche, J. M.; Berry, F. J.; Mørup, S.; Mosselmans, F.*: Tin- and titanium-doped γ-Fe_2O_3 (maghemite),* J. Phys.: Condens. Matter **13**, 10785 (2001)

[Hen03]   Hendy, S.; Brown, S. A.; Hall, B. D.: Phys. Rev. B **68**, 2414 (2003)

[Hua95]   Huang, J. Y.; Wu, Y. K.; Ye, H. Q.: *Phase transformation of cobalt induced by ball milling,* App. Phys. Lett. **66**, 308 (1995)

[Ich99]   Ichikawa, M.: *Metal Clasters and Nanomaterials: an Overveiw*, ed. Braunstein, P.; Oro, L. A.; Raithby, P. R., Weinheim (1999)

[Jol99]   Joly, Y.; Cabaret, D.; Renevier, H.; Natoli, C.R.: *Electron population Analysis by Full-Potential X-ray Absorption Simulations*, Phys. Rev. Lett. **82**, 2398 (1999)

[Jon01]   Spanier, J. E.; Robinson, R. D.; Zhang, F.; Chan, S.-W.; Herman, I. P.: *Size-dependent properties of CeO2-y nanoparticles as studied by Raman scattering,* Physical Review B **64**, ID245407 (2001)

[Kau70]   Kaufman, L.; Bernstein, H.: *Computer Calculation of Phase diagrams*, Academic Press, New York and London (1970)

[Kim00]   Kim, D. K.; Zhang, Y.; Voit, W.; Rao, K. V.; Muhammed, M.: *Synthesis and characterization of surfactant-coated superparamagnetic monodispersed iron oxide nanoparticles*, The 3rd Meeting on Scientific and Clinical Applications of Magnetic Carriers, Rostock Germany (2000)

[Kim02]   Kim, D. K.: *Nanoparticles: Engineering, assembly, and Biomedical Applications*, ISBN 91-7283-265-7 Doctoral Thesis, Royal Institute of Technology (2002)

[Kin04]   Kinge, S.: *PEM-Fuel Cell Catalysts from Nanoscopic Precursors- a Comparative Study*, Der Rheinisch-Westfälischen Technischen Hochschule Aachen , PhD (2004)

[Kiy76]   Kiyama, M.: Bulletin of the Chemical Society of Japan **49**, 1855 (1976)

[Kla80]   Klabunde, K. J.: *Free Atoms and Particles*, Academic Press, New York (1980)

[Kod99]   Kodama, R. H.; Berkowitz, A. E.: *Atomic-scale magnetic modeling of oxide nanoparticles*, Phys. Rev. B **59**, 6321-6336 (1999)

[Köh01]   Köhl, G.: *Röntgenabsorptionsspektroskopie zur Charakterisierung von Katalysatoren für die PEM-Brennstoffzelle*, Dissertation Universität Bonn, BONN-IR-2001-14 (2001)

[Koj82]   Kojima, H.: *Fundamental properties of hexagonal ferrites with magnetioplumbite structure*, Ferromagnetic materials **3**, chap.3, ed. By E. P. Wohlfarth, North-Holland Publ. Comp., Amsterdam (1982)

[Kre01]   Kreibig, U.; Bönnemann, H.; Hormes, J.: Nanostrucutred Metal Clusters and Colloids, Handbook of Surfaces and Interfaces of Materials, **3**, edited by H. S. Halwa (Academic, San Diego), 1-85 (2001)

[Kuz01]   Kuznetsov, M. V.; Pankhurst, Q. A.; Parkin I. P.: *Novel SHS routes to CoTi-doped M-type ferrotes,* Journal of materials science: Materials in Electronics **12**, 533 (2001)

[LaM52]   LaMer, V. K.: Ind. Eng. Chem. **44,** 1270 (1952)

[Lan03]   Landfester, K.; Ram'ýrez, L. P.: *Encapsulated magnetite articles for biomedical application*, J. Phys: Condens. Matter **15**, 1345-1361 (2003)

[Lei96]   Leisner, T.; Rosche, C.; Wolf, F.; Granzer, F.; Wöste, L.: Surf. Rev. Lett. **3**, 1105 (1996)

[Lem78]   Lemonnier, M.; Collet, O.; Depautex, C.; Esteva, J. M.; Raoux, R.: Nucl. Instr. Meth. A **152**, 109 (1978)

[Les96]   Leslie-Pelecky, D. L.; Rieke, R. D.: Chemistry of Materials **8**, 1770 (1996)

[Li00]   Li, S.; Vijay, T. J.: *Cobalt-ferrite nanoparticles: Structure, cation distributions, and magnetic properties*, Journal of Applied Physics **87** (9), 6223-6225 (2000)

[Lim00]   De Lima, J. C.; dos Santos, V. H. F.; Granti, T.A.; de Biasi, R.S.: *A study of nanocristalline cobalt prepared by ball milling*, Cond. Mat. **26**, 10415D (2000)

[Loc02]   Lockman, P. R.; Mumper, R. J.; Khan, M. A.; Allen, D. D.: *Nanoparticle Technology for Drug Delivery Across the Blood-Brain Barrier*, Drug Dev. Ind. Pharm. **28**, 1-12 (2002)

[Maa99]   Maase, M.: *Neue Methoden zur Groeßen- und formselektiven Darstellung von Metallkolloiden*, PhD Thesis, Verlag Mainz, ISBN 3-89653-463-7, Aachen (1999)

[Man98]   Mansour, A. N.; Melendres, C. A.: *Analysis of X-ray Absorption Spectra of some Nickel Oxy-compounds using theoretical Standards*, Journal of Physical Chemistry A, Molecules, spectroscopy, Kinetics, Enviroment & General Theory **102**, 65 (1998)

[Mar91]   Martin, T. P.; Bergmann, T.; Göhlich, H.; Lange, T.: Chem Phys. Lett. **176**, 343 (1991)

[Mat80]   Materlik, G.; Kostroun, V. O.: *Monolithic crystal monochromators for synchrotron radiation with order sorting and polarizing properties*, Review of Scientific Instruments **51**, 86 (1980)

[Mod03]   Modrow, H.; Rahman, O. M.; Richards, R.; Hormes, J.; Bönnemann H.: *Structural characterization of a novel catalyst obtained from nanoscopic NiAlx, by X-ray absorption spectroscopy*, J. Phys. Chem. B **107**, 12221 (2003)

[Mod03b]   Modrow, H.; Bucher, S.; Rehr, J. J.; Ankudinov, A.: Phys. Rev. B **67**, 035123 (2003)

[Mol77]   Mollard, P.; Germi, P.; Rousset, A.: Physica **86-88B**, 1393-1394 (1977)

[Mor01]   Morais, P. C.; Garg, V. K.; Oliveira, A. C.; Silva, L. P.; Azevedo, R. B.; Silva, A. M. L.; Lima, E. C. D.: *Synthesis and characterization of size-controlled cobalt-ferrite-based ionic ferrofluids*, Journal of Magnetism and Magnetic Materials **225**, 37 (2001)

[Mor98]   Moridis, G.J., Borglin, S.E.; Oldenburg, C.M.; Becker, A.: *Theoretical and ExperimentalInvestigations of Ferrofluids for Guiding and Deteting Liquids in the Subsurface*, FY 1997, Annual Report. LBNL Report Number 41069, Lawrence Berkeley National Laboratory, Berkeley, CA (1998)

[Mor99]   Morales, M. P.; Andres-Verges, M.; Veintemillas-Verdaguer, S.; Montero, M. I.; Serna, C. J.: Journal of Magnetism and Magnetic Materials **203**, 146 (1999)

[Muk03]   Mukai, T., Suresh, S., Kita, K., Sasaki, H., Kobayashi, N., Higashi, K., Inoue, A.: *Nanostructured Al-FE alloys produced by e-beam deposition:static and dymanic tensile properties,* Acta Mater. **51**, 4917 (2003)

[Mül02]   Müller, R., Hiergeist, R., Gawalek, W.: *Ba-ferrites magnetic fluids with particle fraction above the superparamagnetic size limit,* 3rd Colloquium SPP1104 (2002)

[Mül03a]   Müller, R.; Hiergeist, R.; Gawalek, W.; Hoell, A.: *Ba-ferrite particles for magnetic liquids with enhanced neel relaxation time and loss investigations*, Magnetohydrodynamics **39** (1), 47-50 (2003)

[Mül03b]   Müller, R.; Hiergeist, R.; Gawalek, W.: *Preparation and properties of magnetic fluids*

based on particles with enhanced anisotropy barrier, 4rd Colloquium SPP1104 (2003)

[Mül04]   Müller, R.; Hiergeist, R.; Gawalek, W.: *Ba-ferrite magnetic fluids with particle fractions above the supermagnetic size limit*, 5th Colloquium SPP1104 (2004)

[Mül94]   Müller, R.; Schüppel, W.; Görnert, P.: *Glass crystallization of nanocrystalline $BaFe_{12-2x}Co_xTi_xO_{19}$ particles*, Electroceramics IV, Proceedings vol.II, 1183-1186, ISBN 3-86073-287-0, Aachen (1994)

[Née49]   Née, L.: Ann. Geophys (C.N.R.S.) **5**, 39 (1949)

[New03]   Newville, M.: *Fundamental of XAFS,* Consortium for Advanced Radiation Sources, University of Chicago, Chicago, IL, Revision 1.4.x (2003)

[New93]   Newville, M.; Livins, P.; Yacoby, Y.; Rehr, J. J.; Stern, E. A.: *Near-edge x-ray-absorption fine structure of Pb: A comparison of theory and experiment*, Physical Review B **47**, 14126-14131 (1993)

[Nie01]   Nietubyc, R.; Sobczak, E.; Attenkofer, K. E.: *X-ray absorption fine structure study of manganese compounds*, Journal of Alloys and Compounds **328**, 126 (2001)

[Nie03]   Nie, X.; Jiang, J.C.; Melets, E.I.; Tung, L.D.; Spinu, L.: J. Appl. Phys. **93**, 4750 (2003)

[Ode03]   Odenbach, S.: *Magnetic Fluids – suspensions of magnetic dipoles and their magnetic control*, J. Phys.: Condens. Matter **15**, 1497-1508 (2003)

[Pan04]   Pantelouris, A.; Modrow, H.; Pantelouris, M.; Hormes, J.; Reinen, D.: *The influence of Coordination Geometry and Valency on the Cr K-edge XANES spectra of selected Chromium compounds*, Chem. Phys. **300**, 13-22 (2004)

[Pap83]   Papirer, E.; Horny, P.; Balard, H.; Anthore, R.; Petipas, C.; Martinet, A.: J. Colloid Interface Sci, **94**, 220 (1983)

[Par04]   Park, S. I.; Lim, J. H.; Kim, J. H.; Yun, H. I.; Roh, J. S.; Kim, C. G.; Kim, C. O.: *Effects of surfactant on properties of magnetic fluids for biomedical application*, physica status solidi (b) **241** (7), 1662-1664 (2004)

[Pau00]   Paulus, U.A.; Endruschat, U.; Feldmeyer, G. J.; Schmidt, T. J.; Bönnemann, H.; Behm, R. J.: *New PtRu Alloy Colloids as Precursors for Fuel Cell Catalysts*, Journal of Catalysis **195**, 383-393 (2000)

[Pop95]   Popplewell, J.; Sakhnini, L.: Journal of Magnetism and Magnetic Materials, **72**, 149 (1995)

[Pri85]   Prinz, G. A.: Phys. Rev Lett. **54**, 1051 (1985)

[Qad01]   Qadri, S. B.; Skelton, E. F.; Dinsmore, A. D.; Hu, J. Z.; Kim, W.; Nelson, C.; Ranta, B. R.: Journal of Appl. Phys. **89**, 115 (2001)

[Ree96]   Reetz, M. T.; Quaiser, M.; Winter, M.; Becker, J. A.; Schaefer, R.; Stimming, U.; Marmann, A.; Vogel, R.; Konno, T.: Angew. Chem. Ind. Ed. **35**, 2092 (1996)

[Ree99]   Reetz, M. T.; Maase, M.: Adv. Mater. **11**, 773 (1999)

[Ric70]   Riches, E. E.: Ceramics (Brit. Pott. Manag. Ass., London) **21**, 12 (1970)

[Rog98]   Roger, J.; Pons, J. N.; Massart, R.; Halbreich, A.; Bacri, J. C.: *Some biomedical applications of ferrofluids*, Eur. Phys. J. AP **5**, 321-325 (1998)

[Rot97]   Rothe, J.: *Zwischen Molekül und Festkörper: Röntgenabsorptionsspektroskopie an Übergangsmetallkolloiden*, Dissertation Universität Bonn, BONN-IR-97-05 (1997)

[Rui91]   Ruiz-López, M. F.; Muńoz-Páez, A: *A theoretical study of the XANES spectra of rutile and anatase,* J.Phys.: Condens. Matter **3**, 8981 (1991)

[Sal02]   Salerno, M.; Krenn, J. R.; Lamprecht, B.; Schider, G.; Ditlbacher, H.; Felidj, N.; Leitner, A.; Aussenegg, F. R.: *Plasmon polaritons in metal nanostructures: The optoelectronic route to nanotechnology,* Opto-electronic Rev. 10, 217 (2002)

[Sar93]   Sarda, Ch.; Rousset, A.: Thermochimica Acta **222**, 21 (1993)

[Say71]   Sayers, D. E.; Stern, E. A.; Lyte, F. W.: *New technique for investigating noncrystalline structures: Fourier analysis of the extended X-ray absorption fine structure,* Phys. Rev. Lett. **27**, 1204-1207 (1971)

[Sch00]   Schmid, G.;Böumle, M.; Beyer, N.: Angew. Chem. Int. Ed. **39**, 182 (2000)

[Sch03]   Schmid, G.: *Nanoparticles - From Theory to Application*, (1. Edition), ISBN 3-527-30507-6 - Wiley-VCH, Weinheim (2003)

[Sch94]   Schmidt, G.: *Clusters and Colloids*, Eds., VCH, Weinheim (1994)

[Sch98]   Schmidt, T. J.; Noeske, M.; Gasteiger, H. A.; Behm, R. J.; Britz, P.; Bönnemann, H.: *PtRu Alloy Colloids as Precursors for Fuel Cell Catalysts*, Journal of Electrochemical Society **145**, 925-931 (1998)

[Smi60]   Smit, J.; Wijn, P. J.: *Ferrite*, Phillips tech. Lib., Eindhoven (1960)

[Sor01]   Sorensen, C. M.: Nanoscale Materials in Chemistry (Ed.: K. J. Klabunde), John Wiley and Sons, Inc., New York, 169 (2001)

[Ste92]   Steinthorsson, S.; Helgason, Ö.; Madsen M.B.; Bender Koch, C.; Bentzon M.D.; Morup, S.: Mineral. Mag. **56**, 185 (1992)

[Sum64]   Sumner, G. G.; Klug, H. P.; Alexander, L. E.: Acta Cryst. **17**, 732 (1964)

[Sun99]   Sun, S.; Murray C. B.: *Synthesis of monodispersed cobalt nanocrystalls and their assembly into magnetic superlattice*, J. Appl. Phys. **85**, 4325 (1999)

[Swe77]   Sweany, R. L.; Brown T. L.: Inorg. Chem. **16**, 415 (1977)

[Ter98]   Teranishi, T.; Miyake, M.: Chem. Mater. **10**, 594 (1998)

[Tho01]   Thompsom, A.: *Electron binding Energies in 'X-ray data Booklet'*, Lawrence Berkeley National Laboratory, University of California, Berkeley (2001)

[Tou99]   Tourinho, F. A.; Depeyrot, J.; da Silva, G. J.; Lara, M. C. L.: *Electric Double Layered Magnetic Fluids (EDL-MF) Based on Spinel Ferrite Nanostructures*, Brazilian Journal of Physics **28**, 413 (1999)

[Tur70]   Turkevitch, J., Kim, G.: Science **169**, 873 (1970)

[Tur85]   Turkevitch, J.: Gold Bull **18**, 86 (1985)

[Tur93]   Turilli, G.; Paoluzi, A.: *Magneto and magneto-optical recording materials*, Ceramics International **19**, 353 (1993)

[Var91]   Varadinov, R.; Nikolov, V.; Peshev, P.; Mitov, I.; Neykov, Kh.: *New solvents for the growth of substituted $BaFe_{12}O_{19}$ single crystals from high-temperature solutions*, Journal of Crystal Growth **110**, 763 (1991)

[Ver99]   Verelst, M.; Ould Ely, T.; Amiens, C.; Snoeck, E.; Lecante, P.; Mosset, M.; Respaud, M.; Broto, J.-M.: Chem. Mater. **11**, 2702 (1999)

[Voi00]   Voisin, C.; Christofilos, D.; Del Fatti, N.; Vallée, F.; Prével, B.; Cottancin, E.; Lermé, J.; Pellarin, M.; Broyer, M.: *Size-Dependent Electron-Electron Interactions in Metal Nanoparticles* , Physical Review Letters **85**, 2200 (2001)

[Wal03]   Wallach, R.: *Solid-state diffusionless transformations and twins*, Materials Science & Metallurgy Metals and Alloys (2003)

[Wat97]   Watzky, M. A.; Finke, R. G.: J. Am. Chem. Soc. **119**, 10382 (1997)

[Wen04]   Wen, F.; Bönnemann, H.; Mynott R. J.; Spliethoff, B.; Weidenthaler, C.; Palina, N.;
           Zinoveva, S.; Modrow, H.: *Preparation of Pt_{13} clusters in the presence of
           trialkylaluminium,* Chem. Comm. (2004 submitted)

[Wil00]   Williams, J. M.; Adetunji, J.; Gregori, M.: *Mössbauer spectroscopic determination of
           magnetic moments of Fe^{3+} and Co^{2+} in substituted barium hexaferrites*, Journal of
           Magnetism and Magnetic Materials **220**, 124-128 (2000)

[Yan97]   Yan, S. H.; Drabold, D. A.; Adams, J. B.; Ordejón, P.; Glassford, K.: J. Phys.: Condens.
           Matter **9**, L39 (1997)

[Yok84]   Yokoyama, H.: Jap. Ann. Rev. electr. Comp. telecomm. **15**, 187 (1984)

[Yu03]   Yu, T.; Shen, Z. X.; Toh, W. S.; Xue, J. M.; Wang, J.: *Size effect on the ferroelectric
           phase transition on $SrBi_2Ta_2O_9$ particles*, J. Appl Phys **94**, 618-620 (2003)

[Zha03]   Zhang, P.; Sham, T. K.: *X-Ray Studies of the Structure and Electronic Behavior of
           Alkanethiolate-Capped Gold Nanoparticles: The Interplay of Size and Surface Effects,*
           Physical Review Letters **90**, 245502 (2003)

[Zha96]   Zhang, Z.; Zhao, B.; Hu, L.: *PVP Protective Mechanism of Ultrafine Silver Powder
           Synthesized by Chemical Reduction Processes*, Journal of Solid State Chemistry **121**,
           105-110 (1996)

[Zho97]   Zhong, W.; Ding, W.; Jang, Y.; Zhang, N.; Du, Y.; Yan, Q.: Journal of the American
           Chemical Society **80**, 3258 (1997)

[Zub02]   Zubarev, A. Y.: *Ferrofluids – Magnetically Controllable Fluids and their Applications*,
           Springer LNP 594, ed. S. Odenbach (2002)

Table of Figures

List of Tables

Curriculum Vitae

December 9, 1979	Born in Samara, Russia (daughter of Mr. Palin Uyrey Mikhailovitch and Mrs. Palina Larisa Aleksandrovna).
September 1986 – June 1996	High School Education, School 79, Samara, Russia. In June 1996 graduated secondary school with first honour school-leaving certificate and gold medal.
September 1992 – June1996	Studying at the class with expending knowledge of nature science.
September 1996 – July 2001	Studying at the Physics department Samara of State University, Russia.
September 1999 – July 2001	Studying at the tree-years Language courses and after that had graduated the qualification 'Translator in the sphere of professional communication' at the Samara State University.
January 2000 – June 2001	Diploma thesis in Physical Institute of Russian Academy of Science, Samara Branch. Theme of science research: Analysis of main gas-dynamic parameters of Chemical Oxygen-Iodine Laser which formed by slit nozzle unit.
June 2001	Graduate Samara State University in June 2001 with First honour Diploma and had qualification 'Physicist. Lecture in physics. Translator in the sphere of professional communication'.
Since November 2001	PhD work with Prof. Dr. J. F. Hormes at the Physics Institute of Bonn University , Bonn, Germany
March 2003	Research assistance (Coloidal Chemistry and synthesis of magnetic nanoparticles and ferrofluids) at the MPI für Kohlenforschung, Mülheim (Ruhr), Germany
October 2003 – January 2004	Carried out the research work in outstanding conditions. Center of Advanced Microstructures and Devises in Baton Rouge, Louisiana, USA

Acknowledgements